HETEROGENEOUS MATERIAL CHARACTERIZATION USING INCOMPLETE AND COMPLETE DATA WITH APPLICATION TO SOFT SOLIDS

A Dissertation

by

YUE MEI

Submitted to the Office of Graduate and Professional Studies of
Texas A&M University
in partial fulfillment of the requirements for the degree of

DOCTOR OF PHILOSOPHY

Chair of Committee,	Sevan Goenezen
Committee Members,	Alan Freed
	Anastasia Muliana
	Raffaella Righetti
Head of Department,	Andreas A. Polycarpou

August 2017

Major Subject: Mechanical Engineering

ABSTRACT

This dissertation proposes and develops novel features into the existing inverse algorithms for characterizing nonhomogeneous material properties of soft solids. Firstly, a new feature that material properties are defined as a piece-wise constant in each element has been implemented in the inverse program. Secondly, to reduce boundary sensitivity of the solution to the inverse problem in elasticity, we modify the objective function using a spatially weighted displacement correlation term. Compared to the conventional objective function, the new formulation performs well in preserving stiffness contrast between the inclusion and background. Then, we present an approach to estimate the nonhomogeneous elastic property distribution using only boundary displacement datasets. We further improve this approach by using force indentation measurements to quantitatively map the elastic properties and analyze the sensitivity of this approach to a variety of factors, e.g., the location and size of the inclusion. Furthermore, we present a method to quantitatively determine the shear modulus distribution using full-field displacements with partially known material properties on the boundary and without any traction or force information. We test its performance using two different types of regularization: total variation diminishing (TVD) and total contrast diminishing (TCD) regularizations. We observe that TCD regularization is capable of mapping the absolute shear modulus distribution, while TVD regularization fails to achieve this. Furthermore, we investigate the feasibility of using the linear elastic inverse solver to solve inverse problems for nonlinear elasticity for large deformations. We conclude that the linear

elastic approximation will overestimate the stiffness contrast between the inclusion and background. We also extend the inverse strategy to map the orthotropic linear elastic parameter distributions. The reconstructions reveal that this method performs well in the presence of low displacement noise levels, while performing poorly with 3% noise. Finally, a feature that maps the viscoelastic behavior of solids using harmonic displacement data has been implemented and tested.

In summary, these new features not only strengthen our understanding in solving the inverse problem for inhomogeneous material property characterization, but also provide a potential technique to characterize nonhomogeneous material properties of soft tissues nondestructively that could be useful in clinical practice.

DEDICATION

To my parents and my wife

ACKNOWLEDGEMENTS

I would like to express my sincere gratitude and appreciation to my adviser, Dr. Goenezen for his guidance and encouragement during my Ph.D. career. Without his patient guidance and endless support, I would not have been able to easily settle down in the US and progress smoothly in my research. More importantly, he also taught me how to think critically and independently, which is crucial for a qualified researcher. This precious treasure will definitely benefit me in my future academic career. He is not only a good teacher, but also a good friend for me to resolve any puzzles that I have. His kindness eased my life in the US that has completely different cultures from China throughout my four years' studies.

I would also like to thank my committee members, Dr. Freed, Dr. Muliana and Dr. Righetti for their input and support throughout the course of this research. In particular, they spent a lot of time in reviewing my work and providing valuable suggestions to my research even though they already have very busy schedules.

I am grateful for my friends and labmates in College Station. Without their companionship and emotional support, my life here would not have been enjoyable.

Thanks also go to the department faculty and staff for making my time at Texas A&M University a great experience. They have built up an extraordinarily excellent campus and academic environment for students.

I would also like to thank my parents, my brother and his wife, my little niece and nephew, and all my other family members. Without their emotional and financial support,

I would not have been able to finish my education from primary to higher education. It is their unconditional devotion and love that has raised me up. I would also like to thank my wife's parents for their support in my overseas study and efforts to take care of my wife.

Special thanks go to my wife, Yuting Wan, thank you for your emotional support and endless love to me. I couldn't have imagined how good my life would get from the moment that I met you. I have enjoyed every moment we've spent together and would like to witness the beauty of the world with you to the end of my life.

CONTRIBUTORS AND FUNDING SOURCES

Contributors

Part 1, faculty committee recognition

This work was supervised by a dissertation committee consisting of Prof. Goenezen, Prof. Freed, Prof. Muliana of the Department of Mechanical Engineering and Prof. Righetti of the Department of Electrical and Computer Science.

Part 2, student/collaborator contributions

All work for the dissertation was completed independently by the student.

Funding Sources

There are no outside funding contributions to acknowledge related to the research and compilation of this document.

TABLE OF CONTENTS

Page

LIST OF FIGURES

Page

LIST OF TABLES

Page

1. INTRODUCTION

Material characterization of nonhomogeneous soft solids has great application in biomechanical engineering and clinical practice, e.g., breast tumor detection. To estimate heterogeneous material property distributions, one approach is to solve an inverse problem using measured displacement fields. In this dissertation, we focus on improving the existing inverse algorithms to assess the heterogeneous isotropic linear elastic and hyperelastic property distributions. We also propose and implement novel inverse algorithms to characterize anisotropic linear elastic paramter distribution and linear viscoelastic parameter distribution of soft solids using measured displacement fields.

1.1 Mechanical testing methods in engineering

Mechanical testing is of great importance to understand the mechanical properties of materials and is essential to assess whether a material is suitable for its intended application. For instance, Young's modulus is a measure of the stiffness of a linear elastic solid. A solid material with a higher Young's modulus will deform less than that having a lower Young's modulus when the same loading and boundary conditions are prescribed. Thus, in structural engineering, the Young's modulus is an important factor in selecting construction and building materials. Mechanical testing to characterize material properties is extremely crucial not only in traditional engineering fields including civil engineering, mechanical engineering, etc., but also in emerging engineering areas such as biomedical engineering. In **Sections 1.1.1** and **1.1.2**, a number of widely-used techniques to

characterize the mechanical properties for homogeneous and nonhomogeneous samples will be discussed, respectively.

1.1.1 Homogeneous material sample testing techniques

Uniaxial tensile and compression testing is one of the most fundamental mechanical testing approaches for homogeneous materials. In this method, a sample with predefined geometry is subject to a controlled uniaxial stretch or contraction, and the testing system records the total uniaxial force, the elongation or shortening in both loading and the lateral directions [1]. With the measured force and deformation, the stress-strain relation can be determined, from which material characteristics can be deduced [2]. Beyond linear elastic properties, these may include nonlinear elastic properties, viscoelastic parameters, or plastic properties via curve fitting using an appropriate constitutive model. Uniaxial tensile testing provides a fairly simple and effective method to characterize the mechanical behavior of solids and has been utilized to measure a wide range of mechanical properties of stiff solids such as alloys [3, 4], concretes [5, 6], and ceramics [7].

Uniaxial testing has also been applied to identify the biomechanical behavior of biological tissues, and considerable effort has been devoted to this area. In 1847, Wertheim performed uniaxial tension experiments to investigate the mechanical behavior of animal tissues and first observed nonlinear stiffening effect of animal tissues (stress increases much faster with increasing strain) from stress-strain curves [8]. The nonlinear stiffening effect has also been observed in other uniaxial testing experiments for different types of soft tissues [9-12] and motivated the advancement of novel hyperelastic constitutive

models specialized for the study of soft tissues such as Humphrey [13], Martins [14] and Veronda–Westmann models [15]. Uniaxial tension testing has also been used to investigate the viscoelastic behavior of soft tissues by recording the prescribed loading and stretch histories. For instance, in Fung's tension experiments, the stress relaxation and creep phenomena were observed for different types of soft tissues including rabbit mesemery [16]. Additionally, Woo et al. performed quasi-static and cyclical extension experiments to study the nonlinear viscoelastic characteristic of ligaments and tendons and developed a general continuum approach to describe the nonlinear viscoelastic behavior using the single integral finite strain model [17]. Experimental observations from uniaxial testing improved constitutive models of soft tissues and promoted the understanding of the mechanics of the human body.

In-plane biaxial testing is also very important in studying the mechanical response of solids. In in-plane biaxial testing, all four edges of the specimen are subjected to loadings. Although biaxial tests are unable to establish the stress-strain relation in three dimensions, they are sufficient to yield stress-strain relation in a 2-D plane for membranous structures such as animal skins. Feng et al. introduced and carried out biaxial in vitro experiments for biological tissues and first verified that animal skins are orthotropic [18, 19]. In addition to the nonlinear and anisotropic nature of human tissue, Feng et al. also observed the strain limiting phenomena of soft tissues in biaxial tests [20]. To study the effect of in-plane shear, Sacks' group developed an experimental method where the material axes of the sample are rotated 45 degrees from the biaxial testing device axes, thus making it possible to produce both shear and normal strains [21]. This method

has been used to study the mechanical behavior of thin tissues, e.g., heart valves [22, 23] and pericardium [21]. However, the authors neglected the shear tractions when mapping stresses from tractions. This leads to the violation of the conservation of angular momentum since the resulting 2nd Piola Kirchhoff stress tensor is not symmetric. This issue was resolved by Freed et al. using a general mapping to obtain the stress components from both normal and shear tractions [24].

Bending testing is another frequently used mechanical testing technique to measure elastic properties and has potential application to characterize the mechanical response of soft tissues. Compared to extension and compression testing of soft tissues, bending testing is capable of providing more accurate evaluation at low stress or strain levels [25]. This statement was also verified in [26] conducting three point bending tests on tissues.

Indentation is a mechanical testing method to measure the mechanical properties of materials by pressing a stiff tip to the surface of the specimen. In this method, measuring the force and depth of the indenter, the mechanical properties can be estimated for given geometry of the indenter. For a non-conforming indenter/sample contact, e.g., the spherical indenter tip is pressed into a flat surface. The Hertzian contact model has been applied to study contact mechanics in the vicinity of the contact region and to estimate the material properties from experimental data. A number of assumptions are made in the Hertzian contact model: The applied strain is very small; the contact area is very small compared to the size of the sample; the contact surface should be frictionless and smooth [27], the sample is homogeneous. These assumptions are often satisfied for stiff materials.

Therefore, the Hertzian contact model performs well in assessing stiffness of stiff engineering materials, e.g., metals.

In biomedical engineering and clinical medicine, indentation testing plays an important role in evaluating biomechanical parameters of bio-solids as well. The application of indentation testing for soft tissues dates back to the 1910s. In 1912, Schade was the first to apply indentations to soft tissues and estimated the elastic properties of skin and associated underlying soft tissues [28]. With the great progress of testing and recording techniques, the accuracy and reliability of the indentation tests for soft tissues vastly improved. Hitherto, the indentation testing technique has been used to quantify purely elastic, viscoelastic, and plastic properties of various tissues including skins at different body sites [29], muscles [30, 31], articular cartilages [32], etc.

In summary, we have discussed a number of commonly used material property testing methods, their applications and limitations in characterizing the mechanical behavior of engineering materials and biological tissues. In general, these methods assume that the material is homogenous, which does not hold for most biological tissues. Thus, mechanical testing approaches for heterogeneous material properties are required. In the next section, several nonhomogeneous sample testing approaches will be discussed.

1.1.2 Nonhomogeneous material sample testing techniques

Indentation testing is also used in mapping heterogeneous material properties. For instance, Kalei developed the depth-sensing micro/nano indentation techniques, in which force and displacement are measured at the micro/nano scale, making it possible to study the local mechanical response of materials in a very small region of the sample [33]. To

this end, material properties throughout the near-surface region can be quantified by changing the location of the indentation. This method has been improved in recent decades and widely used to assess the material properties of various inhomogeneous materials including layered structures [34], rocks [35], coals [36], etc. In biomechanical engineering, nanoindentation has been applied to understand the biomechanical response of nonhomogeneous biological tissues. Lin et al. used atomic force microscopy (AFM) based indentation approach to assess the elastic properties of inhomogeneous tissue phantoms [37, 38]. Hossein K. Heris also utilized AFM based indentation to map the elastic moduli, diffusivity coefficients, along with permeability coefficients at different locations of vocal fold tissue samples [39].

Indentation based mapping of material properties has several drawbacks. First, soft tissue/stiff indenter contact is of very complex interfacial behavior that makes it hard to model the contact area accurately, affecting accurate estimation of material properties. Second, the indentation can merely be applied to the surface area, thus, it is not possible to infer the mechanical property distribution throughout the volume. Third, indentation is a point-wise method, thus, it is time-consuming to map material properties on the surface for a relatively large sample. In addition, indentation testing assumes some regional homogeneity of the sample, while this approximation may not be true for some heterogeneous materials.

One approach to obtain the material property distribution non-destructively in the inner sample regions away from its surface is by done the strain imaging method, which is often referred to as “elastography” [40]. This method assesses the elastic properties

throughout the domain of interest using strain fields, assuming that the Young's modulus can be interpreted to be inversely proportional to the axial strain. The strain fields are computed using full-field displacement fields acquired non-destructively by a variety of imaging modalities such as ultrasound [41, 42], magnetic resonance imaging (MRI) [43, 44], computerized tomography (CT) scan [45, 46], etc. To date, strain imaging has been used in assessing nonhomogeneous elastic properties of soft tissues in clinical practice, e.g., detecting breast tumors from normal tissue. Studies have shown that strain imaging performed better than conventional ultrasound-based imaging techniques and mammography in clinical specificity tests (measuring the proportion of healthy people who are correctly identified as not having breast tumors) [47].

However, strain imaging is merely a qualitative approach to estimate the heterogeneous elastic property distribution and does not rigorously consider the physics, where the stress is not constant for a nonhomogeneous material. Accordingly, the induced artifacts will dominate in the strain images. To illustrate on a simple case, strain imaging will not work for the target problem domain shown in **Figure 1-1**. In this case, though the elastic property distribution is inhomogeneous, the corresponding strain field is homogeneous everywhere for a uniform displacement boundary applied on the top edge. Thus, strain imaging cannot even qualitatively be used to recover the layered elastic property distribution.

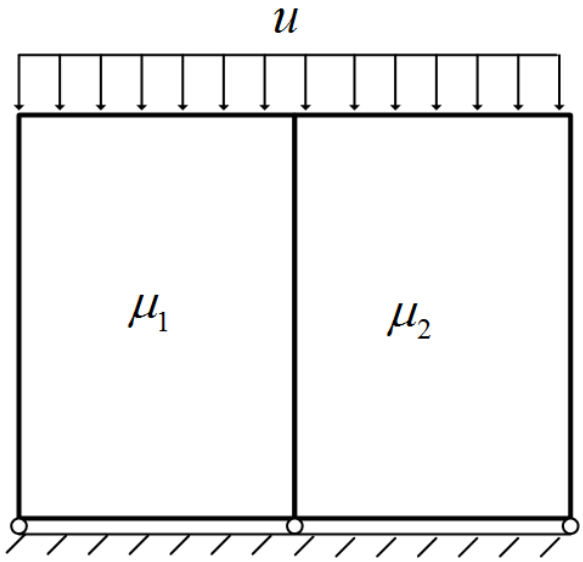

Figure 1-1: A schematic diagram of a layered problem domain ($\mu_1 \neq \mu_2$) subject to uniform compression on the top edge

Another promising technique to map nonhomogeneous material properties is by solving an inverse problem to obtain the spatially varying modulus reconstruction using quasi-static or dynamic deformations. In the quasi-static case of elasticity, solving the inverse problem has been used to determine shear modulus [48], or hyperelastic property [49] distributions using measured displacement fields. Typically, quasi-static displacement fields can be obtained from imaging modalities, while non-zero traction and force measurements cannot be acquired from images [50], e.g., in ultrasound-based imaging. Without any forces, non-zero traction measurements, or known elastic properties in the partial region of the problem domain, only qualitative solutions can be obtained due to the homogeneity of the governing equations [51].

Dynamic signals such as time harmonic or transient displacements can be used to solve the inverse problem as well. In this scenario, material property distribution can be obtained quantitatively using only displacement measurements as the introduction of the inertia term leads to the inhomogeneity of the governing equations. Another advantage of this approach is that dynamic signals such as shear wave are capable of propagating to the innermost part of the human body, thus providing an optimal non-invasive approach to characterize the biomechanical behavior of biological tissues including brain tissues [52], liver tissues [53], etc. Moreover, as many types of soft tissues are highly viscous and dynamic signals will experience phase lag due to viscosity, it is feasible to recover the viscoelastic properties by solving the inverse problem utilizing dynamic signals.

In general, there are two kinds of methods to solve the inverse problem: direct and iterative inversion methods. In direct inversion methods, we solve for the modulus distribution directly from the equilibrium equations [54, 55]. Direct inversion is computationally less costly than iterative inversion approaches. However, the direct inversion requires computing the derivative of measured displacement fields, which will amplify the noise of measured displacements as discussed previously. Another limitation of the direct inversion is that all displacement components must be known to solve the inverse problem. To circumvent these limitations, the inverse problem can be posed as a constrained minimization problem to seek the optimal material property distribution that fits the data. In this thesis, we will employ an iterative approach to estimate heterogeneous material properties and details related to the inverse algorithms will be presented in **Chapter 2**.

1.2 Application of nonhomogeneous sample testing

Mapping the nonhomogeneous material property distribution has potential application in biomechanical engineering and clinical practice, e.g. cancerous tumor detection, assessment of atherosclerosis, understanding neurodegeneration, etc. The following sections will elaborate on several clinical applications of the nonhomogeneous material property characterization of biological tissues.

(1) Breast cancer detection

Breast cancer develops due to the abnormal growth and proliferation of breast cells, these cells accumulate to form a lump or so-called breast tumor. Typically, cancerous tumors are much stiffer than normal tissues. According to [56], for 5% compression applied to a diseased breast tissue sample, the stiffness ratio between cancerous tumor and fatty tissue is roughly 5, while the stiffness ratio increases to 25 for a large compression of 20%. thus it may be feasible to identify cancerous tumors from normal tissues based on nonlinear material property maps.

(2) Assessment of atherosclerosis

According to the report from WHO, Ischemic heart disease (IHD), also known as coronary artery disease (CAD) is the top cause of death from 2002 to 2012 as shown in **Figure 1-2**. This disease is mainly due to atherosclerosis which is characterized by a soft plaque surrounded by a stiff cap [41, 57] and often referred to as “hardening of the arteries”. During this process cholesterol plaques will form, composed of fat, cholesterol, calcium, among other constituents [58]. For a clinician, it is crucial to know if the cap is stable in that an unstable cap can detach from the vessel wall, causing a potential heart

attack or stroke. The assessment of plaque stability requires patient specific knowledge of biomechanical vessel wall properties.

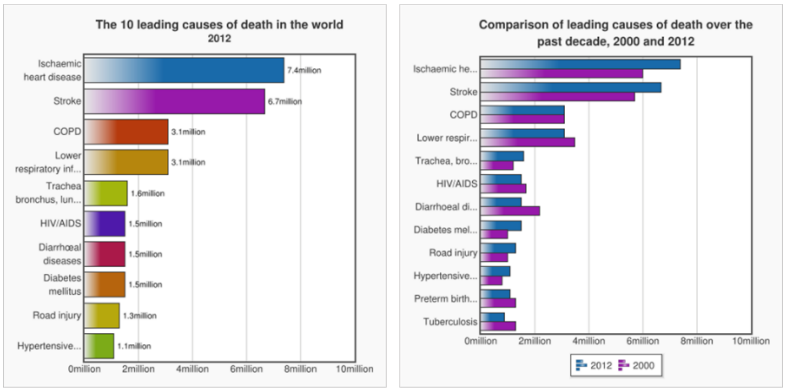

(a) (b)

Figure 1-2: (a) Top ten killers in the world 2012; (b) comparison of leading causes of death over the past decade, 2002 and 2012. [59]

(3) Investigation of brain development and neuro-system diseases

The human brain is a very complex organ that is mainly composed of an outer layer of grey matter and an inner core of white matter. Recent evidence shows that the elastic and viscous behavior of these two matters is different [60]. As a result, it is likely for us to identify the region of the grey and white matter by analyzing the recovered nonhomogeneous biomechanical property distribution of brain tissues. Also, it has been shown that the distinction of microstructures of grey and white matters play a crucial part of brain development [60]. Studies have also shown that the elastic and viscous response of brain tissue alters due to the influence of age [52]. Thus, nonhomogeneous material

property testing is likely to help us to understand the underlying mechanism of age-related neurodegeneration.

(4) Assessment of osteoporosis

Bone tissue is highly porous and its mechanical properties such as porosity and density will frequently alter in a person's lifetime. Bone-related diseases will also change the mechanical response of bones. For instance, osteoporosis is a medical disease in which bones become less dense and more inclined to break and brittle [61]. During the process of osteoporosis, the cavity area increases in the diseased bone, and the increased cavity area will reduce the strength and stiffness of the bone. Thus, mapping the heterogeneous biomechanical properties non-destructively, it may be feasible to detect the precise localization of osteoporosis and distinguish from healthy bone tissue, leading to a targeted treatment plan.

1.3 Organization of the dissertation

This work is based on inverse algorithms implemented by Goenezen et al. [62], and a number of new models, features, and algorithms have been implemented and tested. The organization of this dissertation is as follows:

Chapter 1 is the introduction of the work. It reviews a number of material characterization methods for homogeneous and heterogeneous solids and discusses the potential application of heterogeneous material characterization in biomechanical engineering and clinical medicine.

Chapter 2 reviews the theoretical foundation and numerical formulation of the nonlinear elasticity forward and inverse problems for incompressible materials. In

addition, the element-wise defined material property is introduced into the existing inverse algorithms and tested by numerical examples.

Chapter 3 introduces a spatially weighted objective function to address the issue that the reconstructed shear modulus distribution is sensitive to the boundary. The feasibility of this approach is tested by simulated data.

Chapter 4 presents a state-of-the-art approach to recover the elastic property distribution qualitatively by using only boundary displacement datasets.

Chapter 5 further improves the approach proposed in **Chapter 4** by using boundary displacements and force indentation measurements to quantitatively map the elastic property distribution.

Chapter 6 introduces a quantitative methodology to map the linear elastic property distribution of soft solids from displacements and partially known shear moduli. This new method enables us to obtain a unique solution to the inverse problem.

Chapter 7 investigates the feasibility of using the linear elastic inverse solver in solving the inverse problem in nonlinear elasticity. Reconstructed results using linear and nonlinear elastic inverse solvers are compared.

Chapter 8 discusses the feasibility of using iterative algorithms to solve for anisotropic linear elastic parameter distributions.

Chapter 9 proposes an innovative method to reconstruct the linear viscoelastic material property quantitatively utilizing time harmonic displacement fields.

Chapter 10 concludes this work with a summary and the discussion of future work.

2. ITERATIVE INVERSE PROBLEM IN ELASTICITY

In this chapter, an iterative strategy to solve the nonlinear inverse elasticity problems in the states of plane strain and plane stress will be reviewed. The soft tissues are modeled as an incompressible material using a modified Veronda-Westmann model [15], as this model is frequently used to approximate the nonlinear elastic behavior of the soft tissues [50, 63]. Furthermore, this model has only two material properties that have strong physical interpretations. The inverse problem is posed as a constrained minimization problem where the difference between the measured and computed displacements is minimized in L2 norm. The computed displacement field is obtained solving a forward problem under the current updated material properties. The minimization problem is solved by the limited BFGS method that is a gradient-based scheme and requires evaluating an objective function and its gradient with respect to material properties. As the evaluation of the gradients is a computationally intensive process, we introduce the adjoint method to address this issue [48, 49]. The feasibility of the inverse strategy is tested by simulated data in this chapter.

In the previous work [62], the material property is nodally defined and continuously distributed throughout the problem domain. In **Section 2.3.2**, the feature that the material property constantly defined piecewise in each element will be discussed and tested numerically in the 2-D plane stress case.

2.1 Forward nonlinear elasticity problem in 2D

In the 2D elasticity problem, there are generally two types of problems: plane strain and plane stress problems. The state of plane strain assumes that the out-of-plane strain is zero while the state of plane stress assumes that out-of-plane stress is zero. The governing equations for an incompressible elastic solid in these two cases are very similar. The major difference is that the hydrostatic pressure can be expressed explicitly in terms of the in-plane strain components in plane stress cases. However, in the state of plane strain, the hydrostatic pressure is unknown, thus should be treated as an unknown primary variable in the forward problem. In the following subsections, we will discuss the strong and weak forms of the elasticity forward problem.

2.1.1 Strong form

Let's consider a continuum body moved from the reference (undeformed) configuration Ω_0 at time t=0 to the current configuration Ω at time t. The boundaries in the reference and current frames are denoted by $\partial\Omega_0$ and $\partial\Omega$, respectively. We also assume that a point with the position vector $\mathbf{X}$ in Ω_0 occupies another position vector $\mathbf{x}$ in Ω, thus the motion of this body can be expressed as $\boldsymbol{x} = \boldsymbol{x}(\boldsymbol{X}, \mathrm{t})$. In Lagrange frame, the governing equations in two dimensions can be written as follows:

$$\mathrm{div}(\mathbf{P}) = \mathbf{0} \text{ in } \Omega_0 \tag{2.1}$$

$$\mathbf{u} = \mathbf{g} \text{ in } \Gamma_g \tag{2.2}$$

$$\mathbf{P} \cdot \mathbf{N} = \mathbf{h} \text{ in } \Gamma_h \tag{2.3}$$

where $\mathbf{P}$ is the first Piola-Kirchhoff stress tensor, and $\mathbf{u} = \mathbf{x}(\boldsymbol{X}, t) - \boldsymbol{X}$ is the displacement vector. Γ_g and Γ_h represent the displacement and traction boundaries, respectively. Γ_g and Γ_h constitute the entire boundary of this problem domain without overlapping, that is, $\Gamma_g \cup \Gamma_h = \partial\Omega_0$ and $\Gamma_g \cap \Gamma_h = \varnothing$. $\mathbf{g}$ and $\mathbf{h}$ are the enforced displacement and boundary vectors, respectively. $\mathbf{N}$ is the unit outward vector on the reference frame. Since most tissues are incompressible, the incompressible condition should be satisfied:

$$\det(\mathbf{F}) = 1 \tag{2.4}$$

where $\mathbf{F} = \partial \boldsymbol{x} / \partial \boldsymbol{X}$ is the deformation gradient. To solve the set of equations from **Equations (2.1)** to **(2.4)**, the stress-strain relation should be specified. For an incompressible elasticity, the second Piola-Kirchhoff stress tensor $\mathbf{S}$ can be expressed as:

$$\mathbf{S} = -pJ\mathbf{C}^{-1} + 2\frac{\partial W}{\partial \mathbf{C}} \tag{2.5}$$

Note that the relation between the first and second Piola Kirchoff stress tensors is $\mathbf{P} = \mathbf{FS}$. In **Equation (2.5)** $\mathbf{C} = \mathbf{F}^T\mathbf{F}$ is the right Cauchy Green tensor and $J = \det(\mathbf{F})$ is the Jacobian. *W* denotes the strain energy density function depending on the invariants of the right Cauchy Green tensor $\mathbf{C}$. The hydrostatic pressure *p* is unknown and must be determined in 2D incompressible plane strain or 3D incompressible cases. In the incompressible plane stress case, the hydrostatic pressure can be expressed in terms of in-plane right Cauchy Green tensor components [64], that is

$$p = \frac{2}{C_{33}} \frac{\partial W}{\partial C_{33}} \tag{2.6}$$

where $C_{33} = \left(C_{11} C_{22} - C_{12} C_{12} \right)^{-1}$. Therefore, it is unnecessary to solve for the hydrostatic pressure in the state of plane stress for an isotropic incompressible solid.

As mentioned at the beginning of this chapter, the incompressible hyperelastic strain energy function we will utilize is the modified Veronda-Westmann model proposed in [62]:

$$W = \frac{\mu}{2\gamma} \left(e^{\gamma \left(J^{-2/3} I_1 - 3 \right)} - 1 \right) \tag{2.7}$$

Here, $I_1 = \text{trace}\left(\mathbf{C} \right)$ is the first principle invariant of the right Green strain tensor. Two material parameters μ and γ have different physical interpretations. More specifically, μ is the shear modulus at the infinitesimal strain that controls linear behavior, while γ is the nonlinear parameter that controls the exponentially nonlinear behavior. The advantage of this material model is that each linear and nonlinear behavior is governed by only one material property, respectively. Thus, we could reconstruct shear modulus distribution at a relatively small strain level, and then recover nonlinear parameter distribution using data obtained from a large deformation. This sequential method to characterize linear and nonlinear elastic property was first proposed in [49, 62], and the numerical examples using this approach will be shown in **Section 2.3.1**. The constitutive model can be further reduced to the linear elastic model when the deformation is infinitesimal and the nonlinear parameter is set to zero.

2.1.2 Weak form

In this section, the weak formulation of the equilibrium equations can be easily derived by the following steps: (1) multiplying **Equation (2.1)** with a test function vector and integrating over the reference domain; (2) integrating by parts in order to reduce the order of the governing equations; and (3) enforcing the traction boundary conditions. For instance, in the plane strain case, the statement of weak form is to find $\mathbf{U} \equiv [\mathbf{u}, p] \in \mathrm{M} \times \mathrm{N}$ such that

$$A(\mathbf{W}, \mathbf{U}; \boldsymbol{\beta}) - (\mathbf{w}, \mathbf{h})_{\Gamma_h} = 0 \quad \forall \mathbf{W} \equiv [\boldsymbol{w}, q] \in K \times N \tag{2.8}$$

where

$$A(\mathbf{W}, \mathbf{U}; \boldsymbol{\beta}) = \int_{\Omega_0} w_{i,j} P_{ij} d\Omega_0 + \int_{\Omega_0} q(J-1) d\Omega_0 \tag{2.9}$$

$$(\boldsymbol{w}, \mathbf{h})_{\Gamma_h} = \int_{\Gamma_h} \boldsymbol{w} \cdot \mathbf{h} d\Gamma_h \tag{2.10}$$

In **Equation (2.9)**, **W** is the test function vector and $\boldsymbol{\beta}$ is the vector of material parameters for a given constitutive model. In addition, the incompressible condition is enforced, and q is acted as a Lagrangian multiplier. The function spaces are defined as follows:

$$M = \left\{ \boldsymbol{u} \middle| u_i \in H^1(\Omega_0); u_i = g_i \text{ on } \Gamma_g \right\} \tag{2.11}$$

$$N \subseteq L_2(\Omega_0) \tag{2.12}$$

$$K = \left\{ \boldsymbol{w} \middle| w_i \in H^1(\Omega_0); w_i = 0 \text{ on } \Gamma_g \right\} \tag{2.13}$$

Note that the derivation in the plane stress case is very similar, thus we will not discuss herein.

2.1.3 Stabilization of the mixed finite element formulation

As discussed in **Section 2.1.1**, both displacement and pressure are required to be solved for in the incompressible 2-D plane strain or incompressible 3-D cases, thus a mixed finite element formulation will be established after discretizing the weak form and utilizing the Ritz finite element approach. However, when the equal order interpolating function is utilized to approximate both the displacement and pressure fields, the resulting linearized system does not satisfy the Ladyzenskaja-Babuska-Brezzi (LBB) condition [65, 66] and leads to several numerical issues [67]. To satisfy the LBB condition, we can use different orders of interpolation functions for the displacement and pressure, respectively, but this choice is inconvenient in writing program code. To adopt interpolation functions with the same order in the finite element formulation, we could utilize the stabilized finite element method where an additional stabilization term is introduced, thus the weak formulation is modified. The modified discretized weak form is to find $\mathbf{U}^h = \left[\mathbf{u}^h, p^h\right] \in \mathrm{M}^h \times \mathrm{N}^h$:

$$\begin{aligned} &A\left(\mathbf{W}^h, \mathbf{U}^h; \boldsymbol{\beta}\right) + D\left(\mathbf{W}^h, \mathbf{U}^h; \boldsymbol{\beta}\right) - \left(\mathbf{w}^h, \mathbf{h}\right)_{\Gamma_h} = 0 \\ &\forall \mathbf{W} \in \left[\mathbf{w}^h, q^h\right] \in K^h \times N^h \end{aligned} \tag{2.14}$$

where the stabilization term is given by:

$$D\left(\mathbf{W}^h, \mathbf{U}^h; \boldsymbol{\beta}\right) = -\sum_{i=1}^{N} \left(\tau \nabla \cdot \left(\mathbf{P}\right), \mathbf{F}^{-T} \nabla q^h\right)_{\Omega_0^i} \tag{2.15}$$

Here *i* denotes the *i*-th element and Ω_0^i indicates the domain of the *i*-th element. *N* is the total number of elements, and τ is the stabilization term and chosen following Hughes et al. [67]:

$$\tau = \frac{\alpha h^2}{2\mu} \tag{2.16}$$

In **Equation (2.16)**, we observe that τ is inversely proportional to μ, and proportional to both a factor α and the characteristic element length *h*. The factor α can be chosen between 0 and 1, while the characteristic element length depends on the element type and size. For instance, *h* is the longest edge for a triangular element or the longest diagonal for a bilinear element. With the assistance of **Equation (2.5)**, the stabilization term can be further simplified:

$$\begin{aligned} & D\left(\mathbf{W}^h, \mathbf{U}^h; \boldsymbol{\beta}\right) \\ & = -\sum_{i=1}^{n} 2\left(\tau\nabla\cdot\left(\mathbf{F}\frac{\partial W}{\partial \mathbf{C}}\right), \mathbf{F}^{-T}\nabla q^h\right)_{\Omega_0^i} + \sum_{i=1}^{n}\left(\tau\nabla\cdot\left(p^h J\mathbf{F}\mathbf{C}^{-1}\right), \mathbf{F}^{-\mathrm{T}}\nabla q^h\right)_{\Omega_0^i} \\ & = -\sum_{i=1}^{n}\left(2\tau\mathbf{F}\nabla\cdot\left(\frac{\partial W}{\partial \mathbf{C}}\right), \mathbf{F}^{-\mathrm{T}}\nabla q^h\right)_{\Omega_0^i} + \sum_{i=1}^{n}\left(\tau J\mathbf{F}^{-\mathrm{T}}\nabla p^h, \mathbf{F}^{-\mathrm{T}}\nabla q^h\right)_{\Omega_0^i} \end{aligned} \tag{2.17}$$

Note that the simplification of the first term of the right-hand side in **Equation (2.17)** assumes that the problem domain is discretized by linear triangular elements. The detailed derivation procedure is shown in **Appendix A**.

The modified weak form with stabilization term **(2.14)** should be linearized and solved by Newton's method, and the detailed procedure is shown in **Appendix B**. The stabilized weak form can be discretized and successfully solved by the finite element method with the same order interpolation function for all degrees of freedom [68]. We will utilize the stabilized finite element method to solve the forward problem throughout this dissertation.

2.2 Inverse problem in elasticity

In this work, the inverse elasticity problem is posed to be a constrained optimization problem where the mismatch between measured displacement and the computed displacement fields are minimized. The computed displacement should satisfy the forward elasticity problem under the current estimate of the material property distribution. The optimization problem is solved by a gradient-based method called the limited BFGS algorithm [69-71] where the objective function value and the first order derivative with respect to material properties are required.

2.2.1 The objective function of the inverse problem

The inverse problem is stated as: Given the displacement fields $\mathbf{u}^1_{meas}, \mathbf{u}^2_{meas}, ..., \mathbf{u}^n_{meas}$, find the material properties vector $\boldsymbol{\beta}=[\beta_1, \beta_2, \cdots, \beta_m]$ such that the objective function:

$$F = \frac{1}{2}\sum_{i=1}^{n} w_i \| \mathbf{T}(\mathbf{u}^i - \mathbf{u}^i_{meas}) \|_0^2 + \frac{1}{2}\sum_{j=1}^{m} \alpha_j \mathrm{Reg}\left(\beta_j\right) \tag{2.18}$$

is minimized where the constraint is that the computed displacement field $\mathbf{u}^i$ satisfies the forward problem in elasticity. The first term on the right-hand side of **Equation (2.18)** is referred to as the displacement correlation term that minimizes the difference between the computed and measured displacement fields in L2 norm. The tensor **T** is a diagonal tensor that weights different displacement components differently and each component of this tensor is chosen based on the noise level, e.g., the displacement components with higher noise level contribute less to the objective function. For instance, in ultrasound-based imaging, the displacement component parallel to the transducer axis is much more accurate than the component perpendicular to the axis. Hence, the former displacement

component should be weighed more in the objective function. w_i is a vector to weight for different displacement measurements. The second term in **Equation (2.18)** is called regularization term. The role of this term is to penalize the oscillations in the reconstruction and smooth the final reconstructed modulus distributions. There are numerous regularization types, and the total variation diminishing regularization (TVD regularization) will be frequently used in this dissertation, which is given by:

$$\mathrm{Reg}(\beta_i) = \int_{\Omega} \sqrt{|\nabla \beta_i|^2 + c^2}\, d\Omega \tag{2.19}$$

where c is a small constant to avoid singularity when computing the gradient of the regularization term. TVD regularization is capable of preserving the sharp change of material properties. The regularization factor α_i is used to control the significance of the regularization. If the factor is very small, the final solution will oscillate intensely. On the contrary, the reconstructed results will be oversmoothed with a large regularization factor. How to choose an optimal regularization factor has been studied, and a number of methods have been proposed, e.g., L-curve method [72-75] or smooth criteria [62]. In this work, the regularization factor will be selected based on visual observation such that the overall reconstruction in the problem domain is neither too smooth nor too oscillating. More specifically, we will start with a very high regularization factor and solve the inverse problem, and then keep decreasing the regularization factor until some region of the reconstruction images does not look overly smooth and should start oscillating.

2.2.2 Adjoint method for gradient evaluation

The optimization problem is solved utilizing the gradient-based quasi-Newton method that requires the gradient of the objective function with respect to material properties $\boldsymbol{\beta}$. In a discretization problem, the gradient will also be evaluated in discretized level, and a gradient vector for a specific material property β_i will be constructed. The dimension of the gradient vector depends on the mesh. In most cases, the gradient will be evaluated at every element or node in the discretized problem domain, and this requires solving a forward problem for every nodal or element-wise gradient evaluation. Thereby, the gradient evaluation process is computationally costly. To address this deficiency the adjoint method is introduced [64, 76] and the specific procedure is shown below:

Let's change $\boldsymbol{\beta}$ by an infinitesimal increment to $\boldsymbol{\beta}+\delta\boldsymbol{\beta}$, and the displacement and pressure will change accordingly from $\mathbf{u}^i$ and p^i to $\mathbf{u}^i+\delta\mathbf{u}^i$ and $p^i+\delta p^i$ for *i*-th measurement, respectively. Then we can obtain the relation between $\delta\boldsymbol{u}^i$ and δp^i by differentiating the stabilized weak form **(2.14)**.

$$B\left(\mathbf{W},\delta\mathbf{U}^i;\boldsymbol{\beta},\mathbf{U}^i\right)+C\left(\mathbf{W},\delta\boldsymbol{\beta};\mathbf{U}^i,\boldsymbol{\beta}\right)=0 \tag{2.20}$$

Similarly, differentiating the objective function **(2.18)** yields

$$D_{\boldsymbol{\beta}}F=\sum_{i=1}^{n}\left(w_i\mathbf{T}\delta\mathbf{u}^i,\mathbf{T}(\mathbf{u}^i-\mathbf{u}^i_{meas})\right)+\frac{1}{2}\sum_{j=1}^{m}\alpha_j\mathrm{D}_{\boldsymbol{\beta}}\mathrm{Reg}\left(\beta_j,\delta\beta_j\right) \tag{2.21}$$

Where

$$\mathrm{D}_{\boldsymbol{\beta}}\mathrm{Reg}\left(\beta_j\right)=\lim_{\varepsilon\to 0}\frac{d}{d\varepsilon}\mathrm{Reg}\left(\beta_j+\varepsilon\delta\beta_j\right) \tag{2.22}$$

Let's define another boundary value problem that finds $\bar{\mathbf{W}}^i\in K^h\times N^h$ such that

$$B\left(\bar{\mathbf{W}}^i, \mathbf{V}; \boldsymbol{\beta}, \mathbf{U}^i\right) + \sum_{i=1}^{n}\left(w_i \mathbf{T}\boldsymbol{v}, \mathbf{T}(\mathbf{u}^i - \mathbf{u}^i_{meas})\right) = 0 \qquad \forall \mathbf{V} \in K^h \times N^h \tag{2.23}$$

Replacing $\mathbf{V}$ with $\delta \boldsymbol{U}^i$ in **Equation (2.23)** leads to the adjoint equation:

$$B\left(\bar{\mathbf{W}}^i, \delta\mathbf{U}^i; \boldsymbol{\beta}, \mathbf{U}^i\right) + \sum_{i=1}^{n}\left(w_i \mathbf{T}\delta\mathbf{u}^i, \mathbf{T}(\mathbf{u}^i - \mathbf{u}^i_{meas})\right) = 0 \tag{2.24}$$

We also replace $\mathbf{W}$ in **Equation (2.20)** with $\bar{\mathbf{W}}^i$, which gives

$$B\left(\bar{\mathbf{W}}^i, \delta\mathbf{U}^i; \boldsymbol{\beta}, \mathbf{U}^i\right) + C\left(\bar{\mathbf{W}}^i, \delta\boldsymbol{\beta}; \mathbf{U}^i, \boldsymbol{\beta}\right) = 0 \tag{2.25}$$

Combing **Equations (2.24)** and **(2.25)** yields

$$\sum_{i=1}^{n}\left(w_i \mathbf{T}\delta\mathbf{u}^i, \mathbf{T}(\mathbf{u}^i - \mathbf{u}^i_{meas})\right) - C\left(\bar{\mathbf{W}}^i, \delta\boldsymbol{\beta}; \mathbf{U}^i, \boldsymbol{\beta}\right) = 0 \tag{2.26}$$

Substituting **Equation (2.26)** into **(2.21)**, one can obtain the final expression for the gradient

$$D_{\boldsymbol{\beta}} F = \sum_{i=1}^{n} C\left(\bar{\boldsymbol{W}}^i, \Delta\beta; \beta, \boldsymbol{U}^h\right) + \frac{1}{2}\sum_{j=1}^{m} \alpha_j \mathrm{D}_{\beta_j} \mathrm{Reg}\left(\beta_j, \delta\beta_j\right) \tag{2.27}$$

Hence, the procedure to solve the inverse problem utilizing the adjoint method is summarized as follows:

1) Solving a forward problem with a current estimate of material property distribution to obtain the computed displacement.
2) Using the computed displacement field to solve for $\bar{\mathbf{W}}^i$ by **Equation (2.24)**.
3) Taking $\bar{\mathbf{W}}^i$ into **Equation (2.27)** to evaluate the gradient of the objective function with respect to material properties.

4) Using the objective function and its gradients to evaluate the updated material property distribution by the limited BFGS method.
5) Repeating Step 1) to 4) until the objective function is minimized.

The adjoint method only requires solving one forward problem to evaluate the gradient of the objective function with respect to material properties for each measurement in every minimization iteration, which significantly reduces computational time.

2.2.3 The element-wise TVD regularization

The material properties can also be defined constantly in each element. This choice has potential significance in simulating the mechanical behavior of functional gradient materials (FGM) [77-79] in that for an FGM structure, different materials are bonded together and there is no continuous transition from one material to the other. Hence, we should include the feature of element-wise defined material properties into the inverse algorithms. As the elastic property distribution is spatially discontinuous in the discretized problem domain, the TVD regularization **(2.19)** should be revised and the mathematical derivation for the element-wise TVD regularization are shown below.

Let's consider any two arbitrary neighboring elements A and B as shown in **Figure 2-1** (a). The corresponding values of the material property for A and B are $\boldsymbol{\beta}^A$ and $\boldsymbol{\beta}^B$, respectively. To better analyze this problem, a local coordinate system is introduced where the directions of the two coordinate axes *s* and *t* are along and perpendicular to the interface between these two neighboring elements, respectively. The local coordinate system are defined by rotating the Cartesian coordinate axes by an angle of θ as shown in **Figure 2-1** (b). As the material property distribution is discontinuous in the domain of

interest, the material properties are assumed to be constant at every element to preserve the discontinuous transition. In this case, the material properties do not vary along the interface, i.e. $\partial \boldsymbol{\beta} / \partial s = 0$. In other words, the material properties only depend on the variable *t*. Recall the continuous form of TVD regularization formulation neglecting the constant *c* for elements A and B:

$$\mathrm{Reg}^{AB}(\beta_i) = \int_{\Omega^A \cup \Omega^B} \sqrt{|\nabla \beta_i|^2}\, d\Omega \tag{2.28}$$

According to the rules of coordinate transformation, **Equation (2.28)** can be rewritten in terms of *s* and *t*, that is:

$$\mathrm{Reg}^{AB}(\beta_i) = \int_{\Omega^A \cup \Omega^B} \left|\frac{\partial \beta_i}{\partial t}\right| dt ds = l \left|\frac{\partial \beta_i}{\partial t}\right| \tag{2.29}$$

To achieve **Equation (2.29)**, the condition, $\partial \beta_i / \partial s = 0$, is utilized. Based on the jump condition, the TVD formulation can be further reduced to:

$$\mathrm{Reg}^{AB}(\beta_i) = l^{AB} \left|\beta_i^A - \beta_i^B\right| \tag{2.30}$$

where l^{AB} is the length of the interface between the elements A and B, and the discretized TVD regularization is also linearly proportional to the shear modulus difference between the neighboring elements. To avoid the singularity issue when taking the gradient of the discretized regularization, a constant *c* is also introduced as :

$$\mathrm{Reg}^{AB}(\beta_i) = l^{AB} \sqrt{\left(\beta_i^A - \beta_i^B\right)^2 + c^2} \tag{2.31}$$

This new formulation has been successfully implemented into our iterative inverse solver, and we will test the new feature with a numerical example in **Section 2.3.2**.

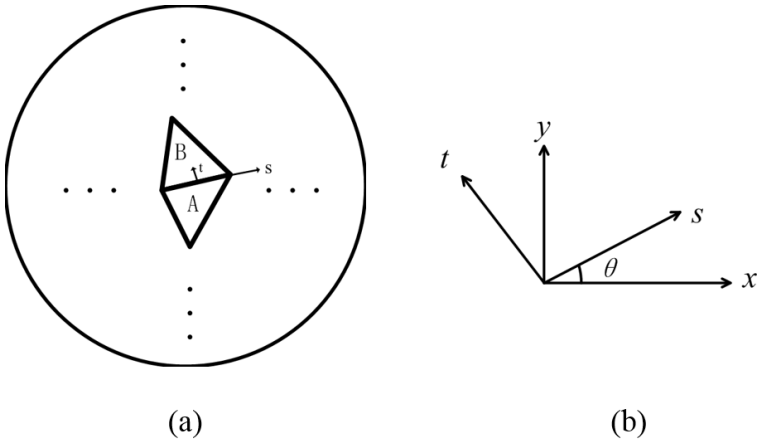

Figure 2-1: (a) The schematic diagram of two neighboring elements A and B in the discretized problem domain; (b) the coordinate transformation from the global coordinate system and the local coordinate system.

2.3 Numerical results

In this Section, the inverse algorithms discussed previously will be tested numerically. The measured displacement field is acquired by solving a forward problem in elasticity using the finite element approach. To mimic the experimental data, 3% white Gaussian noise is introduced to the full-field displacement field. Both the displacement and pressure are interpolated by linear interpolation functions in each element in the 2-D plane strain case for the incompressible material, and the material properties are defined in each node in **Section 2.3.1** or each element in **Section 2.3.2**. In **Section 2.3.1**, we will adopt the linear function to interpolate material properties and use the modified Veronda-Westmann model **(2.7)** in the state of plane strain to model the mechanical response of soft solids. In **Section 2.3.2**, the problem domain is assumed in the state of incompressible

plane stress, and the shear modulus is interpolated constantly in each element, thus the shear modulus is distributed discontinuously throughout the domain.

2.3.1 Numerical results for nodally defined material properties

The simulated tissue in this section is modeled using the modified Veronda-Westmann law **(2.7)**. To reconstruct the shear modulus and nonlinear parameter distributions of the problem domain, we could employ two approaches. A common way is to assess them simultaneously, but the quality of reconstructions is inferior [62]. An alternative idea is to reconstruct shear modulus and nonlinear parameter distributions sequentially. As discussed in **Section 2.1.1**, the shear modulus and nonlinear parameter govern the linear and nonlinear behaviors, respectively. Thus we are able to reconstruct shear modulus by applying an infinitesimal deformation first and then reconstruct the nonlinear modulus by applying a large deformation. This approach takes advantage of the physical meaning of each material parameter, and its proof of concept has been successfully shown by simulations and experiments [49, 62]. In this section, we will present a numerical example of the sequential method. The problem domain is a unit square as depicted in **Figure 2-2** which mimics a diseased breast tissue. The inclusion inside represents a tumor with a radius of 0.2, the rest part represents the normal tissue. The shear modulus and nonlinear parameter ratios of the inclusion to the background are 5:1 and 10:1, respectively. We apply compression on the top edge and restrict the vertical motion of the bottom edge. To avoid the rigid body motion, we fix the center node of the bottom. The other two sides are traction free.

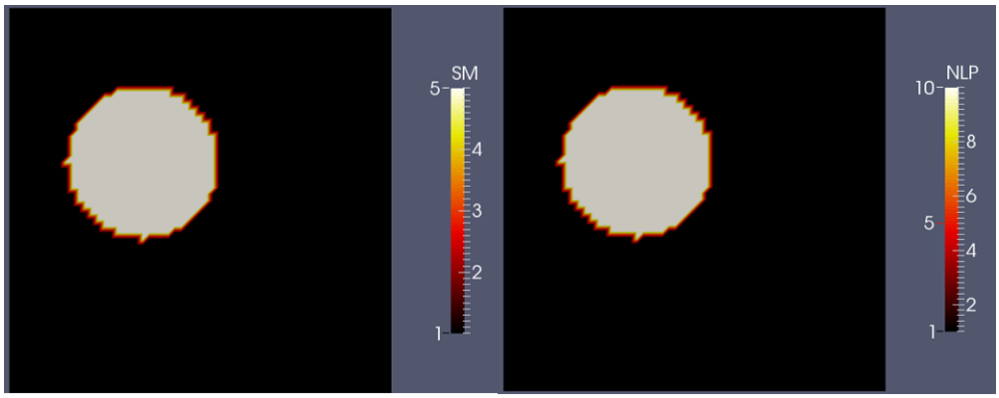

(a) (b)

Figure 2-2: Problem domain of a diseased tissue model: (a) target shear modulus distribution; (b) target nonlinear parameter distribution.

We first apply 0.2% compression on the top. In this case, the nonlinear behavior of the simulated phantom can be neglected, thus the shear moduli can be recovered independently. We then apply 20% compression on the top side, and the nonlinear effect will become significant. In this case, given the reconstructed shear modulus acquired earlier, the nonlinear parameter can be determined. The target problem domain and reconstructed results are presented in **Figure 2-2** and **Figure 2-3,** respectively.

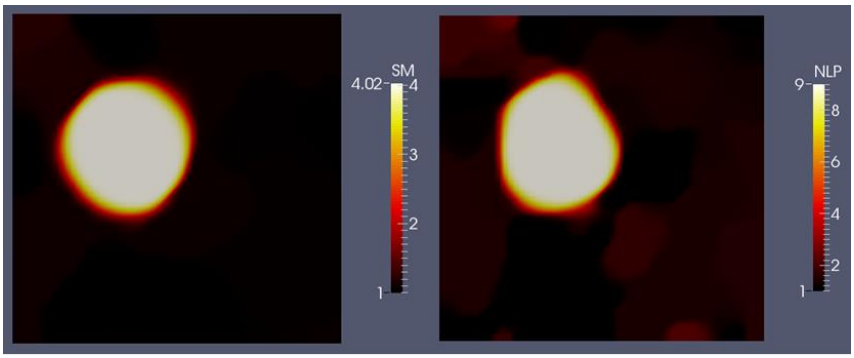

Figure 2-3: Reconstruction results for the target distribution shown in **Figure 2-2**. (a) reconstructed shear modulus distribution; (b) reconstructed nonlinear parameter distribution.

In **Figure 2-3**, the regularization factors are selected as 5.0×10^{-11} for the shear modulus and 3.5×10^{-8} for the nonlinear parameter, respectively. It is clear to see that both the shear modulus and nonlinear parameters of this large inclusion are well recovered. However, the shape of the inclusion of the shear modulus reconstruction is recovered better than in the nonlinear parameter reconstruction. Similar trends are also observed in [49, 62].

2.3.2 Numerical results for element-wise material properties

The numerical example presented in this section is very similar to the case shown in **Section 2.3.1**, and the problem domain is shown in **Figure 2-4** (a). In this scenario, we set the nonlinear parameter to zero, and the shear modulus value in the inclusion is 10 times larger than that of the background. We apply a uniformly distributed vertical displacement of 0.01 on the top edge, and the boundary conditions in other three sides are

the same as those used in **Section 2.3.1**. The elastic solid is assumed in the state of plane stress, and we utilize 3600 bilinear elements to discretize the problem domain. Note that the piece-wise constant material property is utilized in the FEM model to preserve the discontinuity of shear moduli crossing the interface between the inclusion and background in this numerical example.

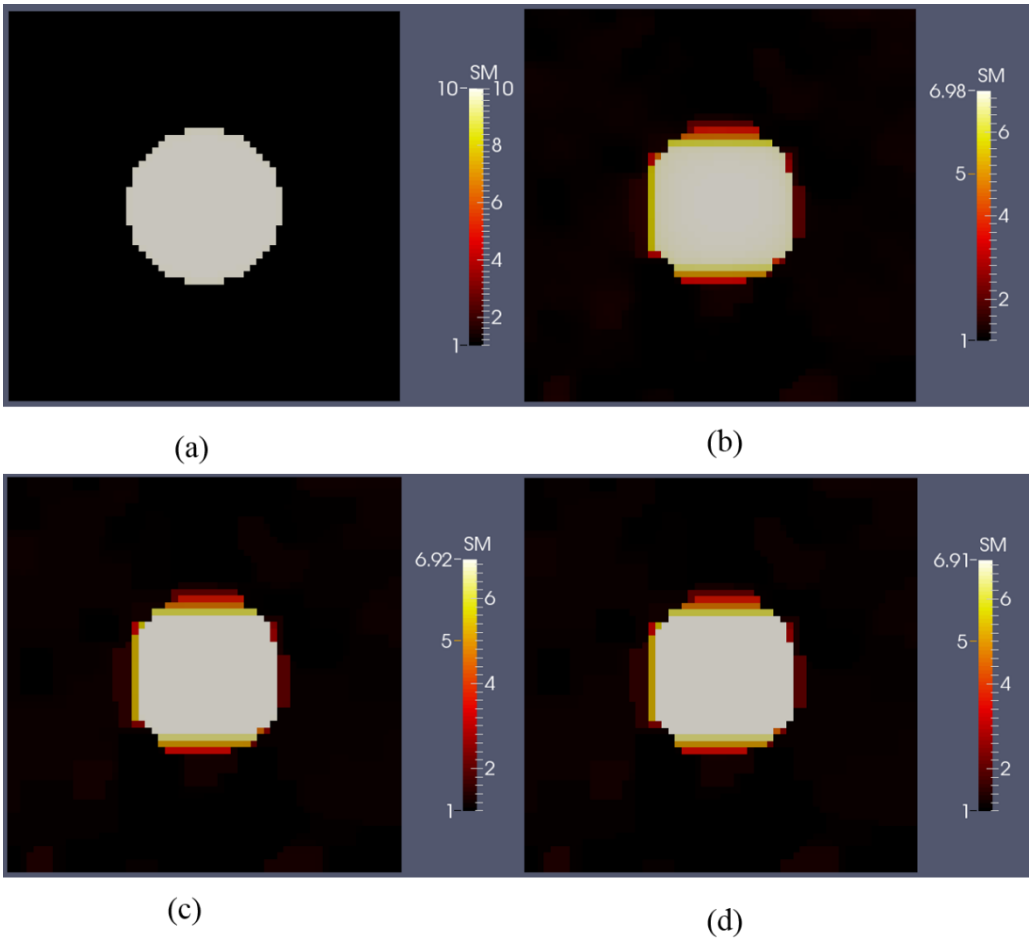

Figure 2-4: (a) Target shear modulus distribution; (b)-(d) shear modulus reconstruction when the constant c is selected to be 10^{-1},$10^{-1.5}$ and 10^{-2}, respectively.

Figure 2-4 (b) to (d) exhibit the reconstructions of shear modulus distribution with respect to the different constants c (c=10^{-1}, $10^{-1.5}$ and 10^{-2}, respectively) in the presence of 3% noise. The regularization factors for all cases are chosen as 3.0×10^{-10}. According to these results, subtle differences in the shear modulus value as well as the shape of the inclusion are observed in the reconstructions using different constants c. Moreover, we also observe that there is no continuous transition of shear modulus between two neighboring elements. Thus, this method may have some potential in reconstructing FGM structures having discontinuous interfaces between different materials.

2.4 Conclusions

In this chapter, we elaborate on the mathematical foundation of the iterative inverse problem in finite deformations and exhibits several numerical examples to test the feasibility of the inverse scheme. To test the inverse algorithms, we firstly solve a forward problem to obtain the simulated data, and the simulated data is used as the measured field in solving the inverse problem. In the inverse problem, 3% white Gaussian noise is added throughout the problem domain to mimic the experimental data. The inverse problem is posed to be an optimization problem and solved by the limited BFGS method. We observed that the stiff inclusion in the problem domain is mapped well in both the stiffness value and the shape. The reconstructed results demonstrate the robustness of the in-house inverse algorithms.

3. REDUCED BOUNDARY SENSITIVITY AND IMPROVED CONTRAST OF THE REGULARIZED INVERSE PROBLEM SOLUTION IN ELASTICITY[*]

Recently, we realized that this inverse strategy to solve for the shear modulus distribution depends on the deformation field. In other words, the shear modulus reconstruction is sensitive to changing boundary conditions for a given problem domain. In this chapter, we demonstrate that this issue occurs when two inclusions, e.g., representing two tumors, in a homogeneous background are presented. We illustrate that the strain field and the total variation (TV) regularization play a key role in the elastic parameter reconstruction. We address this issue utilizing a spatially weighted displacement correlation term as a function of the strain field. We thoroughly discuss these observations in **Section 3.4** and derive a coupled 1-D analytical expression to analyze our findings. We observe that boundary sensitivity 1) occurs independent of noise, and 2) can be reduced by modifying the displacement correlation term by a strain dependent term. The 1-D results closely resemble the results obtained from the 2-D continuum model. Our analysis shows that the modified objective function works for any number of similar sized inclusions embedded in a soft background with distinct inclusion stiffness values. This analysis however is constrained by the fact that the inclusions may not share the same horizontal position, while the vertical position of each inclusion may be arbitrary.

Furthermore, we improve the contrast of the elastic parameter reconstructions utilizing a spatially varying regularization factor in a posterior step, while at the same time yielding a smoother elastic parameter reconstruction.

3.1 Spatially weighted displacement correlation method

The proposed inverse formulation involves a modification of the objective function given as

$$F = \frac{1}{2}\sum_{i}^{n} \| \mathbf{W}^i (\mathbf{u}^i - \mathbf{u}^i_{meas}) \|_2^2 + \frac{1}{2}\alpha \int_{\Omega} \sqrt{|\nabla \mu|^2 + c^2}\, d\Omega \tag{3.1}$$

where $\mathbf{W}^i$ is a weighting function of the measured normal strain components $\boldsymbol{\varepsilon}^i_{xx}$, $\boldsymbol{\varepsilon}^i_{yy}$, and $\boldsymbol{\varepsilon}^i_{zz}$ corresponding to the *i*-th deformation field:

$$\mathbf{W}^i = \begin{pmatrix} \frac{1}{\boldsymbol{\varepsilon}^i_{xx}} & 0 & 0 \\ 0 & \frac{1}{\boldsymbol{\varepsilon}^i_{yy}} & 0 \\ 0 & 0 & \frac{1}{\boldsymbol{\varepsilon}^i_{zz}} \end{pmatrix} \tag{3.2}$$

The contribution of shear strain components is neglected in the weighting function as the shear strain is small compared to the normal strain for the uniaxial compression simulation performed in this chapter. As discussed earlier, we assume that the deformation field is in two-dimensional space, thus we omit the displacement and strain components in the *z*-direction. Furthermore, assuming that we have only one "measured" displacement field, and that the displacement component in the *x* direction is highly noisy and does not contribute to the objective function, **Equation (3.1)** reduces to:

$$F = \frac{1}{2} \| \frac{(u_y - (u_{meas})_y)}{\varepsilon_{yy}} \|_2^2 + \frac{1}{2} \alpha \int_\Omega \sqrt{|\nabla \mu|^2 + c^2} d\Omega \tag{3.3}$$

Note that we do not utilize the measured strain field directly in **Equations (3.2)** and **(3.3)** to spatially weight the displacement correlation term, as it contains highly amplified noise levels. We have decided to utilize the strain field from the final computed displacement field after solving the inverse problem according to the method presented in **Section 3.2**. An alternative approach would be to filter the noisy "measured" strain field, but from our experience the computed strain field yields superior quality in the reconstructed shear modulus distribution. We will investigate the modified objective function further in the Discussion section (**Section 3.4**) and compare this to the conventional inverse formulation.

3.2 Spatially varying regularization factor

We solve the inverse problem in a posterior step utilizing the shear modulus distribution from the solution of the inverse problem with the spatially weighted displacement correlation term according to **Section 3.1**. To this end, we express the regularization factor in terms of the shear modulus distribution obtained utilizing **Equation (3.3)**. The new regularization factor is given by

$$\bar{\alpha} = \frac{\alpha}{\mu} \tag{3.4}$$

Thus the new regularization factor is a function of the spatial coordinates.

$$F = \frac{1}{2} \| \frac{(u_y - (u_{meas})_y)}{\varepsilon_{yy}} \|_2^2 + \frac{1}{2} \int_\Omega \bar{\alpha} \sqrt{|\nabla \bar{\mu}|^2 + c^2} d\Omega \tag{3.5}$$

We denote the unknown shear modulus distribution in **Equation (3.5)** by $\bar{\mu}$ to distinguish it from the known shear modulus in **Equation (3.4)**. In [57] a spatially treated regularization term has been presented for atherosclerotic plaques with known non-homogeneous morphology of the plaque in the artery from spatial priors.

3.3 Results

The limited BFGS method is utilized to solve the constrained optimization problem, which requires the computation of the gradient of the objective function with respect to the unknown elastic parameter distribution at each minimization call. We will stop the minimization procedure when fully converged, thus the total number of iterations is about 3000 to 6000 in the proceeding results. All reconstructions in **Section 3.3** utilize the displacement field, determined from the forward problem for the boundary conditions given in after adding about 3% of white Gaussian noise. The regularization constant *c* for all these reconstructions is chosen to be 0.01. The initial guess of the shear modulus is 1 over the whole domain, and the lower and upper bounds for the search region of the unknown shear modulus distribution are between 1 and 30, respectively.

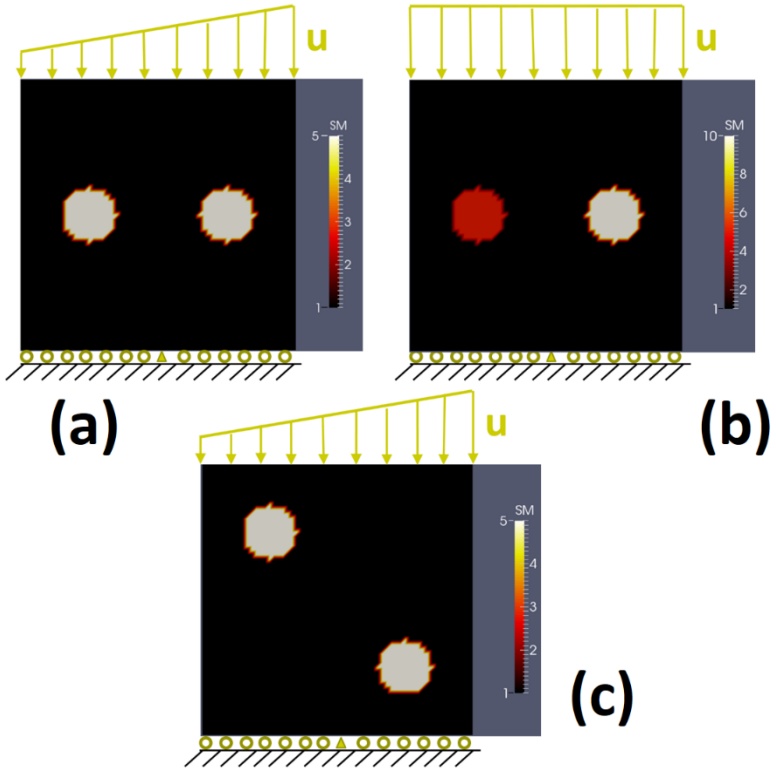

Figure 3-1: Given are the following target shear modulus distributions: (a) Two horizontally positioned inclusions with $\mu = 5$ in a homogeneous background of $\mu = 1$. (b) Two horizontally positioned inclusions with $\mu = 5$ in the left inclusion, $\mu = 10$ in the right inclusion and $\mu = 1$ in the background. (c) Two inclusions positioned on the diagonal of the unit square, with $\mu = 5$ in both inclusions, and $\mu = 1$ in the background.

3.3.1 Results for the iterative, regularized inverse problem

In this section we present results of the regularized inverse problem using the methodology reviewed in **Section 2.2** and the examples from **Figure 3-1**. **Figure 3-2** represents the shear modulus reconstructions for the target shear modulus distribution given in **Figure 3-1** (a) for the case with a uniform compression. In **Figure 3-2**, the left reconstruction corresponds to a regularization factor of 8.0E-10 and the right

reconstruction corresponds to a regularization factor of 2.5E-10. Clearly, both inclusions are well recovered as well as their shear modulus values. The plots on the bottom of **Figure 3-2** represent the shear modulus values along a horizontal line through the center of both inclusions for each shear modulus reconstruction. The horizontal centerline plot for the target shear modulus distribution is included in these plots as comparison.

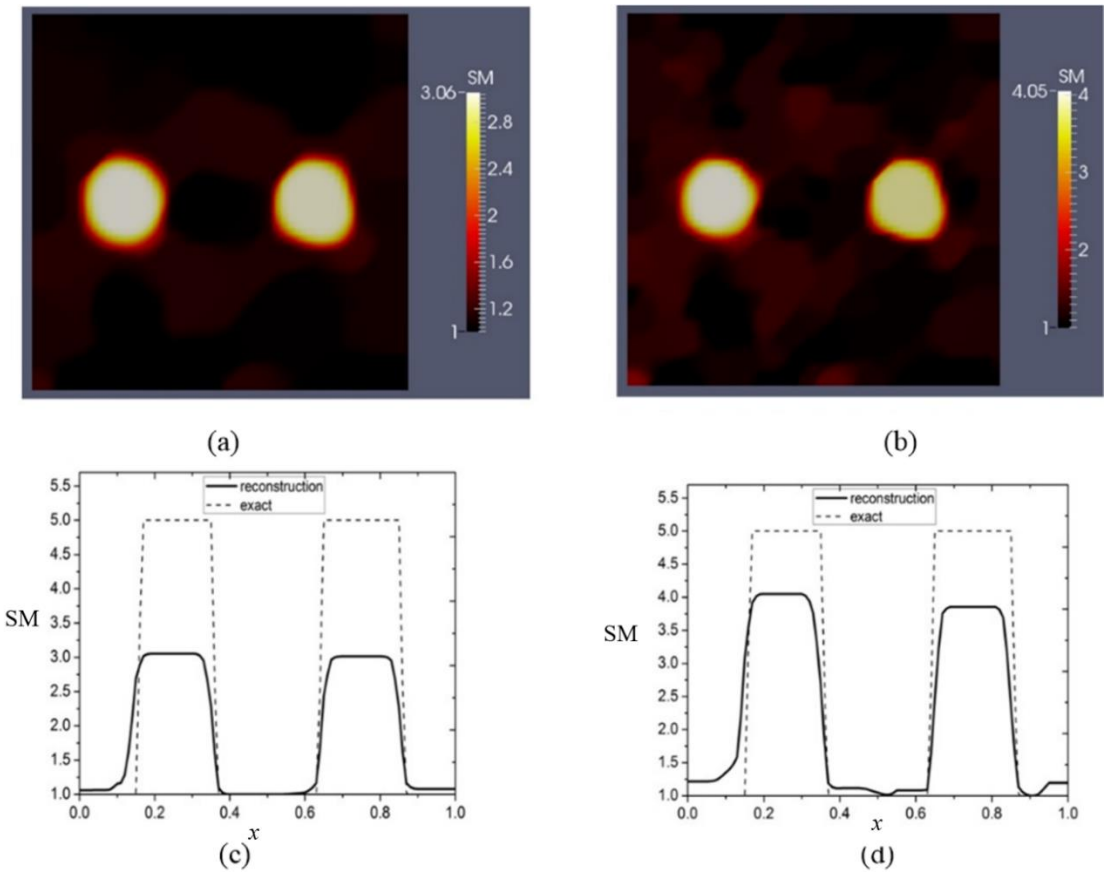

Figure 3-2: (Top) Shear modulus reconstructions for the problem domain in **Figure 3-1** (a) with uniform compression for two regularization factors. (Bottom) Plot of shear modulus values along the horizontal centerline through both inclusions.

Now, we demonstrate that the conventional solution of the regularized inverse problem, posed as a constrained minimization problem, leads to undesired shear modulus reconstructions when boundary conditions are altered to a linear displacement compression. The shear modulus reconstruction is given in **Figure 3-3** for a regularization factor of 5.0E-10 (left column) and 1.2E-10 (right column). We observe that the shape of the inclusions are well recovered, however, the shear modulus values within each inclusion differ significantly from each other. Clearly, the current solution of the inverse problem appears to be dependent on the choice of boundary conditions or similarly related, the displacement field. We will elaborate on this further in **Section 3.4** and show for a set of shear modulus distributions that the solution of the inverse problem is in fact sensitive to the strain distribution.

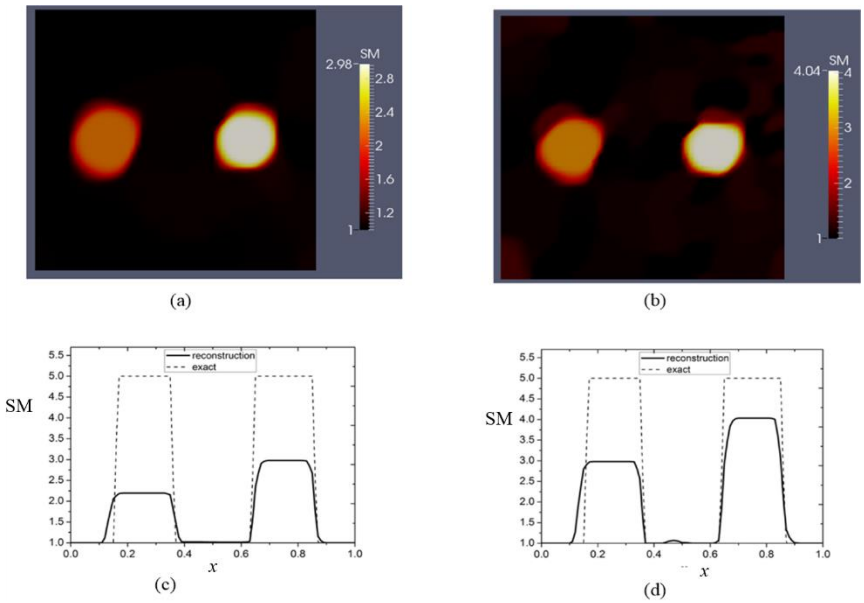

Figure 3-3: (Top) Shear modulus reconstructions for the problem domain in **Figure 3-1** (a) with linear compression for two regularization factors. (Bottom) Plot of shear modulus values along the horizontal centerline through both inclusions.

In **Figure 3-4** we reconstruct the target shear modulus distribution given in **Figure 3-1** (b) for a displacement field determined under a uniform compression. The location of the inclusions is the same as before, but the right inclusion is by a factor of 2 stiffer than the left inclusion. The reconstructed shear modulus distribution in **Figure 3-4** is given for a regularization factor of 1.0E-10 (left plot) and a regularization factor of 5.0E-11 (right plot). We observe that the shape of the inclusions are well recovered, while the reconstructed shear modulus values between the left and right inclusion differ significantly with respect to their contrast loss. For example, comparing the horizontal centerline plots between the target and reconstructed shear modulus distribution, we observe that the shear modulus value in the left inclusion is well recovered, while the shear modulus value in the

right inclusion is significantly underestimated (**Figure 3-4**, left column). In other words, the relative loss in contrast of left inclusion to background versus right inclusion to background is different, despite the fact that a uniform compression is utilized. This leads to a discussion on the effect of strain rather than the displacement field causing these undesired artifacts (see **Section 3.4**).

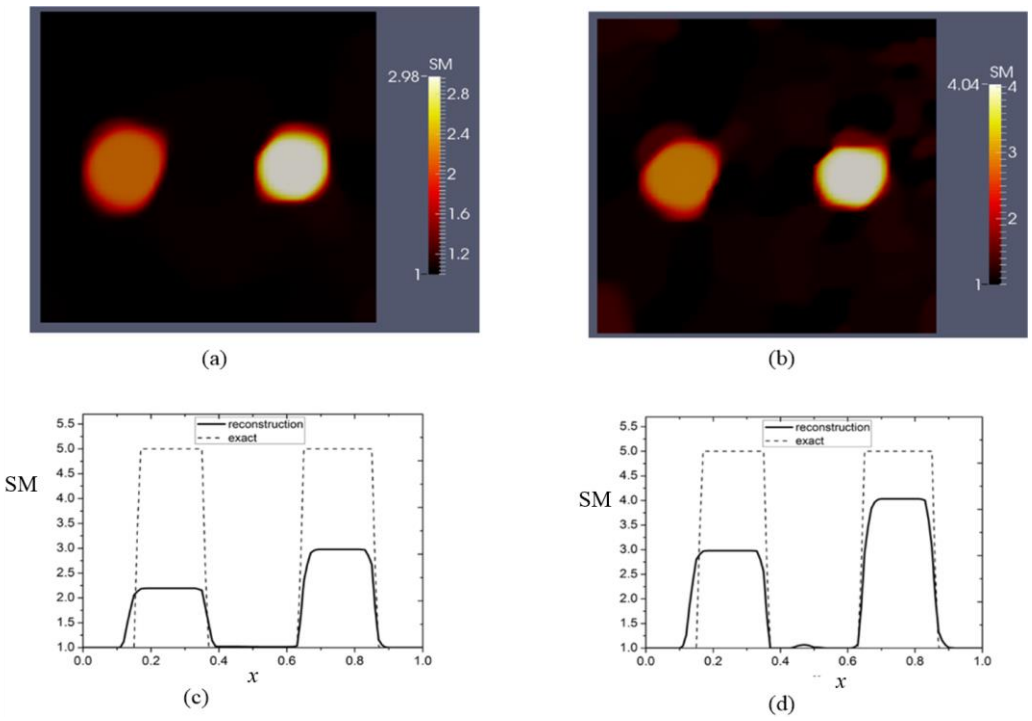

Figure 3-4: (Top) Shear modulus reconstructions for the problem domain given in **Figure 3-1**(b) with uniform compression for two regularization factors. We note that the target shear modulus in the left inclusion is 5 and the right inclusion is 10. (Bottom) Plot of the shear modulus values along the horizontal centerline through both inclusions.

In **Figure 3-5**, we demonstrate that the conventional solution of the regularized inverse problem, posed as a constrained minimization problem, also fails to yield proper reconstructions of the shear modulus values, when the inclusions are positioned diagonally

as given in **Figure 3-1** (c). On the other hand, the shape of the inclusions are well recovered as observed before. The compression on the top edge varies linearly as described at the beginning of this section, thus the strain in the left inclusion will be much smaller than in the right inclusion. The shear modulus reconstructions of the left and right images in **Figure 3-5** are computed for a regularization factor of 4.0E-10 and 1.0E-10. The left inclusion is clearly underestimated as can be seen in the shear modulus curves plotted over the centerline passing through the center of both inclusions.

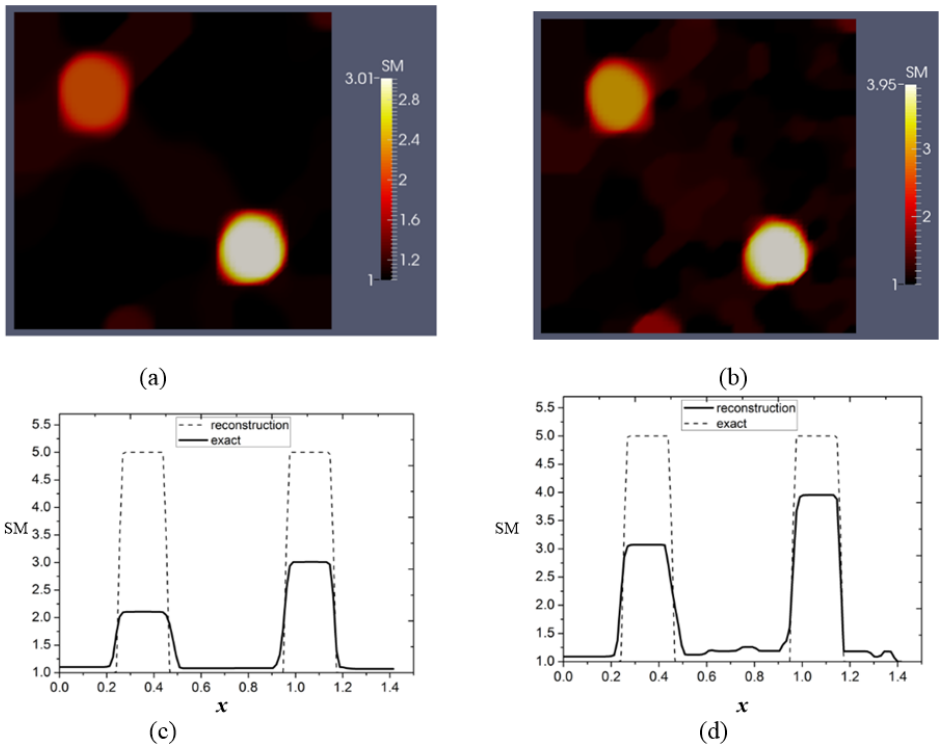

Figure 3-5: (Top) Shear modulus reconstructions for the problem domain given in **Figure 3-1** (c) with linear compression for two regularization factors. The inclusions are located along the diagonal. (Bottom) Plot of the shear modulus values along the diagonal line through the center of both inclusions.

3.3.2 Results for the iterative, regularized inverse problem utilizing a spatially weighted displacement correlation

The modified inverse problem statement, weighing the displacement correlation term with the reciprocal strain distribution has been introduced in **Sections 3.1** and **3.2**. We will show that this formulation reduces the sensitivity of the reconstructions presented earlier.

Figure 3-6 shows the shear modulus reconstruction obtained for the target shear modulus distribution given in **Figure 3-1** (a) and the measured displacement data from the linear compression boundary. The shape of the inclusion is well recovered and the difference in the shear modulus values between both inclusions reduced significantly. The regularization factor has been chosen to be 3E-5.

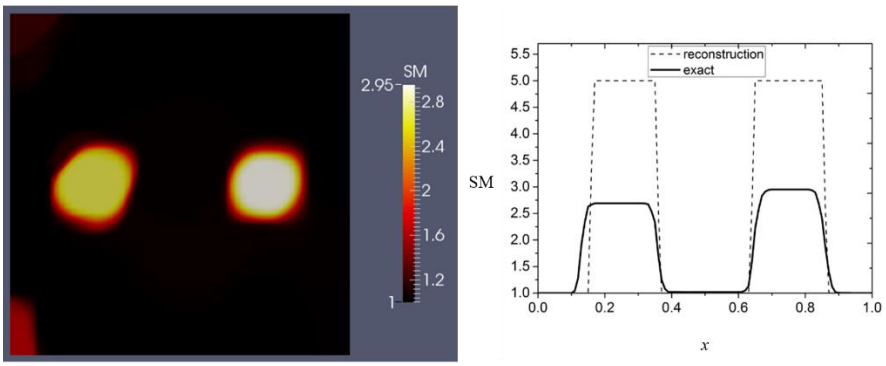

Figure 3-6: (Left) Shear modulus reconstruction for the target shear modulus distribution from **Figure 3-1**(a) with varying compression boundary. (Right) Shear modulus plot versus the horizontal line through the center of both inclusions for the reconstructed and target shear modulus distribution.

Figure 3-7 represents the shear modulus reconstruction for the target shear modulus distribution defined in **Figure 3-1** (b) with two inclusions having distinct stiffness values. A regularization factor of 7.0E-6 is chosen, leading to a smooth shear modulus distribution. The inclusions are well recovered, and the relative contrast loss in each inclusion is more consistent as further discussed later.

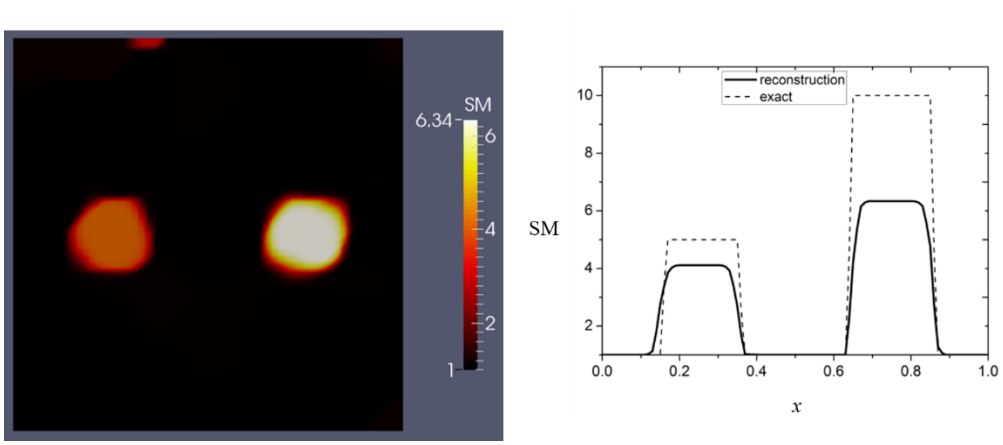

Figure 3-7: (Left) Shear modulus reconstruction for the target shear modulus distribution from **Figure 3-1**(b) with uniform compression boundary. (Right) Shear modulus plot versus the horizontal line through the center of both inclusions for the reconstructed and target shear modulus distribution.

The proposed method also works well for the diagonally positioned inclusion model with linear boundary compression (see **Figure 3-8**). The difference in the shear modulus values between both inclusions is very small as can be clearly seen in the curve plot of the shear modulus values along the diagonal line passing through the center of both inclusions. A regularization factor of 2.5E-5 has been chosen in the inverse problem solution.

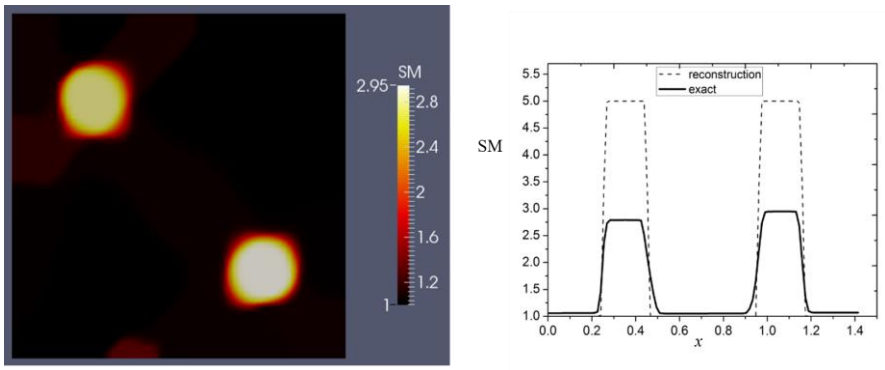

Figure 3-8: (Left) Shear modulus reconstruction for the target shear modulus distribution from **Figure 3-1** (c) with linear compression boundary. (Right) Shear modulus plot versus the diagonal line through the center of both inclusions for the reconstructed and target shear modulus distribution.

3.3.3 Results for the iterative, regularized inverse problem utilizing a spatially varying regularization factor

The regularization factor in the previous results in **Section 3.3.2** were intentionally chosen to be large. While a large regularization factor leads to very smooth and well recovered inclusion shapes, it compromises the overall contrast of the shear modulus values. In this section, we will utilize the results from **Section 3.3.2** and perform a posterior inverse solution step to improve the contrast, while retaining the smoothness quality of the reconstructions. For this, we update the regularization factor such that it becomes a spatial function defined in **Section 3.2**.

Applying this methodology to the target shear modulus distribution given in **Figure 3-1** (a) with linear compression boundary results in a significant increase in shear modulus contrast in the inclusions as shown in **Figure 3-9**. We observe that the

background is very smooth overall. We have selected a regularization factor of 3.5E-5 for this case.

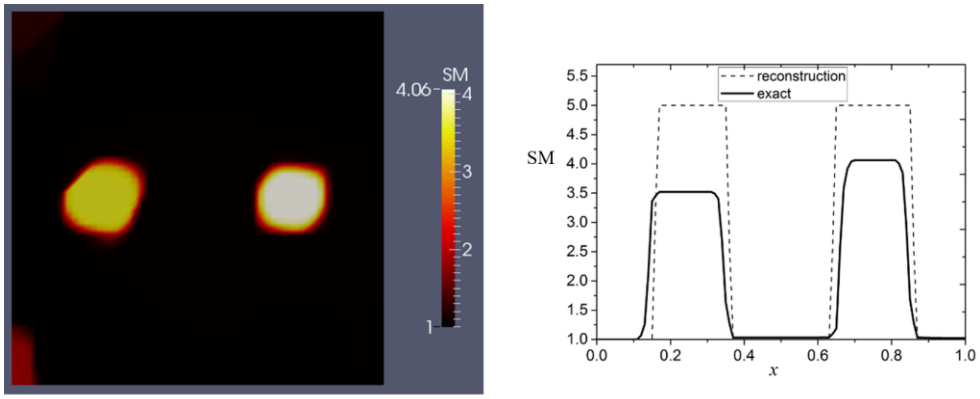

Figure 3-9: (Left) Shear modulus reconstruction utilizing the methodology introduced in **Section 3.2**. The target shear modulus distribution is given in **Figure 3-1** (a). (Right) Shear modulus values along the horizontal centerline passing through the center of both inclusions for the target and reconstructed values.

The shear modulus reconstruction corresponding to the target distribution in **Figure 3-1** (b) is given in **Figure 3-10**. We observe that the shear modulus contrast in both inclusions improves significantly, while the background remains smooth and the inclusion shapes are well recovered.

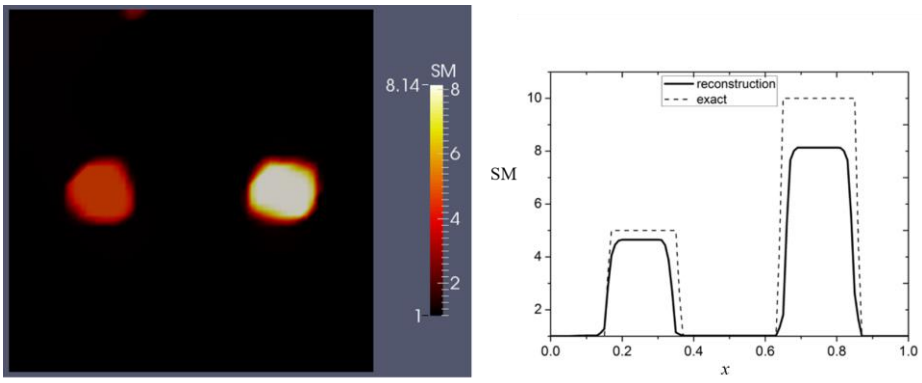

Figure 3-10: (Left) Shear modulus reconstruction utilizing the methodology introduced in **Section 3.2**. The target shear modulus distribution is given in **Figure 3-1** (b). (Right) Plot of the shear modulus values along the horizontal centerline passing through the center of both inclusions for the target and reconstructed values.

Finally, the shear modulus reconstruction for the target shear modulus distribution in **Figure 3-1** (c) with diagonal positioned inclusions is given in **Figure 3-11**, utilizing the inverse solution introduced in **Section 3.2**. Again, the shear modulus contrast improves significantly without compromising the quality of the recovered inclusion shape and the overall smoothness of the shear modulus distribution.

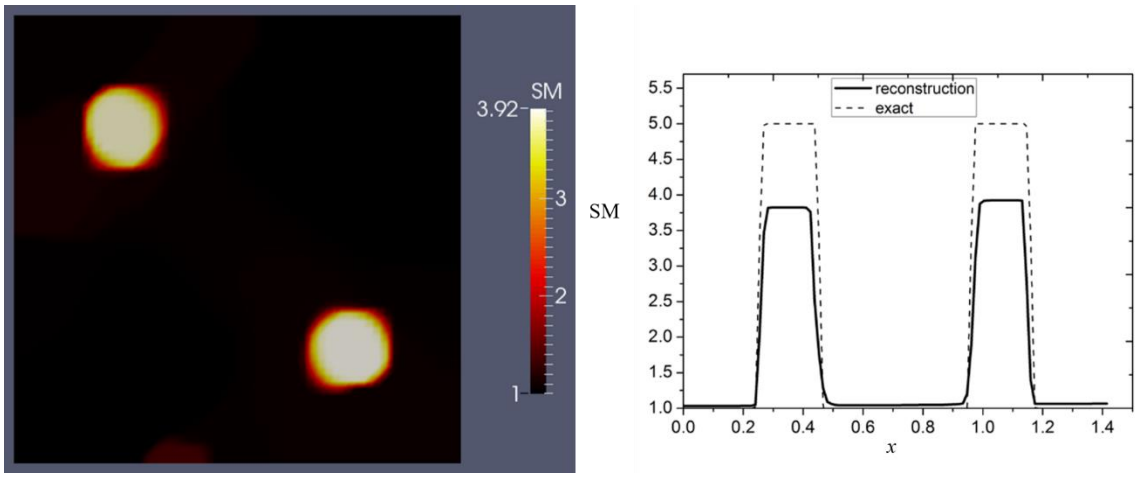

Figure 3-11: (Left) Shear modulus reconstruction utilizing the methodology introduced in **Section 3.2**. The target shear modulus distribution is given in **Figure 3-1** (a). (Right) Plot of the shear modulus along the diagonal centerline passing through the center of both inclusions for the target and reconstructed values.

3.4 Discussion

In this Chapter, we have presented a novel formulation to solve the regularized inverse problem, posed as a constrained minimization problem subject to the constrained of the equilibrium equations. In a first step, we have modified the displacement correlation term, introducing a weighting function in terms of the strain components. We have tested this new methodology successfully with hypothetical data determined from three target shear modulus distributions given in **Figure 3-1**. All these examples have in common that they comprise of two inclusions in a homogeneous background. In the first example (see **Figure 3-1**(a)) with two horizontal positioned inclusions of same stiffness value, we have shown that the conventional inverse method recovers the shear modulus distribution well (see **Figure 3-2**) when a uniform displacement compression is applied. However,

changing the boundary to a linear displacement compression, e.g. collecting ultrasound data while the ultrasound transducer is tilted, the recovered shear modulus values in both inclusions are significantly different. One could now conclude that the linear displacement compression results in small displacements in the left inclusion and large displacements in the right inclusion, thus are treated unequally in the displacement correlation term [80]. However, in the second example, the inclusions are horizontally positioned and have distinct stiffness values, while a uniform displacement compression is applied on the top boundary, and the inverse problem is solved utilizing the conventional approach. We note that in this example, the displacements in both inclusions are similar, while the strain is smaller in the stiffer right inclusion. We expect that the reconstructed shear modulus values in both inclusions are underestimated consistently. In other words, the relative difference of target and reconstructed shear modulus in each inclusion should be about same. This requirement is clearly not satisfied in the shear modulus reconstructions in **Figure 3-4** determined with the conventional inverse method. We note that it is not correct to say that the left inclusion is "better" recovered than the right inclusion. This is because in practical applications, we do not know the actual target modulus distribution, thus the reconstructions can only be properly interpreted if they are consistently underestimated. The novel proposed formulation addresses this issue successfully as shown in **Figure 3-7.** In the last example (see **Figure 3-1** (c)), we position the target inclusions with same stiffness values diagonally and apply a linear displacement compression on the top boundary. We note that this causes strains similar to the example in **Figure 3-1** (a), but the displacements in the inclusions are significantly different. Again, the conventional

method yields significant differences in the reconstructed shear modulus values in both inclusions. In particular, the inclusion with the lower strain has the lower reconstructed shear modulus value (see **Figure 3-5**). This difference in the reconstructed shear modulus is significantly reduced utilizing the novel inverse formulation (see **Figure 3-8**).

The examples utilized in this paper, clearly demonstrate that the strain field is a potential candidate that is likely to influence the reconstruction of μ. To gain confidence in our shear modulus reconstructions and further investigate key variables in the new formulation, we derive a 1-D analogue given in **Figure 3-12**. Two non-homogeneous bars in parallel are connected by two rigid plates, where the bottom plate is fixed and the top plate can be tilted to apply different compression levels on each bar, denoted by u^i . The length a^i (i=1,2) is analogue to the stiff inclusion diameter. The stiffness value in the inclusions will be chosen according to the cases discussed earlier, and the remaining region of the bar will have a stiffness value of 1. The objective function to be minimized is

$$F = \sum_{i=1}^{2} F^i = \sum_{i=1}^{2} \frac{1}{2} \int_0^1 \left(u_{com}^i - n \cdot u_{exact}^i \right)^2 \mathrm{d}y + \alpha \left| \mu_{in}^i - \mu_b^i \right| \tag{3.6}$$

where F^1 and F^2 are contributions to the objective function from the left (i=1) and right (i=2) bar, respectively. In **Equation (3.6)** u_{com}^i and u_{exact}^i denote the computed and exact displacement field, respectively, and n is a factor to test our analysis for sensitivity (similar to noise). The second term is TVD regularization analytically expressed in 1-D for the non-homogeneous bar, where μ_{in}^i is the inclusion stiffness and μ_b^i is the background stiffness. We may set $\mu_b^i = 1$ as the reconstructions are purely relative, i.e.,

off by a multiplicative factor. Next, we express the displacement field given that the strain is piecewise constant in the background and inclusion.

$$u_{com}^{i}=\begin{cases} b^{i}\cdot\varepsilon_{b}^{i}+a^{i}\cdot\varepsilon_{in}^{i}+\left(y-b^{i}-a^{i}\right)\varepsilon_{b}^{i} & \text{when } b^{i}+a^{i}<y\le 1 \\ b^{i}\cdot\varepsilon_{b}^{i}+\left(y-b^{i}\right)\varepsilon_{in}^{i} & \text{when } b^{i}<y\le b^{i}+a^{i} \\ y\cdot\varepsilon_{b}^{i} & \text{when } 0<y\le b^{i} \end{cases} \tag{3.7}$$

where $\bar{\varepsilon}_{b}^{i}$ and $\bar{\varepsilon}_{in}^{i}$ are the computed strains in the background and the inclusion, respectively, and the index i=1, 2 denotes the left and right inclusion. Similarly, the exact displacement field u_{exact}^{i} can be expressed by replacing the strains in **Equation (3.7)** by the exact strains $\bar{\varepsilon}_{b}^{i}$ and $\bar{\varepsilon}_{in}^{i}$. As the stress in each bar is constant, we have the relationship $\varepsilon_{b}^{i}=\mu_{in}^{i}\cdot\varepsilon_{in}^{i}$ and $\bar{\varepsilon}_{b}^{i}=\bar{\mu}_{in}^{i}\cdot\bar{\varepsilon}_{in}^{i}$ where the bars denote the exact (target) variables. From this relationship and kinematics, we obtain

$$\varepsilon_{b}^{i}=u^{i}/\left(\left(1-a^{i}\right)+a^{i}/\mu_{in}^{i}\right) \text{ and } \bar{\varepsilon}_{b}^{i}=\bar{u}^{i}/\left(\left(1-a^{i}\right)+a^{i}/\bar{\mu}_{in}^{i}\right) \tag{3.8}$$

where u^{i} and $\bar{u}^{i}$ are the noisy and exact displacement loadings applied on the top of the bars. From **Equations (3.7)** to **(3.8)** the objective function in **Equation (3.6)** can be expressed in terms of the unknown μ_{in}^{i}, thus, allows to determine the gradient

$$\frac{\partial F^{i}}{\partial\mu_{in}^{i}}=\frac{f^{i}}{3\left(\mu_{in}^{i}\left(-1+a^{i}\right)-a^{i}\right)^{3}\left(\bar{\mu}_{in}^{i}\left(-1+a^{i}\right)-a^{i}\right)}+\alpha=0 \qquad i=1,2 \tag{3.9}$$

where

$$
\begin{aligned}
f^i = & \\
& +u^i a^i \mu_{in}^i \left(-\bar{\mu}_{in}^i \left(u^i - n\cdot\bar{u}^i\right)\left(-1+a^i\right)\left(\left(-1+a^i\right)^3 + 3b^i\left(-1+a^i\right)a^i + 3\left(b^i\right)^2\left(1+a^i\right)\right)\right) \\
& +u^i \left(a^i\right)^2 \mu_{in}^i \left(-n\cdot u_{exact}^i \left(-1+a^i\right)\left(3+3\left(b^i\right)^2 + 3b^i\left(-2+a^i\right) - 4a^i + \left(a^i\right)^2\right)\right) \\
& +\left(u^i\right)^2 \left(a^i\right)^2 \mu_{in}^i \left(\left(-1+a^i\right)^3 + 3b^i\left(-1+a^i\right)a^i + 3\left(b^i\right)^2\left(1+a^i\right)\right) \\
& +u^i \left(a^i\right)^2 \mu_{in}^i \left(-\left(u^i - n\cdot\bar{u}^i\right)a^i \left(3+3\left(b^i\right)^2 + 3b^i\left(-2+a^i\right) - 4a^i + \left(a^i\right)^2\right)\right) \\
& +\left(u^i\right)^2 \left(a^i\right)^2 \mu_{in}^i \bar{\mu}_{in}^i \left(\left(-1+a^i\right)\left(3\left(-1+a^i\right)^2 + \left(-4+3a^i\right)a^i + \left(a^i\right)^2\right)\right) \\
& +u^i \left(a^i\right)^2 \mu_{in}^i \bar{\mu}_{in}^i \left(-n\cdot\bar{u}^i \left(\left(-1+a^i\right)^3 + 3b^i\left(-1+a^i\right)a^i + 3\left(b^i\right)\left(1+a^i\right)\right)\right)
\end{aligned}
\tag{3.10}
$$

The regularization factor in the left and right bar are the same, and therefore we can relate the left and right bar from **Equation (3.9)** by

$$
\frac{f^1}{3\left(\mu_{in}^1\left(-1+a^1\right)-a^1\right)^3\left(\bar{\mu}_{in}^1\left(-1+a^1\right)-a^1\right)} = \frac{f^2}{3\left(\mu_{in}^2\left(-1+a^2\right)-a^2\right)^3\left(\bar{\mu}_{in}^2\left(-1+a^2\right)-a^2\right)} \tag{3.11}
$$

As with **Equation (3.11)** one can obtain the expression for the spatially weighted displacement correlation term (not shown here). Next, we know that the shear modulus reconstructions in the inclusions will be underestimated, thus, we will proceed as follows: Fix the right stiffness value to the reconstructed value observed in the 2-D for the cases discussed in the **Section 3.3** and solve for the stiffness modulus in the left inclusion. The results in **Table 3-1** and **Table 3-2** clearly show that our 1-D analogue, while simple, can closely reproduce the trends observed in the 2-D inverse solution, thus confirms that the observations in the 2-D model are not due to convergence related issues. Furthermore, we note that the observed trends are independent of the perturbation (noise) applied to the displacement field. We have made this same observation in our 2-D models (not shown

here). Thus we conclude that the regularization term drives these ambiguous reconstructions and not the inherent noise level.

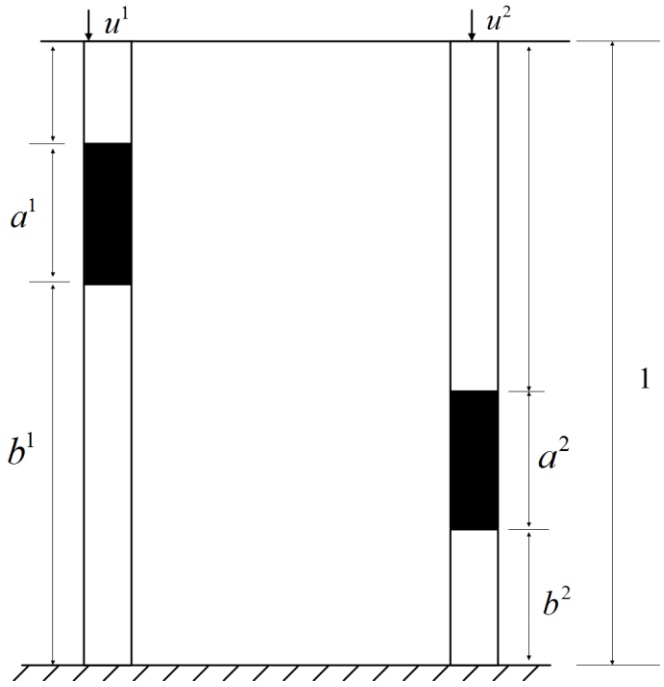

Figure 3-12: 1-D analogue of previous shear modulus inclusions, represented by two non-homogeneous bars.

Table 3-1: Comparison of reconstructions for left inclusion with 2-D model, 1-D model, and 1-D model with noise. The conventional objective function is used.

	2D continuum model		1D bar model (n=1)		1D bar model (|n-1|=1.5%)	
	left inclusion	right inclusion	left inclusion	right inclusion	left inclusion	right incluison
case1	2.2	2.98	2.06	2.98	2.07	2.98
case2	4.86	6.44	4.39	6.44	4.37	6.44
case3	2.15	3.01	2.08	3.01	2.21	3.01

Table 3-2: Comparison of reconstructions for left inclusion with 2-D model, 1-D model, and 1-D model with noise. The spatially weighted objective function is used.

	2D continuum model		1D bar model (n=1)		1D bar model (|n-1|=1.5%)	
	left inclusion	right inclusion	left inclusion	right inclusion	left inclusion	right incluison
case1	2.69	2.95	2.95	2.95	2.96	2.95
case2	4.11	6.34	3.66	6.44	3.64	6.44
case3	2.69	2.95	2.95	2.95	3.06	2.95

To motivate the spatial weighted factor as a function of strain, we will discard the noise as it has limited influence on the observed results, and to simplify the following analysis. Furthermore, we will assume that the left and right inclusion have the same diameter of 0.2 and the inclusions can be positioned such that the relationship $b_1 = 0.8 - b_2$ holds, which will cancel out terms dependent on b_1 and b_2. Thus, **Equation (3.11)** simplifies to

$$\frac{\left(\mu_{in}^1 - \bar{\mu}_{in}^1\right)\left(\mu_{in}^2(-1+a)-a\right)^3}{\left(\mu_{in}^2 - \bar{\mu}_{in}^2\right)\left(\mu_{in}^1(-1+a)-a\right)^3} = \frac{\left(\bar{u}^2\right)^2\left(\bar{\mu}_{in}^1(-1+a)-a\right)}{\left(\bar{u}^1\right)^2\left(\bar{\mu}_{in}^2(-1+a)-a\right)} = \frac{\bar{u}^2\bar{\varepsilon}_{in}^2}{\bar{u}^1\bar{\varepsilon}_{in}^1} \tag{3.12}$$

where a is the left and right inclusion size with $a = 0.2$ for the proceeding analysis. The right hand side of **Equation(3.12)** follows from kinematics and equilibrium. We fix $\mu_{in}^2 = 0.8\bar{\mu}_{in}^2$ assuming a 20% contrast loss in the right inclusion, and solve the shear modulus variable μ_{in}^1 in the left inclusion. It is important to acknowledge that $\bar{u}^1$ can be applied independently of $\bar{u}^2$, thus solving for μ_{in}^1 will strongly depend on this displacement boundary. The expression for the spatially weighted regularization case is given by

$$\frac{\left(\mu_{in}^{1}-\bar{\mu}_{in}^{1}\right)\left(\mu_{in}^{2}\left(-1+a\right)-a\right)^{3}}{\left(\mu_{in}^{2}-\bar{\mu}_{in}^{2}\right)\left(\mu_{in}^{1}\left(-1+a\right)-a\right)^{3}}=\frac{\left(1+\left(\left(\bar{\mu}_{in}^{1}\right)^{2}-1\right)a\right)\left(\bar{\mu}_{in}^{1}\left(-1+a\right)-a\right)}{\left(1+\left(\left(\bar{\mu}_{in}^{2}\right)^{2}-1\right)a\right)\left(\bar{\mu}_{in}^{2}\left(-1+a\right)-a\right)} \tag{3.13}$$

Equation (3.13) clearly shows that the solution for μ_{in}^{1} does not depend on the applied boundary condition using the spatially weighted formulation. As the contrast in the right inclusion has been assumed to be underestimated by 20%, we expect the left inclusion to be underestimated by 20% as well. Keeping this in mind, we plot the error defined by $\left[\left(\mu_{in}^{1}-0.8\bar{\mu}_{in}^{1}\right)/\left(0.8\bar{\mu}_{in}^{1}\right)\right]100\%$ over $\bar{\mu}_{in}^{2}$ for different $\bar{\mu}_{in}^{1}$ (=3, 4, 5, 6, 7, 8, 9, 10 from top curve to bottom curve) for the conventional method in **Figure 3-13** and the spatially weighted displacement correlation in **Figure 3-14**. The displacement boundary ratio between right and left boundary is set to 2. We observe that the error for the conventional method reaches about 70%, while the reconstruction error in the new method is about 22%. The plots also reveal that the error in the new method is zero when the stiffness values in left and right inclusion are same, while for the conventional method it is about 25%. We note that the error plot will change for different displacement boundaries using the conventional method, but will remain the same for the spatially weighted displacement correlation term. Finally, this approach can be generalized for more than two bars, i.e., multiple bars with inclusions in parallel, and the above analysis will hold as each bar will can be decoupled in the minimization analysis.

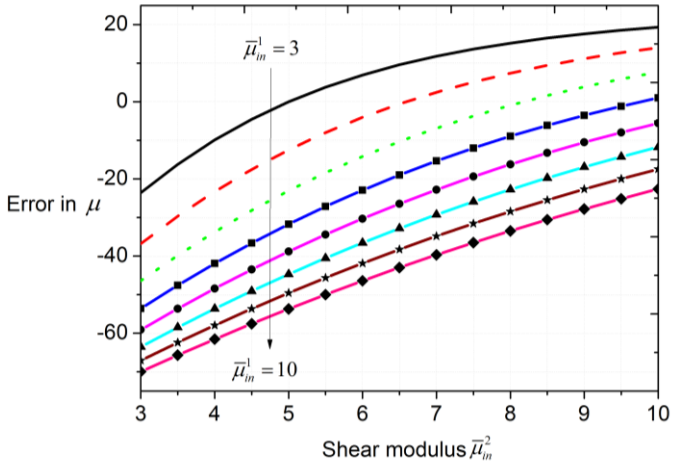

Figure 3-13: Error plot of the reconstructed shear modulus in the left inclusion over the exact shear modulus in the right inclusion $\bar{\mu}_{in}^{2}$ for different shear modulus values in the left inclusion $\bar{\mu}_{in}^{1}$ (=3, 4, 5, 6, 7, 8, 9, 10). The conventional method has been used.

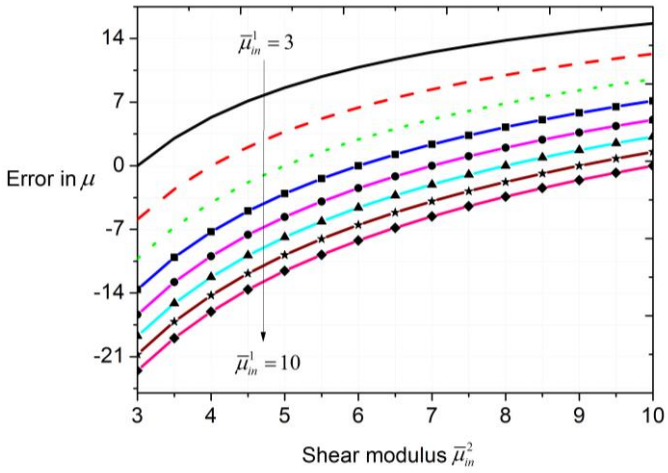

Figure 3-14: Error plot of the reconstructed shear modulus in the left inclusion over the exact shear modulus in the right inclusion $\bar{\mu}_{in}^{2}$ for different shear modulus values in the left inclusion $\bar{\mu}_{in}^{1}$ (=3, 4, 5, 6, 7, 8, 9, 10). The new spatially weighted method has been used.

3.5 Conclusions

We have shown that the conventional regularized inverse problem formulation posed as a minimization problem results in ambiguous shear modulus reconstructions and depends on the choice of boundary conditions. We have observed this on simulated data created from solving the forward problem for a predefined target shear modulus distribution. We have reduced the boundary sensitivity of the regularized inverse solution by weighting the displacement correlation term with the inverse strain tensor having only normal strain components. We have derived a 1-D analogue and shown analytically that our inverse strategy will work for an arbitrary number of same sized inclusions with different stiffness values. The 1-D model analysis has the limitation that it does not account for inclusions sharing the same horizontal coordinate (i.e., vertically shifted), though it can be expanded to include these cases as well. While our reconstructions clearly show the limitations of the conventional approach, the spatially weighted method needs to be investigated further. We also note that these observations were analyzed for the total variation regularization and may not be held for other types of regularizations. However, the results and analysis in this chapter provide a better understanding in the solution of the regularized inverse problem, and may help to analyze other regularization types in a similar fashion. Finally, we have drastically improved the contrast of the shear modulus reconstructions without compromising the overall quality. This has been achieved in a posterior inverse solution step, expressing the regularization factor as a spatial function of the coordinates rather than as a constant.

4. ESTIMATING THE ELASTIC DISTRIBUTION FROM SURFACE DEFORMATIONS*

In this chapter, we will solve the inverse problem in elasticity in a hypothetical study for the shear modulus distribution using only surface deformations. This methodology does not require any priori information about the problem domain. It is based on finite element techniques, and the shear modulus distribution is represented as unknowns on the mesh nodes and interpolated with finite element shape functions. Thus, the number of unknown shear modulus values are equal to the total number of finite element nodes. We will test this method on a problem domain consisting of an inclusion embedded in a homogeneous background, and recover the shear modulus distribution using simulated surface displacement fields. Additionally, we add noise to the data to mimic measured surface deformations from recorded digital camera images.

4.1 Inverse problem formulation utilizing measured surface displacement

One "natural" way to formulate the inverse problem statement is as follows: Find the shear modulus distribution μ such that the objective function:

$$F = \sum_{i=1}^{n} \int_{\Gamma_i} (\mathbf{u}^i - \mathbf{u}^i_{meas})^2 d\Gamma + \alpha \, \mathrm{Reg}(\mu) \tag{4.1}$$

* Reprinted with permission from" Estimating the non-homogeneous elastic modulus distribution from surface deformations" by Mei, Y., Fulmer, R., Raja, V., Wang, S., & Goenezen, S., 2016. International Journal of Solids and Structures, 83, 73-80. Copyright [2016] Elsevier.

is minimized under the constraint of the forward elasticity problem. The first term is the displacement correlation term, minimizing the square of the misfit between the computed $\mathbf{u}^i$ and measured $\mathbf{u}^i_{meas}$ surface deformations on the problem boundary. The summation indicates that this formulation can accommodate multiple surface displacement fields, where *n* denotes the total number of observations. It is emphasized that the boundary integral Γ_i is intentionally augmented with the index *i* to accommodate surface displacement data on varying boundaries. This is because it may not be feasible to observe data on the same sub-boundary domain for each experiment. The second term is the so-called regularization term to penalize oscillations in the final solution of the shear modulus distribution. We will define the particular regularization type later on.

The inverse problem formulation in **Equation (4.1)** is expressed analogous to [48, 49, 62, 64, 80-85], but differs in that the predicted and measured displacements are correlated on the surface while the referenced approaches correlate the displacements in the entire interior of the problem domain. Discretizing **Equation (4.1)** with finite element techniques is straightforward. This will be demonstrated for one displacement field to reduce notations, this is

$$F = \int_{\Gamma} (\Delta \mathbf{u})^2 d\Gamma + \alpha \,\mathrm{Reg}(\mu) \tag{4.2}$$

Where $\Delta \mathbf{u} = \mathbf{u} - \mathbf{u}_{meas}$. The finite element interpolation yields

$$F = \sum_{e=1}^{N} \int_{\Gamma_e} [\sum_{j=1}^{N_e} \Delta \mathbf{u}_j^e N_j^e(\mathbf{x})]^2 d\Gamma + \alpha \,\mathrm{Re}\, g(\sum_{k=1}^{N_n} \mu_j N_j(\mathbf{x})) \tag{4.3}$$

where N , N_g , and N_n denote the total number of finite elements on the boundary, the number of nodes on each element, and the total number of mesh nodes in the problem domain, respectively. Further, $N_j^e(\mathbf{x})$ denotes the shape function for the *j*-th node corresponding to the *e*-th linear triangular element. While this approach appears to be reasonable, we employed an alternative formulation to facilitate implementation. More precisely, we have used domain integrals over finite elements at the boundary, given by

$$F = \sum_{e=1}^{\bar{N}} \int_{\Omega_e} [\sum_{j=1}^{\bar{N}_e} \Delta \mathbf{u}_j^e N_j^e(\mathbf{x})]^2 d\Omega + \alpha \operatorname{Re} g(\sum_{k=1}^{N_n} \mu_j N_j(\mathbf{x})) \tag{4.4}$$

where $\bar{N}$ denotes the total number of domain elements at the boundary and $\bar{N}_g$ denotes the number of element nodes on the boundary of the corresponding elements. It is noted that only displacement information on the boundaries are assumed to be known, despite the integration over element domains. This more "unnatural" approach has been performed to use the current framework of the existing inverse solver written for minimizing the misfit in displacements over the volume integral. In the following we will analyze the implications of using **Equation (4.3)** versus **Equation (4.4)** on a uniform mesh given in **Figure 4-1**.

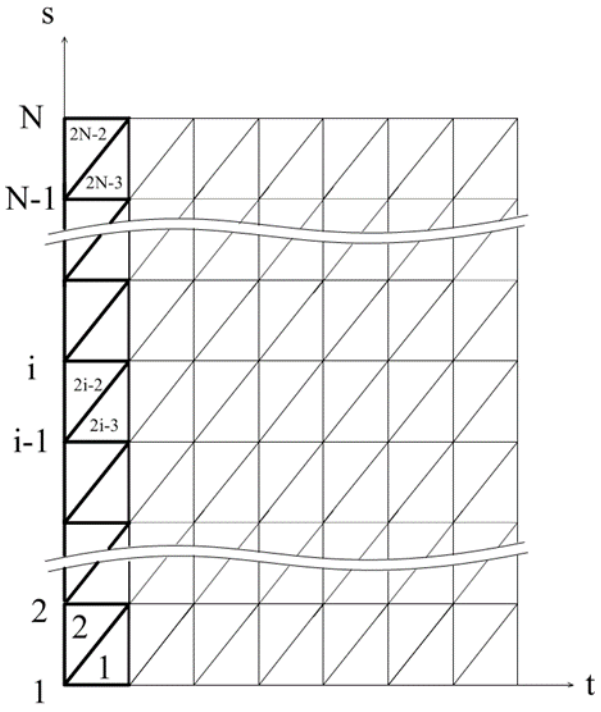

Figure 4-1: Finite elements are shown for a mesh along one boundary of a rectangular problem domain with uniform mesh (see bold region). The coordinate axis s is aligned with the left boundary. The boundary elements have a width *a* and height *b*. This configuration is utilized to analyze the effect of the weights in the objective function arising from a domain integral formulation.

The coordinates span along one boundary edge of a problem domain in two-dimensional space, and we discard the other boundary edges to simplify the analysis (see bold elements in **Figure 4-1**). The width of the elements along the t coordinate is denoted by *a*, and the height along the s coordinate of the elements is denoted by *b*. Evaluating **Equation (4.4)**for the boundary elements given in **Figure 4-1** yields:

$$F = \frac{ab}{6}\Delta u_1^{\,2} + \sum_{i=2}^{N-1}\left(\frac{ab}{4}\Delta u_i^{\,2} + \frac{ab}{12}\Delta u_{i-1}\Delta u_i\right) + \frac{ab}{12}\Delta u_N^{\,2} + \alpha\,\mathrm{Re}\,g\left(\sum_{k=1}^{N_n}\mu_j N_j(\mathbf{x})\right) \qquad (4.5)$$

and evaluating **Equation (4.3)** for the boundary integral yields:

$$F = \frac{b}{3}\Delta u_1^{\,2} + \sum_{i=2}^{N-1}\left(\frac{2b}{3}\Delta u_i^{\,2} + \frac{b}{3}\Delta u_{i-1}\Delta u_i\right) + \frac{b}{3}\Delta u_N^{\,2} + \alpha \,\mathrm{Re}\, g(\sum_{k=1}^{N_n}\mu_j N_j(\mathbf{x})) \qquad (4.6)$$

It is apparent that the displacement correlation term in **Equation (4.5)** contains the element width *a* and element height *b* in every term, thus can be factorized. Further, dividing **Equation (4.5)** by a factor of *ab* will not change the final solution, i.e., the location of the minimum does not change. Thus we can rewrite **Equation (4.5)** as

$$F = \frac{1}{6}\Delta u_1^{\,2} + \sum_{i=2}^{N-1}\left(\frac{1}{4}\Delta u_i^{\,2} + \frac{1}{12}\Delta u_{i-1}\Delta u_i\right) + \frac{1}{12}\Delta u_N^{\,2} + \bar{\alpha} \,\mathrm{Re}\, g(\sum_{k=1}^{N_n}\mu_j N_j(\mathbf{x})) \qquad (4.7)$$

In **Equation (4.7)**, we have substituted $\bar{\alpha}$ for $\frac{\alpha}{ab}$. Similarly, in **Equation (4.7)** we can factorize b from the displacement correlation term and divide the entire expression by $4b$, resulting in

$$F = \frac{1}{12}\Delta u_1^{\,2} + \sum_{i=2}^{N-1}\left(\frac{1}{6}\Delta u_i^{\,2} + \frac{1}{12}\Delta u_{i-1}\Delta u_i\right) + \frac{1}{12}\Delta u_N^{\,2} + \bar{\alpha} \,\mathrm{Re}\, g(\sum_{k=1}^{N_n}\mu_j N_j(\mathbf{x})) \qquad (4.8)$$

where we have substituted $\bar{\alpha}$ for α / b. Now we observe that for a uniform mesh the objective function for the domain integral in **Equation (4.7)** and the boundary integral in **Equation (4.8)** differ by their weights. It is noted that these weights are independent of the element size for a uniform mesh.

In this chapter, the feasibility to solve the inverse problem in elasticity with the formulation introduced in **Equation (4.4)** will be tested with hypothetical displacement data, representing "measured" displacement data on the surface of the problem domain. The hypothetical displacement data will be created by solving the finite element forward

problem for a given non-homogeneous shear modulus distribution and boundary conditions. The problem domain is given in **Figure 4-2** with a square domain of unit length on each side. The shear modulus distribution is given with a stiff inclusion having a value of 5 and a soft homogeneous background having a value of 1. The inclusion diameter is given with 0.4 units. The arrows on the boundary represent the indentation at various locations to deform the problem domain. From **Figure 4-2** (a) to (c), we applied the indentation on the top, left, and right edges, respectively. The motion of the corresponding opposite side is restricted in the direction of the indentation, and the center node on that edge is fixed in all directions to avoid rigid body.

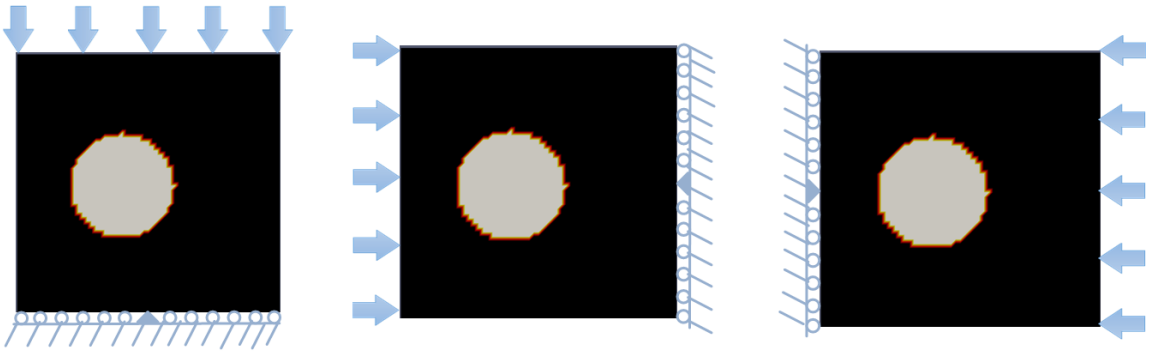

Figure 4-2: Target shear modulus distribution consists of a stiff inclusion ($\mu = 5$) in a soft back-ground ($\mu = 1$). The arrows indicate the indentation locations and directions for different boundary conditions.

Each indentation induces a displacement of 0.05 units on the corresponding node and perpendicular to the corresponding boundary. We note that only 15 arrows are shown in **Figure 4-2**, while a total of 27 displacement fields are actually created for this study.

We model the material in two-dimensional space, in particular in-plane strain for an incompressible material. The finite element mesh consists of 7200 linear triangular

elements, and the displacement as well as the pressure variables are interpolated with linear shape functions. Numerical instability in the pressure variable due to the incompressibility constraint and the violation of the LBB conditions has been addressed according to [49, 68, 86], using stabilized finite element methods. This has been discussed in detail in **Chapter 2**.

In order to mimic displacement data obtained from digital camera images, we add 1% and 2.5% white Gaussian noise to the surface displacement field obtained from the solution of the forward problem. The noise level is defined by $100\%\sqrt{\sum_{i=1}^{\bar{N}}((\mathbf{u}_{meas}^{surf})_i-(\mathbf{u}_{surf})_i)^2/\sum_{i=1}^{\bar{N}}(\mathbf{u}_{surf})_i^2}$, where $(\mathbf{u}_{meas}^{surf})_i$ and $(\mathbf{u}_{surf})_i$ denote the measured and computed displacement (for given target shear modulus distribution) at node *i*, respectively.

4.2 Results

We will test the feasibility of solving the inverse problem with the formulation presented in **Section 4.2**. To this end, we will utilize a varying number of surface displacement fields at varying noise levels to reconstruct the shear modulus distribution.

Figure 4-3 (b) to (d) represent the shear modulus reconstructions from 9, 15, and 27 surface displacement fields without noise, induced by indentations of 0.05 displacement units. A regularization factor of $\alpha = 10^{-11}$ has been selected for all shear modulus reconstructions without noise. The indentations are evenly distributed on the three "visible" sides of the specimen, i.e. for the case with 9, 15, and 27 displacement fields we have 3, 5, and 9 indentations on each edge, respectively. The target shear

modulus distribution is given in **Figure 4-2** (a) to facilitate comparison with the shear modulus reconstructions. The shear modulus is well recovered using only 9 surface displacement fields. The shear modulus ratio of inclusion to background is well recovered with about 4.3. With increasing number of displacement fields (see **Figure 4-3 (**c) and (d)) the circular shape of the inclusion improves as well as the shear modulus values overall. In **Figure 4-4** the shear modulus distribution corresponding to **Figure 4-3** (a) to (d) is plotted along a horizontal line through the center of the inclusion.

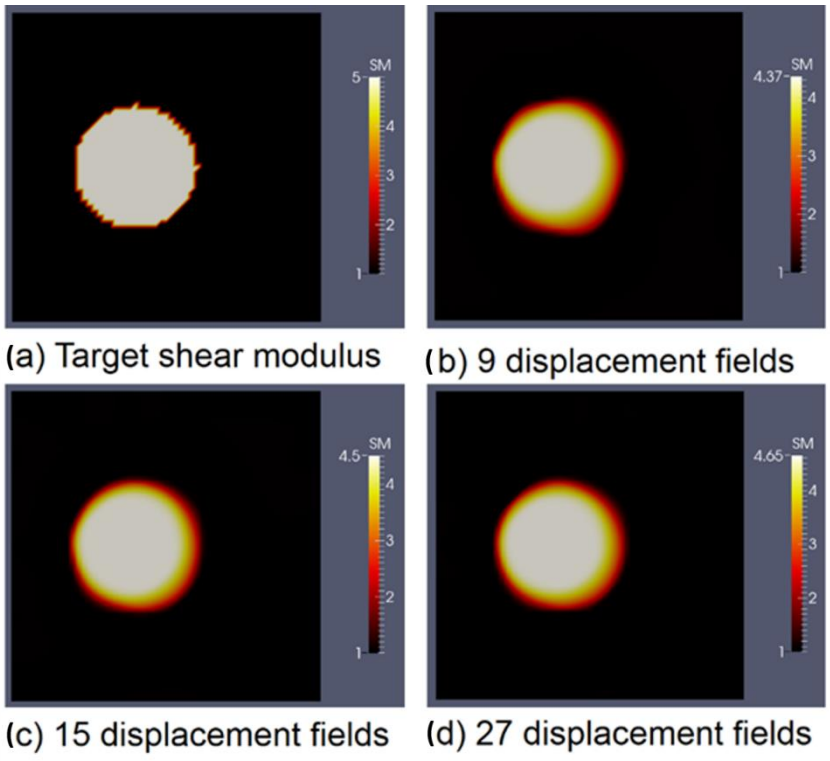

Figure 4-3: Target shear modulus distribution given in (a) for the problem domain defined in **Figure 4-2** for comparison with the shear modulus reconstructions utilizing various number of displacement fields (b)–(d).The displacement data used in these reconstructions contains no noise.

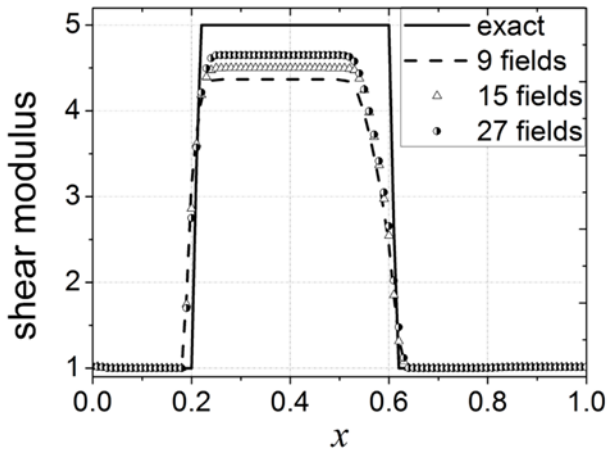

Figure 4-4: Shear modulus plot over the horizontal line through the center of the inclusion for the target (exact) and reconstructed shear modulus distribution.

In **Figure 4-5** (b) to (d) the shear modulus reconstructions are given for 9, 15, and 27 displacement fields, respectively, where each displacement field contains about 1% noise. **Figure 4-5** (a) represents the actual target shear modulus distribution and is provided for comparison. A regularization factor of $\alpha = 6 \cdot 10^{-11}$ has been selected for all shear modulus reconstructions with 1% noise. The shear modulus ratio of inclusion to background is about 3.54 with 9 surface displacement fields and increases to about 3.8 using 27 surface displacement fields. Furthermore, the shape of the inclusion becomes more circular with an increasing number of surface displacement fields. In **Figure 4-6** we plot the shear modulus values over the horizontal line passing through the center of the inclusion for the reconstructions given in **Figure 4-6**.

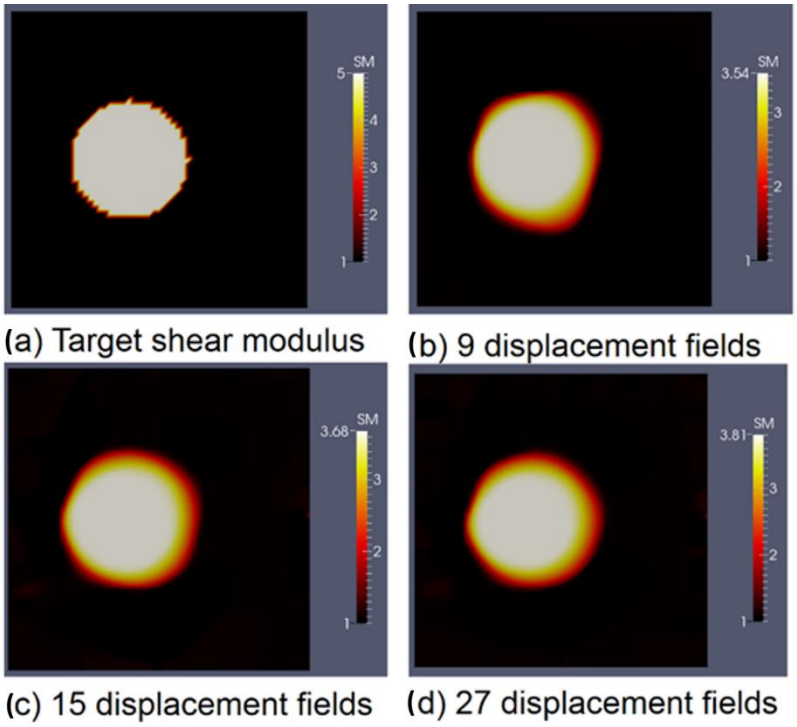

Figure 4-5: Target shear modulus distribution given in (a) for the problem domain defined in **Figure 4-2** for comparison with the shear modulus reconstructions utilizing various number of displacement fields (b) to (d). The displacement data used in these reconstructions contains 1% noise.

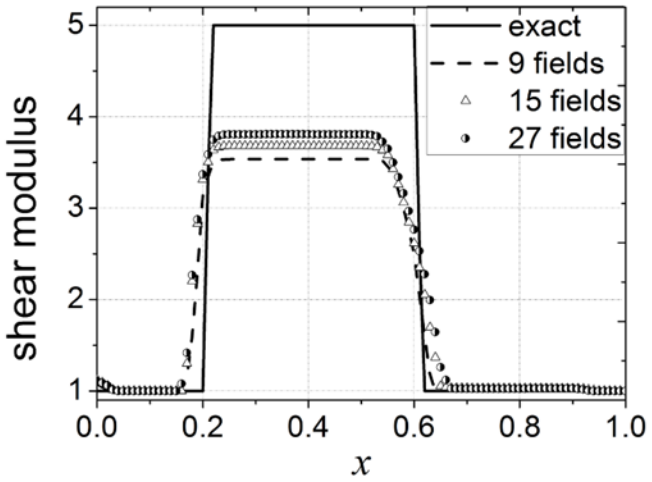

Figure 4-6: Shear modulus plot over the horizontal line through the center of the inclusion for the target (exact) and reconstructed shear modulus distribution.

The shear modulus reconstruction for 2.5% noise in the surface displacement data is given in **Figure 4-7** (b) to (d) for 9, 15, and 27 displacement fields together with the target shear modulus distribution in **Figure 4-7** (a). The corresponding shear modulus plot over the horizontal line through the center of the inclusion is given in **Figure 4-8**. A regularization factor of $\alpha = 10^{-10}$ has been selected for all shear modulus reconstructions with 2.5% noise. The shear modulus ratio of inclusion to background is about 3.25 utilizing 9 surface displacement fields and increases to 3.6 utilizing 27 surface displacement fields. The shape of the circular inclusion improves with an increasing number of surface displacement fields. We note that the shear modulus ratio of inclusion to background does not improve when increasing the total number of surface displacement fields from 9 to 15 (see **Figure 4-7** (b) to (d), respectively), while the shape of the inclusion clearly improves and becomes more circular.

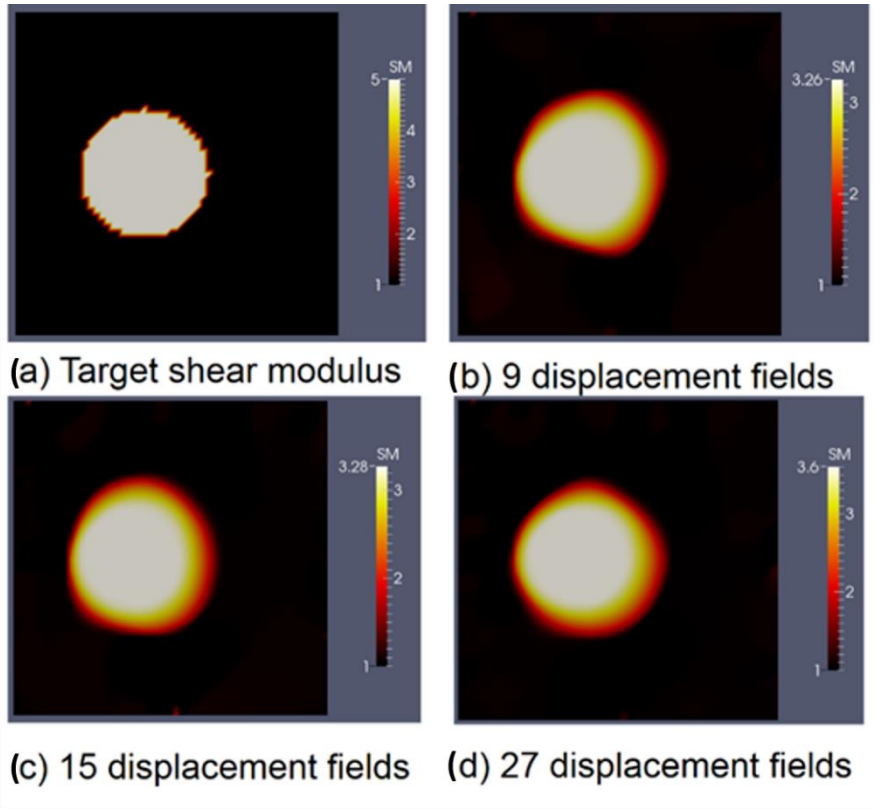

Figure 4-7: Target shear modulus distribution given in (a) for the problem domain defined in **Figure 4-2** for comparison with the shear modulus reconstructions utilizing various number of displacement fields (b) to (d). The displacement data utilized in these reconstructions contains 2.5% noise.

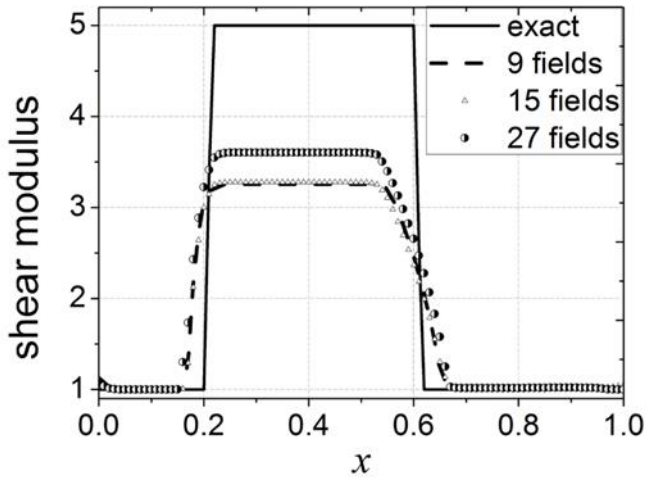

Figure 4-8: Shear modulus plot over the horizontal line through the center of the inclusion for the target (exact) and reconstructed shear modulus distribution.

In practical applications digital cameras may have only a limited view on the specimen's surface. Thus, the displacement data may only be known in partial boundary regions. Thus, we have tested two scenarios. In the first case, we apply 5 indentations on the top edge, evenly distributed. In the second case, 5 indentations are applied on the top and left edge each. In both cases, we will use the displacement data only on the edge where the indentation is applied and introduce 2.5% noise into the surface displacement field. The reconstructed shear modulus distribution for case one is shown in **Figure 4-9** (a) and for case two is shown in **Figure 4-9** (b) for a regularization factor of $\alpha = 10^{-11}$.

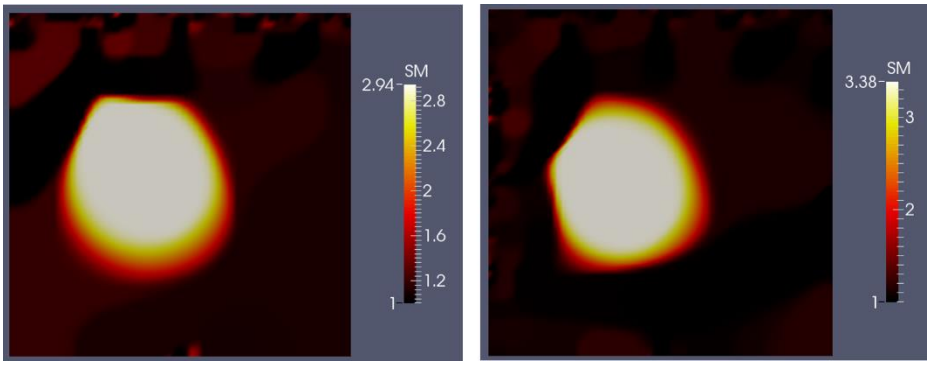

Figure 4-9: (a) Reconstructed shear modulus distribution when 5 indentations are applied on the top edge. (b) Reconstructed shear modulus distribution when 5 indentations are applied on the top and left edges. In (a) and (b) surface displacement fields are used only on the edge where the indentation is applied.

To analyze the sensitivity of this method to the size of the inclusion, we tested this with the target shear modulus distribution given in **Figure 4-10** (a), where we reduce the diameter of the inclusion to 0.2, and 3 displacement fields are evenly distributed on the top, left, and right edges each. The reconstructed shear modulus distribution is given in **Figure 4-10** (b) for 1% noise in the surface displacements. Compared with the target shear modulus distribution as shown in **Figure 4-10** (a), the new method is capable of detecting the location of the inclusion. However, the shear modulus value in the inclusion is significantly off. In addition, the size of the inclusion becomes larger. We also decreased the noise level to 0.1% which improves the reconstructed inclusion value and shape (see **Figure 4-10** (c)). However, it is still significantly off from the target shear modulus distribution. This does not necessarily imply the limitation of this method as elaborated in **Section 4.3**.

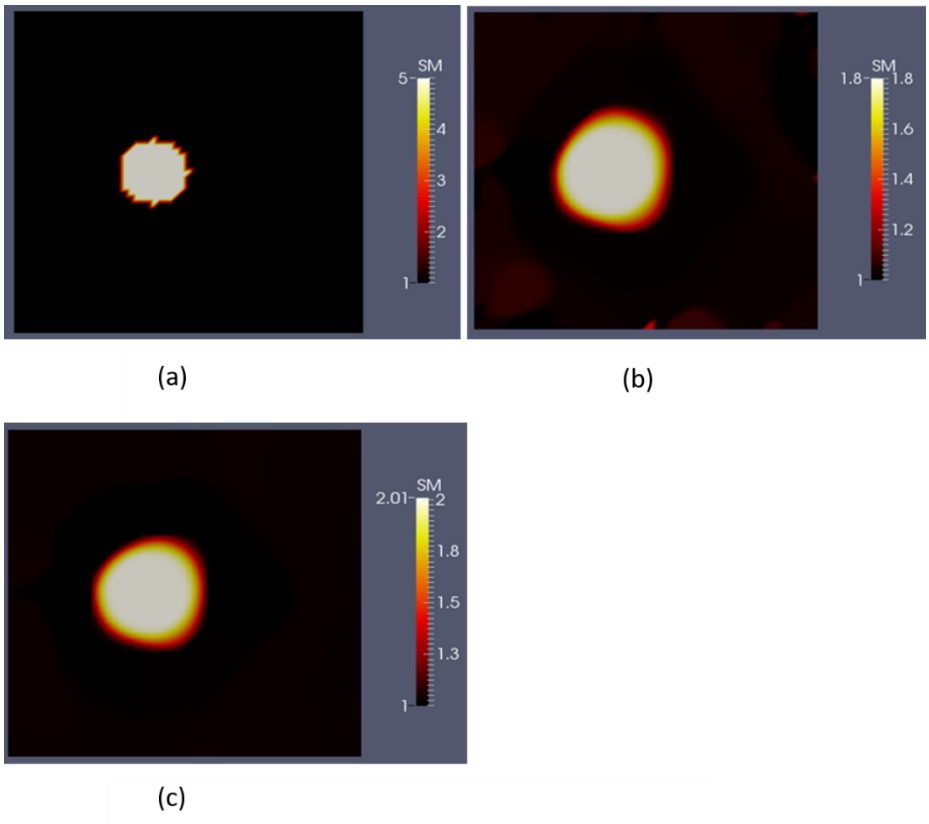

Figure 4-10: Target shear modulus distribution given in (a), and reconstructed shear modulus with 1% noise in (b) and reconstructed shear modulus with 0.1% noise in (c).

4.3 Discussions

In this chapter we have presented a novel approach to solve the inverse problem in elasticity for the shear modulus distribution from displacement data that is measured only on the exterior of the specimen. This can be done using two digital cameras positioned at distinct locations and recording digital cameras before and after inducing the deformation field. These digital camera images can be processed to infer the three-dimensional surface deformation. We have tested this method with simulated surface displacement data,

created by solving the forward problem for a problem domain defined with a stiff inclusion embedded in a softer background. We have intentionally placed the inclusion off centered to avoid displacement fields being symmetric in the problem domain, which could be interpreted as some kind of inverse crime. The surface displacements were a direct result of the indentations applied at distinct location on the specimen's boundary. We have solved the inverse problem with 9, 15, and 27 surface displacement fields and added 1% and 2.5% noise to the surface displacement data. This noise level is reasonable as shown in [87] where the surface displacement error obtained with digital camera images had a noise level of about 1%.

We have made the following observations in our reconstructions: 1) The shear modulus ratio of the inclusion to the background improves with increasing number of surface displacement fields, 2) The shape of the reconstructed inclusion improves with an increasing number of surface displacement fields, 3) The shear modulus ratio of inclusion to background reduces significantly with increasing noise level, 4) The shape of the reconstructed inclusion deteriorates slightly with increasing noise level. In fact, the shape of the inclusion is well preserved despite the high noise level which is mainly due to the proper choice of the regularization type. The inclusion size in the target domain had a large diameter. Smaller diameters will be harder to recover as their absence will not change the resulting surface displacement field significantly. However, with decreasing noise level and increasing the "richness" of the data set, this issue can be addressed. Thus, future work will focus on the investigation of inclusion size detectability to the noise level with a rich data set.

In **Figure 4-9** (a) and (b) we also tested two cases where only limited surface displacement data was available. We observe that it is feasible to recover the shear modulus distribution with limited surface data. However, the shape of the inclusion becomes worse, and the shear modulus value decreases. This is because using partial surface deformations will reduce the "richness" of the data set, and could be addressed by including additional surface displacements induced by shear forces and indentations that are not perpendicular to the boundary edge.

All shear modulus reconstructions presented in this paper are only correct up to a multiplicative factor. In other words, multiplying the shear modulus distributions by an arbitrary constant would result in the same displacement field. This is due to the fact that no Neumann boundary conditions were utilized in the boundary data. We note that an absolute shear modulus reconstruction can be obtained if the indentation force is known or if the shear modulus value is known somewhere in the problem domain, e.g. through measurements on the surface of the specimen.

Alternative and successful techniques to solve the inverse problem in finite elasticity rely mainly on displacement measurements from magnetic resonance imaging and ultrasound techniques. These techniques have the advantage that they can image the interior of the specimen, thus provide displacement data in the entire interior of the specimen. This rich data set reduces the need of utilizing a large number of displacement fields. For example, in [49, 80] the target shear modulus distribution could be reconstructed utilizing only 1 to 2 displacement fields. This implies that the computational cost reduces significantly as the forward problem and adjoint problem are solved for each

displacement field separately [48, 49, 62, 80, 82]. On the other hand, measuring surface deformations requires only a set of digital cameras (about 2-4) to image the surface of the specimen before and after the indentation. Thus the experimental set up is significantly cheaper as compared to ultrasound or magnetic resonance techniques. An advantage of using surface displacement data to solve the inverse problem lies in the fact that force indentations can be measured with simple force sensors. This results in absolute reconstructions of the shear modulus distribution and increases in general the information content, thus making the overall solution of the inverse problem "more unique".

4.4 Conclusions

We have tested the feasibility to solve the inverse problem in finite elasticity for the shear modulus distribution utilizing "hypothetical" measured surface displacement fields. We have successfully recovered the shear modulus distribution for a stiff inclusion in a homogeneous background, assuming that the shear modulus is unknown on the finite element nodes of the problem domain. This method has potential as a novel diagnostic imaging modality to detect tumors surrounded by healthy tissue from their stiffness contrast. We observed that the quality of the shear modulus reconstructions depend on the noise level inherent in measured surface displacement data. Furthermore, the reconstruction quality depends on the number of surface displacement fields utilized to solve the inverse problem.

We note that displacement indentations were prescribed rather than force indentations. This results in shear modulus reconstructions being true only up to a multiplicative factor. Thus, future work involves the use of force indentation, which will

clearly yield absolute shear modulus reconstructions. Applying force boundary conditions may also result in improved reconstructions as they provide more “information” for the inversion process in general. In the next chapter, we will test this methodology with domains having multiple objectives with different sizes. In particular, we will investigate the feasibility to detect small objects positioned far from the boundary.

5. MAPPING THE ELASTIC BEHAVIOR OF SOLIDS QUANTITATIVELY FROM LIMITED KNOWN DISPLACEMENTS ON SPECIMEN BOUNDARIES[*]

In **Chapter 4**, the deformations were induced by applying a displacement indentation, and no force or traction was assumed to be known, resulting in a shear modulus reconstruction being off by a multiplicative factor [51]. Furthermore, only one inclusion in a homogeneous background was simulated. Even though we did not assume any particular form of inhomogeneity, the question may still arise if this approach has the capability to recover more than one inclusion.

In this chapter, we will test the feasibility to recover the shear modulus distribution (1) of one or two inclusions; (2) absolutely (i.e., quantitatively) by including known (measured) force indentations; (3) utilizing boundary displacements from partial boundaries of the specimen for convenient data collection; and (4) utilizing a curved boundary domain. The paper is organized as follows: In **Section 5.1**, we review the mathematical foundation along with the computational procedure for the inverse algorithms; in **Section 5.2**, we test the inverse algorithms with simulated experiments for various geometric domains and shear modulus distributions; in **Section 5.3**, we discuss the numerical results and end with conclusions in **Section 5.4**.

---

[*]Reprinted with permission from"Mechanics Based Tomography: A Preliminary Feasibility Study." by Mei, Y., Wang, S., Shen, X., Rabke, S., & Goenezen, S., 2017. Sensors, 17(5), 1075. Copyright [2017] Molecular Diversity Preservation International and Multidisciplinary Digital Publishing Institute.

5.1 Review of inverse algorithms using limited boundary displacements

In this paper, the material is still assumed to be isotropic, heterogeneous, linear elastic, and in the state of incompressible plane strain. The inverse algorithms utilized in this chapter is very similar to that used in **Chapter 4**, thus we will not thoroughly discuss herein. Comparing this work to the previous chapter, we also assume that the applied force is known together with the induced displacement at that point. As such, the resulting shear modulus distribution will be recovered quantitatively. Finally, we add the same noise level to the simulated boundary displacements (random noise), force and corresponding displacement indentation to study the sensitivity of the mapped shear moduli to noisy data.

5.2 Numerical results with simulated experiments

5.2.1 Case 1: A square model with a small inclusion

First, we consider a 1 cm × 1 cm square with a small inclusion with a radius of 0.1 cm surrounded by a softer homogeneous background material as shown in **Figure 5-1**. The coordinate of the center of the inclusion is (0.4 cm, 0.5 cm), the target shear modulus value of the background is 10 kPa, and the stiffness in the inclusion is 50 kPa. With regards to boundary conditions, we fix the bottom edge in both directions for all simulations. In **Figure 5-1** (a), forces are applied pairwise on the left and right side simultaneously and are aligned horizontally but in the opposite direction (net force is zero). Each pairwise applied force induces a displacement on the top boundary (see the green line in **Figure 5-1** (a)). Varying the location of the pairwise applied forces vertically and sequentially provides a rich number of boundary displacement data sets on the top face (green line). In **Figure 5-1** (b), single force indentations are applied on the top boundary edge

sequentially, in order to induce boundary displacements (for each single force indentation) on the left boundary edge (see green vertical line in **Figure 5-1** (a)). In **Figure 5-1** (c), single force indentations are applied on the top boundary edge sequentially, in order to induce boundary displacements (for each single force indentation) on the right boundary edge (see green vertical line in **Figure 5-1** (c). Varying the location of applied force indentation as shown in **Figure 5-1** (b), (c), we obtain a rich boundary displacement data set. Simulated displacement measurements are highlighted on the boundary edge with a green line as shown in **Figure 5-1**(a)–(c). Furthermore, each indentation induces a force of 0.05 N on the corresponding node in the problem domain. This force will induce small deformations that are suitable for displacement measurements using a digital image correlation system. The problem domain is discretized with 7200 linear triangular elements (61 nodes are uniformly distributed in each direction). The boundary displacement is assumed to be measured on the edge with no applied force indentation. In standard indentation tests, the displacement at the indentation can be measured with high accuracy; therefore, this information will also be included in the inverse solution process.

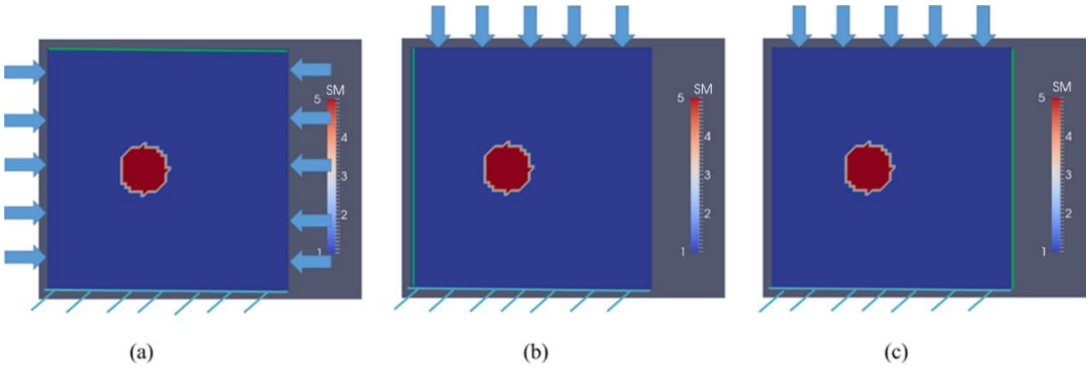

Figure 5-1: The problem domain with a stiff inclusion surrounded by a soft background. The arrows indicate the indentation locations, and the green line represents the side of known or measured displacements. (a) the indentations are sequentially applied pairwise at both lateral sides (net force is zero), and we utilize boundary displacements on the top edge as measured data; (b) the indentation is applied on the top edge, and we utilize boundary displacements on the left edge as measured data; (c) the indentation is applied on the top edge, and we utilize boundary displacements on the right edge as measured data (unit in the scale bar: 10 kPa). Note: "SM" stands for shear modulus.

Figure 5-2 and **Figure 5-3** show the reconstructed shear modulus distribution with respect to the noise levels of 0.1%, and 1%, respectively. In both figures, (b), (c) represent the results for 7 and 13 boundary displacement data sets, respectively. 7 displacement boundary data sets are obtained according to **Figure 5-1** (a), 3 boundary displacement data sets are obtained according to **Figure 5-1** (b), and 3 boundary displacement data sets are obtained according to **Figure 5-1** (c).

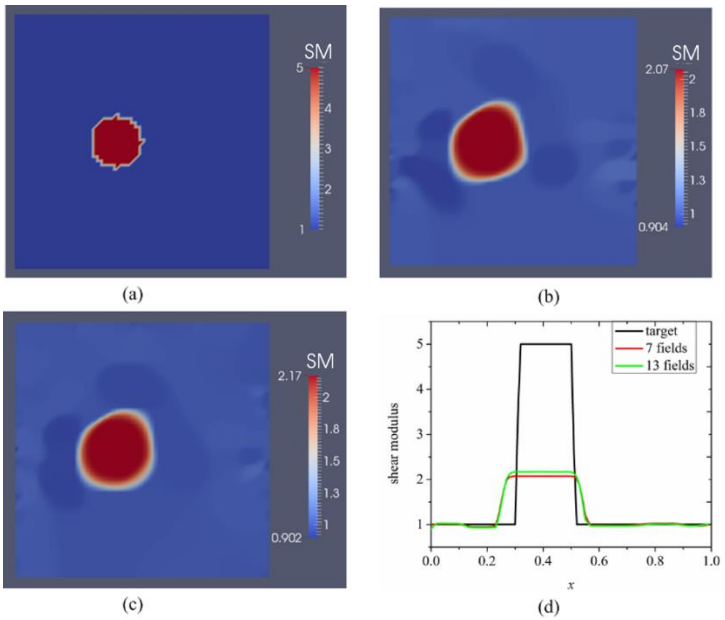

Figure 5-2: Shear modulus reconstructions for 0.1% noise. (a) target shear modulus distribution for comparison; (b), (c) reconstructed shear modulus distribution using 7 and 13 boundary displacement data sets, respectively; (d) shear modulus plot over the horizontal line through the center of the inclusion for the target and reconstructed shear modulus distribution (unit in the scale bar: 10 kPa). Note: "SM" stands for shear modulus.

The shear modulus values are plotted over the horizontal line passing through the center of the small inclusion in **Figure 5-2** (d) and **Figure 5-3** (d). The regularization factors for **Figure 5-2** and **Figure 5-3** were chosen to be 10^{-11} and 10^{-10}, respectively. In **Figure 5-2**, the reconstructions reveal that the location of the inclusion can be detected and the shape of the inclusion is well preserved. However, the inclusion seems to be larger than the target and the reconstructed shear modulus value of the inclusion is underestimated. Furthermore, with increasing number of displacement data sets, both the shape and the shear modulus value of the inclusion slightly improve, as shown in **Figure 5-2** (b),(c). More precisely, the reconstructed shear modulus value in the inclusion

increases slightly from 2.07 to 2.17, and the recovered inclusion becomes more circular as shown in **Figure 5-2** (c). We have also performed the reconstruction without noise and observed that the shear modulus distribution is very similar to the reconstructions in **Figure 5-2** (not shown here).

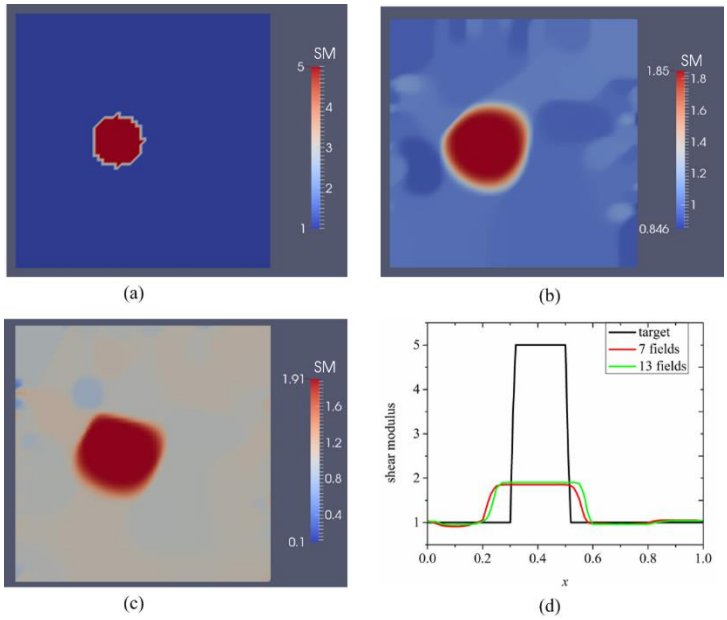

Figure 5-3: Shear modulus reconstructions for 1.0% noise. (a) target shear modulus distribution for comparison; (b), (c) reconstructed shear modulus distribution using 7 and 13 boundary displacement data sets, respectively; (d) shear modulus plot over the horizontal line through the center of the inclusion for the target and reconstructed shear modulus distribution (unit in the scale bar: 10 kPa). Note: "SM" stands for shear modulus.

In **Figure 5-3** (b), we observe that with 1% noise level the recovered inclusion is larger than in the previous example with 0.1% noise level. Furthermore, the background has stronger oscillations due to the higher noise level. The reconstructions with 1% noise

do not improve much with increasing number of displacement data sets used in **Figure 5-3** (c). Nevertheless, we are able to detect the location of the inclusion center.

To better analyze the accuracy of the reconstructions in **Figure 5-2** and **Figure 5-3**, we define a relative error to quantitatively evaluate the error between the recovered and target shear modulus distributions that is, $e = \sqrt{\sum_{i=1}^{N_n} \left(\mu_i - \mu_i^{\circ}\right)^2 \Big/ \sum_{i=1}^{N_n} \left(\mu_i^{\circ}\right)^2} \times 100\%$, where N_n , μ_i and μ_i° are the total number of nodes throughout the problem domain, nodal recovered shear modulus and nodal target shear modulus, receptively. The relative error for each case presented in **Figure 5-2** and **Figure 5-3** are shown in **Table 5-1**. **Table 5-1** illustrates that increasing the number of boundary displacement datasets and decreasing the noise level improves the mapped shear modulus only slightly for Case 1.

Table 5-1: Error between the recovered and target shear modulus distributions for each case presented in **Figure 5-2** and **Figure 5-3**

Noise Level	**L2 Error**	
	7 Displacement Datasets	**13 Displacement Datasets**
0.1%	41.51%	40.39%
1%	43.89%	43.48%

5.2.2 Case 2: A semi-Circle model with one or two inclusions

The second example in **Figure 5-4** is a semi-circle with an inclusion that can be thought of as an idealized breast with an idealized tumor mimicking inclusion. The radii of the semi-circle and the inclusion are 7.5 cm and 1 cm, respectively. This problem domain is discretized with 7632 linear triangular elements. The exact shear moduli of the background and inclusion are 5 kPa and 25 kPa, respectively. To solve the forward problem in elasticity, we fix the bottom edge and apply indentations with a nodal force of 0.27 N on the top curved edge sequentially (the location and direction of each indentation are indicated by a yellow arrow in **Figure 5-4** (a)–(c)). Similar to Case 1, the force will induce a small deformation of the simulated phantom. In this case, we assume that boundary displacements can be measured on the entire top curved edge. **Figure 5-5** (b)–(d) represent the recovered shear modulus distributions with 5, 10, and 15 boundary displacement data sets, respectively. In this case, no noise is introduced, and the regularization factor is chosen to be 10^{-11}. In general, we observe that the inclusion shape can be visualized well, while its shear modulus value is significantly underestimated by about 20%. Additionally, increasing the total number of displacement fields slightly improves both the reconstructed shear modulus value and the shape of the inclusions. The mapped shear modulus value in the inclusion increases from about 16.5 kPa to 19.1 kPa using 15 boundary displacement data sets as shown in **Figure 5-5**. It is also notable that the reconstructed shear modulus value in the inclusion reaches approximately 80% of the target value.

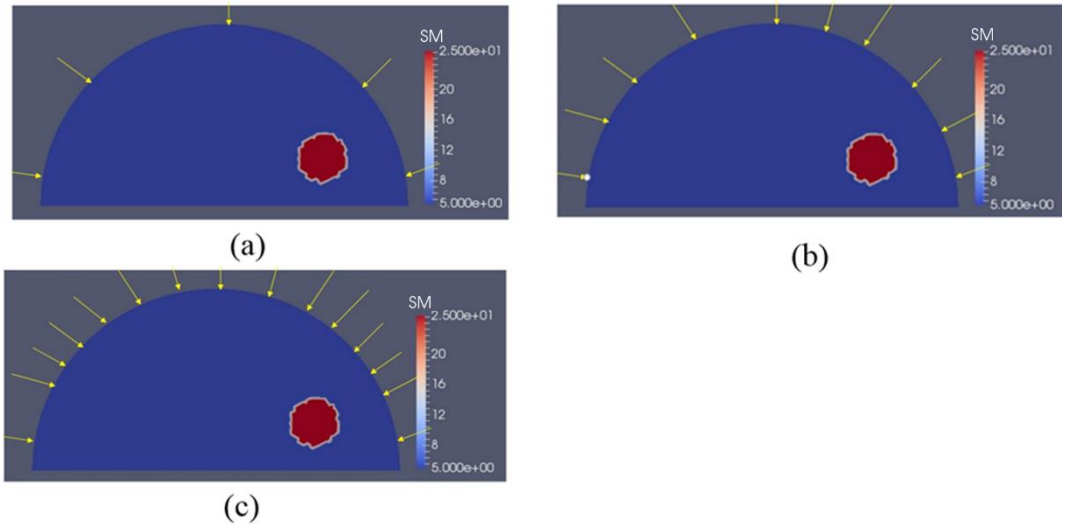

Figure 5-4: The problem domain for a semi-circle with a stiff inclusion surrounded by a soft background. The yellow arrows indicate the indentation locations, and measured boundary displacements are simulated on the top curve. (a) 5 arrows representing 5 sequentially applied forces to obtain boundary displacement data sets; (b) 10 arrows representing 10 sequentially applied forces to obtain boundary displacement data sets; and (c) 15 arrows representing 15 sequentially applied forces to obtain boundary displacement data sets (unit in the scale bar: kPa). Note: "SM" stands for shear modulus.

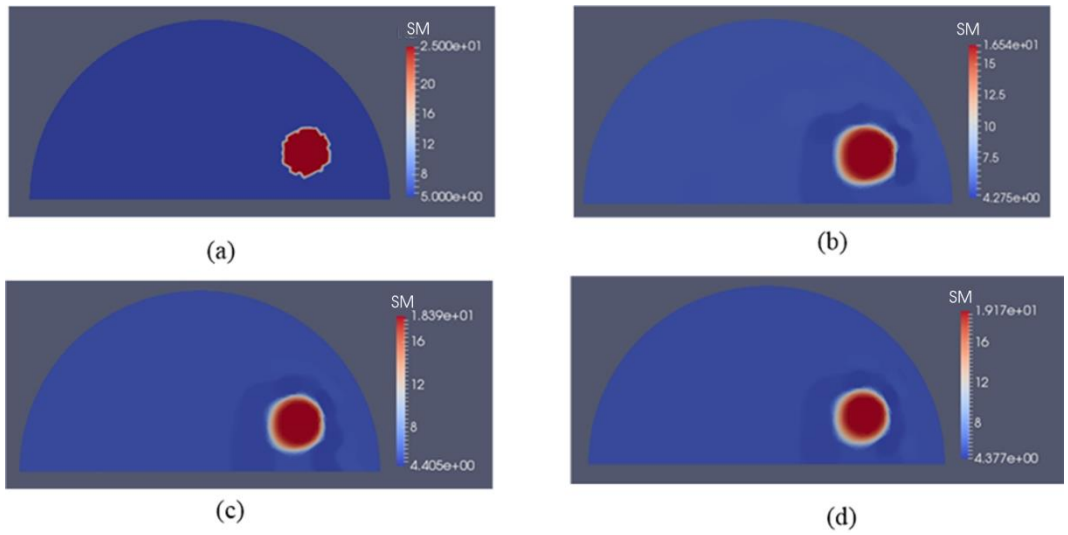

Figure 5-5: Shear modulus reconstructions without noise in boundary displacements. (a) target shear modulus distribution for comparison; (b)–(d) reconstructed shear modulus

distribution using 5, 10 and 15 boundary displacement data sets, respectively (unit in the scale bar: kPa). Note: “SM” stands for shear modulus.

Figure 5-6 (b)–(d) represents the recovered shear modulus distributions for a noise level of 1% with 5, 10, and 15 displacement data sets, respectively, for a regularization factor of 10^{-10}. Compared to the case without noise, the recovered shear modulus distribution degrades significantly. The shear modulus value in the inclusion is roughly 15 kPa and does not change much with varying number of boundary displacement data sets. We also observe strong oscillations occurring throughout the problem domain, in particular, close to the curved edge.

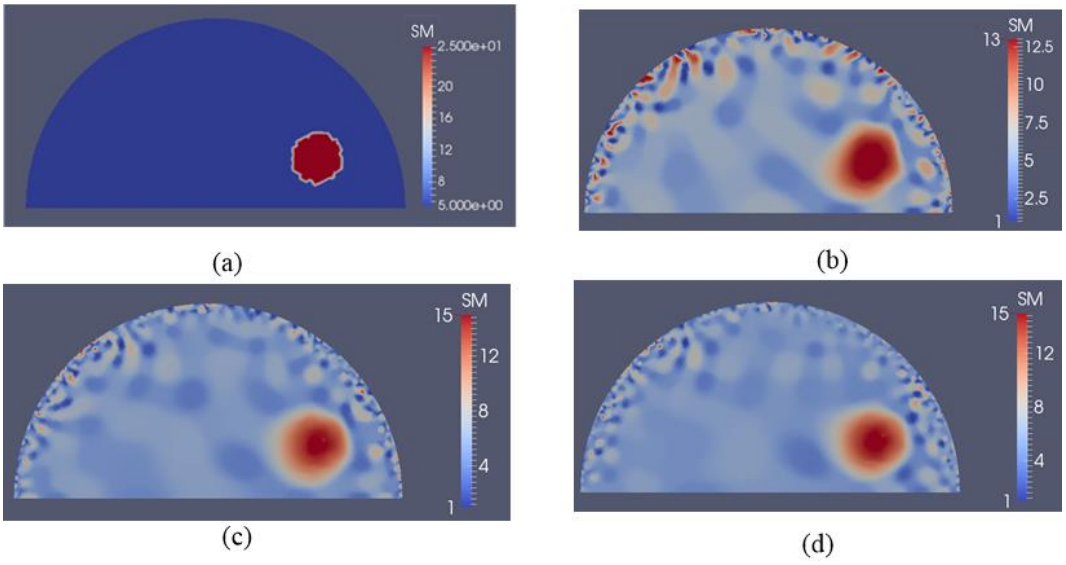

Figure 5-6: Shear modulus reconstructions with 1% noise. (a) target shear modulus distribution for comparison; (b)–(d) reconstructed shear modulus distribution using 5, 10,

and 15 boundary displacement data sets, respectively (unit in the scale bar: kPa). Note: "SM" stands for shear modulus**.**

Figure 5-7 (b)–(d) represent shear modulus reconstructions for a very high noise level of 5% with 5, 10 and 15 boundary displacement datasets, respectively. A regularization factor of 10^{-9} was selected in this case. In comparison with the reconstruction with 1% noise level in **Figure 5-6**, we observe that the noise artifacts are significantly amplified, with peaks closer to the boundary. We also computed the relative error for all cases presented in **Figure 5-5–5-7** as shown in **Table 5-2**. As expected, the accuracy in reconstruction results improves with a lower noise level as well as more displacement datasets.

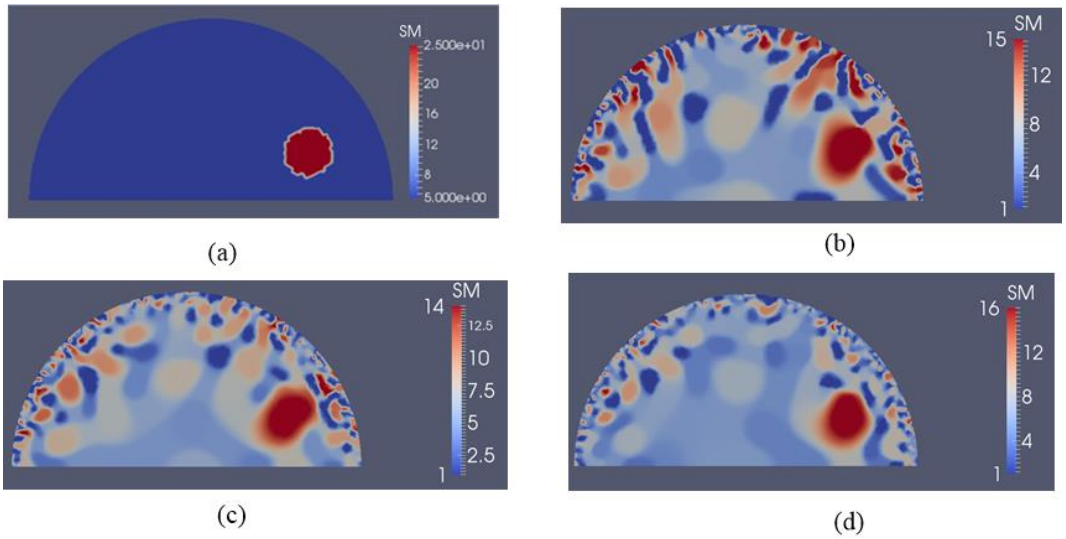

Figure 5-7: Shear modulus reconstructions with 5% noise. (a) target shear modulus distribution for comparison; (b)–(d) reconstructed shear modulus distribution using 5, 10,

and 15 boundary displacement data sets, respectively (unit in the scale bar: kPa). Note: "SM" stands for shear modulus.

Table 5-2: Error between the recovered and target shear modulus distributions for the cases presented in **Figure 5-5**–**5-7**

Noise Level	L2 Error		
	5 Displacement Datasets	10 Displacement Datasets	15 Displacement Datasets
0%	28.68%	23.91%	22.52%
1%	45.40%	40.66%	38.30%
5%	69.26%	56.25%	50.78%

In **Figure 5-8** (a), we test a slightly different target problem domain from the previous one in **Figure 5-4** (a), (b), where the location of the stiff inclusion is positioned further away from the boundary. The boundary conditions, i.e., the applied force boundaries are the same as in the previous examples as well. The reconstructed shear modulus distribution is given in **Figure 5-8** (b), (c) for 5 and 10 boundary displacement data sets, respectively, with a noise level of 0.1%. The regularization factor was chosen to be 10^{-10}. We observe that the inclusion can be recovered despite its deeper location and being further away from the top boundary. In **Figure 5-9**, we increase the noise level to 1% using the same number of boundary displacement data sets, but increase the regularization factor to 5×10^{-10}. The reconstructed shear modulus values deteriorate

together with the shape of the inclusion compared to the previously lower noise level. Nevertheless, the inclusion shape and location are detectable.

To test the sensitivity to detect smaller inclusions, we have reduced the size of the inclusion to a radius of 0.5 cm in **Figure 5-10** (a). The applied forces were the same as in **Figure 5-4** (a), (b). The reconstructed shear modulus distributions are shown in **Figure 5-10** (b), (c) for 5 and 10 boundary displacement data sets, respectively, with a noise level of 0.1% and a regularization factor of 3×10^{-10}. In **Figure 5-11**, we increase the noise level to 1% for the same displacement boundary data sets using a regularization factor of 7×10^{-10}. Overall, we observe that the location and shape of the inclusion is preserved, while the size is overestimated and the shear modulus value in the inclusion is underestimated.

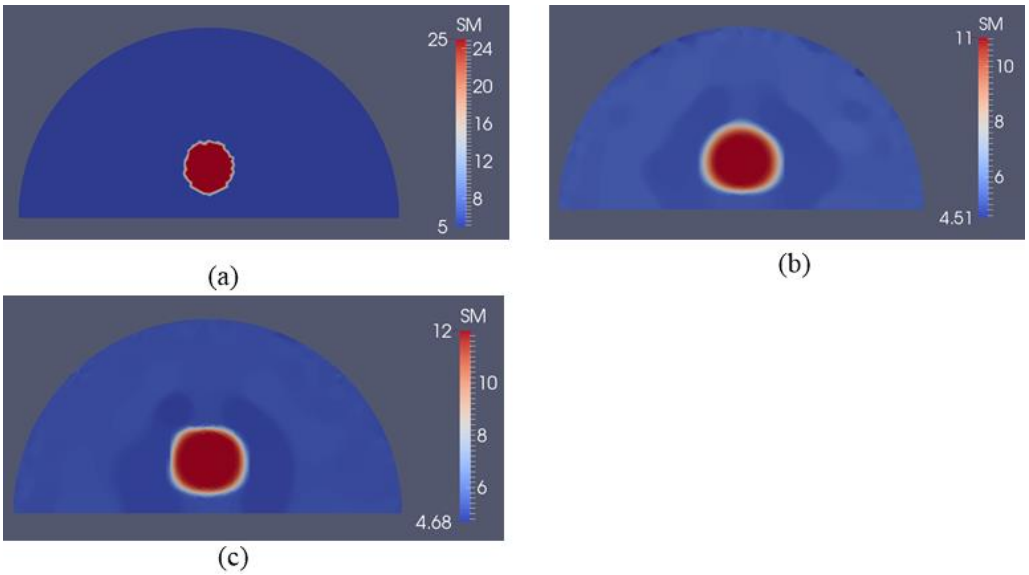

Figure 5-8: Shear modulus reconstructions with 0.1% noise. (a) target shear modulus distribution with varied inclusion depth in comparison to previous target problem domain in Figure 4(a), (b); (b), (c) reconstructed shear modulus distribution using 5 and 10 boundary displacement data sets, respectively (unit in the scale bar: kPa). Note: "SM" stands for shear modulus.

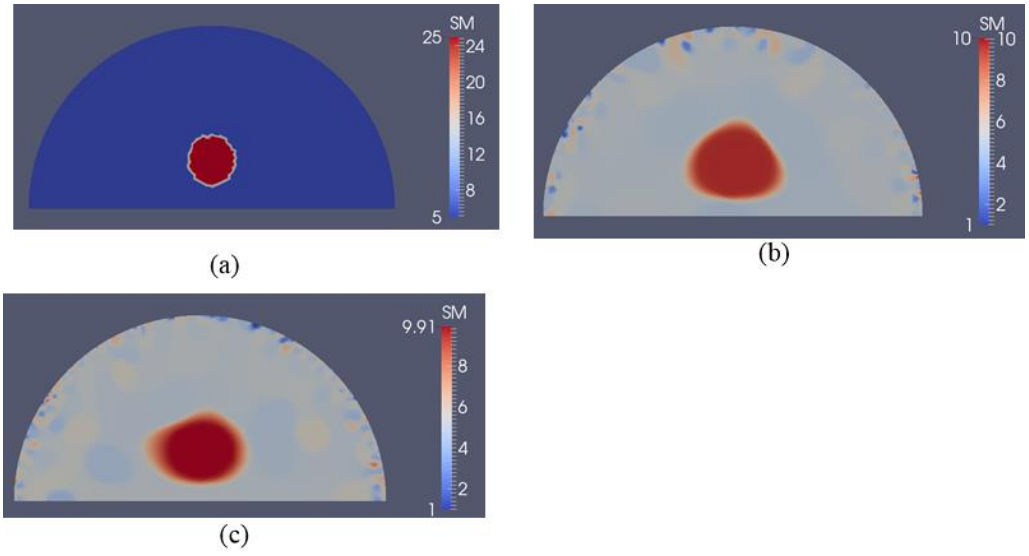

Figure 5-9: Shear modulus reconstructions with 1% noise. (a) target shear modulus distribution with varied inclusion depth in comparison to previous target problem domain in Figure 4(a), (b); (b), (c) reconstructed shear modulus distribution using 5 and 10

boundary displacement data sets, respectively (unit in the scale bar: kPa). Note: “SM” stands for shear modulus.

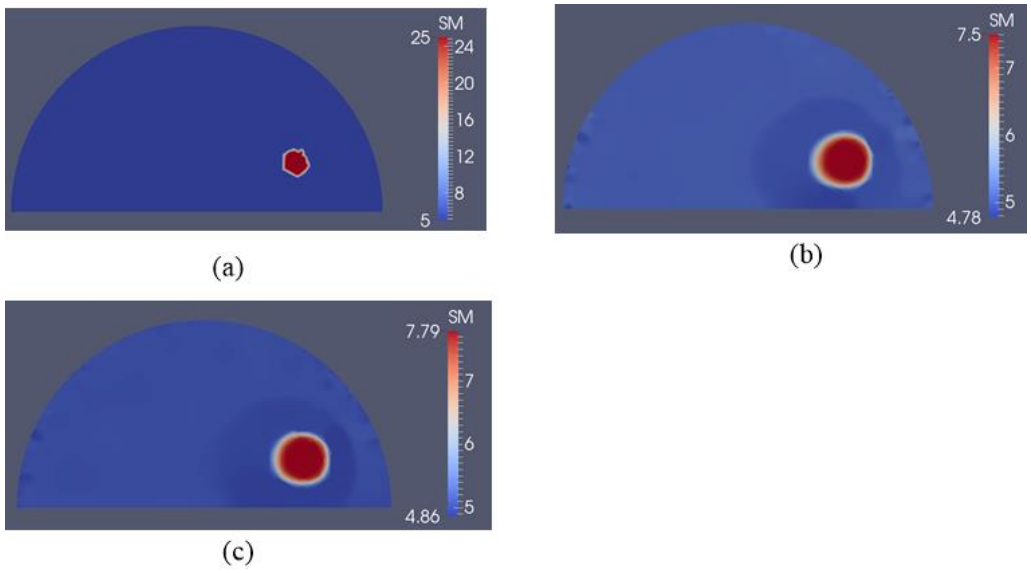

Figure 5-10: Shear modulus reconstruction with 0.1% noise. (a) target shear modulus distribution with a smaller inclusion radius of 0.5 cm is defined to study detectability of the inclusion to its size; (b), (c) reconstructed shear modulus distribution using 5 and 10 boundary displacement data sets, respectively (unit in the scale bar: kPa). Note: “SM” stands for shear modulus.

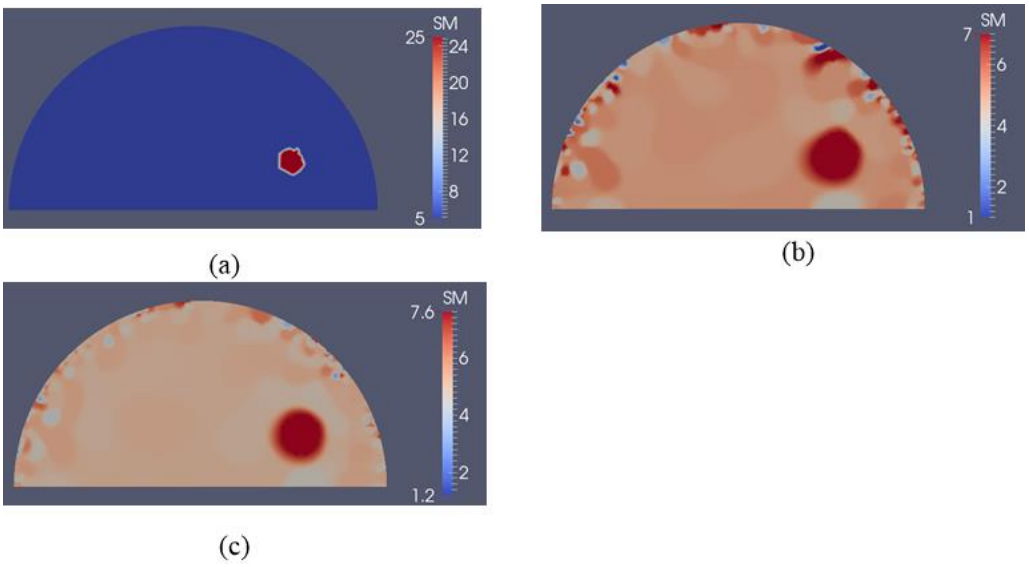

Figure 5-11: Shear modulus reconstruction with 1% noise. (a) target shear modulus distribution with a smaller inclusion radius of 0.5 cm is defined to study detectability of the inclusion to its size; (b), (c) reconstructed shear modulus distribution using 5 and 10 boundary displacement data sets, respectively (unit in the scale bar: kPa). Note: "SM" stands for shear modulus.

To test shape detectability of this approach, we define the target problem domain given in **Figure 5-12** (a) with an elliptic shaped inclusion. We apply the same boundary conditions as in **Figure 5-4** (a), (b) and add 0.1% noise to boundary displacements. The reconstructed shear modulus distributions are shown in **Figure 5-12** (b), (c) for 5 and 10 boundary displacement data sets, respectively, for a regularization factor of 5×10^{-11}. We observe that the reconstructed inclusion shape follows the trend of an ellipse. In **Figure 5-13**, the noise level is increased to 1%, the regularization factor is chosen to be 5×10^{-10} and the shape deteriorates as anticipated, but an elliptic shape-like trend appears to be present.

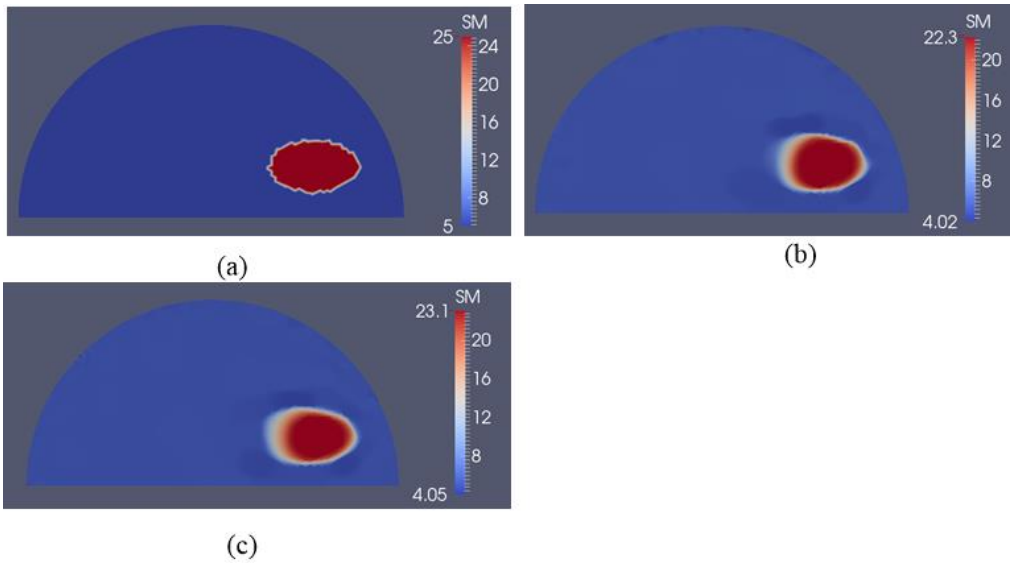

Figure 5-12: Shear modulus reconstructions with 0.1% noise. (a) target shear modulus distribution with an elliptic shaped inclusion is defined to study detectability of the inclusion shape; (b), (c) reconstructed shear modulus distribution using 5 and 10 boundary displacement data sets, respectively (unit in the scale bar: kPa). Note: "SM" stands for shear modulus.

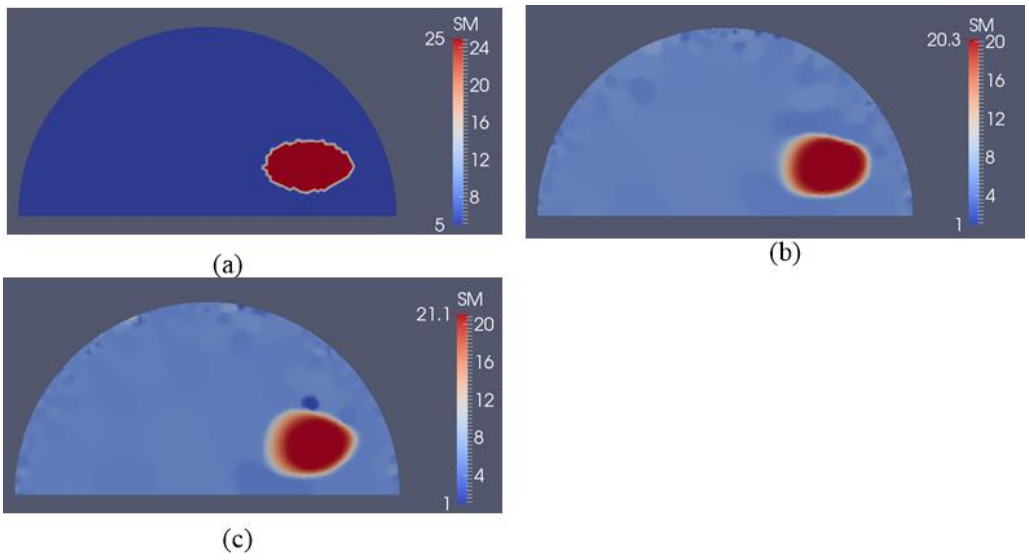

Figure 5-13: Shear modulus reconstructions with 1% noise. (a) target shear modulus distribution with an elliptic shaped inclusion is defined to study detectability of the inclusion shape; (b), (c) reconstructed shear modulus distribution using 5 and 10 boundary

displacement data sets, respectively (unit in the scale bar: kPa). Note: "SM" stands for shear modulus.

Next, we investigate the detectability of inclusions to varying stiffness contrasts. To this end, we specify target problem domains on the left column in **Figure 5-14** with varying shear modulus values in the inclusion from 7.5 kPa to 100 kPa from the top to bottom row, respectively, while the background shear modulus value remains the same with 5 kPa. We utilize 5 and 10 boundary displacement data sets from solving the forward problem using force indentations according to **Figure 5-4** (a), (b) and adding 0.1% noise. The reconstructions with 5 and 10 boundary displacement data sets are shown in columns 2 and 3, respectively. It appears that the stiffness contrast ratio of 2 according to row 2 in **Figure 5-14** yields the best reconstructions. Decreasing or increasing the stiffness contrast ratio will compromise the accuracy of the shear modulus reconstructions. For the target shear modulus inclusion values of 50 and 100 (see last two rows in **Figure 5-14**), the reconstructed shear modulus values are very similar. The regularization factors were selected to be the same for each row in **Figure 5-14** with 10^{-10}, 10^{-10}, 5×10^{-11}, 5×10^{-11} and 5×10^{-11} starting from the top row down to the bottom row. Similarly, in **Figure 5-15**, the sensitivity of the reconstructions to the stiffness inclusion to the background ratio was analyzed for a noise level of 1%. The regularization factors from the top row to the bottom row were 5×10^{-9}, 2×10^{-9}, 1×10^{-10}, 3×10^{-10} and 3×10^{-10}, respectively. Increasing the noise level to 1% appears to yield the best reconstructions for a stiffness contrast of 1.5, shown in the first row of **Figure 5-15**.

In **Figure 5-16** (a), we have two stiff inclusions with shear modulus values of 25 kPa. In this case, we also apply radial indentations of 0.27 N and simulate displacement measurements on the top boundary edge. We utilize 5 and 10 displacement data sets in the presence of 0.1% noise to solve the inverse problem, and the mapped shear modulus distributions are shown in **Figure 5-16** (b), (c), respectively. The regularization factor was chosen to be 10^{-10}. The reconstructions reveal that both inclusions can be visualized and detected, while the shear modulus values are significantly underestimated. Furthermore, we note that the stiffness contrast of the left inclusion is more underestimated than that of the right inclusion. This is likely due to boundary sensitivity thoroughly discussed by the authors in [80, 88]. In **Figure 5-17** and **Figure 5-18**, we increase the noise level to 1% and 5%, respectively. The regularization factor for 1% noise level is chosen to be 3×10^{-10} and for 5% is chosen to be 5×10^{-10}. While the shear modulus reconstruction with the high noise level of 5% is dominated by noise artifacts, the inclusions can be visualized to some extent. In **Table 5-3**, we compute the relative error for every case with two inclusions presented in **Figure 5-16–5-18** and observe a similar trend that the accuracy in reconstruction results improves with a lower noise level as well as more displacement datasets observed in **Table 5-2**.

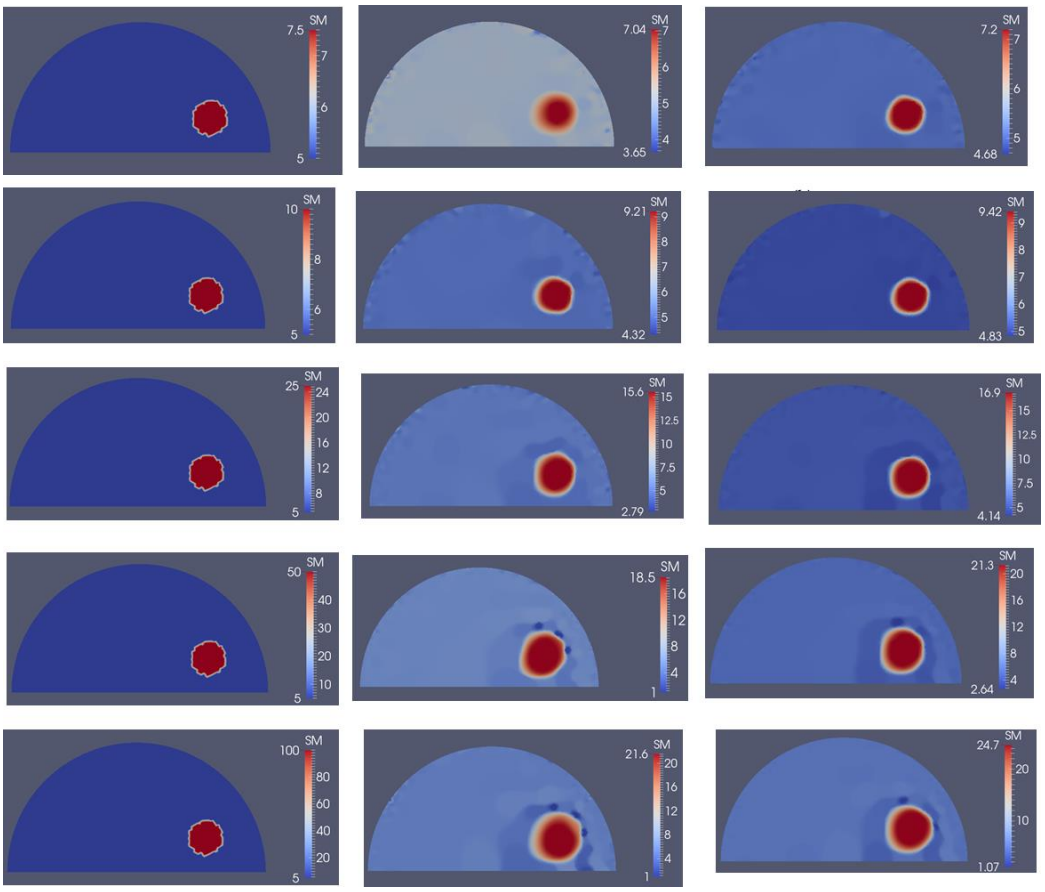

Figure 5-14: Problem domain with target shear modulus distribution is defined in the first column with varying shear modulus values in the inclusion from 7.5 kPa (top row) to 100 kPa (bottom row) to test the feasibility range of stiffness detection. Column 2 and column 3 represent the shear modulus reconstructions with 5 and 10 boundary displacement data sets, respectively, using 0.1% noise.

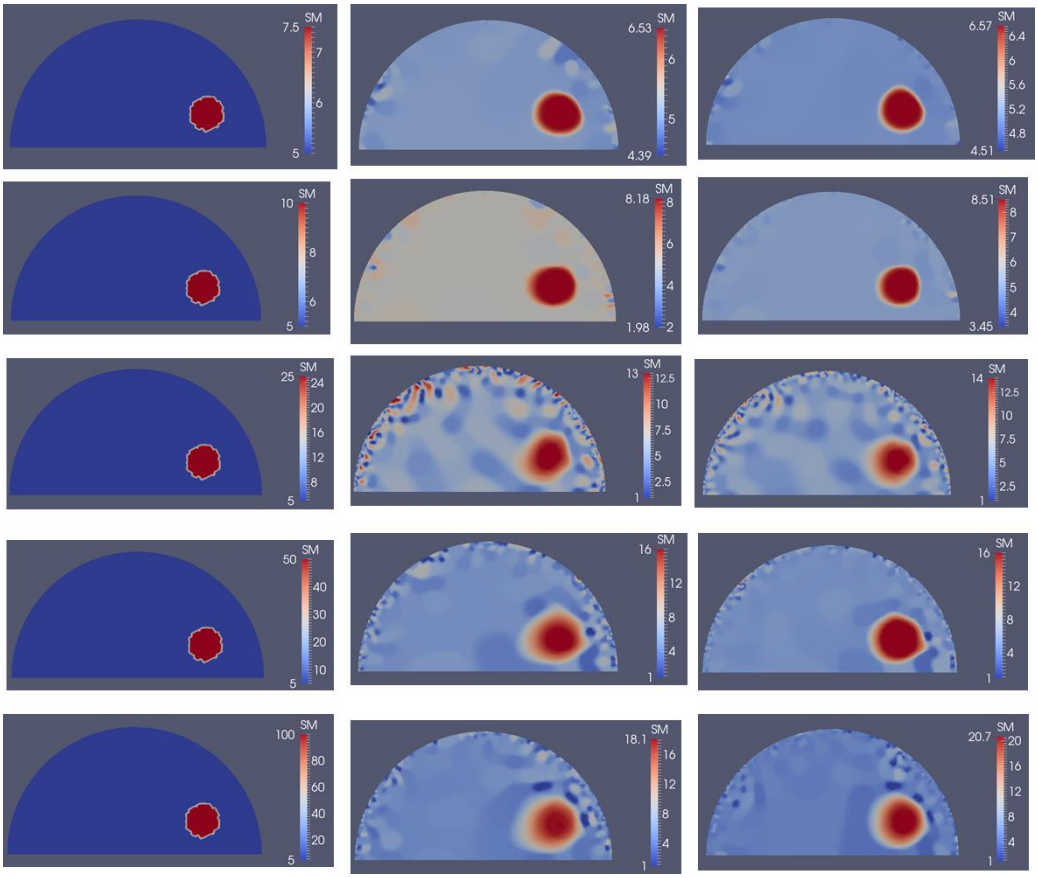

Figure 5-15: Problem domain with target shear modulus distribution is defined in the first column with varying shear modulus values in the inclusion from 7.5 kPa (top row) to 100 kPa (bottom row) to test the feasibility range of stiffness detection. Column 2 and column 3 represent the shear modulus reconstructions with 5 and 10 boundary displacement data sets, respectively, using 1% noise.

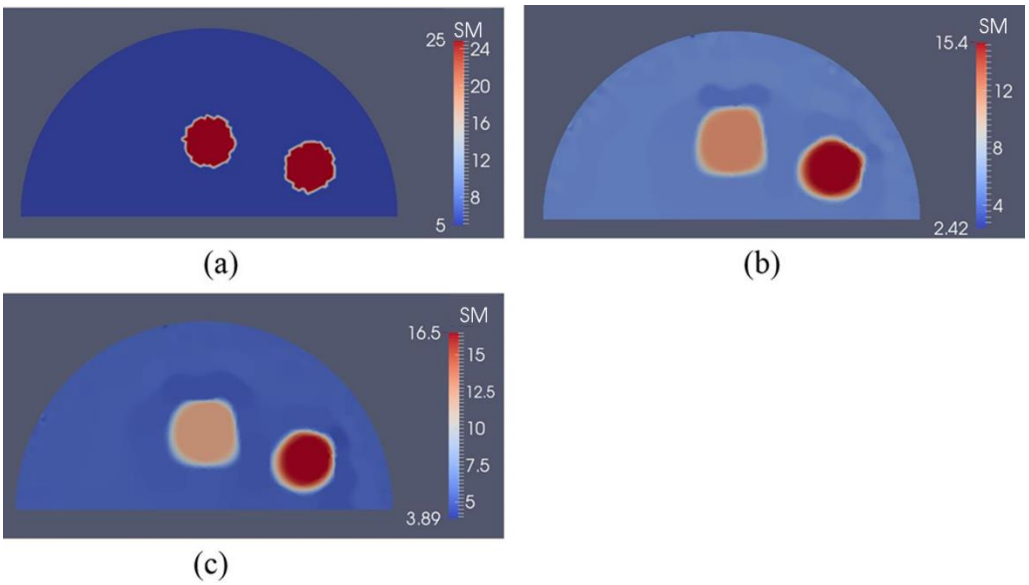

Figure 5-16: Shear modulus reconstructions with 0.1% noise. (a) target shear modulus distribution for comparison; (b), (c) reconstructed shear modulus distribution using 5 and 10 boundary displacement data sets, respectively (unit in the scale bar: kPa). Note: "SM" stands for shear modulus.

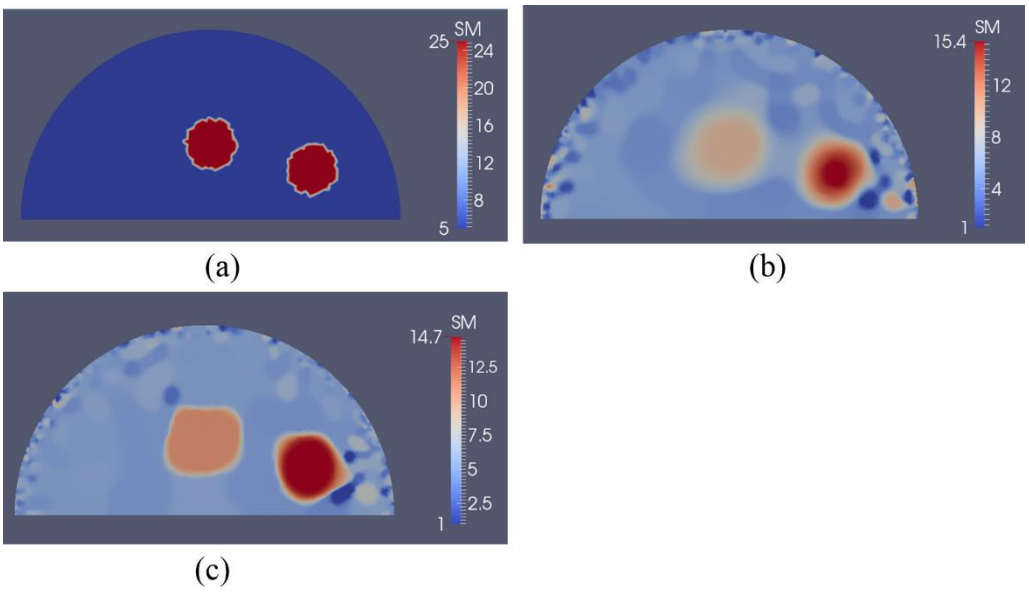

Figure 5-17: Shear modulus reconstructions with 1% noise. (a) target shear modulus distribution for comparison; (b), (c) reconstructed shear modulus distribution using 5 and

10 boundary displacement data sets, respectively (unit in the scale bar: kPa). Note: “SM” stands for shear modulus.

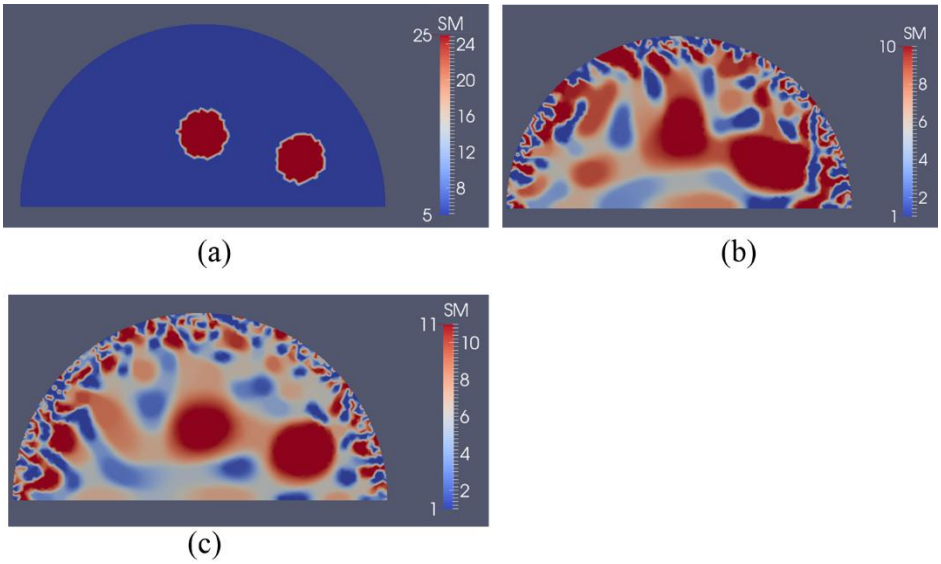

Figure 5-18: Shear modulus reconstructions with 5% noise. (a) target shear modulus distribution for comparison; (b), (c) reconstructed shear modulus distribution using 5 and 10 boundary displacement data sets, respectively (unit in the scale bar: kPa). Note: “SM” stands for shear modulus.

Table 5-3: Error between the recovered and target shear modulus distributions for the cases presented in **Figure 5-16–5-18**.

Noise Level	L2 Error	
	5 Displacement Datasets	10 Displacement Datasets
0.1%	42.12%	39.83%
1%	48.24%	45.92%
5%	68.01%	61.29%

5.3 Discussion

In this work, a quantitative approach was introduced to characterize the shear modulus distribution using solely boundary displacements together with force information, and its feasibility has been tested using various simulated experiments. The inverse problem is posed as a minimization problem subject to the constraint of the equilibrium equations in elasticity. Unlike most inverse algorithms requiring measured displacements throughout the entire domain, i.e., full-field displacements, the method presented in this paper merely requires measurements on the boundaries. This facilitates data collection for engineering materials by using digital cameras and a digital image correlation system, yielding a low-cost imaging modality. In addition, displacements on the boundary can be conveniently measured with high resolution [89].

In our previous publication [90], we utilized displacement indentations as boundary conditions. Thus, the resulting shear modulus distribution was only recovered up to a multiplicative factor. In this paper, we assumed that the applied force is known, leading to quantitatively/absolutely reconstructed shear modulus values. One of the challenges we faced here was the sensitivity of the optimization method to the initial guess, while, for the relative shear modulus reconstructions, the optimization method converged for a wide range of initial guesses.

The first case could represent a tissue engineered material, where growth and remodeling of tissue scaffold by cells has progressed spatially. Thus, the inclusion could represent a hypothetical overproduction of collagen fibers, while the background could represent lower density of collagen fiber accumulation. This simulated case represents a

challenging problem domain, since the inclusion is small and significantly away from the boundary edges (see **Figure 5-1–5-3**). We note that we do not make any assumptions about any presence of inclusions for all examples in this paper, but assume that the shear modulus is unknown on the finite element mesh nodes. Furthermore, for Case 1, we only measure one side for each indentation, which carries very little information pertaining to its interior shear modulus distribution. Nevertheless, the inverse scheme presented in this paper is capable of characterizing the non-homogenous shear modulus distribution well in the presence of noise levels (0.1%) that are inherent in actual measurements using digital image correlation systems. The reconstruction results reveal that the inverse algorithms are sufficiently robust to detect the location as well as the shape of the inclusion, while they fail to accurately reconstruct the target shear modulus value. For the case with 1% noise (see **Figure 5-3** (b), (c)), the reconstructed inclusion becomes much larger, and the shear modulus value in the inclusion is further underestimated. It is notable that the target inclusion area times the target inclusion value is preserved in that it is equal to the area of the reconstructed inclusion times the area of the reconstructed shear modulus value in the inclusion. This may be due to a lack of known boundary displacements (only used on partial boundaries) leading to uniqueness issues. Adding additional boundary displacement data sets does not significantly improve the reconstructions. Thus, to ensure an accurate and unique solution, displacements from the entire boundary should be used as discussed in the next case or deformations induced that could lead to a unique reconstruction.

For the second case, we have modeled a semi-circle with a shear modulus of 5 kPa according to measured fatty tissues and representing an idealized breast. The semi-circle consists of a stiff inclusion with a shear modulus value of 25 kPa, representing an idealized cancerous tumor (see **Figure 5-4–5-6**). Here, the deformation of the curved top boundary edge is assumed to be measured and used to solve the inverse problem. Since the bottom edge is fixed in both directions, we actually have used the entire displacement information on the boundary to solve the inverse problem. We conclude that this leads to a much better reconstructed inclusion compared to the previous case.

To show that this novel approach is not confined to one inclusion only, we have also tested the inverse algorithms for simulated experiments with two inclusions as shown in **Figure 5-16-5-18**. Clearly, the inverse algorithms are still capable of mapping the inclusion shapes, but underestimate the shear modulus values as in the one inclusion case. We observe that the left inclusion in **Figure 5-16** is more underestimated than the right inclusion. The reason for this is that the solution of the inverse problem is sensitive to boundary conditions when regularizing the problem as discussed in [80, 88].

In addition, we have added various noise levels into the boundary displacements to test the robustness of the novel inverse scheme herein. For experimentally relevant noise levels of about 0.1%, we observe that (1) the shape and size of the inclusion can be well recovered if the inclusion is medium sized; (2) the shear modulus value in the inclusion is underestimated; (3) the shape of the inclusion is preserved; (4) the size of the reconstructed inclusion is significantly overestimated for very small inclusions; (5) the stiffness contrast improves for a target stiffness contrast of about 1.5 to 2 and dramatically deteriorates for

stiffness contrasts beyond 10. The shear modulus reconstructions deteriorate significantly for higher noise levels, tested in this paper at up to about 5%.

We also performed a simple experiment to estimate the noise level in boundary displacement measurements utilizing a digital image correlation system using digital cameras. In the experimental setup shown in **Figure 5-19**, the ramp is subject to rigid body rotation along the left end of the ramp. The height on the right end of the ramp was altered using the columns shown in **Figure 5-19** (b). This will result in linear deflection of the top surface along the axial direction, used to validate the accuracy of the measurements obtained with the digital image correlation system. We defined a relative error $\sqrt{\sum_{i=1}^{T}\left(z_i - z_i^{\circ}\right)^2 \Big/ \sum_{i=1}^{T}\left(z_i^{\circ}\right)^2} \times 100\%$ along the major axis of the ramp, where T, z_i and z_i° are the total number of data points along the line, the measured deflection at those points and the curve fitting data from a linear function, respectively. We observe that the relative error is about 0.06% which is significantly lower than the noise levels significantly used in the simulations presented in this chapter.

Figure 5-19: The experimental setup to perform noise analysis of the boundary displacement measurements utilizing a digital image correlation system. (a) top view of the experimental setup with digital cameras focusing on the ramp's top face; (b) side view of the ramp with three columns having different height.

The inclusion to background stiffness contrast plays an important role in recovering the shear modulus distribution. We observe in **Figure 5-14** and **Figure 5-15** that the quality of the shear modulus reconstructions depends on the target stiffness ratio of inclusion to background. It is important to note that small stiffness contrasts of 7.5/5 (inclusion/background) can be well recovered. With increasing stiffness contrast ratio, the shear modulus reconstructions perform poorly; however, the shape of the inclusions is well-preserved in all cases for a noise level of 0.1%. Beyond a stiffness contrast ratio of 50 to 5, the shear modulus reconstructions do not differ much. This can be explained by the fact that the boundary displacements will not differ much either since the stiff inclusion behaves like a "rigid" object, i.e., the inclusion does not change its deformation field significantly beyond this stiffness ratio.

In all of the reconstructions presented in this paper, we added the same noise level for the displacement boundary, force and corresponding displacement indentation (i.e., displacement at force location), though they are not necessarily the same. However, from our experience, the reconstructions will not be sensitive to deviations in the noise level in force and corresponding displacement indentation. Furthermore, uncertainties in the location of force indentation are acknowledged and not investigated in this chapter. Conducting the experiments carefully by marking the locations of force indentation, these uncertainties can be well controlled. To further elaborate on this, we pursue the following thought process: applying a force indentation at some predefined location will induce boundary displacements. Now, applying that same force indentation by some small incremental offset from the original location will result in a second set of boundary displacements. These two sets of boundary displacements will be very close, thus the resulting reconstructions would be anticipated to be close as well. As the offset of force location increases, the discrepancy between the boundary displacement sets will increase. This discrepancy can be understood as some kind of noise level in the boundary displacements as analyzed in this paper, and the reconstructions will depend on this discrepancy. We note, however, that this "noise" level from the discrepancy of boundary displacements is not random as utilized in this chapter. A future analysis of this uncertainty will provide insight for experimental design.

In this work, we assumed that the simulated solids are in two-dimensional space and in the state of plane strain. Real world applications are in three-dimensional space and their reduction to plane strain may not always be feasible. Thus, future efforts will focus

on extending this approach to three dimensions. Since many boundary displacements are needed, this is computationally intensive and may require further optimization of the in-house written program. However, collecting boundary displacement data in three-dimensional space using digital cameras is relatively convenient. Furthermore, recording digital camera images on boundary displacements of shapes that are more complex than a block or a hemisphere may be conveniently conducted.

5.4 Conclusions

In this chapter, we have presented a novel and quantitative approach to determine the shear modulus distribution using boundary displacements together with applied force information. The feasibility of this approach has been tested with various simulated experiments. We observe that we can detect the location of the inclusion with various noise levels and preserve the shape of the inclusion well in the presence of 0.1% white Gaussian noise level in the boundary displacements. The results also illustrate that the shear modulus value is underestimated, and its inclusion size is larger than the target inclusion when incomplete displacement boundary information is utilized in the inverse problem. When complete boundary data is utilized as displayed in Case 2, the overall solution to the inverse problem becomes more unique. In fact, we observe that for the first case with a square domain, knowing displacements on a small boundary region does not yield a unique solution, despite the low noise level and a large number of boundary displacement data sets. More studies are required to enforce uniqueness with limited boundary region measurements. We have also observed that, with an increasing number of displacement datasets utilized, the reconstruction results will improve at lower noise

levels when boundary displacements are known everywhere, while no significant improvements are observed for higher noise levels and displacement measurements at partial boundaries. In summary, this novel approach has the potential to nondestructively and quantitatively map the heterogeneous elastic property distribution by utilizing displacements measured only on the specimen's boundary together with the force indentation measurements.

6. REGULARIZING THE INVERSE PROBLEM FOR PARTIALLY KNOWN ELASTIC MODULUS VALUES[*]

The biomechanical behavior of tissues can be determined from observed displacement fields using imaging modalities such as magnetic resonance imaging (MRI) [91-95], ultrasound [40, 82, 96-98], and optical coherence tomography (OCT) [99, 100]. Initially, axial strain images were computed from the gradient of the displacement field and interpreted as the inverse stiffness of the tissue. This approach has the advantage to be quasi-real time and has shown potential in detecting diseased tissues. Alternative approaches followed that took into account constitutive models to infer the heterogeneous model parameters of the tissue from displacement fields. These methods can be categorized into 2 groups, i.e., solving model parameters from 1) dynamic displacement data [93, 94, 101, 102], and 2) quasi static displacement data [49, 54, 62, 80-85]. In 1) shear wave displacements are induced and measured with OCT, MR techniques, or ultrasound. The solution to this inverse problem does not require the knowledge of traction boundary conditions, and the resulting model parameters are in general quantitative or absolute. In general, the storage and loss modulus can be determined for a range of frequencies, from which the viscoelastic model parameters can be determined. In 2) quasi-static displacement fields are mainly observed from ultrasound techniques, more precisely,

[*] Reprinted with permission from" Regularizing biomechanical maps for partially known material properties" by Mei, Y., Tajderi, M. & Goenezen, S., 2017. International Journal of Applied Mechanics, 9(2) 1750020.Copyright [2017] World Scientific Publishing.

by recording a sequence of radio frequency signals while the tissue's region of interest is gently compressed with the ultrasound transducer. Well established cross-correlation and block matching techniques are then employed to compute the displacement field [40, 84, 97, 103]. This method has the advantage that large displacements can be acquired to characterize the tissue's nonlinear response [49, 50, 62, 82, 83, 104]. However, this approach does not provide any information on traction or forces, as these cannot be measured with currently available ultrasound transducers. Thus, the elastic modulus distribution can at best only be reconstructed relatively, i.e. up to a multiplicative factor.

In this chapter, we will determine the biomechanical behavior of a theoretical atherosclerotic plaque and a stiff tumor embedded in soft background tissue from simulated quasi-static displacement fields and assuming that the elastic modulus is quantitatively known at certain regions on the boundary. The elastic modulus on these known regions could for example be measured using atomic force microscopy (AFM) [105-108] or Brillouin spectroscopy [109-112]. We will treat tissue as a linear elastic material assuming that the deformations overall are small, but this approach can be expanded to nonlinear material models. We pose the inverse problem as a constrained minimization problem with regularization and show that the regularization type plays a key role to successfully incorporate the known elastic modulus values into the solution procedure. More precisely, we test the total variation diminishing regularization (TVD) [49, 80, 82, 84] and a recently introduced new regularization type that we refer to as total contrast diminishing (TCD) [62, 113]. We show that the elastic modulus reconstructions with TVD regularization perform poorly while TCD regularization results in stable

absolute elastic modulus reconstruction in the presence of high noise levels. To the best of our knowledge, heterogeneous elastic modulus distribution has not been determined quantitatively using quasi-static displacement fields and partially known elastic modulus values from the solution of the regularized and constrained minimization problem. This formulation is designed to incorporate partially known elastic modulus values such that the elastic modulus distribution is driven to a unique solution.

6.1 Methods

We create simulated data to test the inverse solution procedure for a theoretical atherosclerotic plaque and a breast tumor with predefined target shear modulus distributions by solving the equations of equilibrium using finite element techniques. The displacement field from the solution of the forward problem in **Section 6.1.1** will be augmented with white Gaussian noise and represents the "measured" displacement field, in practice obtained using ultrasound imaging techniques. In **Section 6.1.2** we briefly review the inverse problem formulation and introduce two specific types of regularization, TVD and TCD regularization.

6.1.1 Forward problem in 2D plane stress linear elasticity

The strong form is as follows: Find the displacement **u** such that the equations of equilibrium in **Equation (6.1)** and Dirichlet boundary conditions in **Equation (6.2)** and Neumann boundary conditions in **Equation (6.3)** given by:

$$\operatorname{div}(\boldsymbol{\sigma}) = \mathbf{0} \text{ in } \Omega \tag{6.1}$$

$$\mathbf{u} = \mathbf{u}_{\circ} \text{ in } \Gamma_u \tag{6.2}$$

$$\boldsymbol{\sigma} \cdot \mathbf{n} = \boldsymbol{\sigma}_{\circ} \text{ in } \Gamma_\sigma \tag{6.3}$$

are satisfied. Here, $\boldsymbol{\sigma}$ is the Cauchy stress in the region of interest Ω , Γ_u and Γ_σ denote the Neumann and Dirichlet boundaries, and $\Gamma_u \cap \Gamma_\sigma$ represents the complete boundary for the problem domain and $\Gamma_u \cap \Gamma_\sigma = \varnothing$. Furthermore, $\mathbf{u}_\circ$ and $\boldsymbol{\sigma}_\circ$ are the prescribed displacement and traction on the boundary, respectively, and ***n*** is the outward unit normal vector on the traction boundary. It is straight forward to derive the weak form and discretize it using Galerkin's method. To reduce computational complexity, the models in this paper are modeled in plane stress, while the material in three dimensional space is constrained to be incompressible. Thus, the stress strain relationship in two dimensional space simplifies to only one unknown elastic modulus parameter:

$$\sigma_{ij} = 2\mu\varepsilon_{ij} + 2\mu\varepsilon_{kk}\delta_{ij} \tag{6.4}$$

where $i, j, k = 1$ or 2 and μ denotes the unknown shear modulus. $\varepsilon_{ij} = \frac{1}{2}\left(u_{i,j} + u_{j,i}\right)$ is the small strain tensor.

6.1.2 TVD and TCD regularization in regularized inverse problem

Throughout this chapter, we will adopt two types of regularization: the total diminishing variation (TVD) and the total contrast diminishing (TCD) regularization [62, 113] given by:

$$\mathrm{Reg}(\mu) = \frac{1}{2}\int_\Omega \sqrt{(\nabla\mu)^2 + c^2}\, d\Omega \quad \text{TVD} \tag{6.5}$$

$$\mathrm{Reg}(\mu) = \frac{1}{2}\int_\Omega \frac{\sqrt{(\nabla\mu)^2 + c^2}}{\mu} d\Omega \quad \text{TCD} \tag{6.6}$$

In **Equation (6.5)** and **(6.6)**, *c* is a small constant to avoid singularity when taking the gradient with respect to the shear modulus. The main distinction between these two types is that TVD will penalize the difference in shear modulus contrast, while TCD will penalize the logarithmic ratio in shear modulus contrast [62, 113]. In **Equation (6.6)** the regularization factor α controls the weight of the regularization term. The regularization factor has been chosen based on Morozov's discrepancy principle, which states that the difference between the computed and measured displacement field should not be smaller than the order of the noise level. The equations are discretized using finite element techniques, and the shear modulus are defined as unknowns on the finite element nodes and interpolated with finite element shape functions. This implies that the total number of unknowns is equal to the total number of nodes in the finite element mesh.

6.1.3 Uniqueness issue of inverse problem

If only quasi-static displacement information boundary conditions and traction free boundary conditions are utilized to solve the inverse problem, we can solely obtain the relative shear modulus distribution, which can be easily shown mathematically. Assume that a relative shear modulus distribution $\mu_r(\mathbf{x})$ satisfies the equilibrium with enforced displacement and zero traction boundary conditions:

$$\begin{aligned} &\operatorname{div}\left(2\mu_r(\mathbf{x})\left(\boldsymbol{\varepsilon}+\mathbf{I}tr(\boldsymbol{\varepsilon})\right)\right)=0 && \text{on } \Omega \\ &\mathbf{u}=\mathbf{u}_\circ && \text{on } \Gamma_g \\ &\mathbf{t}=\mathbf{0} && \text{on } \Gamma_h \end{aligned} \tag{6.7}$$

Multiplying μ_r with any multiplicative factor $\mu_\circ$ yields anther shear modulus distribution $\mu(x) = \mu_\circ \mu_r(x)$ that satisfies all the required equations for the same displacement fields.

$$\begin{aligned} &\operatorname{div}\left(2\mu(\mathbf{x})\left(\boldsymbol{\varepsilon} + \mathbf{I}tr(\boldsymbol{\varepsilon})\right)\right) = 0 \qquad \text{on } \Omega \\ &\mathbf{u} = \mathbf{u}_\circ \qquad\qquad\qquad\qquad \text{on } \Gamma_g \\ &\mathbf{t} = \mathbf{0} \qquad\qquad\qquad\qquad\ \ \text{on } \Gamma_h \end{aligned} \tag{6.8}$$

will be satisfied for any μ. Thus, we are not able to obtain the absolute shear modulus distribution from the governing equations together with these boundary conditions. Non-zero traction boundary condition or total force measurements would result in an absolute shear modulus distribution, i.e., μ would not be arbitrary. However, in this work, we assume that shear moduli on some part of the specimen's boundary are known from measurements. To illustrate this for a special case in one dimension, let us consider a nonhomogeneous elastic rod with a fixed end as shown in **Figure 6-1**. μ_1 and μ_2 are the target elastic modulus values on the black and white parts, respectively. As the stress is the same in the two parts, the following relation is obtained:

$$\frac{\varepsilon_2}{\varepsilon_1} = \frac{\mu_1}{\mu_2} \tag{6.9}$$

where ε_1 and ε_2 are measured strain of the black and white parts, respectively. **Equation (6.9)** will be satisfied for any multiplicative factor of μ_1 and μ_2. Let us now assume that the shear modulus of the black part is known through measurements and denoted with μ_1^m. Then we can solve for $\mu_2 = (\varepsilon_1 / \varepsilon_2) \times \mu_1^m$ absolutely.

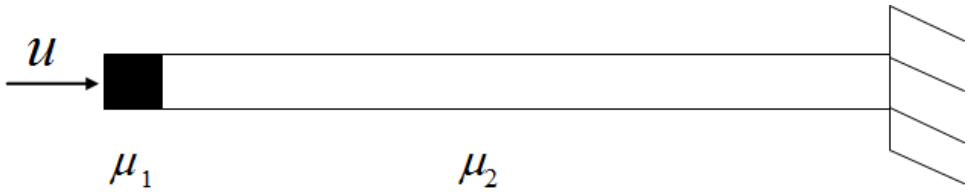

Figure 6-1: Diagram on a non-homogenous bar subjected to axial compression.

6.2 Numerical results

In the first example, we consider a unit square with two inclusions positioned in horizontal direction as shown in **Figure 6-2** (a). The shear modulus contrast of inclusion to background (5;1) is akin to an actual breast tumor surrounded by healthy tissue [56, 114]. We create two displacement fields and these two displacement fields are utilized to solve the inverse problem together, the first one by applying a 5% uniform displacement compression on the top edge and restricting the vertical motion of the bottom edge as shown in **Figure 6-2** (a). To avoid rigid body motion, the center node on the bottom edge is fixed in all directions. All remaining unspecified boundaries are traction free. The second displacement field is created by applying a 5% displacement compression on the left edge and restricting the horizontal motion of the right edge as shown in **Figure 6-2** (b). In this case, the center node on the right edge is fixed in all directions, and the other two edges are traction free. The finite element mesh consists of 3600 bilinear elements. The simulated displacement data is computed by solving the forward problem, and 3% random noise is introduced into the displacement field to represent measured noisy data. Furthermore, we consider two scenarios where the shear modulus is partially known on the boundary at 1) one point (see arrow in **Figure 6-2** (c) and (d)), and 2) on the entire top

edge. We confine the search region for the unknown shear modulus variables between 0.1 and 30.0, and solve the inverse problem with TCD and TVD regularization. **Figure 6-2** (c) and (d) show the shear modulus reconstruction with TVD regularization and TCD regularization for the case that the shear modulus value is imposed on the upper left corner. Furthermore, the horizontal centerline plots for the shear modulus values through the center of both inclusions is given in **Figure 6-2** (e) for the exact distribution and the reconstructions using TCD and TVD regularization. The regularization factor for the reconstruction with TVD and TCD regularization are chosen to be 1.0e-7 and 2.0e-8, respectively. We observe that with TCD regularization the shape of the inclusions is well recovered and the shear modulus values are close to the target values. TVD regularization, however, results in a shear modulus distribution about 4-5 times less than the target shear modulus distribution. Thus, it appears that TVD regularization drives the solution to the lowest possible value while preserving its relative contrast. The shear modulus reconstruction for case 2) where μ is imposed on the top boundary edge is given in **Figure 6-3** (c) and (d) using TVD and TCD regularization. We observe a similar trend to case 1) in that TCD regularization yields a well recovered shear modulus distribution, while TVD regularization is off by a multiplicative factor of about 4-5 (excluding the shear modulus values imposed on the top edge). The horizontal centerline plot through both inclusions is given for both regularizations together with the exact reconstruction for comparison. The regularization factors for TVD and TCD regularization were chosen to be 1.0e-7 and 2.0e-8, respectively.

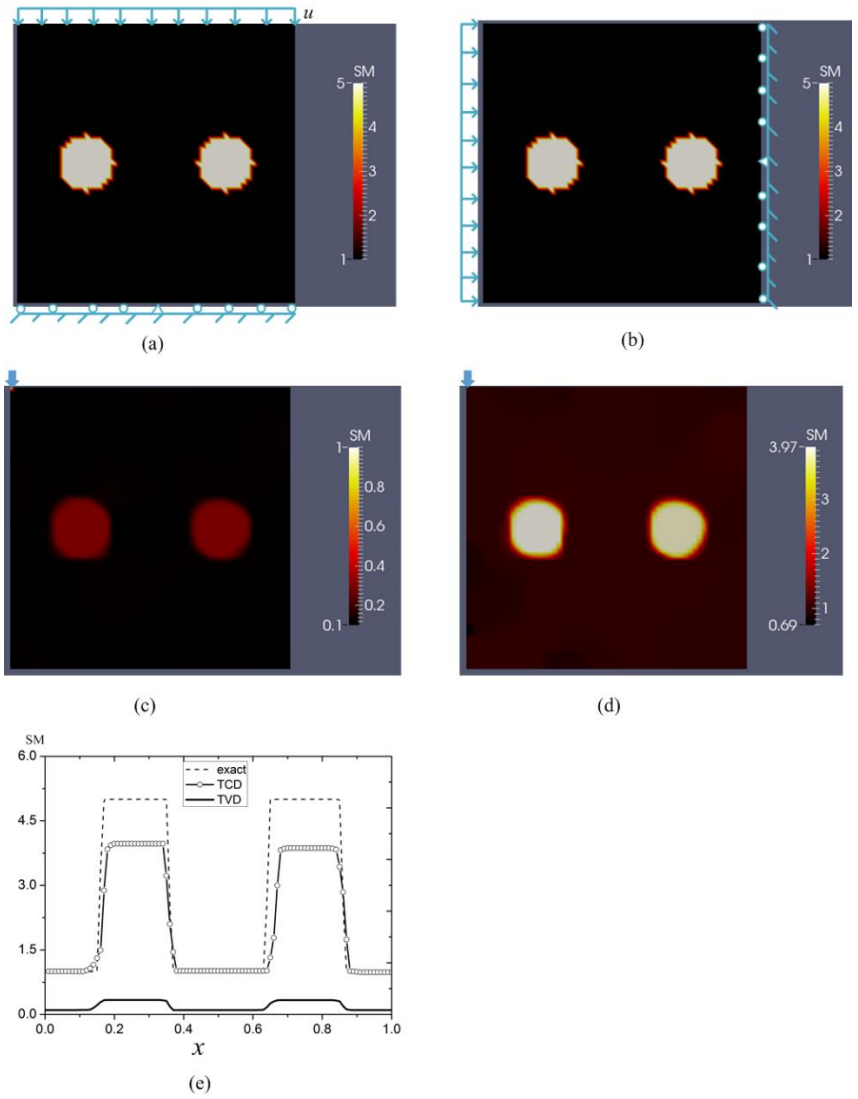

Figure 6-2: (a) Theoretical model: two horizontally positioned inclusions with shear modulus value of 5 in a homogenous background with shear modulus value of 1. The displacement boundary conditions are applied in y direction; (b) theoretical model: two horizontally positioned inclusions with shear modulus value of 5 in a homogenous background with shear modulus value of 1. The displacement boundary conditions are applied in x direction; (c) reconstructed shear modulus distribution over the domain when TVD regularization is utilized. In this case, the shear modulus of the upper left node is fixed; (d) reconstructed shear modulus distribution over the domain when TCD regularization is utilized. In this case, the shear modulus of the upper left node is fixed; (e) comparison of shear modulus variation along the horizontal center line. The dashed line, solid line and empty circles represent exact distribution, reconstruction results by TVD and TCD method, respectively.

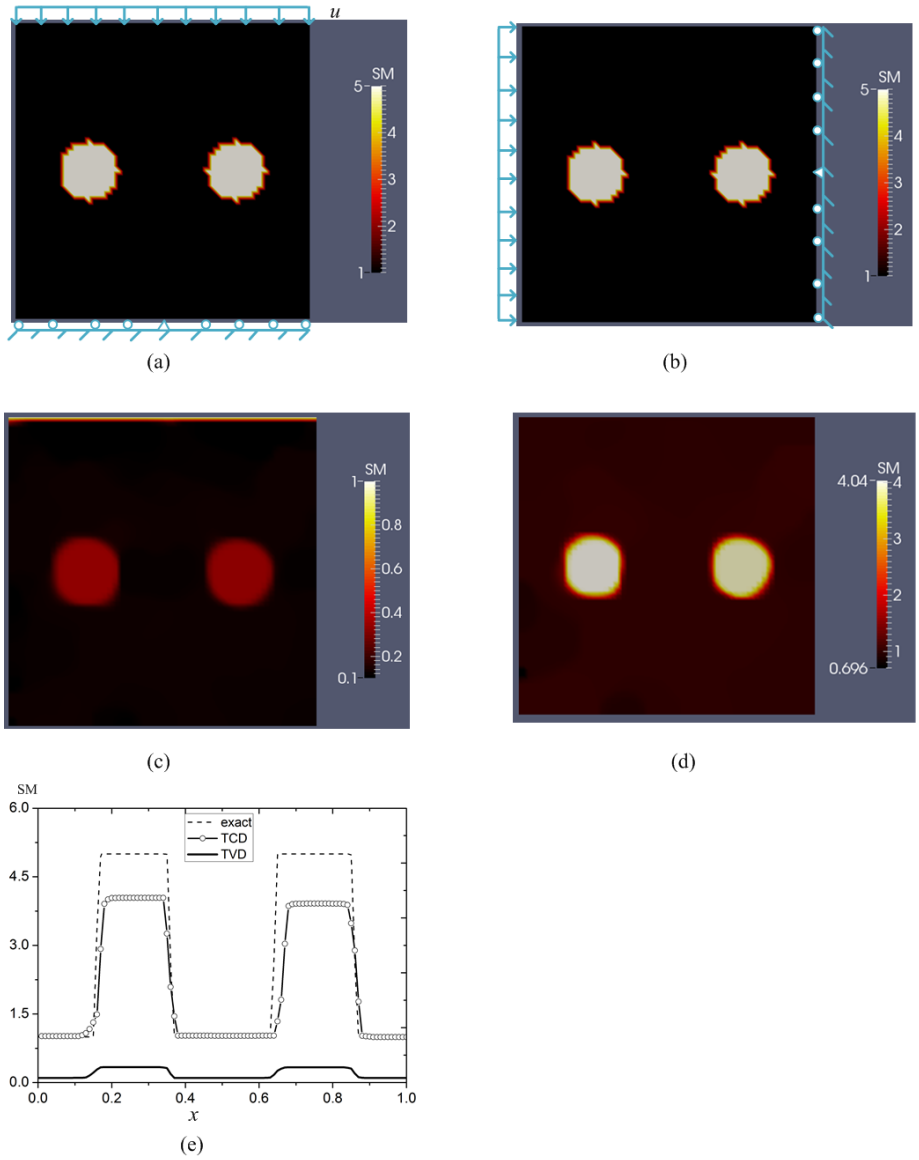

Figure 6-3: (a) Theoretical model: two horizontally positioned inclusions with shear modulus value of 5 in a homogenous background with shear modulus value of 1. The displacement boundary conditions are applied in *y* direction; (b) theoretical model: two horizontally positioned inclusions with shear modulus value of 5 in a homogenous background with shear modulus value of 1. The displacement boundary conditions are applied in *x* direction; (c) reconstructed shear modulus distribution with TVD regularization. In this case, the shear modulus of the entire top edge is fixed; (d) reconstructed shear modulus distribution over the domain when TCD regularization is utilized. In this case, the shear modulus of the entire top edge is fixed; (e) comparison of

shear modulus variation along the horizontal center line. The dashed line, solid line and empty circles represent exact distribution, reconstruction results by TVD method and TCD method, respectively.

To analyze the sensitivity to various noise levels, we also add 10% noise into the displacement fields which corresponds to a displacement SNR of 10 dB. **Figure 6-4** (c) and (d) show the recovered shear modulus distributions with TVD and TCD regularization for the case that the shear modulus is known and prescribed on the upper left corner. In this case, the regularization factor for the reconstruction with TVD and TCD method are chosen to be 1.5e-7 and 6.5e-8, respectively. We observe that the absolute shear modulus distribution is mapped well using TCD regularization despite the high displacement noise level, while the TVD regularization still fails to map the shear modulus distribution absolutely. Additionally, compared to **Figure 6-2** (d), the shear modulus of the right inclusion is more underestimated than the left inclusion. **Figure 6-5** (c) and (d) exhibit the shear modulus reconstruction for the case that the shear moduli are imposed on the entire top boundary edge utilizing TVD and TCD regularization, respectively. In this case, the regularization factors are selected to be 2.0e-7 and 6.0e-8, respectively. Similar trends are observed in this case.

In all numerical cases presented above, the shear modulus distributions using TVD regularization are off by a multiplicative factor of about 10, while the shear modulus distributions using TCD regularization are quantitatively recovered.

For the case that the shear moduli on the entire top edge are fixed, it is unrealistic to utilize the exact shear modulus value, thus, in the following we will add 10% noise into

the “measured” shear moduli. **Figure 6-6** (c) and (d) represent the shear modulus reconstructions using TVD and TCD regularization when 10% noise is introduced to both the displacements and shear moduli measurements. In this case, the regularization factors are 2e-7 and 6e-8 for the TVD and TCD regularization cases, respectively. As shown in **Figure 6-6** (d), TCD regularization still performs well for this challenging case with a noise level well beyond expected in experiments.

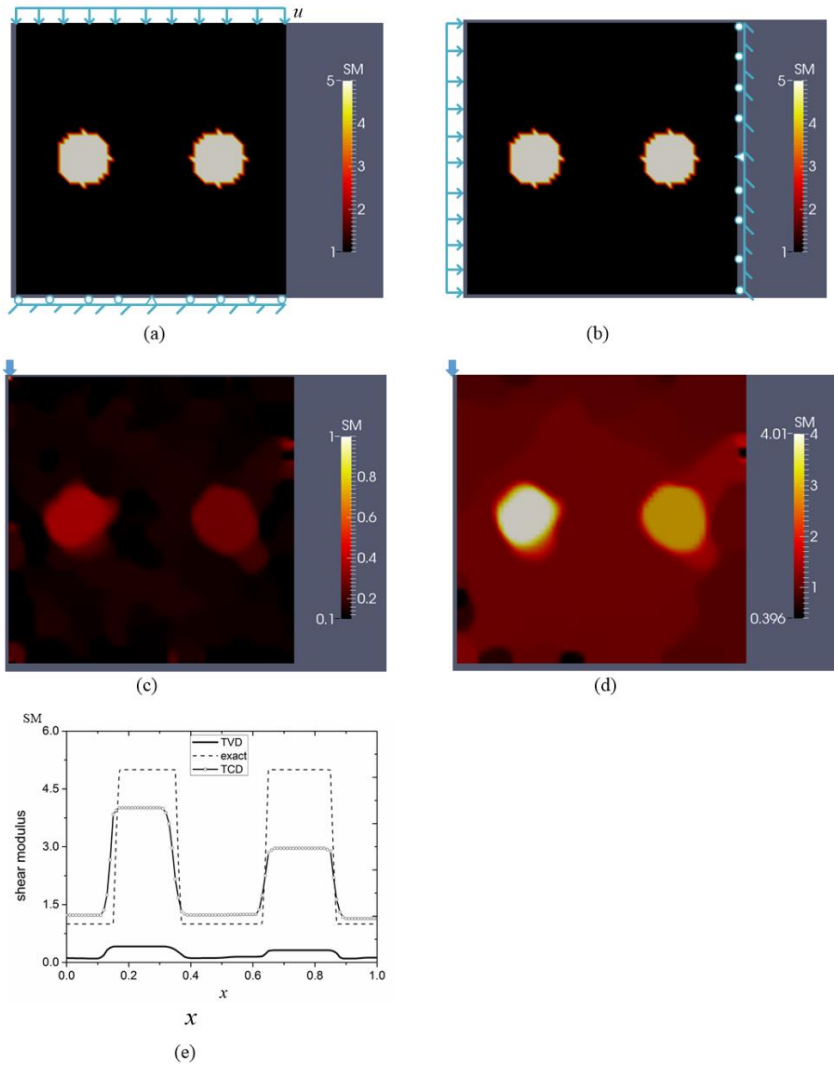

Figure 6-4: (a) Theoretical model: two horizontally positioned inclusions with shear modulus value of 5 in a homogenous background with shear modulus value of 1. The displacement boundary conditions are applied in y direction; (b) theoretical model: two horizontally positioned inclusions with shear modulus value of 5 in a homogenous background with shear modulus value of 1. The displacement boundary conditions are applied in x direction; (c) reconstructed shear modulus distribution over the domain when TVD regularization is utilized. In this case, the shear modulus of the upper left node is fixed; (d) reconstructed shear modulus distribution over the domain when TCD regularization is utilized. In this case, the shear modulus of the upper left node is fixed; (e) comparison of shear modulus variation along the horizontal center line. The dashed line, solid line and empty circles represent exact distribution, reconstructions with TVD method, and TCD method, respectively.

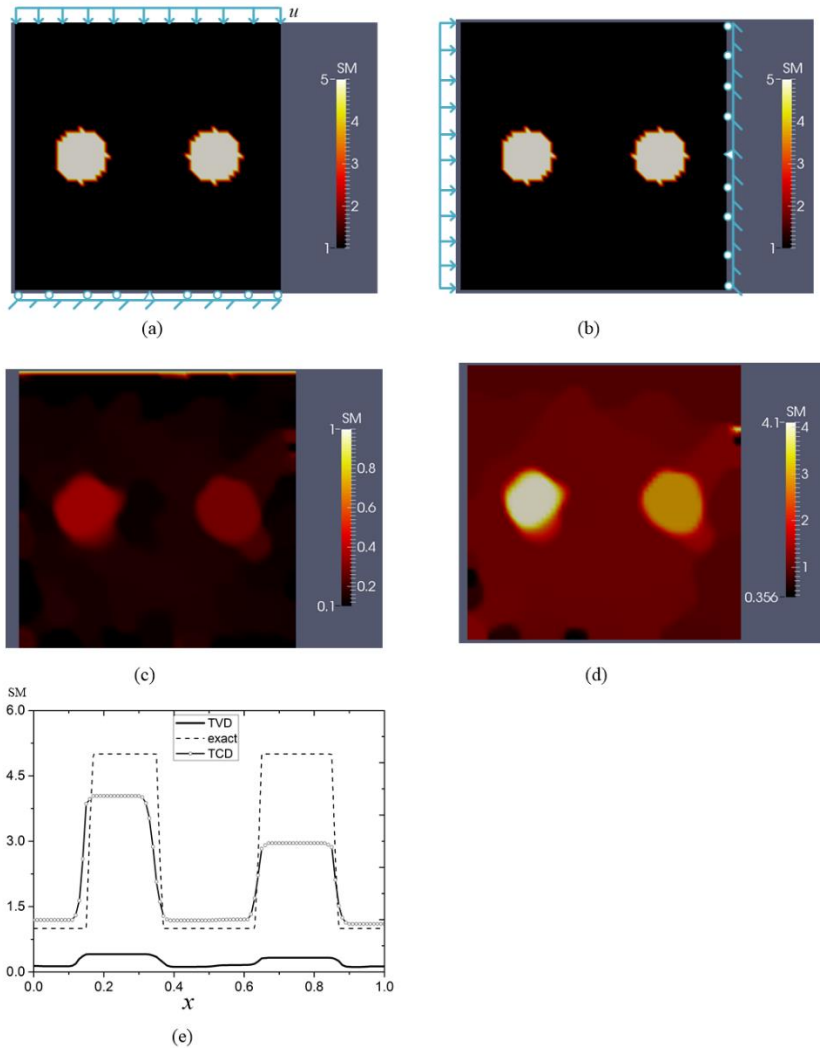

Figure 6-5: (a) Theoretical model: two horizontally positioned inclusions with shear modulus value of 5 in a homogenous background with shear modulus value of 1. The displacement boundary conditions are applied in *y* direction; (b) theoretical model: two horizontally positioned inclusions with shear modulus value of 5 in a homogenous background with shear modulus value of 1. The displacement boundary conditions are applied in *x* direction; (c) reconstructed shear modulus distribution over the domain when TVD regularization is utilized. In this case, the shear modulus of the entire top edge is fixed; (d) reconstructed shear modulus distribution over the domain when TCD regularization is utilized. In this case, the shear modulus of the entire top edge is fixed; (e) comparison of shear modulus variation along the horizontal center line. The dashed line, solid line and empty circles represent exact distribution, reconstruction results by TVD and TCD method, respectively.

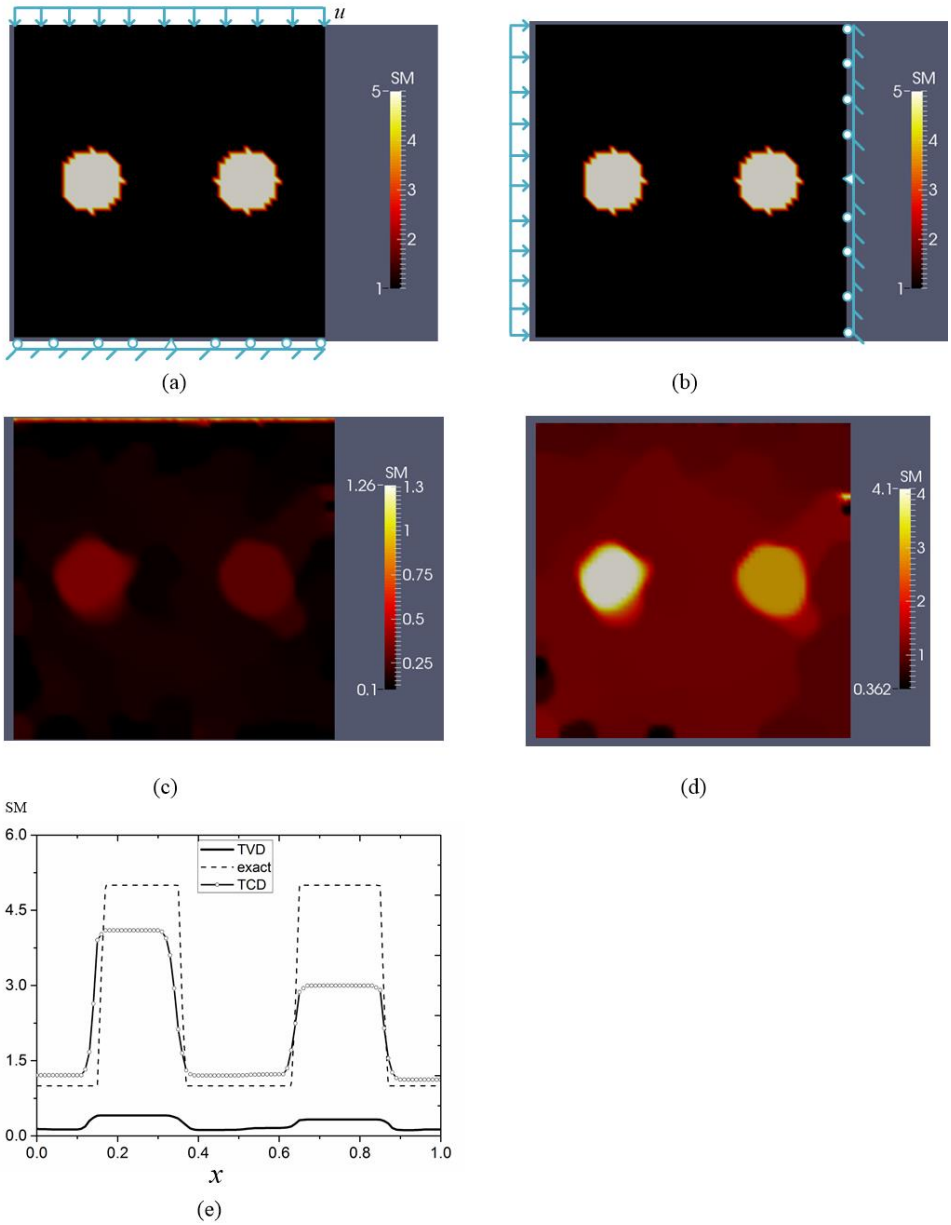

Figure 6-6: Problem domain is given in (a) and (b) with different boundary conditions. The shear modulus in the homogeneous background is set to 1 and the shear modulus in the inclusions is set to 5. (c) reconstructed shear modulus distribution with TVD regularization. In this case, the shear modulus of the entire top edge is fixed; (d) reconstructed shear modulus distribution with TCD regularization. In this case, the shear modulus of the entire top edge is fixed; (e) comparison of shear modulus variation along the horizontal center line. The dashed line, solid line and empty circles represent the exact distribution, reconstruction results by TVD and TCD method, respectively.

We have also tested the inverse algorithms with a theoretical atherosclerotic plaque shown in **Figure 6-7** (a), consisting of a soft lipid inclusion with $\mu = 0.33\text{MPa}$, surrounded by a stiff cap with $\mu = 0.5\text{MPa}$, and a healthy arterial wall with $\mu = 0.00833\text{MPa}$. The arterial geometry and the shear modulus distribution were reported in [115, 116] for an atherosclerotic coronary artery. To solve the forward elasticity problem and create simulated displacement data, we mesh the arterial domain with 1425 bilinear elements and impose boundary conditions as follows. Neumann boundary conditions are prescribed at the inner and outer arterial wall, with a uniform intraluminal pressure of 15.9 kPa, and traction free boundary conditions at the outer wall. To avoid rigid body motion, we fix one node on the outer wall in both direction and restrict the horizontal motion on the node opposite to the symmetry axis of the plaque. Then, we add 1% noise to the displacement field to simulate actual noisy "measured" displacement data. This displacement field is used to solve for the target shear modulus distribution, where the boundary conditions for the forward elasticity problem is chosen to be Dirichlet at the intraluminal wall and traction free at the outer wall. This represents the scenario that the intraluminal pressure measurement is not available. We will reconstruct the shear modulus distribution quantitatively by prescribing only one point on the outer wall. Finally, the search domain for the shear modulus distribution is confined to [0.00833 MPa, 3.0 MPa], and the regularization factor for TVD is set to $\alpha = 5.0e-7$ and for TCD is set to $\alpha = 1.0e-7$. The shear modulus reconstruction is given in **Figure 6-7** (b) and (c) for TVD and TCD regularization, respectively, and both figures are rescaled to better visualize the results. We observe similarly to the previous example that TCD regularization results in absolute

shear modulus reconstructions, while TVD regularization yields a shear modulus reconstruction off by a multiplicative factor. Furthermore, in both reconstructions, the lipid region is much better recovered than the cap region.

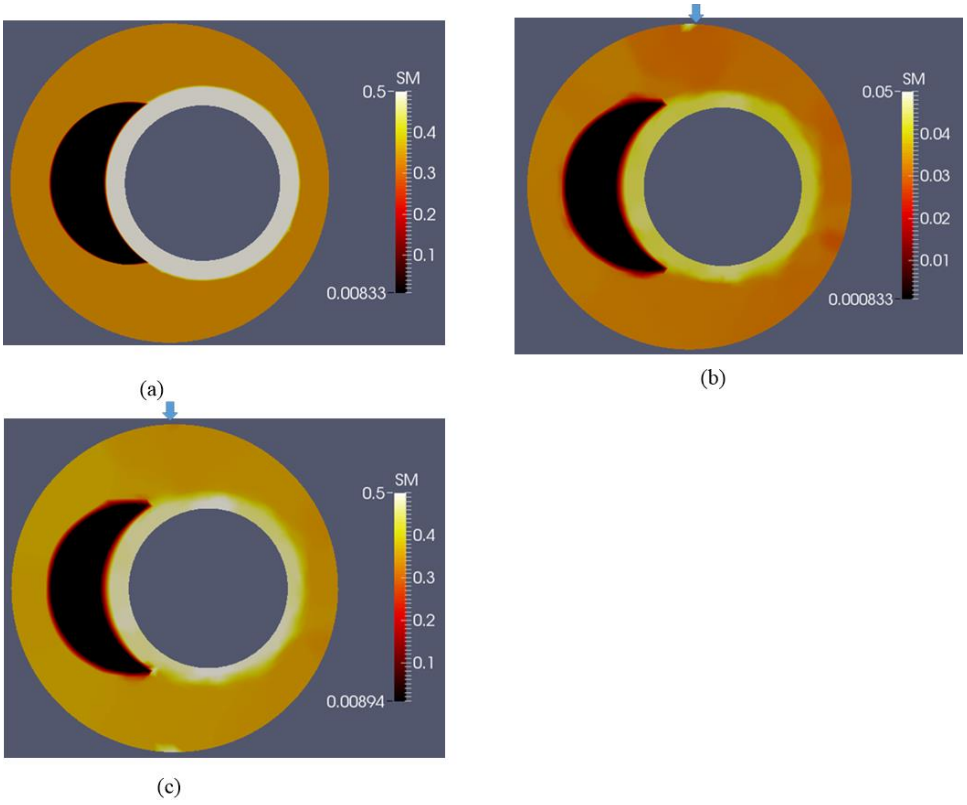

Figure 6-7: (a) Theoretical model of the cross section of an atherosclerotic artery and shear modulus distribution of this problem domain; (b) rescaled reconstructed shear modulus distribution over the domain when TVD regularization is utilized (set the maximum shear modulus value of the scale bar to 0.5). In this case, the shear modulus of the top node is fixed (see arrow); (c) rescaled reconstructed shear modulus distribution when TCD regularization is utilized (set the maximum shear modulus value of the scale bar to 0.5). In this case, the shear modulus of the top node is fixed (see arrow).

We also add 10% noise into the displacement data for the second numerical example. **Figure 6-8** (b) and (c) are the mapped shear modulus distributions when TVD

and TCD regularization are utilized, respectively. In this case, the regularization factor for TVD and TCD are set to 2e-5 and 5e-7, respectively. We observe that the shape and the shear modulus values of the simulated lipid are well preserved using TCD regularization. Compared to the results with 1% noise, higher noise levels lead to stronger oscillations. Additionally, the cap seems to be mapped badly and cannot be distinguished from the background.

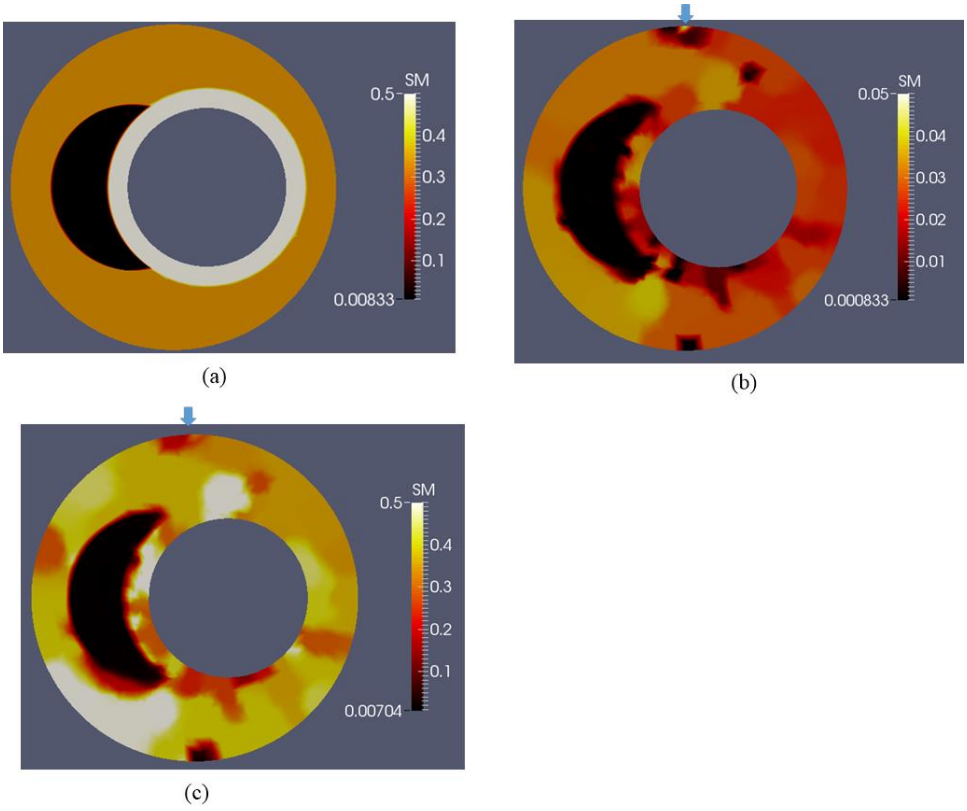

Figure 6-8: (a) Target shear modulus distribution of an idealized cross-section with an atherosclerotic plaque and shear modulus distribution of this problem domain; (b) reconstructed shear modulus distribution with TVD regularization (set the maximum shear modulus value of the scale bar to 0.5). In this case, the shear modulus of the top node is assumed to be known (see arrow); (c) reconstructed shear modulus distribution with TCD regularization (set the maximum shear modulus value of the scale bar to 0.5). In this case, the shear modulus of the top node is assumed to be known (see arrow).

6.3 Discussion

In this chapter, we have investigated the effect of regularization on the solution of the inverse elasticity problem with partially known measured shear modulus values on some boundary. The inverse problem is posed as a constrained minimization problem, and two types of regularization have been considered, TVD and TCD regularization. In previous works [80, 82] TVD regularization worked well for problems where the shear modulus was reconstructed relatively, i.e., up to a multiplicative factor. TCD regularization has been introduced in [62, 113] to address distortions in the shear modulus reconstructions with TVD regularization, when measured total force data is incorporated in the objective function. In the present work, we assumed that solely displacement data is known in the entire problem domain (e.g. from ultrasound imaging), and no non-trivial traction boundary condition or force measurement is available.

To steer the shear modulus reconstruction to a unique solution, we assume that

is known on some region of the boundary. The shear moduli on the boundary might be obtained from, for example from AFM [105-108] or Brillouin spectroscopy [109-112] measurements. Though the proof of concept for AFM and Brilliouin spectroscopy measurements has been shown theoretically and experimentally, their clinical feasibility still needs more investigation.

The inversion technique proposed herein is highly robust. We have investigated the sensitivity of this inverse solution approach to various noise levels. To this end, we tested the inverse solution with as high as 10% noise in the displacement field and observed that while the shear modulus contrast decreased, the overall shear modulus reconstruction was yet well recovered and the inclusions were detectable. We have also tested our inverse scheme for robustness by changing the initial guess and observed that the inverse problem converged to the correct shear modulus distribution for a wide range of initial guesses (not shown here).

We have considered two theoretical examples with clinical relevance, an atherosclerotic plaque and two breast tumors embedded in a normal tissue. Visualizing the stiffness property distribution of tissues provides an alternative disease detection approach in medical imaging. This can be done as the disease alters the micro-structure of the tissue's constituents, resulting in alterations of the biomechanical properties at the macroscopic structure. For example, normal arterial tissue is made up of endothelia cell, elastic connective tissue and smooth muscles. Atherosclerosis is sometimes also referred to as "hardening of the arteries", and during this process cholesterol plaques will form, composed of fat, cholesterol, calcium, among other constituents [58]. More specifically, the damaged endothelial cells lining the inner wall of blood vessels leads to LDL cholesterol deposition in the artery wall between the endothelial cells and connective tissue. To prevent further invasion of cholesterol, macrophages are mobilized to absorb LDL cholesterol which results in the formation of foam cells, the start of plaque formation [117]. Typically, a stiff cap forms and surrounds a soft inclusion. For a clinician, it is

crucial to know if the cap is stable and this requires patient specific knowledge of the biomechanical response. Similarly, breast cancer tissues change their biomechanical properties due to collagen fiber accumulation and changes in their crimp [118]. Thus, the biomechanical properties of breast tissues can potentially be used to screen for tumors and/or as a diagnostic imaging tool. In this work, we have provided a quantitative approach to determine the heterogeneous linear biomechanical properties of these two theoretical examples from known displacement fields and partially known biomechanical properties on some small boundary. We emphasize that the linear material model does not represent actual tissue response, as the tissue's biomechanical response is known to be nonlinear, viscoelastic, and anisotropic. The work presented in this paper is based on a simple linear elastic model to acknowledge the inherent problems in parameter identification and providing solutions based on a proper choice of regularization type. To map model parameters from other constitutive models (e.g. nonlinear hyperelastic models) may require different forms of regularization.

We utilized two regularization types, TVD and TCD regularization. We observed that for TVD regularization the shear modulus reconstruction is not reconstructed quantitatively, but rather relatively. More precisely, the reconstructions settle down to the lowest possible value given by the lower bound in the search algorithms, in spite of the prescribed shear modulus values on the problem boundary. TCD regularization on the other hand makes full use of the prescribed shear modulus values and steers the reconstructions of the shear modulus to a unique solution. To understand why TCD regularization outperforms TVD regularization when data is prescribed, we need to

understand how they penalize oscillations in the shear modulus distribution. It can be shown that TVD regularization penalizes the difference in oscillations, while TCD penalizes the logarithmic ratio. This difference leads to the observation that the shear modulus distributions using TVD regularization are off by a multiplicative factor, while the shear modulus distributions using TCD regularization are quantitatively recovered.

To elaborate on this further, let us first consider the case without imposing the shear modulus value anywhere. In this case, as shown in **Equations (6.7)** and **(6.8)** , only relative shear modulus distribution μ_r can be acquired while the multiplicative factor $\mu_\circ$ will not affect the displacement solution and with that will also not affect the displacement correlation term. Thus, $\mu_\circ$ will drop down to the lowest possible value (depending on the lower bound imposed by the optimization algorithm) to minimize the regularization term when TVD regularization is used. This can be illustrated for the one-dimensional case shown in **Figure 6-1**, where the TVD regularization term can be simplified to $\mu_\circ \mu_1 |\mu_r - 1|$ after setting the small constant *c* to zero. Further, the displacement field depends only on the relative shear modulus ratio of $\mu_r = \mu_2 / \mu_1$ when only displacement boundaries are imposed. The multiplicative factor $\mu_\circ$ will then drive down to the lowest value possible.

Once we impose the shear moduli on some region of the problem domain, the displacement field and with that the displacement correlation term depends on the absolute shear modulus distribution. On the other hand, the TVD regularization term will try to strive to a minimum value by reducing the "multiplicative factor". Thus there is some compromise between the displacement correlation term and the regularization term. Since

we have noisy data and utilize relatively large regularization factors, the regularization term might play a dominating role in determining the shear modulus distribution, and therefore the "multiplicative factor" will settle down to the lowest possible value. Here the lower bound of the search domain is 0.1 resulting in a shear modulus distribution that is 10 times less than the exact shear modulus in the first numerical example.

TCD regularization in one-dimensional case having two shear modulus values, simplifies to $\log\left(\frac{\mu_\circ \mu_2}{\mu_\circ \mu_1}\right) = \log\left(\mu_r\right)$ after neglecting the small constant *c*. It is observed from this equation that the multiplicative factor appears in the nominator and denominator and therefore cancels out. Thus, TCD regularization does not depend on any multiplicative factor, and therefore the shear modulus distribution is absolutely determined after prescribing a shear modulus value in one point.

The breast tumor example has been tested with prescribed shear modulus at one node (**Figure 6-2** and **Figure 6-4**) and with a prescribed shear modulus along the entire top boundary edge (**Figure 6-3, Figure 6-5**, **Figure 6-6**). We observe that prescribing more known shear modulus values does not fix the issues observed with TVD regularization. Additionally, the shear modulus reconstruction with TCD regularization does not improve when prescribing more data points with 3% or higher noise levels. For the case of plane stress for an incompressible material in three-dimensional space, one displacement field along with one known shear modulus value at one point ensure a unique solution. However, in general prescribing the shear modulus value only at one point will not necessarily result in a unique shear modulus reconstruction. In fact, according to [119]

the shear modulus values must be known at four locations to ensure uniqueness if two independent measured displacement fields are given for the incompressible plain strain case.

For the second numerical example, we observe a similar trend that prescribing shear modulus on one node, TCD regularization results in an absolute shear modulus distribution, while TVD fails in doing so. Nevertheless, we should note that the cap does not recover well and cannot be distinguished from the background when the noise level is higher (see **Figure 6-8**). There are two factors likely contributing to this phenomenon. The target shear modulus value of normal tissue is approximately 40 times larger than that of the lipid, while the target shear modulus of the cap is merely 1.5 times larger than normal vessel tissue. For this reason, it may be harder to reconstruct the cap and distinguish it from normal tissue. More likely however is the fact that uniqueness issues occur since the vessel wall and the cap without the lipid plaque represent a structure close to be axisymmetric as discussed in [41]. Since the cap consists of a uniform layer, it is very challenging to recover its shear modulus value, and this becomes more challenging with increasing noise levels.

6.4 Conclusion

We solved the inverse problem in elasticity, posed as a regularized and constrained minimization problem for a known displacement field and partially known shear modulus values on the boundary. We investigated the effect of regularization and observed that TCD regularization successfully reconstructs the quantitative shear modulus distribution with prescribed shear modulus values on a boundary node and boundary edge in the

absence of traction boundary data. TVD regularization on the other hand fails to recover the shear modulus distribution quantitatively. We have utilized two theoretical examples to test these methods, an atherosclerotic plaque and breast tumor inclusions embedded in a soft background. These examples were chosen due to their high clinical relevance, and quantifying their patient specific biomechanical properties could potentially advance screening, prognostic methods, and surgical planning.

7. FEASIBILITY AND RELIABILITY OF A LINEAR ELASTIC SOLVER IN SOLVING INVERSE PROBLEMS IN NONLINEAR ELASTICITY

In **Chapter 2**, we have presented a general framework of recovering the inhomogeneous linear and hyperelastic property distributions using nonlinear elastic inverse algorithms. The current in-house inverse solver is also capable of solving the inverse problem to recover shear modulus distribution using linear elastic inverse algorithms. The essential difference between inverse problems in linear and nonlinear elasticity is that the latter takes account of the nonlinear elastic stress-strain relationship, i.e., the modified Veronda-Westmann model, and the geometric nonlinearity. In the latter case, if the material nonlinearity is minor, e.g., the nonlinear parameter $\gamma = 0$ in modified Veronda-Westmann model, the stress-strain relation will approach the linear relation even for large deformations.

Now, we might raise the following question: Can we make a proper estimation of the elastic property distribution of a soft solid subject to large deformations using a linear elastic inverse approach? In this chapter, we will characterize the inhomogeneous shear modulus distributions of soft materials using both linear and nonlinear elastic inverse algorithms. We perform this feasibility study utilizing both experimental and simulated data. In **Section 7.1**, the experimental set-up to measure full-field phantom data and the theoretical background of the linear and nonlinear elastic inverse algorithms will be discussed. In **Section 7.2**, the reconstruction results obtained by these two approaches are presented and compared. In **Section 7.3**, we will discuss the reconstructions presented in

Section 7.2 and use a simple 1-D analytical approach to explain what we have observed in reconstructions. We will conclude the work in **Section 7.4**.

7.1 Methods

7.1.1 Composite sample and digital imaging data acquisition

A soft and composite sample consisting of two cylindrical inclusions with 2.8 cm and 2.1 cm diameters is manufactured and the dimension is shown in **Figure 7-1** (a). The thickness of the sample is 0.6 cm. The inclusions and background are each made up of a different silicon material, leading to distinct mechanical behaviors. As indicated in the uniaxial tensile tests with INSTRON machine (see **Figure 7-1** (b)), the stiffness of the inclusions is approximately 2.5 times larger than that of the background. We also observe that the material nonlinearity in the stress-strain curves of both materials is insignificant, i.e., the stress-strain relation is almost linear for large deformations less than 30% stretch.

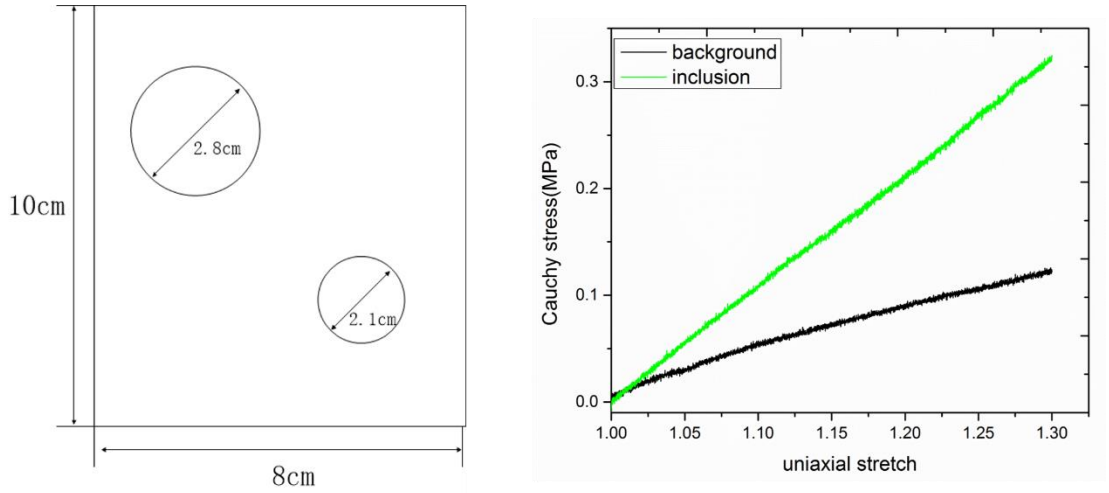

Figure 7-1: (a) The dimensions of the composite phantom; (b) plots of the uniaxial Cauchy stress versus the stretch of background and inclusion materials.

To deform the soft phantoms, we fix the top edge and pull down the bottom edge of the sample. By taking images of the sample in the undeformed and deformed states, we are able to calculate the displacement data accordingly.

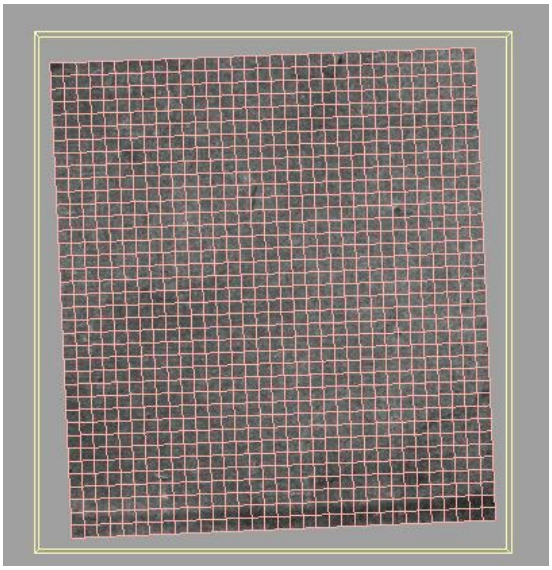

Figure 7-2: The domain of interest delineated from images taken by two digital cameras.

7.1.2 Modulus reconstruction

With the acquired full field displacement field throughout the region of interest of the sample, the recovered shear modulus distribution can be obtained utilizing the regularized inverse algorithms discussed in the previous chapters. As the inverse algorithms have been thoroughly discussed in previous chapters, I will not elaborate herein. In this chapter, we adopt a hyperelastic model to study the mechanical behavior of the silicon sample undergoing finite deformations. As the stress-strain relations of both the background and the inclusion materials are nearly linear even for larger deformations as shown in **Figure 7-1** (b), we utilize the simplest hyperelastic model, the neo-Hookean model, to study the nonlinear elastic behavior of the phantom, and the strain energy density function for an incompressible neo-Hookean solid is given as

$$W = \frac{\mu}{2}\left(J^{-2/3} I_1 - 3\right) \tag{7.1}$$

Utilizing **Equation (7.1)**, we could derive the associated Cauchy stress and 2nd Piola-Kirchhoff stress tensors. Note that the modified Veronda-Westmann model will reduce to the neo-Hookean model if we set the nonlinear parameter to zero. This interesting observation reveals that the level of the material nonlinearity of the neo-Hookean model is fairly low. For small strains and rotations, the neo-Hookean model will further reduce to the linear elastic model where the stress-strain relation is written as

$$\sigma_{ij} = 2\mu\varepsilon_{ij} + p\delta_{ij} \tag{7.2}$$

where $i, j, k = 1$ or 2. $\varepsilon_{ij} = \frac{1}{2}\left(u_{i,j} + u_{j,i}\right)$ is the small strain tensor and p is the hydrostatic pressure.

To compare the difference of linear elastic and neo-Hookean models, we plot the stress variation over the stretch in the case of uniaxial extension when $\mu = 1$ as shown in **Figure 7-3**. In this case, we utilize the Cauchy stress for the neo-Hookean material as a comparison. We observe that these curves nearly coincide with each other when the stretch is very small, while the Cauchy stress increases faster than the stress predicted by the linear elastic model with increasing stretch. This observation clearly indicates that when the deformation is small, the linear elastic law is a good approximation to analyze the mechanical behavior of neo-Hookean materials. Even so, it is incapable of predicting the mechanical behavior of nonlinear elasticity undergoing large deformations.

Now the question is that what will happen if we utilize the linear elastic model to solve the inverse problem in nonlinear elasticity. In the following sections, we will attempt to seek the answer.

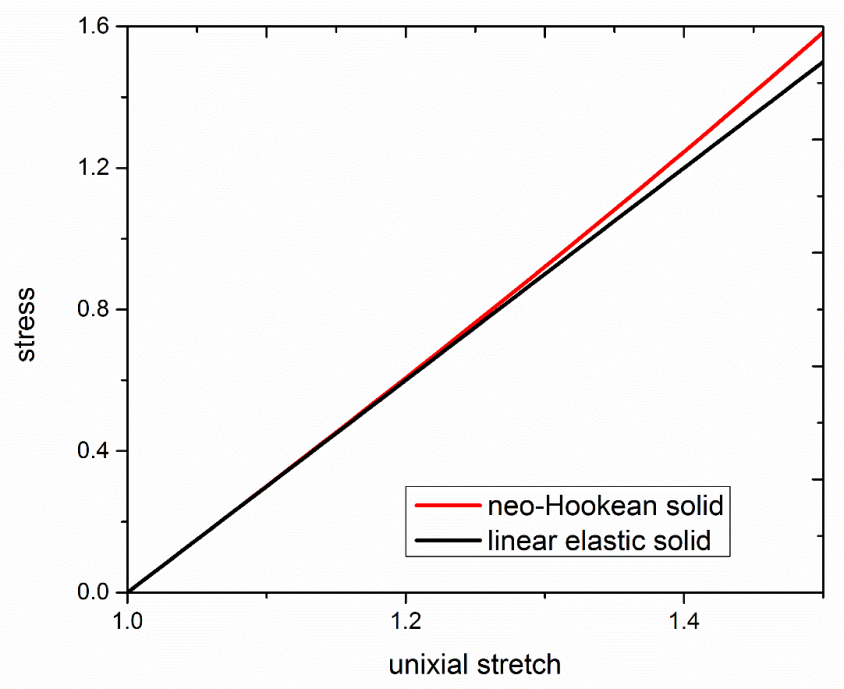

Figure 7-3: Plots of uniaxial stress versus the stretch of neo-Hookean and linear elastic solids when the shear modulus is set to 1. Note that the stress measure used for neo-Hookean solid is Cauchy stress.

7.2 Results

7.2.1 Modulus reconstruction obtained by utilizing phantom data

We first solve the inverse problem by utilizing phantom data and compare the differences in the shear modulus reconstruction results using the linear elastic and neo-Hookean models. In the inverse problem, the problem domain of interest (see **Figure 7-4**) is discretized by 1221 bilinear elements, and only the vertical displacement component is minimized since it is more accurate than the horizontal displacement component.

Regarding the boundary conditions, displacements in both directions on all four edges of the problem domain are prescribed. As only displacements are utilized to solve the inverse problem without using any non-zero traction, force, or partially known shear modulus, the shear modulus distribution is mapped qualitatively, i.e. by a multiplicative factor. **Figure 7-4** shows the shear modulus reconstructions utilizing the linear elastic and neo-Hookean models in the case of roughly 2% extension. In this case, the regularization factor for both cases is selected as 6.0×10^{-4}. Note that in both cases, we utilize the same regularization factor for the sake of comparison. It is apparent that both linear elastic and neo-Hookean models are capable of detecting the location and preserving the shape of these two inclusions well. However, the mapped shear modulus values in inclusions employing the linear elastic model are larger compared to the results using the neo-Hookean model. Meanwhile, comparing the recovered shear modulus values in two inclusions, we find that the smaller inclusion is underestimated.

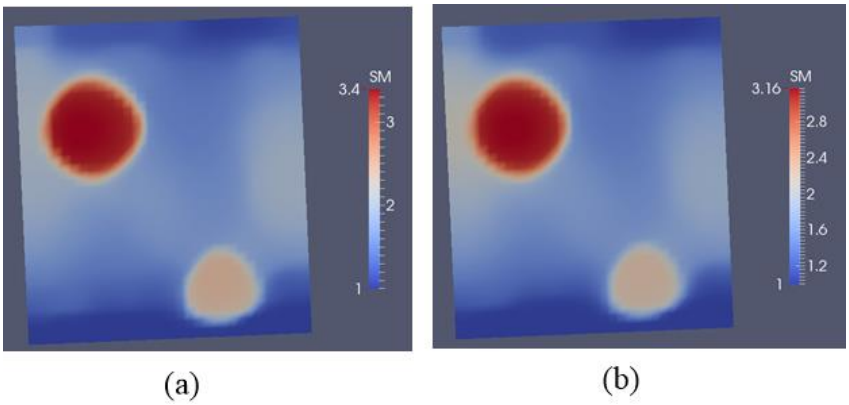

Figure 7-4: Shear modulus reconstructions using (a) linear elastic model; (b) neo-Hookean model.

Figure 7-5 shows the shear modulus reconstructions utilizing the linear elastic and neo-Hookean models in the case of roughly 18% extension, and the regularization factor utilized for both cases is 7.0×10^{-3}. We observe a similar trend to **Figure 7-4** in that the shear modulus values in inclusions using the linear elastic model are larger than the shear moduli predicted by the neo-Hookean model.

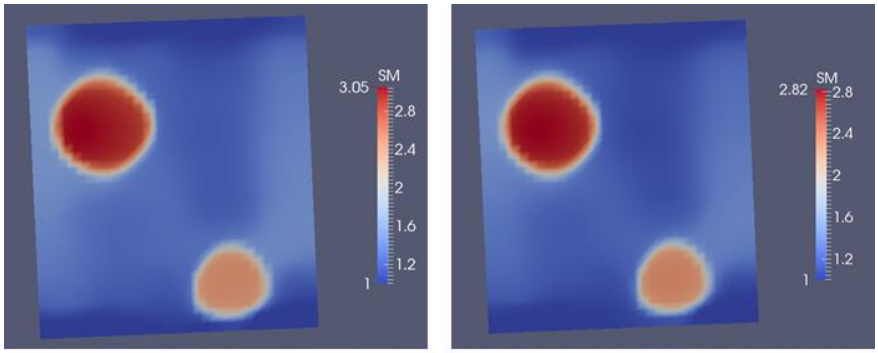

(a) (b)

Figure 7-5: Shear modulus reconstructions using (a) linear elastic model; (b) neo-Hookean model.

7.2.2 Modulus reconstruction obtained by utilizing simulated data

We also utilize simulated data to solve the inverse problem. The simulated data is obtained solving a forward problem where the unit square problem domain (see **Figure 7-6**) is discretized by 3600 bilinear elements. We create two inclusions with different sizes to resemble the soft phantom sample used in **Section 7.2.1**. Meanwhile, we utilize the neo-Hookean model to approximate the mechanical behavior of the hypothetical phantom, and

the target shear modulus values in the inclusions and background are 2 and 1, respectively. This stiffness ratio is close to that of the phantom specimen. The boundary conditions prescribed in the forward simulation are slightly different from those in experiments: we apply uniform extension on the top edge and restrict the vertical motion of the bottom edge. To avoid the rigid body motion, the center node of the bottom edge is fixed in both directions. In solving the inverse problem, we utilize the same displacement boundary conditions prescribed in the forward problem. Additionally, we minimize full-field displacements in vertical direction, and 3% random noise is added to the displacement field.

Figure 7-6 exhibits the reconstructed shear modulus distributions using the linear elastic and neo-Hookean models with the regularization factor of 10^{-8}. In this case, we apply 2% deformation to the simulated phantom. It is obvious that the shape and location of both small and large inclusions are recovered well. We also observe that the shear moduli in the inclusions are larger using the linear elastic model compared to those predicted shear moduli using the neo-Hookean model. Besides, the recovered stiffness in the smaller inclusion is smaller than that in the large inclusion. These trends are also observed in the previous case. For a large deformation of 15% extension as shown in **Figure 7-7** where the regularization factor is selected as 5.0×10^{-7}, the reconstructed shear modulus values in inclusions using the linear elastic model are also larger than those using the neo-Hookean model. In summary, the reconstructions utilizing the simulated data exhibit a very similar trend to the case of the experimental data.

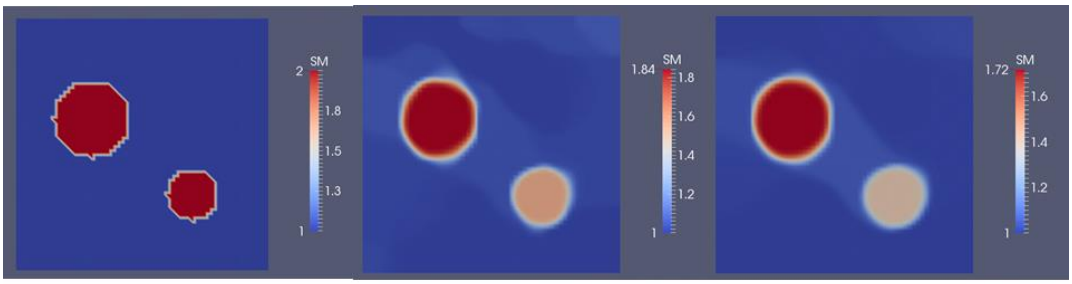

(a) (b) (c)

Figure 7-6: (a) Target shear modulus distribution; shear modulus reconstructions using (b) linear elastic model; (c) neo-Hookean model.

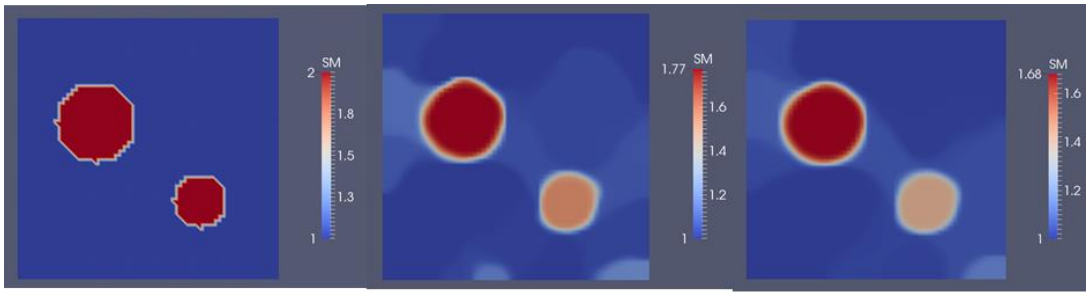

(a) (b) (c)

Figure 7-7: (a) Target shear modulus distribution; shear modulus reconstructions using (b) linear elastic model; (c) neo-Hookean model.

7.3 Discussion

In this chapter, we utilized the iterative approach to solve inverse problems using linear and nonlinear elastic models with experimental and simulated data. The measured datasets were acquired by the experimental and simulated phantoms subjected to small and large deformations. We also analyzed and compared the reconstructed results for

different constitutive models, i.e., linear and neo-Hookean constitutive models with small and large deformations. This work is helpful to understand the feasibility of linear elastic approximation in solving the inverse problem for soft solids, e.g., biological tissues, subjected to larger deformations.

In the first case in **Section 7.2**, we solved the inverse problem by utilizing the phantom data. This phantom sample is inhomogeneous with two stiff inclusions embedded in the soft background. The stiffness contrasts between the inclusions and the background are both roughly 2.5, which is significantly lower than the stiffness ratio of the breast tumor to the normal fat tissue [56]. The displacement field of the sample was measured with high accuracy by a digital imaging correlation system. The accuracy of the DIC system to measure surface displacements has been verified in **Chapter 5**. In solving the inverse problem, we specified the entire displacement boundary of the problem domain and minimized the vertical displacement component in the objective function. According to the reconstructions, the inclusions can be well recovered in both the shape and shear modulus values even when the stiffness contrast between the inclusions and the background is fairly low. We also observed that the shear modulus value in the small inclusion is underestimated, and the reason for this will be discussed below. In addition, comparing to the neo-Hookean model, we observed that the stiffness contrast is overestimated for a linear elastic model in both small and large deformation cases. We will then employ a one-dimensional analysis to explain why this occurs.

The second case in **Section 7.2** is a numerical example that mimics the soft phantom used earlier. In this case, the measured displacement fields were obtained by

solving forward problems for a neo-Hookean solid subjected to small and large deformations. We solved the inverse problem for shear modulus distributions using both linear and neo-Hookean models. Additionally, only the vertical displacement component is minimized in the presence of 3% noise. In this numerical case, we observed a similar trend to the previous case in that the stiffness of the small inclusion is underestimated and the linear elastic hypothesis will overestimate the shear moduli. We will explain these two issues in the following.

(1) The stiffness of the small inclusion is smaller than that of the large inclusion.

In order to explain what we have observed in the two-dimensional case, let us utilize the 1-D coupled model (see **Figure 3-12** in **Chapter 3)** for analysis. In this case, we assume these two bars follow the linear elastic law instead of the neo-Hookean law since the linear elastic problem is easier to solve and this issue occurred in both inverse solvers. Thus, we are able to directly employ **Equation (3.11)** for analysis with $\bar{u}^1 = \bar{u}^2 < 0$ and $\bar{\mu}_{in}^1 = \bar{\mu}_{in}^2$ which is consistent with the 2-D numerical examples presented earlier, and also assume $a^1 < a^2$ which demonstrates the dimension of the left inclusion is smaller than the right one. If we revisit the relative error $\left[\left(\mu_{in}^1 - 0.8\bar{\mu}_{in}^1\right)/\left(0.8\bar{\mu}_{in}^1\right)\right]100\%$, we will find that a negative relative error reveals the stiffness of the small inclusion is underestimated more than the stiffness of the large inclusion. **Figure 7-8** plots the relative error over the target shear modulus values in the inclusions for two scenarios. The red line represents the case where the two inclusions are located in the center of the two bars, respectively. The prescribed parameters used in this case are:

$a^1 = 0.4,\ a^2 = 0.2, b^1 = 0.3, b^2 = 0.4$. The green line corresponds to the case where small and large inclusions are placed downwards and upwards, respectively, that is, $a^1 = 0.4,\ a^2 = 0.2, b^1 = 0.5, b^2 = 0.3$. We observe that the relative error is always negative, which means that the smaller inclusion is underestimated more than the large inclusion. Furthermore, this underestimation becomes more significant when the two inclusions are placed diagonally.

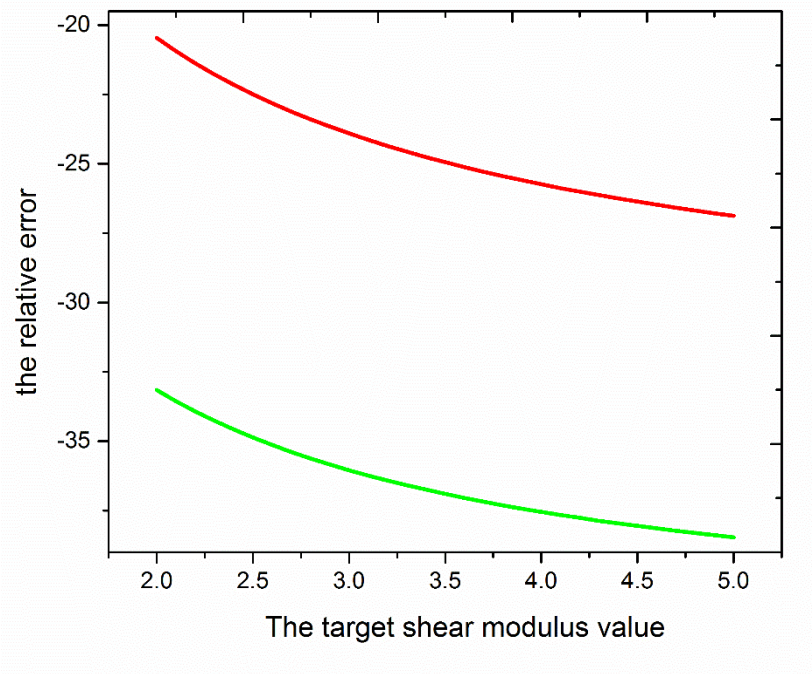

Figure 7-8: The relative error over different target shear modulus values in inclusions. Red line represents the case where the two inclusions are located in the center of the two bars. Green line corresponds to the case where small and large inclusions are placed downwards and upwards, respectively.

(2) The mapped stiffness of the inclusions are underestimated using the linear inverse solver.

In this case, let us consider a nonhomogeneous and hyperelastic bar as shown in **Figure 7-9**, where the stiffness of the black and white regions are denoted by $\overline{\mu}_{in}$ and $\overline{\mu}_{b}$, respectively. The black and white regions mimic the inclusion and background in two-dimensional cases, respectively. We fix the bar at its bottom end and apply a displacement of $u_{\circ}$ at the top end. The total length of the bar is denoted by *L*, the length of the black region is represented by *a*, and the distance between the bottom end of the black region and the fixed end of the bar is denoted by *b*. Given that the stretches are piecewise constants in the black and white regions, one can yield the displacement field u_{exact} along the bar:

$$u_{exact} = \begin{cases} b \cdot \lambda_b + a \cdot \lambda_{in} + (y - b - a)\lambda_b & \text{when } b+a<y \le 1 \\ b \cdot \lambda_b + (y - b)\lambda_a & \text{when } b<y \le b+a \\ y \cdot \lambda_b & \text{when } 0<y \le b \end{cases} \tag{7.3}$$

where λ_a and λ_b are stretches in the inclusion and background, respectively. Since the 2nd Piola-Kirchhoff stress of the inclusion equals that of the background due to the constant axial force in the bar, one can derive the following relationship between λ_a and λ_b:

$$\overline{\mu}_{in}\left(1-\frac{1}{\lambda_a^3}\right) = \overline{\mu}_{b}\left(1-\frac{1}{\lambda_b^3}\right) \tag{7.4}$$

Moreover, the displacement on the top end of the bar is $u_{\circ}$, thus leading to another relation between λ_a and λ_b, that is:

$$u_{\circ} = \lambda_a a + \lambda_b \left(L - a\right) - L \tag{7.5}$$

Thereby, with the assistance of **Equations (7.4)** and **(7.5)** , we are capable of acquiring λ_a and λ_b , and further determining the displacement field u_{exact} by virtue of **Equation (7.3)**. The displacement field u_{exact} is used as the measured displacement in the inverse problem. The objective function in the 1-D case can be written as

$$F = \frac{1}{2}\int_0^1 \left(u_{com} - u_{exact}\right)^2 \mathrm{d}y + \alpha \left|\mu_{in} - \mu_b\right| \tag{7.6}$$

where μ_b and μ_{in} are the estimated stiffness of the background and inclusion, respectively. In addition, u_{com} represents the computed displacement. The formula of the 1-D objective function has been thoroughly discussed in **Chapter 3**. Clearly, $\mu_{in} = \overline{\mu}_{in}$ and $\mu_b = \overline{\mu}_b$ when $\alpha = 0$ if the same constitutive model is used to predict the mechanical response of the bar in the inverse problem. However, adopting the linearized strain measure to solve the inverse problem yields the following computed displacement field u_{com}:

$$u_{com} = \begin{cases} b \cdot \varepsilon_b + a \cdot \varepsilon_{in} + \left(y - b - a\right)\varepsilon_b^i & \text{when } b+a<y \le 1 \\ b \cdot \varepsilon_b + \left(y - b\right)\varepsilon_{in} & \text{when } b<y \le b+a \\ y \cdot \varepsilon_b & \text{when } 0<y \le b \end{cases} \tag{7.7}$$

where ε_b and ε_{in} are the computed strains of the background and inclusion, respectively. As the stress in this bar is constant, we have the relationship $\mu_{in}\varepsilon_{in} = \mu_b\varepsilon_b$. Combining this relationship with the kinematic constraint yields the explicit expression of ε_b and ε_{in}:

$$\varepsilon_b = u_{\circ} / \left(\left(L - a\right) + a\mu_b / \mu_{in}\right) \text{ and } \varepsilon_{in} = u_{\circ} / \left(\left(L - a\right)\mu_{in} / \mu_b + a\right) \tag{7.8}$$

We also fix $\mu_b = 1$ as the stiffness distribution is relatively mapped. Thereby, the objective function is merely a function of the inclusion stiffness μ_{in}. Minimizing the objective function yields the following equation:

$$\frac{\partial F}{\partial \mu_{in}} = 0 \tag{7.9}$$

which can be utilized to determine the inclusion stiffness μ_{in}. **Figure 7-10** exhibits the recovered inclusion stiffness over various external displacements from 0.02L (2% deformation) to 0.2L (20% deformation) for different exact inclusion stiffness $\bar{\mu}_{in}$ (=2,3,4,5) when the regularization factor α is set to zero. In this case, other parameters utilized in **Figure 7-10** are as follows: $L = 1$, $a = 0.2$, and $b = 0.4$.

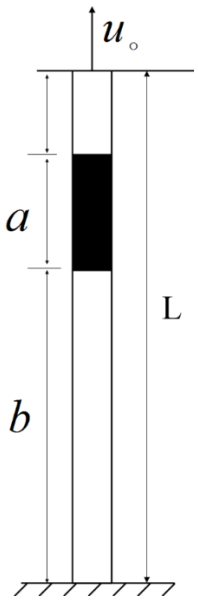

Figure 7-9: 1-D nonhomogeneous elastic bar subject to uniaxial extension.

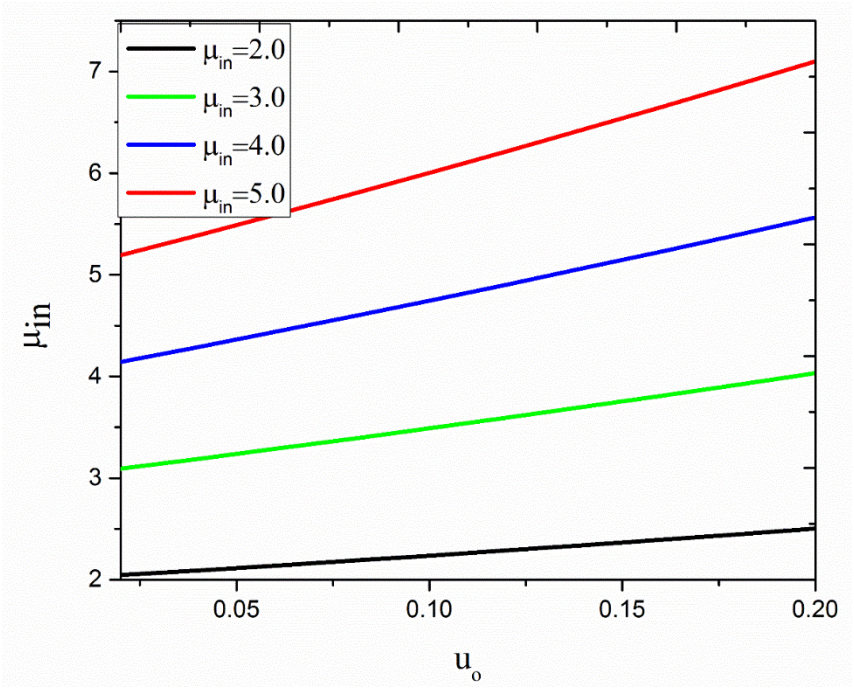

Figure 7-10: Plot of the reconstructed shear modulus in the inclusion over the external displacements at the top end of the bar for different exact stiffness values in the inclusion $\bar{\mu}_{in}$ (=2, 3, 4, 5).

As shown in **Figure 7-10**, it is clear that the recovered shear modulus in the inclusion is overestimated regardless of small or large deformations when the linearized theory is employed. Thus this 1-D theoretical analysis validates what we have observed in 2-D cases. Meanwhile, we also observe that the estimated inclusion shear modulus value increases with the increment of the external loading and the target stiffness contrast. In particular, the estimated inclusion stiffness is roughly 1.4 times larger than the exact stiffness when the target shear modulus is 5 and the external displacement $u_{\circ} = 0.2$. This observation provides a fairly important insight in the inverse problem in elasticity, that is,

the linear elastic assumption can be applied for characterizing elastic property distribution of soft solids undergoing a very small deformation, e.g., less than 2% deformation, as the overestimation of the recovered inclusion stiffness is infinitesimal. However, it will induce a larger error when the external loading becomes larger, especially for a problem domain with a substantially large target stiffness ratio. We should note that the phenomenon that the overestimation of the stiffness contrast becomes more significant with increasing external loading was not observed in the 2-D results presented in **Section 7.2**. The reason for this is that the stiffness of the inclusions is very close to that of the background, thus the inclusion behaves very similarly to the background. As such, the resulting full-field displacement will be highly sensitive to the noise, thus highly affecting the final reconstruction results.

7.4 Conclusions

In this chapter, we have presented a thorough study on the feasibility of the linear elastic approximation in solving inverse problems for a neo-Hookean solid in two-dimensional space. Both experimental and simulated displacement datasets have been introduced to solve the inverse problem. The experimental data of a soft and nonhomogeneous phantom is obtained with high accuracy by a digital camera correlation system. According to the shear modulus reconstructions for both the simulated and experimental examples, we have observed that the mapped shear moduli are well recovered in the size and the location of the stiff inclusions using both the linear and non-linear models. However, the linear elastic model overestimated the shear modulus values in the inclusions. To better analyze this, we have performed a one-dimensional theoretical

analysis to explain the observation of the 2-D reconstruction results. In this 1-D theoretical analysis, we also observed that the stiffness contrast is overestimated significantly when the linear elastic model is adopted. Additionally, we also found that the overestimation becomes more significant with the increase of the external loading and target stiffness contrast. Overall, this work provides a good understanding of the feasibility and reliability of the use of the linearized theory to solve the inverse problem using the data measured from a neo-Hookean solid.

8. QUANTIFYING THE ANISOTROPIC LINEAR ELASTIC BEHAVIOR OF SOFT SOLIDS

In previous chapters, the main focus was to identify the material property distribution for a nonhomogeneous isotropic elasticity. However, a large number of biological tissues like bones and skins are anisotropic elastic materials. Meanwhile, anisotropic elastic parameters might be altered due to diseases, e.g., the anisotropic elastic properties of a bone become smaller during the process of osteoporosis. Thus, the assessment and knowledge of nonhomogeneous and anisotropic elastic properties of tissues might be of clinical significance. However, due to the ill-posed nature of the inverse problem and a large number of unknown material properties in the anisotropic constitutive models, identification of heterogeneous anisotropic elastic properties is poorly addressed. Shore et al. recovered the heterogeneous 3-D transverse anisotropic elastic property distribution for bone tissues assuming the fiber direction is known [120]. According to the observation of the reconstruction results, the mapped material property distributions are highly sensitive to the noise. A similar trend was also observed in another work [121] where 2-D orthotropic linear elastic property distribution is poorly mapped in the presence of only 1% noise.

In this chapter, we propose and develop an iterative inverse methodology to recover the orthotropic linear elastic property distributions in 2-D. We fully take advantage of the inverse solvers presented in **Chapter 2** and implement the novel feature of anisotropy into the existing algorithms. The theoretical background of this new feature

will be elaborated in **Section 8.1**, and we will test it with numerical experiments in **Section 8.2**. In **Section 8.3**, we discuss the numerical results and end with conclusions in **Section 8.4**.

8.1 Forward and inverse problems in 2-D orthotropic linear elasticity

The strong form of the forward problem in anisotropic linear elasticity in the 2-D case is stated as: Find the displacement **u** such that the equilibrium equations and the prescribed Neumann and Dirichlet boundary conditions are satisfied. In 2-D orthotropic linear elasticity, the constitutive law can be represented as:

$$\begin{Bmatrix} \sigma_{xx} \\ \sigma_{yy} \\ \sigma_{xy} \end{Bmatrix} = \begin{bmatrix} C_{11} & C_{12} & 0 \\ C_{12} & C_{22} & 0 \\ 0 & 0 & C_{66} \end{bmatrix} \begin{Bmatrix} \varepsilon_{xx} \\ \varepsilon_{yy} \\ \varepsilon_{xy} \end{Bmatrix} \tag{8.1}$$

In this case, material axes are aligned with the x-y axes as shown in **Figure 8-1** (a). It is noted that there is no coupling effect of shear and axial deformations. In other words, shear stresses will only produce shear strains, and normal stresses will only result in normal strains. If the material axes are not aligned with the x-y axes, e.g., the material axes are rotated counter-clockwise from the x-y coordinate system by an angle of θ as shown in **Figure 8-1** (b), the stress-strain relation will be rewritten as:

$$\begin{Bmatrix} \sigma_{xx} \\ \sigma_{yy} \\ \sigma_{xy} \end{Bmatrix} = \begin{bmatrix} \tilde{C}_{11} & \tilde{C}_{12} & \tilde{C}_{13} \\ C_{12} & \tilde{C}_{22} & \tilde{C}_{23} \\ \tilde{C}_{13} & \tilde{C}_{23} & \tilde{C}_{66} \end{bmatrix} \begin{Bmatrix} \varepsilon_{xx} \\ \varepsilon_{yy} \\ \gamma_{xy} \end{Bmatrix} \tag{8.2}$$

The material parameters in **Equation (8.2)** can be expressed in terms of $C_{11}, C_{12}, C_{22}, C_{66}$ and θ, that is,

$$
\begin{aligned}
\tilde{C}_{11} &= C_{11}\cos^4\theta + C_{22}\sin^4\theta + 2\left(C_{12}+2C_{66}\right)\sin^2\theta\cos^2\theta \\
\tilde{C}_{22} &= C_{11}\sin^4\theta + C_{22}\cos^4\theta + 2\left(C_{12}+2C_{66}\right)\sin^2\theta\cos^2\theta \\
\tilde{C}_{12} &= \left(C_{11}+C_{22}-4C_{66}\right)\sin^2\theta\cos^2\theta + C_{12}\left(\cos^4\theta+\sin^4\theta\right) \\
\tilde{C}_{66} &= \left(C_{11}+C_{22}-2C_{12}-2C_{66}\right)\sin^2\theta\cos^2\theta + C_{66}\left(\cos^4\theta+\sin^4\theta\right) \\
\tilde{C}_{16} &= \left(C_{11}-C_{12}-2C_{66}\right)\sin\theta\cos^3\theta - \left(C_{22}-C_{12}-2C_{66}\right)\sin^3\theta\cos\theta \\
\tilde{C}_{26} &= \left(C_{11}-C_{12}-2C_{66}\right)\sin^3\theta\cos\theta - \left(C_{22}-C_{12}-2C_{66}\right)\sin\theta\cos^3\theta
\end{aligned}
\tag{8.3}
$$

The derivation of **Equation (8.3)** requires coordinate transformation of stress and strain tensors, and has been shown in [122]. With the constitutive law **(8.2)** or **(8.3)**, the governing equations, and the prescribed boundary conditions, we can solve the forward problem adopting the finite element approach to obtain simulated displacement fields.

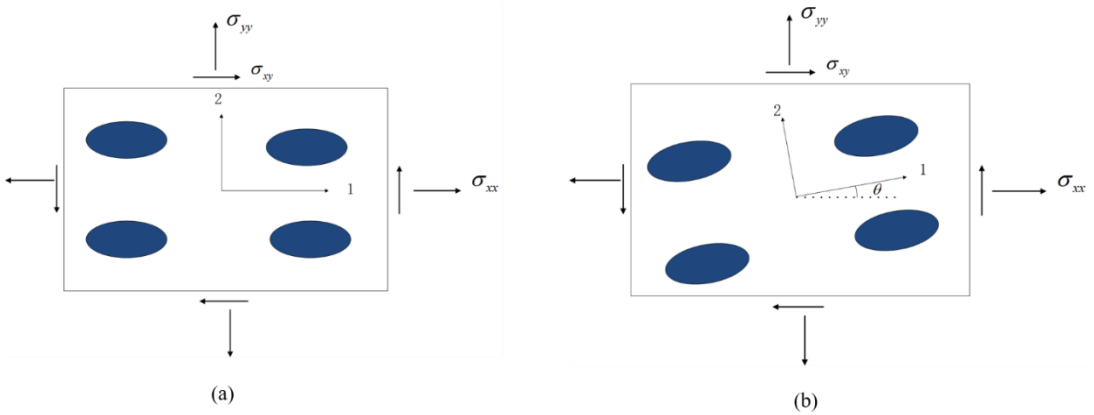

Figure 8-1: A schematic diagram of the cross section of a microstructure of an orthotropic material where the elliptic fibre bundles are in dark blue color. (a) The material axes are aligned with reference axes; (b) the material axes are not aligned with reference axes.

In this chapter, we utilize the iterative inverse strategy to solve the inverse problem in 2-D orthotropic linear elasticity. In the inverse problem, the unknown material parameter vector $\beta = [C_{11}\ C_{12}\ C_{22}\ C_{66}\ \theta]$. As we did in the previous chapters, we utilize the adjoint method to evaluate the gradient of the objective function with respect to the material properties, which allows us to solve the optimization problem by the limited BFGS method. As the implementation of the novel feature is very similar to what we have discussed in **Chapter 2**, we will not discuss herein. In the next section (**Section 8.2**), we will show the feasibility of the inverse scheme to recover the anisotropic material property distributions quantitatively using simulated displacements together with traction data. We should note that for a 2-D orthotropic linear elasticity, a large number of unknowns must be determined, thus leading to the uniqueness issue. To address this issue, we will solve the inverse problem using multiple full-field displacement fields acquired from different simulated mechanical tests. In order to test the robustness of the inverse algorithms, we add the same noise level throughout the displacement field together with applied tractions.

8.2 Results

In this section, the performance of the iterative inverse strategy to characterize the non-homogeneous anisotropic linear elastic material properties will be tested by simulated data. Let us consider a 1cm×1cm square problem domain as shown in the first column of **Figure 8-2**, which is discretized by 900 bilinear elements. In this problem domain, there is a stiff inclusion with a radius of 0.1cm embedded in the soft background. The specific material parameters for the background and inclusion are shown in **Table 8-1**. In this case, the material parameters of the soft background are taken from the parameters of a healthy

human skin [123]. Meanwhile, we assume the material axes of both background and inclusion are known and aligned with the reference axes, i.e., $\theta = 0$. To obtain the multiple simulated datasets, we solve forward problems of the same problem domain with different loading and boundary conditions as shown in **Figure 8-3**. In this figure, Case (a) and (b) are uniaxial extension tests, Case (c) and (d) are shear tests, and Case (e) and (f) are biaxial tests. Regarding displacement boundary conditions for each case, we restrict are uniaxial extension the motion in both directions on the bottom edge in Case (a) and (c), and on the left edge in Case (b) and (d). For the last two cases, we restrict axial motion in both left and bottom edges. The prescribed non-zero tractions in each case are $t_x = 3\text{kPa}, t_y = 3\text{kPa}, t_{xy} = 1.5\text{kPa}$ and $t_x^2 = -3\text{kPa}$.

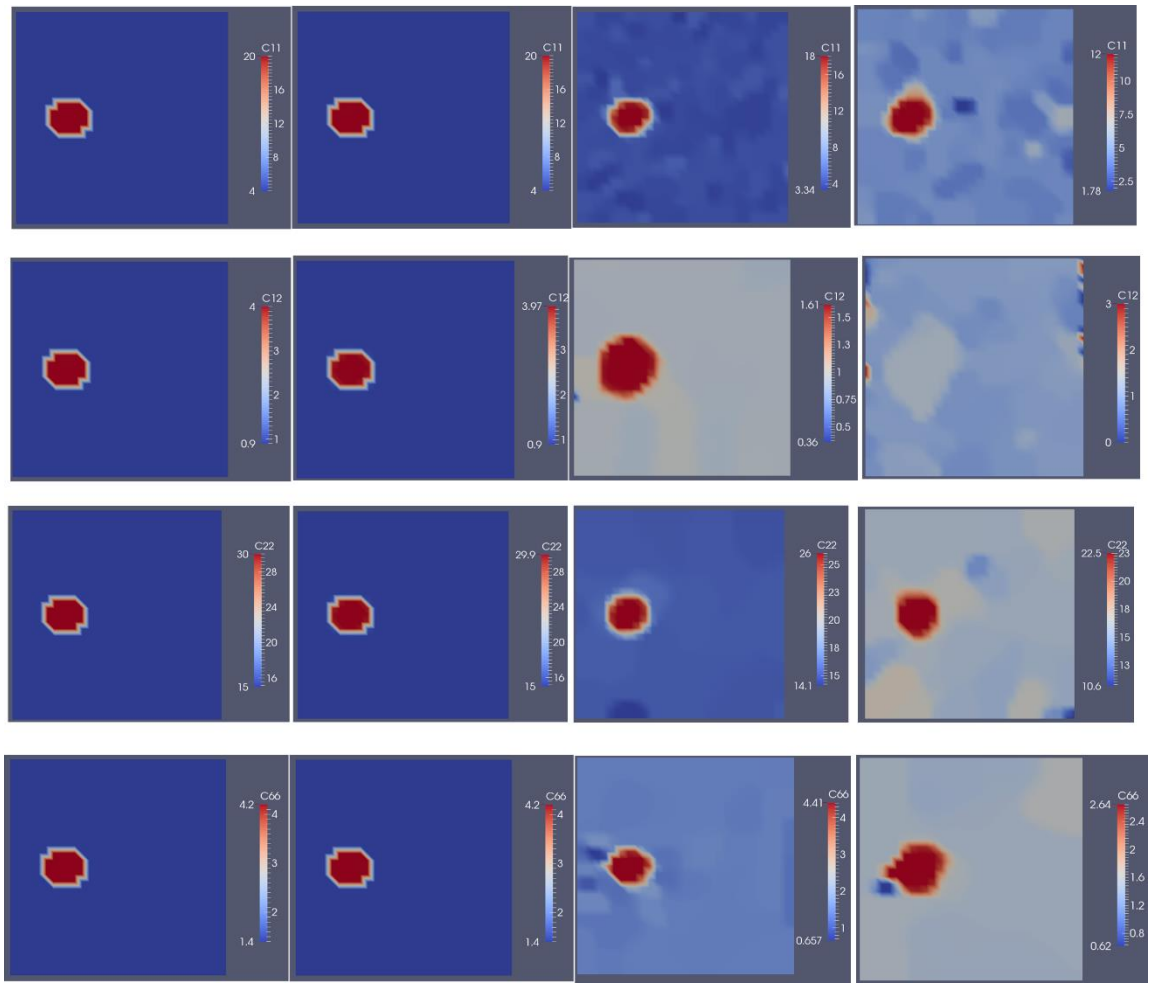

Figure 8-2: Problem domain with target modulus distributions are defined in the first column and material parameter distributions($C_{11}, C_{12}, C_{22}, C_{66}$ **)** are presented from top row to bottom row, respectively. Column 2 to Column 4 represent the parameter reconstructions with 4 displacement measurements using 0, 0.1%, and 1% noise, respectively.

Table 8-1: Target orthotropic linear elastic material parameters in **Figure 8-2**.

	C_{11}(kPa)	C_{12}(kPa)	C_{22}(kPa)	C_{66}(kPa)	$\theta(^{\circ})$
background	5	9	150	14	0
inclusion	20	40	300	42	0

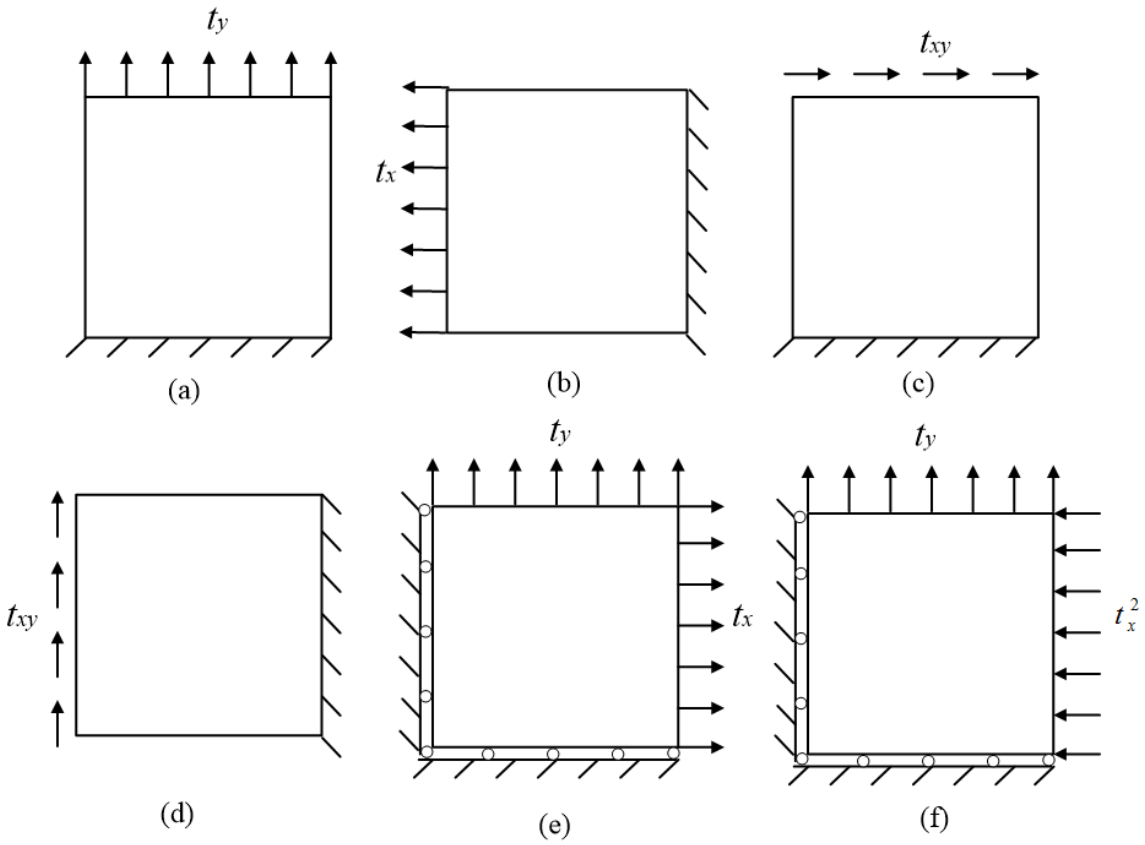

Figure 8-3: Cases used in solving forward and inverse problems.

Table 8-2: Regularization factors used in each case presented in **Figure 8-2**.

	C_{11}	C_{12}	C_{22}	C_{66}
0% noise	10^{-12}	10^{-12}	10^{-12}	10^{-12}
1% noise	5.0×10^{-10}	2.0×10^{-10}	1.0×10^{-10}	2.0×10^{-10}
3% noise	3.0×10^{-9}	5.0×10^{-10}	2.0×10^{-10}	2.0×10^{-9}

In solving the inverse problem, we utilize multiple full-field displacement measurements acquired from solving forward problems. To quantitatively determine the material property distributions, we will use the non-zero traction boundary conditions in the inverse problem as well. **Figure 8-2** represents the reconstructions using 4 full-field displacement measurements (using the first 4 cases in **Figure 8-3**) in the presence of different noise levels: 0%, 1%, and 3% noise are utilized in Column 2, 3, 4, respectively. The regularization factors for each material parameter are listed in **Table 8-2**. We observe that the recovered parameter distributions are fairly close to the target orthotropic linear elastic property distributions (see the first column in **Figure 8-2**) in the case of no noise. Meanwhile, in the presence of 1% noise, all the parameter distributions except for the material parameter C_{12} are still well-recovered in both the shape and parameter values of the inclusion. In the reconstruction of the parameter C_{12}, the shape of the inclusion becomes larger and the parameter value is much smaller than the target. With 3% noise (see the last column in **Figure 8-2**), we are incapable of recovering well in that all material property values in the inclusion are much lower than the target. Furthermore, the shape of

the inclusion in the modulus reconstruction image of each parameter is distorted, especially for the parameter C_{12}. We also collect two more displacement measurements from biaxial testing (Case (e) and (f) in **Figure 8-3**) and utilize 6 total displacement fields to solve the inverse problem. The associated reconstructions are displayed in **Figure 8-4**. The regularization factors used in this case are listed in **Table 8-3**. With low noise level, the orthotropic elastic parameter distributions can be quantitatively determined in good quality similar to the trend presented in **Figure 8-2**, while they are poorly recovered for a high noise level. We also observe that in the case of 3% noise, the shape and the inclusion value in the mapped distribution of the parameter C_{12} improve with increasing total number of displacement measurements.

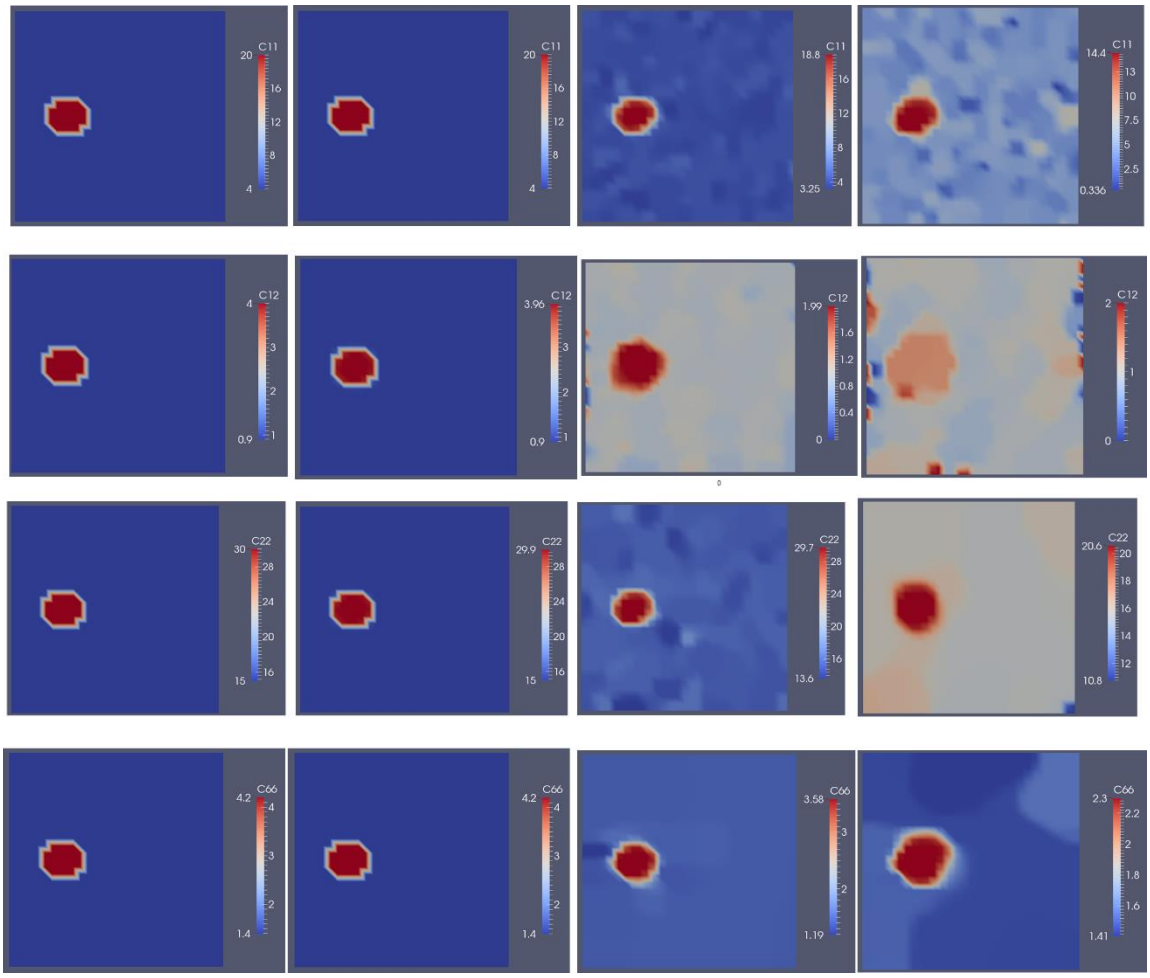

Figure 8-4: Problem domain with target modulus distributions are defined in the first column and material parameter distributions ($C_{11}, C_{12}, C_{22}, C_{66}$) are presented from top row to bottom row, respectively. Column 2 to Column 4 represent the parameter reconstructions with 6 displacement measurements using 0, 0.1%, and 1% noise, respectively.

Table 8-3: Regularization factors used in each case presented in **Figure 8-4**.

	C_{11}	C_{12}	C_{22}	C_{66}
0% noise	10^{-12}	10^{-12}	10^{-12}	10^{-12}
1% noise	3.0×10^{-10}	5.0×10^{-11}	2.0×10^{-11}	3.0×10^{-10}
3% noise	1.0×10^{-9}	2.0×10^{-10}	3.0×10^{-10}	2.0×10^{-9}

In practice, the rotation angle of material axes is also unknown. Therefore, we also need to test the performance of the inverse algorithms to recover the rotation angle θ. In this case, we still use the same problem domain and the same boundary conditions utilized in the first example to solve the forward problems and collect multiple displacement fields. However, the target rotation angle of the inclusion is different from that used in the first example as shown in **Table 8-5**. We also utilize a similar strategy to solve the inverse problems. **Figure 8-5** and **Figure 8-6** exhibit the material property distributions using 4 and 6 full-field displacement measurements, respectively, with noise levels from 0% to 3%. The reconstruction results show that in the case of no or low noise levels, the material property distributions are generally recovered well, whereas the rotation angle of the material axes θ in the case of 1% noise is recovered worse than other parameters, i.e., the shape of the inclusion of the distribution of θ is distorted. Additionally, the reconstructions are of poor quality for the case with the higher noise level. More specifically, the shape of the inclusion is poorly mapped, and the material property values in the inclusion are significantly underestimated.

Table 8-4: Target orthotropic linear elastic material parameters in **Figure 8-2**.

	C_{11}(kPa)	C_{12}(kPa)	C_{22}(kPa)	C_{66}(kPa)	$\theta(^{\circ})$
background	5	9	150	14	0
inclusion	20	40	300	42	30

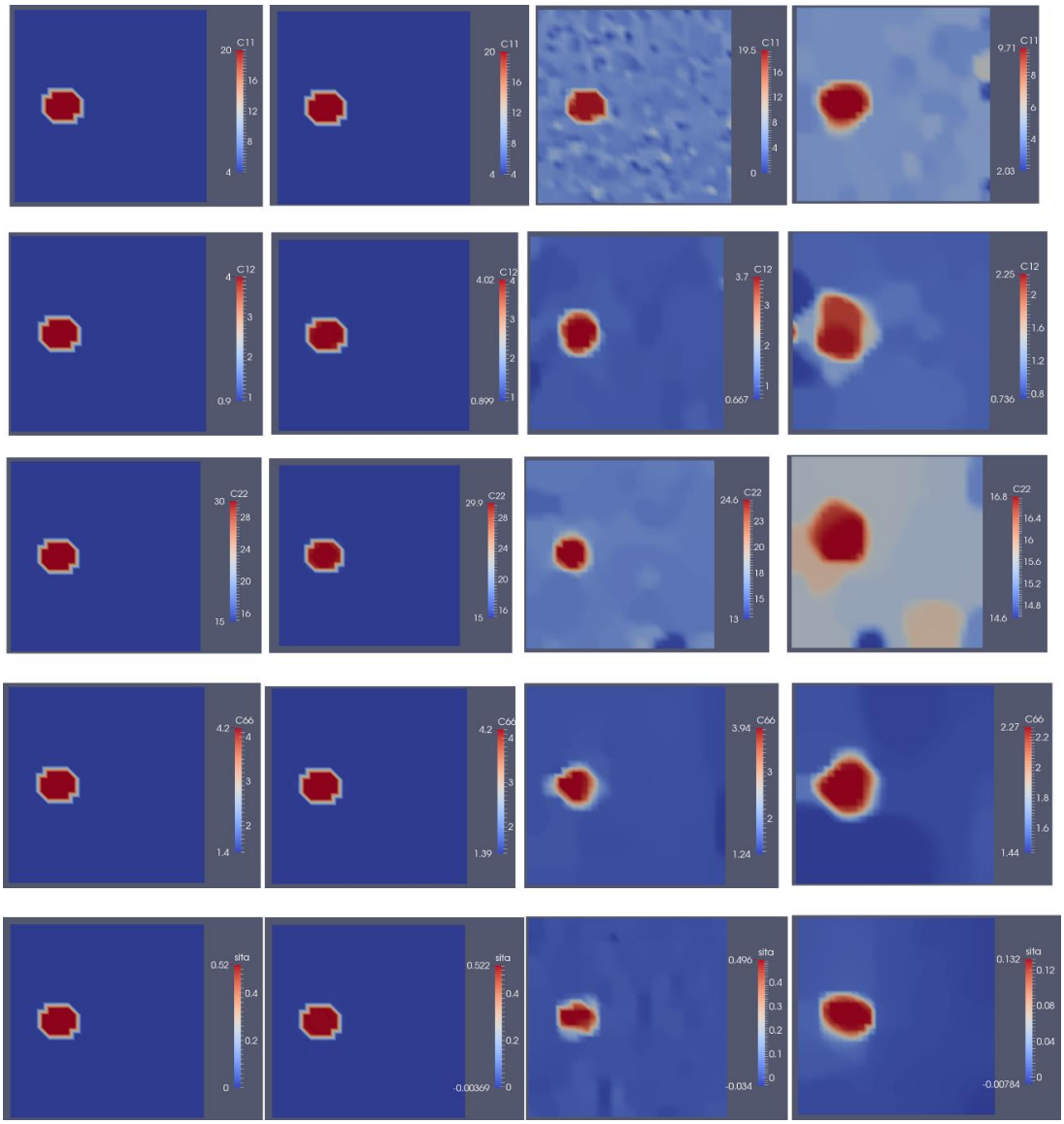

Figure 8-5: Problem domain with target modulus distributions are defined in the first column and material parameter distributions ($C_{11}, C_{12}, C_{22}, C_{66}, \theta$) are presented from top row to bottom row, respectively. Column 2 to Column 4 represent the parameter reconstructions with 4 displacement measurements using 0, 0.1%, and 1% noise, respectively. Note that the unit of rotation θ used in the last row is radian.

Table 8-5: Regularization factors used in each case presented in **Figure 8-5.**

	C_{11}	C_{12}	C_{22}	C_{66}	θ
0% noise	10^{-12}	10^{-12}	10^{-12}	10^{-12}	10^{-12}
1% noise	1.0×10^{-10}	8.0×10^{-11}	5.0×10^{-11}	3.0×10^{-10}	9.0×10^{-10}
3% noise	5.0×10^{-9}	1.0×10^{-9}	4.0×10^{-10}	4.0×10^{-9}	2.5×10^{-8}

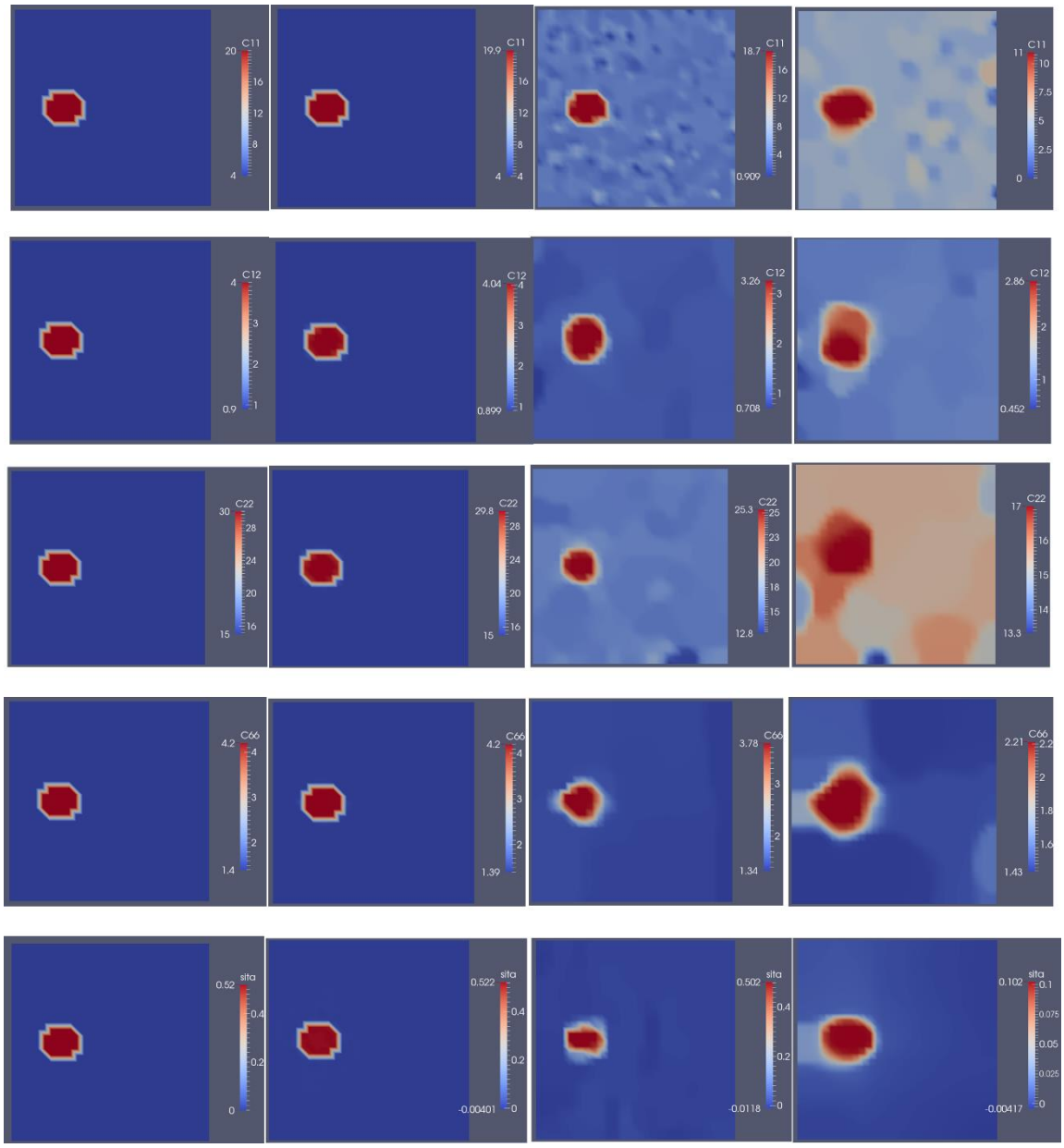

Figure 8-6: Problem domain with target modulus distributions are defined in the first column and material parameter distributions ($C_{11}, C_{12}, C_{22}, C_{66}$, θ) are presented from top row to bottom row, respectively. Column 2 to column 4 represent the parameter reconstructions with 6 displacement measurements using 0, 0.1%, and 1% noise, respectively. Note that the unit of rotation θ used in the last row is in radian.

Table 8-6: Regularization factors used in each case presented in **Figure 8-6.**

	C_{11}	C_{12}	C_{22}	C_{66}	θ
0% noise	10^{-12}	10^{-12}	10^{-12}	10^{-12}	10^{-12}
1% noise	1.0×10^{-10}	8.0×10^{-11}	3.0×10^{-11}	3.0×10^{-10}	9.0×10^{-10}
3% noise	2.0×10^{-9}	4.0×10^{-10}	2.0×10^{-10}	2.0×10^{-9}	3.0×10^{-8}

8.3 Discussion

In this work, we presented a methodology to quantitatively identify the heterogeneous parameter distributions for a 2-D orthotropic linear elasticity, and its feasibility was tested successfully by numerical experiments. Unlike the previous works on mapping the non-homogenous anisotropic material property distributions [120, 121], non-zero tractions were introduced and prescribed in solving the inverse problem herein, which ensures a quantitative solution.

We tested the performance of the novel inverse scheme by using simulated data. The simulated datasets were acquired by solving forward problems with a target non-homogenous material property distribution. In the inverse problem, multiple simulated full-field displacement datasets acquired from uniaxial, shear, and biaxial tests were used to map the material property distributions. The reconstruction results revealed that the anisotropic linear elastic property distributions are very sensitive to the noise. When the noise level is low, e.g. less than 1% noise, all parameters in the 2-D orthotropic linear elastic law were mapped well, while poorly reconstructed in the presence of a higher noise level, e.g., 3% noise. Compared to the reconstructions for isotropic elastic solids, the reconstructions presented in this work were poorly mapped in the same noise level. The phenomenon of the high sensitivity of the reconstructed anisotropic linear elastic

parameter distributions to the noise is also observed in other similar works [120, 121]. In those works, even with 1% noise or less, the heterogeneous anisotropic parameters were not recovered well. The reason for this might be the fact that in the estimation of anisotropic parameters, the uniqueness issue becomes more serious as a large number of unknown material parameters in the constitutive law must be determined, e.g., five material parameters in the 2-D orthotropic linear elastic model.

We recovered all material parameters $C_{11}, C_{12}, C_{22}, C_{66}$ and θ simultaneously in this chapter; however, this approach is difficult to ensure a unique solution for a variety of coupled material parameters in the constitutive law. An alternative way is to estimate each material parameter separately in terms of their physical interpretations. For instance, C_{66} might be determined separately from other parameters using shear deformations. Thus, future work will focus on proposing sequential methods to recover anisotropic elastic property distributions.

This work is a preliminary study to present the proof of concept of recovering the heterogeneous anisotropic material property distributions using iterative inverse algorithms, and we merely introduced the 2-D orthotropic linear elastic feature in the inverse algorithms. However, the current inverse scheme can be easily generalized to 2-D transversely anisotropic, or 3-D anisotropic elastic cases that may have more clinical significance.

8.4 Conclusions

In this chapter, we have presented a quantitative approach to identify the 2-D heterogeneous, orthotropic, linear elastic material property distributions of biological

tissues. The feasibility of this approach has been tested by multiple full-field simulated datasets. We have observed that the mapped anisotropic elastic parameter distributions are of good quality with low noise levels, while poorly recovered in the presence of as high as 3% noise. This work is a preliminary study to determine the nonhomogeneous anisotropic property distributions quantitatively and non-invasively. Future work will focus on generalizing this approach to the three-dimensional cases and developing more effective approaches to improve the quality of reconstructions.

9. MAPPING THE VISCOELASTIC BEHAVIOR OF SOFT SOLIDS FROM TIME HARMONIC MOTION

Time harmonic particle motion can be used to map the viscoelastic mechanical behavior of solids, such as biological tissues and synthetic polymers. More precisely, shear waves are induced by mechanical excitations [124] on the specimen's surface or internally through acoustic sources [125]. Shear waves are created directly or indirectly by mode conversion, e.g. after impact loading [126] . The storage and loss moduli are frequency dependent parameters and can be mapped for a spring-dashpot model in the frequency domain. These parameters were determined by minimizing the error in the constitutive equation [127] or directly from the governing partial differential equations allowing for point-wise computation for the material properties, thus reducing computational time drastically [128-132]. The latter usually assumes local homogeneity of the material properties to simplify the mapping procedure, resulting in the well-known form of the Helmholtz equations. This assumption, however, comes at a cost of accuracy in recovering regions with high gradients in material properties. Further, higher order derivatives of noisy strain amplitudes are utilized, leading to amplified noise levels in measured data.

In this chapter, we will recover the heterogeneous distribution of the storage and loss modulus for measured complex valued displacement amplitudes from simulated experiments. The problem is posed as a constrained minimization problem with a regularized objective function that is subject to the constraint of the forward problem formulated in the frequency domain and solved with finite element techniques. In **Section**

9.1, we start with a brief review of the finite element formulation to solve the forward problem in the frequency domain. Then the inverse problem formulation is stated and the adjoint equations are derived to evaluate the gradient of the objective function. In **Section 9.2** we test the quality of the reconstructions with respect to shape of inclusion and parameter value distribution. Further, the sensitivity of the reconstructions to changes in loss angle, driving frequency, and positioning of inhomogeneous inclusions is investigated and observations thoroughly discussed and theoretically analyzed in **Section 9.3**.

9.1 Method

In this section, we will discuss the forward and inverse problem of the viscoelastic problem in the frequency domain. The forward problem is to find the complex valued displacement field in the problem domain when the moduli distribution is known. The inverse problem is posed as a constrained minimization problem, where the equation of motion for time harmonic excitation depicts the constraint. The performance of the inverse algorithms to characterize viscoelastic moduli will be tested with simulated experiments, acquired by solving a forward problem. We will discuss the forward and inverse problem in detail in the following subsections.

9.1.1 Forward problem in viscoelasticity

For time harmonic motion, the equation of motion is expressed as:

$$\begin{aligned} \nabla\boldsymbol{\sigma} + \rho\omega^2\mathbf{u} &= 0 \quad && \text{on } \Omega \\ \mathbf{u} &= \mathbf{h} && \text{on } \Gamma_h \\ \boldsymbol{\sigma}\cdot\mathbf{n} &= \mathbf{g} && \text{on } \Gamma_g \end{aligned} \tag{9.1}$$

where $\boldsymbol{\sigma}$ is complex-valued Cauchy stress and $\mathbf{u}$ is the complex-valued displacement of the solid in the domain of interest Ω. ρ denotes the density and $\omega = 2\pi f$ denotes the angular frequency, where f is the driving frequency of excitation. **h** and **g** are prescribed displacement and traction values on the boundary Γ_h and Γ_g, respectively. The boundary Γ_h and Γ_g constitute the entire boundary of the domain Ω. In addition, **n** represents the outward unit normal vector along the boundary. We assume that the solid is incompressible in 3-D space, with the incompressible condition given by

$$\operatorname{tr}(\nabla \mathbf{u}) = 0 \tag{9.2}$$

Based on small deformation theory this implies that the summation of normal strain components is zero. We also assume the solid is in the state of plane stress and the correspondingly linear viscoelastic stress-strain relation is given by:

$$\sigma_{ij} = 2\mu^* \varepsilon_{ij} + 2\mu^* \varepsilon_{kk} \delta_{ij} \tag{9.3}$$

where $i, j, k = 1$ or 2 and $\varepsilon_{ij} = \frac{1}{2}\left(u_{i,j} + u_{j,i}\right)$ is the small strain tensor. Also, $\mu^* = \mu_r + i\mu_i$ denotes the unknown complex shear modulus where μ_r and μ_i are the storage and loss moduli, respectively. The complex modulus can also be written as $\mu = \mu_r\left(1 + i\tan(\delta)\right)$ where $\delta = \arctan\left(\mu_i / \mu_r\right)$ is the loss angle. We will solve the forward problem from **Equations (9.1)** to **(9.3)** using standard finite element methods that leads to the following linear algebraic:

$$\mathbf{KU} - w^2\mathbf{MU} = \mathbf{F} \tag{9.4}$$

In **Equation (9.4)** **K** and **M** are the stiffness matrix and mass matrix, respectively, and **F** is the external force vector. The nodal vector **U** represents the real and imaginary displacement components and has length of $2\times N\times 2$ in two-dimensional space, where N represents the total number of nodes. We solve **Equation (9.4)** for **U** to simulate experimental displacement data acquisition.

9.1.2 Inverse problem formulation

The inverse problem is posed as a constrained optimization problem where the correlation between the computed and measured amplitude of the complex displacement fields are minimized in the L-2 norm. In particular, given the nodal vector of the measured complex valued displacements $\mathbf{U}^1_{meas}, \mathbf{U}^2_{meas}, ..., \mathbf{U}^n_{meas}$, find the storage modulus and loss modulus $\beta = [\mu_r \ \mu_i]$ such that the objective function:

$$F = \frac{1}{2}\sum_{i=1}^{n} \| \mathbf{D}(\mathbf{U}^i - \mathbf{U}^i_{meas}) \|_0^2 + \frac{1}{2}\sum_{j=1}^{2} \alpha_j \mathrm{Reg}\left(\beta_j\right) \tag{9.5}$$

is minimized subject to the constraint of the forward problem in **Equation (9.5)**. In **Equation (9.5)**, the first term is the displacement correlation term, and the computed displacement $\mathbf{U}^i$ is a function of the storage and loss modulus and satisfies the forward problem discussed in **Section 9.1.1**. The summation allows accommodation of measurements from multiple experiments, indexed with the superscript i . Spatial dependencies of $\beta_j, \mathbf{U}^i,$ and $\mathbf{U}^i_{meas}$ were omitted in **Equation (9.5)** to reduce notation. The linear operator D results from a continuous displacement field, approximated with finite element shape functions. The second term in **Equation (9.5)** represents a regularization term to penalize and smooth the mapped moduli. Its relative contribution to

the objective function is controlled by the regularization factor α_j. A large regularization factor will lead to overly smoothed moduli reconstructions, while a smaller one will amplify the measurement noise in the reconstructions, thus producing serious oscillation. The optimal α_j can be selected based on Morozov's discrepancy principle or a smoothness measure based on standard deviations in some small region of the domain [49, 62]. There are numerous regularization types, and the total variation diminishing (TVD) regularization method is employed in this work, given by

$$\mathrm{Reg}\left(\beta_j\right) = \int_{\Omega} \sqrt{|\nabla \beta_j|^2 + c^2}\, d\Omega \tag{9.6}$$

Here, the constant c in the regularization term is chosen to be small to avoid singularities when taking derivatives of the objective function with respect to the material parameters. The optimization problem is solved using the limited BFGS method which is a gradient-based method [70, 71]. It requires the objective function value and its gradient with respect to material properties. Computing the gradient in a straightforward manner is computationally cost prohibitive, thus, we adopt the adjoint method to address this issue similarly to [48, 76]. We will develop the adjoint equations for the inverse problem in the frequency domain in detail in the next section. Once the objective function and its gradient are evaluated for the current estimate of moduli distribution, the limited BFGS method provides an updated moduli distribution, and the entire process is repeated until the objective function value does not drop significantly.

9.1.3 The adjoint method

The storage and loss modulus are defined as nodal unknowns in the finite element mesh and interpolated throughout the problem domain with linear finite element shape functions. The gradient of the objective function will be evaluated at each node with respect to the nodal moduli β_{jm} where the index *j* represents the loss or storage modulus and *m* the global node number, yielding

$$\frac{\partial F}{\partial \beta_{jm}} = \sum_{i=1}^{n} \left\langle \mathbf{D}(\mathbf{U}^i - \mathbf{U}^i_{meas}), \mathbf{D}\frac{\partial \mathbf{U}^i}{\partial \beta_{jm}} \right\rangle + \frac{1}{2}\sum_{j=1}^{2} \alpha_j \frac{\partial \mathrm{Reg}\left(\beta_{jm}\right)}{\partial \beta_{jm}} \tag{9.7}$$

where n denotes the total number of nodes in the finite element mesh. $\langle u\ , v \rangle$ is an inner product operator defined by $\int u \cdot v \mathrm{d}\Omega$. The expression $\partial \mathbf{U}^i / \partial \beta_{jm}$ in **Equation (9.7)** will be determined from **Equation (9.4)** by differentiation with respect to β_{jm} leading to

$$\frac{\partial \mathbf{U}^i}{\partial \beta_{jm}} = -\left(\mathbf{K} - w^2\mathbf{M}\right)^{-1} \frac{\partial \mathbf{K}}{\partial \beta_{jm}} \mathbf{U}^i \tag{9.8}$$

Substituting **Equation (9.8)** into **Equation (9.7)** yields

$$\frac{\partial F}{\partial \beta_{jm}} = \sum_{i=1}^{n} \left\langle \mathbf{D}(\mathbf{U}^i - \mathbf{U}^i_{meas}), -\mathbf{D}\left(\mathbf{K} - \omega^2\mathbf{M}\right)^{-1} \frac{\partial \mathbf{K}}{\partial \beta_{jm}} \mathbf{U}^i \right\rangle + \frac{1}{2}\sum_{j=1}^{2} \alpha_j \frac{\partial \mathrm{Reg}\left(\beta_{jm}\right)}{\partial \beta_{jm}} \tag{9.9}$$

Equation (9.9) can be used to evaluate the gradient, however, it is computationally a costly process as it requires the solution of **Equation (9.8)** for each node and each material property. This implies that the inverse problem requires solving ($2 \times N + 1$) forward problems at each minimization iteration, where N denotes the total number of nodes. Further, this includes one forward problem to calculate the computed displacement and

the factor 2 for the two moduli, namely the storage and loss modulus. An Alternative way to evaluate the nodal gradient of the objective function is to utilize the adjoint method. To this end, we rewrite **Equation (9.9)** by

$$\frac{\partial F}{\partial \beta_{jm}} = \sum_{i=1}^{n} \left\langle -\left(\mathbf{K} - \omega^2 \mathbf{M}\right)^{-\mathrm{T}} \mathbf{D}^T \mathbf{D}\left(\mathbf{U}^i - \mathbf{U}^i_{meas}\right), \frac{\partial \mathbf{K}}{\partial \beta_{jm}} \mathbf{U}^i \right\rangle + \frac{1}{2} \sum_{j=1}^{2} \alpha_j \frac{\partial \mathrm{Reg}\left(\beta_{jm}\right)}{\partial \beta_{jm}} \quad (9.10)$$

and define another forward problem given by:

$$\left(\mathbf{K} - \omega^2 \mathbf{M}\right)^{\mathrm{T}} \mathbf{W} = -\mathbf{D}^T \mathbf{D}\left(\mathbf{U}^i - \mathbf{U}^i_{meas}\right) \quad (9.11)$$

After evaluating $\mathbf{w}$ by solving Equation **(9.11)**, we can compute the gradient of the objective function with respect to nodal moduli via

$$\frac{\partial F}{\partial \beta_{jm}} = \sum_{i=1}^{n} \left\langle \mathbf{W}, \frac{\partial \mathbf{K}}{\partial \beta_{jm}} \mathbf{U}^i \right\rangle + \frac{1}{2} \sum_{j=1}^{2} \alpha_j \frac{\partial \mathrm{Reg}\left(\beta_{jm}\right)}{\partial \beta_{jm}} \quad (9.12)$$

We note that this strategy requires the solution of two forward problems at each minimization iteration, thus reduces computational time drastically. Finally, we observe that for the particular problem in this chapter, the linear operator $\left(\mathbf{K} - \omega^2 \mathbf{M}\right)$ is self-adjoint.

To test the performance of these inverse algorithms, we simulate experimental datasets using finite element methods. More precisely, we will firstly solve a forward problem with a target/defined storage and loss modulus distribution to obtain the displacement field. We will then add 3% white Gaussian random noise to the complex valued displacement amplitude to mimic experimental data. Next, noisy displacement fields will be used to solve the inverse problem for the storage and loss modulus

distribution. Finally, the reconstructed material distribution will be compared with the target distribution to assess performance.

9.2 Numerical results

In this section, several experiments will be simulated with the algorithms discussed in the previous section and the inverse procedure tested for robustness. To this end, the problem domain in **Figure 9-1** (a) and (b) is defined with a circular inclusion embedded in a 1cm×1cm square background to represent a composite material. The storage modulus in the inclusion and background are 500 Pa and 100 Pa, respectively. The loss tangent $\tan\delta = 0.1$ and 0.08 are for the background and inclusion, respectively. This indicates that the solid represents a low damping material. We apply 1% cosinusoidal shear on the top surface, and fix the bottom edge as shown in **Figure 9-1**. The other two sides are traction free. We discretize the problem domain with 3600 bilinear finite elements and solve the forward problem at three driving frequencies of 20Hz, 150Hz, and 300Hz. As mentioned in the previous section, 3% white Gaussian noise is added to the displacement field. **Figure 9-2** (a), (c), and (e) represent the reconstructed storage modulus distribution at driving frequencies of 20 Hz, 150 Hz and 300 Hz, respectively. **Figure 9-2** (b), (d), and (f) represent the corresponding reconstructed loss modulus distributions. The regularization factor is selected as shown in **Table 9-1**.

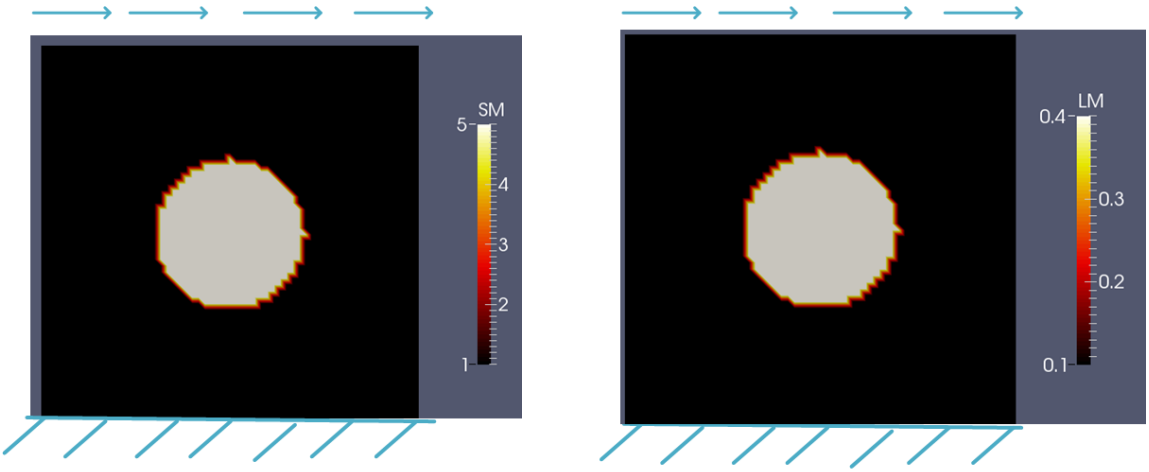

(a) (b)

Figure 9-1: Problem domain for a simulated tissue (a) the target storage modulus distribution; (b) the target loss modulus distribution (unit: 100 Pa).

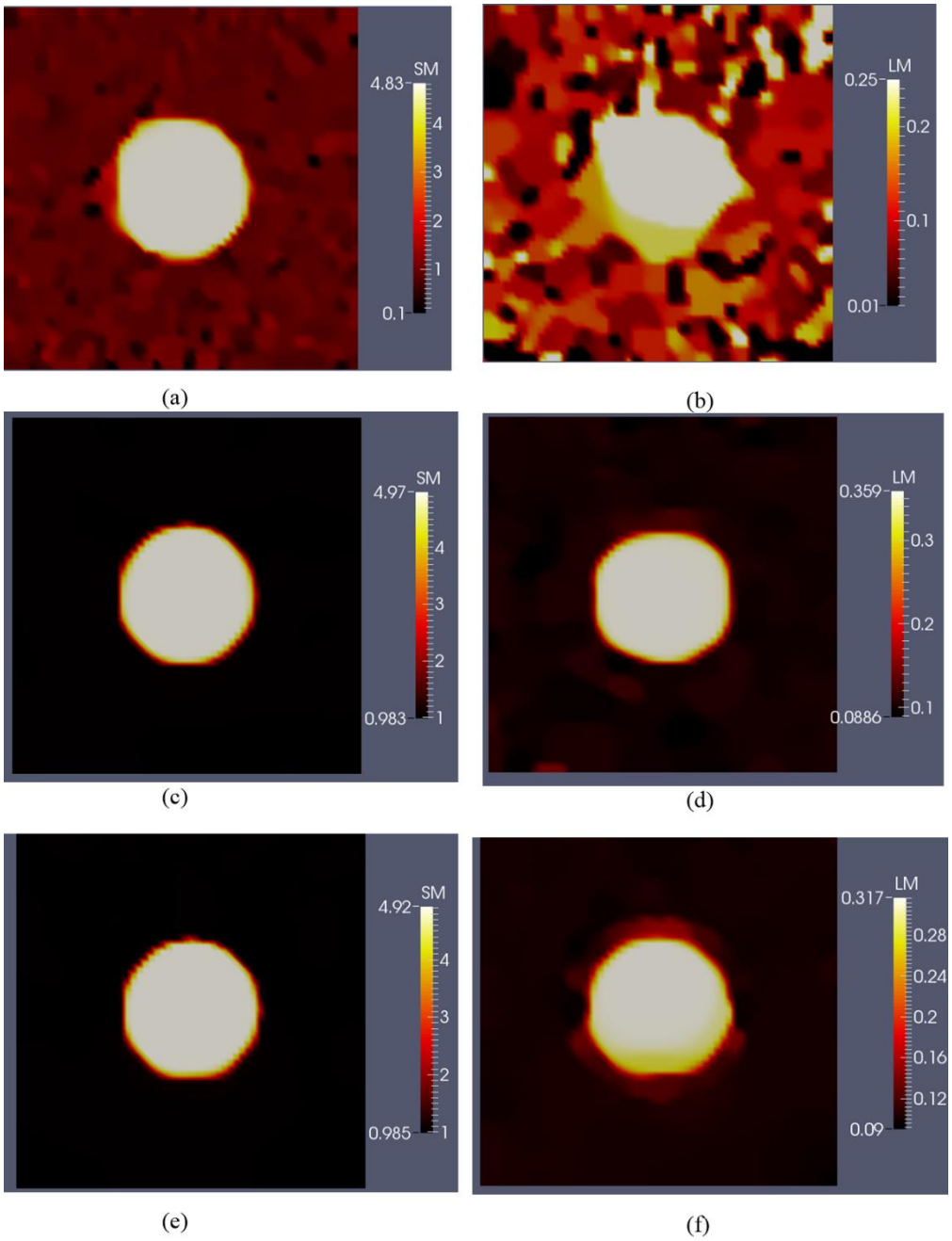

Figure 9-2: Reconstructed viscoelastic modulus distribution for the problem domain in **Figure 9-1**. (a) Reconstructed storage modulus distribution when the driving frequency is 20Hz; (b) reconstructed loss modulus distribution when the driving frequency is 20Hz; (c) reconstructed storage modulus distribution when the driving frequency is 150Hz; (d) reconstructed loss modulus distribution when the driving frequency is 150Hz; (e) reconstructed storage modulus distribution when the driving frequency is 300Hz; (f)

reconstructed loss modulus distribution when the driving frequency is 300Hz (unit: 100 Pa).

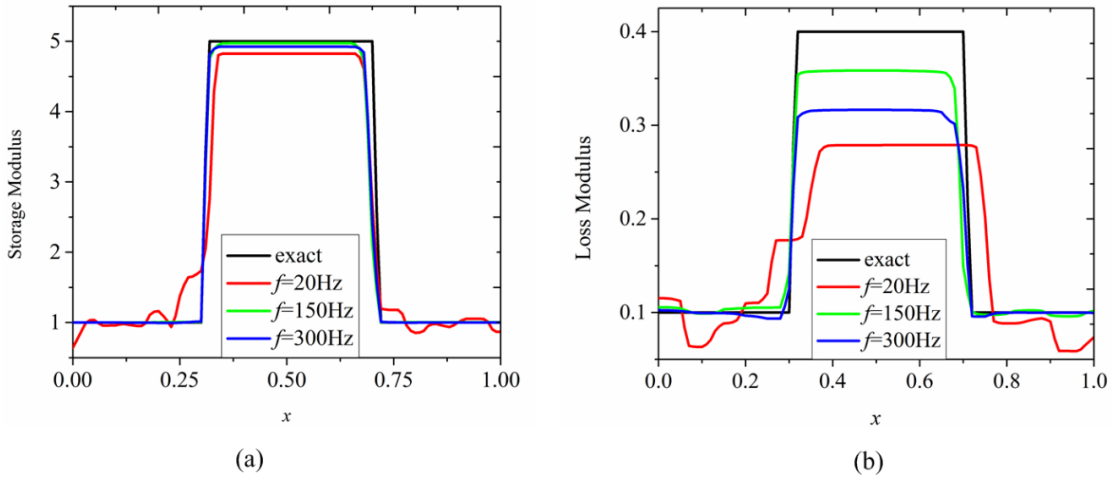

Figure 9-3: Horizontal centerline plot from left to right for the exact and reconstructed modulus distribution for (a) the storage modulus plot ; (b) the loss modulus plot (unit: 100 Pa).

Table 9-1: Regularization factors used for the reconstructions in **Figure 9-2**.

	f=20Hz	f=150Hz	f=300Hz
α for storage modulus	1.0e-9	8.0e-9	8.0e-9
α for loss modulus	1.0e-9	5.0e-9	7.0e-9

Comparing the target storage and loss modulus distribution from **Figure 9-1** with the reconstructions in **Figure 9-2**, it is observed that the reconstructed storage modulus distribution is of superior quality than the reconstructed loss modulus. The reconstructed storage modulus value in the inclusion is very close to the target at higher frequencies of

150 Hz and 300 Hz and background oscillations diminish as shown in the horizontal centerline plot in **Figure 9-3** (a). The loss modulus is recovered well at higher frequencies of 150 Hz and 300 Hz, but yields poor reconstructions at 20 Hz (see **Figure 9-2** (b)). This will be thoroughly discussed in the next section.

Next, we consider a problem domain with a higher loss angle, shown in **Figure 9-4** (a) and (b). In this case, the target loss tangent of the background and inclusion are 0.5 and 0.4, respectively. In addition, the storage distribution is the same as the previous case. **Figure 9-5** and **Figure 9-6** are the reconstruction results for the moduli distribution and the corresponding horizontal centerline plot of the moduli from the left to right, respectively. The reconstructed storage modulus distribution in **Figure 9-5** (a), (c), and (e) remain to be of high quality and the loss modulus for the frequency of 20 Hz improves significantly compared to the previous case with lower loss angle. In addition, for the highest frequency of 300Hz, the reconstructed storage and loss modulus in **Figure 9-5** (f) becomes worse when comparing to the case of lower loss angle. The loss modulus distribution worsens drastically, in particular, the size of its inclusion becomes significantly smaller than the target. In **Figure 9-7** we place the inclusions for the storage and loss modulus from **Figure 9-4** upwards. We observe that both, the storage and loss modulus reconstructions in **Figure 9-8** (a) and (b), respectively, improve dramatically, and the inclusion size of the loss modulus reaches the target inclusion size as shown in **Figure 9-8** (b). In this case, the regularization factors for the storage modulus and the loss modulus are 5.0e-11 and 7.0e-11, respectively.

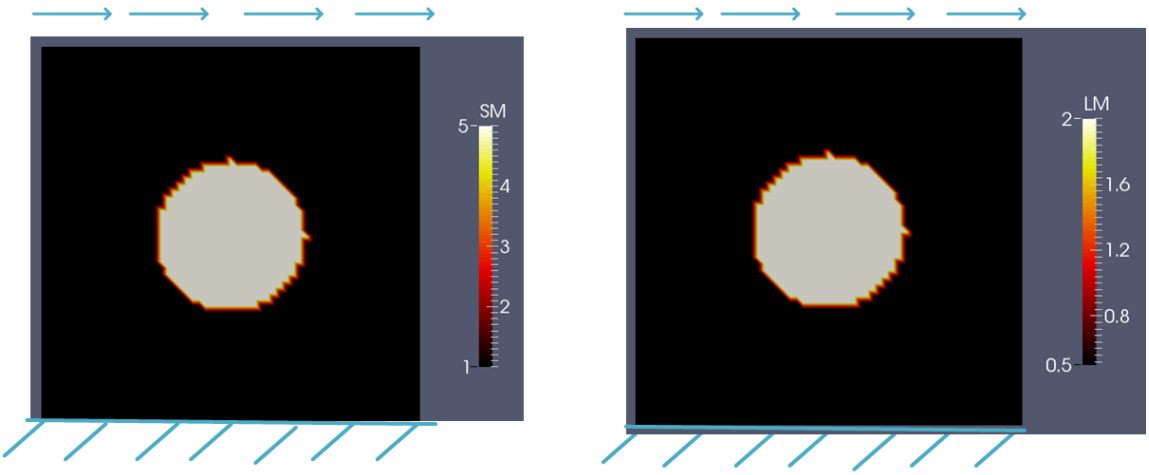

(a) (b)

Figure 9-4: Problem domain for a simulated tissue with a higher loss angle (a) the target storage modulus distribution; (b) the target loss modulus distribution (unit: 100 Pa).

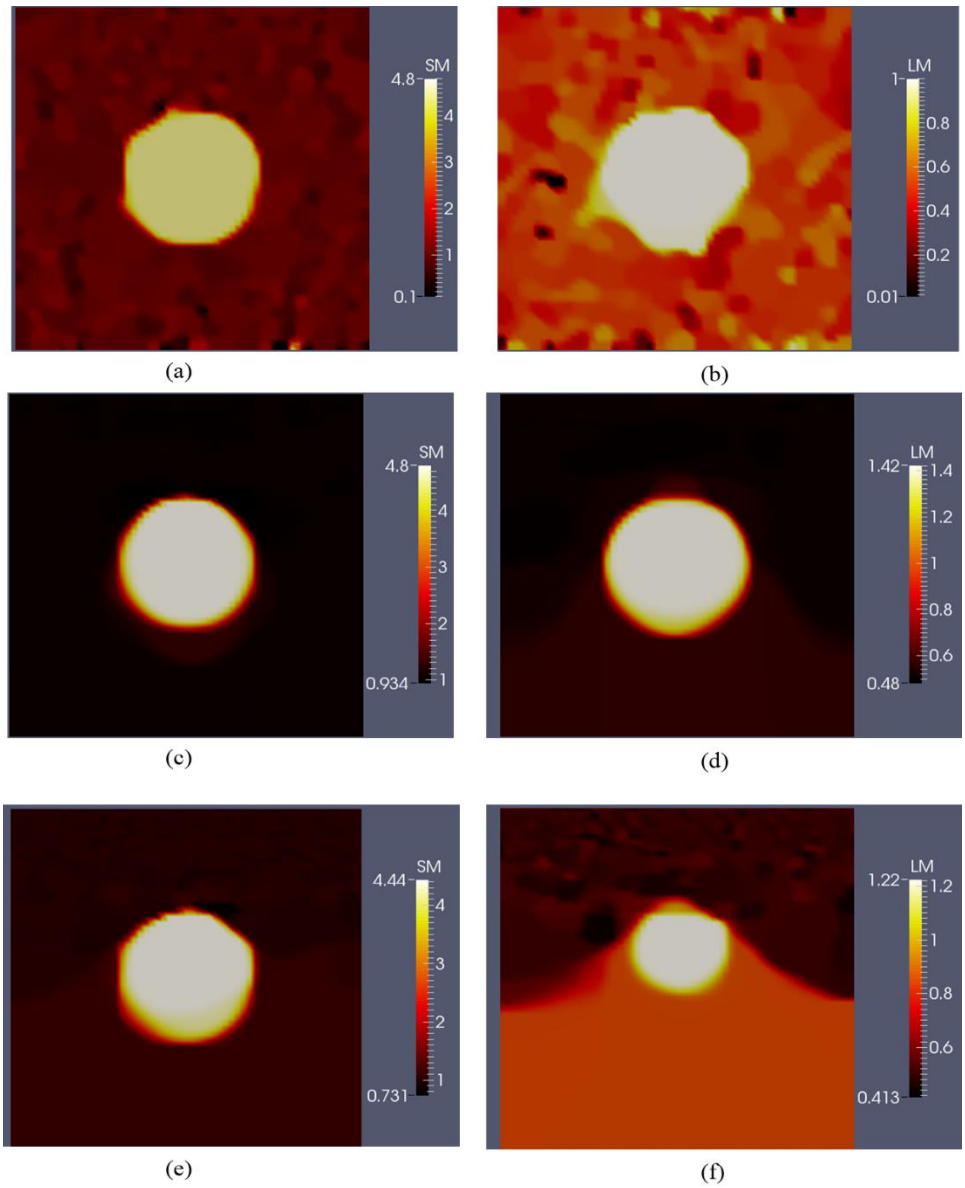

Figure 9-5: Reconstructed viscoelastic modulus distribution for the problem domain given in **Figure 9-4**. (a) Reconstructed storage modulus distribution for a driving frequency of 20Hz; (b) reconstructed loss modulus distribution for a driving frequency of 20Hz; (c) reconstructed storage modulus distribution for a driving frequency of 150Hz; (d) reconstructed loss modulus distribution for a driving frequency of 150 Hz; (e) reconstructed storage modulus distribution for a driving frequency of 300 Hz; (f) reconstructed loss modulus distribution for a driving frequency of 300Hz (unit: 100 Pa).

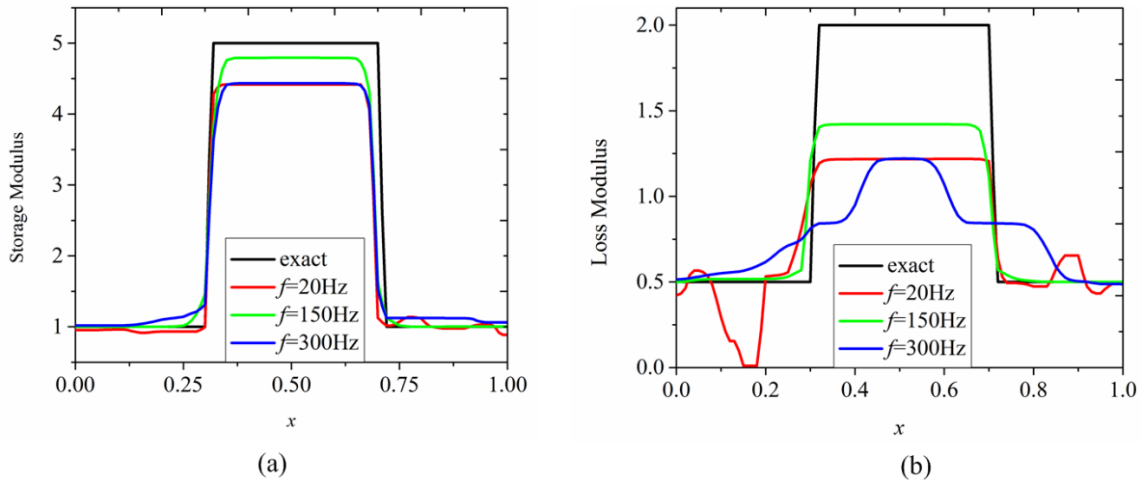

(a) (b)

Figure 9-6: Horizontal centerline plot from left to right for the exact and reconstructed modulus distribution in the case of higher loss angle for (a) the storage modulus plot ; (b) the loss modulus plot(unit: 100 Pa).

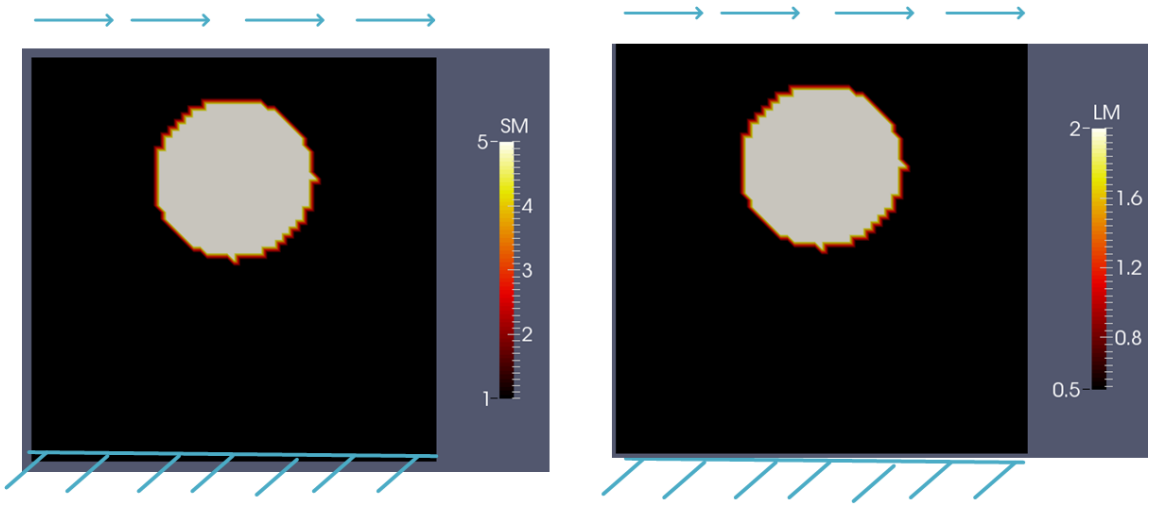

(a) (b)

Figure 9-7: Problem domain for a higher loss angle (a) target storage modulus distribution; (b) target loss modulus distribution. In this case, the location of the inclusion is shifted upwards closer to the excitation source.

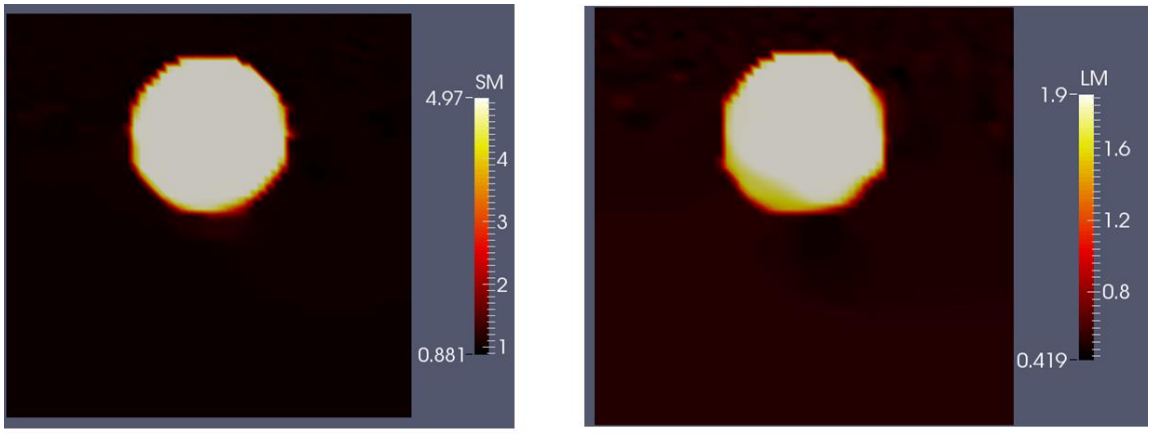

(a) (b)

Figure 9-8: Reconstructed viscoelastic modulus distribution for the problem domain where the inclusion is placed upwards. (a) Reconstructed storage modulus distribution when the driving frequency is 300 Hz; (b) reconstructed loss modulus distribution when the driving frequency is 300 Hz (unit: 100 Pa).

Table 9-2: Regularization factors used in **Figure 9-5**.

	f=20Hz	f=150Hz	f=300Hz
α for storage modulus	2.0e-10	5.0e-10	5.0e-11
α for loss modulus	3.0e-10	1.0e-9	7.0e-11

9.3 Discussions

In this chapter, a novel inverse algorithm has been utilized to reconstruct the storage and loss modulus distribution for a viscoelastic material behavior. We have tested the feasibility of this inverse scheme by several numerical examples presented in **Section 9.2**. We observed that for a composite material with a lower target loss angle given in **Figure 9-1** (a) and (b), the loss modulus reconstructions improve by increasing the driving

frequency shown in **Figure 9-2** (d) and (f). For a problem with a higher target loss angle (see **Figure 9-4** (a) and (b)), the loss modulus reconstruction improves for the case with 20Hz driving frequency as shown in **Figure 9-5** (b). However, increasing the frequency results in poor loss modulus reconstructions as shown in **Figure 9-5** (f). As for the storage modulus, we observe that all reconstructions are mapped with high accuracy regardless of the driving frequencies being utilized. The best result is obtained when the driving frequency is chosen to be 150 Hz, and the reconstructed solution closely resembles the target distribution. It is also worth mentioning that for this case the background is smooth and does not reveal any oscillations.

Another important observation is that the wavelength with 20 Hz driving frequency is estimated as 1.6 cm, which is much larger than the size of the tumor. In clinical medicine, Some techniques are based on the wavelength, thus if the wavelength is larger than the inclusion size, the inclusion may not be well resolved and may be undetectable [133, 134]. The method presented in this paper is robust and allows to characterize inclusions that are smaller than the wavelength is very large.

To understand the factors and how they relate to the poorly recovered loss moduli, we focus on a semi-infinite one-dimensional vibrating string that can be described by:

$$\rho\omega^2 u = \mu^* \frac{\partial^2 u}{\partial x^2} \tag{9.13}$$

We impose the boundary condition $u(x=0) = u_o$. When the loss angle is small, **Equation (9.13)** can be solved for the complex displacement as detailed in [135, 136] and is given here by

$$u(x) = u_o e^{i\omega x/c} e^{-x\frac{\omega}{2c}\tan\delta} \tag{9.14}$$

Where $c = \sqrt{\mu_r / \rho}$ is the shear wave speed. The first exponential in **Equation (9.14)** determines how the wave propagates without attenuation. The second exponential term is the attenuation term and controls how the amplitude decreases due to viscous effects. This solution qualitatively reveals that both the wave propagation term and the attenuation term are dependent on the storage modulus, while the loss modulus appears only in the attenuation term. Thus, the attenuation provides the information to map the loss modulus. Inspecting the attenuation term, it can be clearly seen that the quality of the loss modulus reconstruction is highly influenced by the driving frequency. For a fixed wave speed, if the frequency is very small or large, the attenuation term will be close to 1 or 0, respectively. For these two scenarios, the resulting displacement will not vary significantly for a wide range of loss moduli, e.g., choosing two different loss moduli that are substantially different will lead to a small difference in their respective displacements. Thus, it is highly challenging to map the loss modulus in the presence of noise in the displacements. Therefore, the quality of reconstructing the loss modulus distribution is highly correlated with the driving frequency. To reconstruct the loss modulus distribution well, the frequency may neither be chosen to be too high nor too low. Compared with the two-dimensional continuum model, the one-dimensional semi-infinite model neglects the influence of the reflective wave. Analyzing this model, though simplified, helps to better understand why the driving frequency affects the final reconstruction qualitatively.

To take into account possible wave reflections, a finite one-dimensional vibrating string with a length of L will be analyzed in the following. We assume that the string is linearly viscoelastic, and the boundary conditions are given by $u(x=0)=0$ and $u(x=L)=u_o$. The corresponding solution to this problem is given by:

$$u(x)=u_o\frac{\sin k^* x}{\sin k^* L}=u_o\frac{-e^{k_i(L-x)}e^{ik_r x}-e^{-k_i(L+x)}e^{-ik_r x}}{e^{ik_r L}-e^{-2k_i L}e^{-ik_r L}} \tag{9.15}$$

Where $k^*=k_r-ik_i$ is the complex wavenumber. $k_r=\omega/c$, and $k_i=\omega\tan\delta/2c$ assuming that the loss angle is relatively small. It is not easy to interpret **Equation (9.15)**, hence, we plot the displacement for varying loss moduli values over the finite one-dimensional domain. To this end, we specify the length of the string $\mathrm{L}=1$, the amplitude $u_o=1$. The range of loss moduli is selected to represent similar values as being used for the two-dimensional continuum model. **Figure 9-9** (a) and (b) represent the real part and the imaginary part of the complex-valued displacement with respect to different loss modulus values of 0.1, 0.2, 0.3 and 0.4 for the driving frequency at 20 Hz, respectively and the storage modulus is set to 5.0. All four curves (each curve for a different loss modulus) nearly coincide with respect to the real part of the complex displacement (see **Figure 9-9** (a)). Though varying the loss modulus leads to significant differences in the imaginary displacement response as shown in **Figure 9-9** (b), they are overall quite small compared to the real part of the complex displacement. As such, its contribution to the objective function will be small as well. Consequently, the loss modulus distribution is reconstructed poorly as shown in **Figure 9-2** (b) for noisy data.

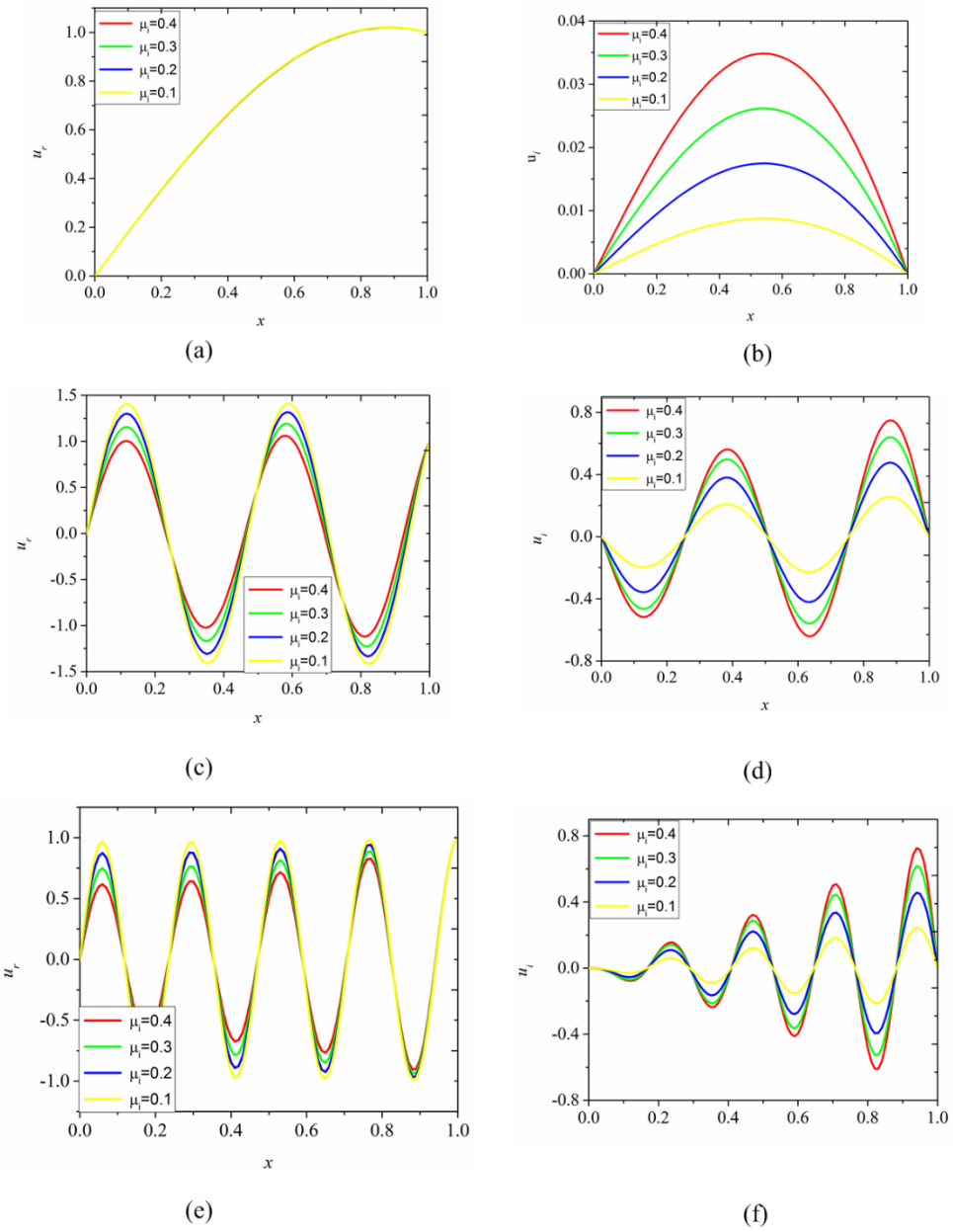

Figure 9-9: Variation of displacement field along an one-dimensional vibrating string subjected to harmonic motion when the loss modulus is set to 0.1, 0.2, 0.3, 0.4.(a) Real part of the complex-valued displacement field when the driving frequency is 20 Hz; (b) imaginary part of the complex-valued displacement field when the driving frequency is 20 Hz; (c) real part of the complex-valued displacement field when the driving frequency is 150 Hz; (d) imaginary part of the complex-valued displacement field when the driving frequency is 150 Hz; (e) real part of the complex-valued displacement field when the driving frequency is 300 Hz; (f) imaginary part of the complex-valued displacement field when the driving frequency is 300 Hz.

In **Figure 9-9** (c) and (d) we plot the real and imaginary displacement for a driving frequency of 150 Hz, respectively, and observe that they vary significantly with varying loss moduli. Similar observations are made for a driving frequency of 300 Hz (see **Figure 9-9** (e) and (f)). Consequently, the solution to the inverse problem will not be too sensitive to noise as it was demonstrated in the two-dimensional loss modulus reconstructions in **Figure 9-2** (d) and (f).

Increasing the loss angle by keeping the storage modulus to be same and increasing the loss modulus for the two-dimensional problem will yield a slightly improved reconstruction as shown in **Figure 9-5** (b). This can be explained by **Equation (9.15)** as well. To this end, we plot the real part and imaginary part of the complex-valued displacement for different loss moduli of 0.5, 1.0, 1.5, and 2 in **Figure 9-10** (a) and (b), respectively. For a driving frequency of 20 Hz the difference in the displacements becomes more pronounced as compared to the lower loss angle utilized in **Figure 9-9** (a) and (b). Further, the imaginary part of the complex-valued displacement for each loss modulus value is a few factors larger than for the smaller loss angle. As a result, the inclusion shape improves in the reconstructed loss modulus distribution as shown in **Figure 9-5** (b). For a higher frequency of 300 Hz, we also plot each displacement when the loss modulus is set to 0.5, 1.0, 1.5 and 2.0, respectively as shown in **Figure 9-10** (e) and (f). When the loss modulus is selected to be large (in the case of loss modulus being 2.0), it can be clearly seen that the displacement attenuates quickly to zero. Hence, if the inclusion is further down of the excitation source (see problem domain in **Figure 9-5**), it cannot be well recovered. More precisely, noise will dominate attenuated small displacement values. On

the contrary, if the location of the tumor is close to the location of excitation as shown in **Figure 9-7**, the reconstruction will be less influenced by the noise as the displacement in that region is much larger than anywhere else. Thus, the inclusion can be recovered well for this case as shown in **Figure 9-8**. Revisiting the result in **Figure 9-8** (b), the reconstructed loss modulus distribution and with that the inclusion shape improves significantly when the target inclusion is placed upwards closer to the excitation source.

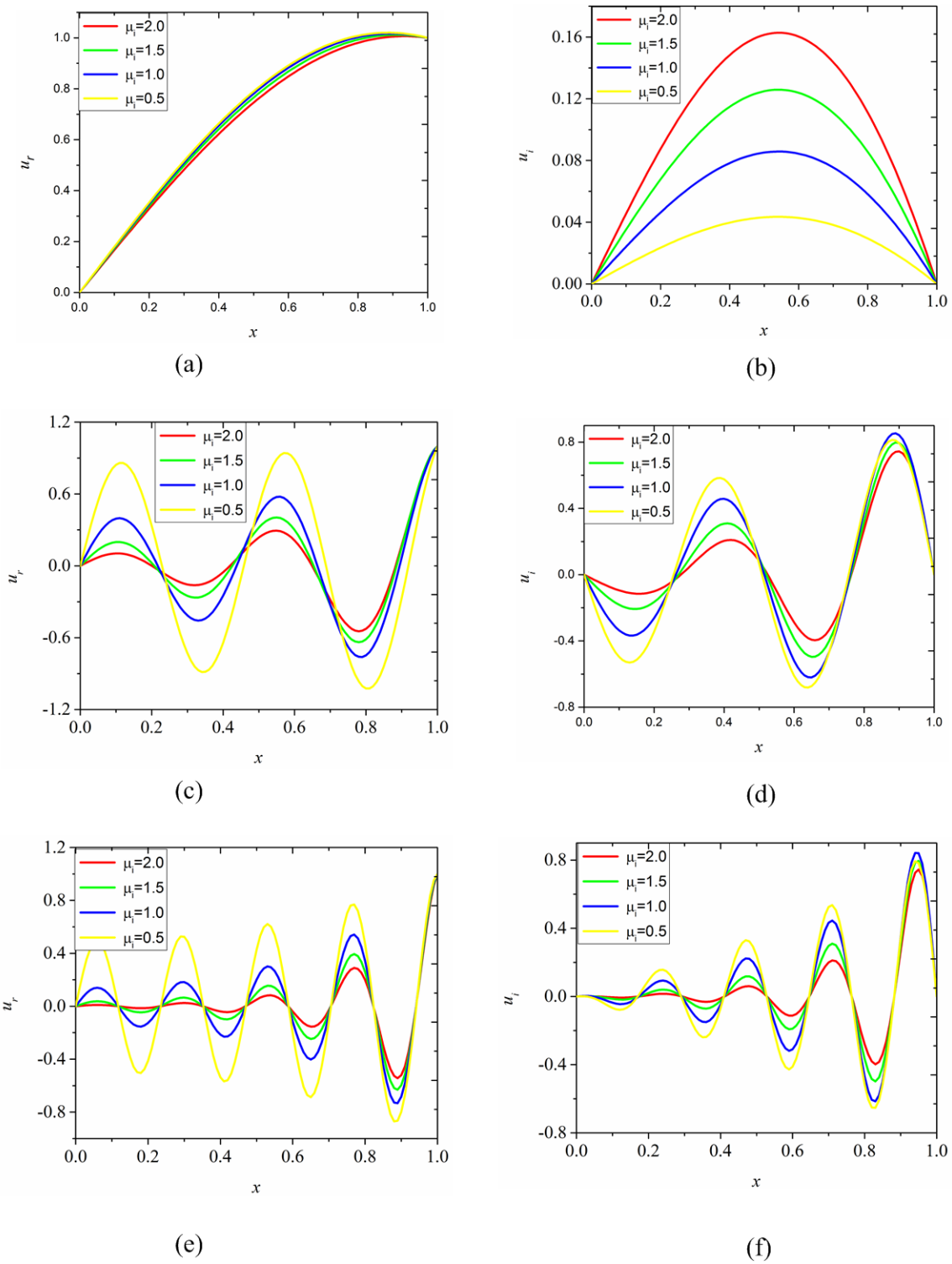

Figure 9-10: Variation of displacement field along an one-dimensional vibrating string subjected to harmonic motion when the loss modulus is set to 0.5, 1.0, 1.5, 2.0.(a) Real part of the complex-valued displacement field when the driving frequency is 20 Hz ; (b)

the imaginary part of the complex-valued displacement field when the driving frequency is 20 Hz; (c) real part of the complex-valued displacement field when the driving frequency is 150 Hz; (d) imaginary part of the complex-valued displacement field when the driving frequency is 150 Hz; (e) real part of the complex-valued displacement field when the driving frequency is 300 Hz; (f) imaginary part of the complex-valued displacement field when the driving frequency is 300 Hz.

9.4 Conclusions

In this chapter, we have tested the feasibility to solve the inverse problem for the viscoelastic moduli distribution utilizing simulated experiments. Full-field displacement data was assumed to be of time harmonic nature and assumed to be known, e.g., from imaging modalities. We have tested several numerical cases with different target viscoelastic modulus distributions and different driving frequencies. In most cases, the inverse algorithm works well despite high white Gaussian noise levels of 3% in the displacement. The storage modulus appears to be more robust than the loss modulus reconstruction. We discussed the factors that influence the quality of the loss modulus reconstruction and recovering inclusion shape. These depend on the frequency, location of the inclusion, and the loss angle. To investigate the influence of these factors analytically, we analyzed a one-dimensional vibrating string and correlated the findings to the observations of the two-dimensional reconstructions. The study in this chapter may be useful in choosing an optimal location to excite the domain and the range of frequencies used. Finally, it is noted that an accurate reconstruction of the storage and loss modulus at various frequencies is essential to relate them to the actual viscoelastic material properties of a given viscoelastic model.

10. CONCLUSIONS AND FUTURE WORK

In this dissertation, we have proposed and implemented several new features into the inverse algorithms developed in [62]. First of all, a new feature that the material property is defined constantly in each element is introduced, and the corresponding regularization term has been modified based on the Rankine–Hugoniot jump conditions. The new feature has been tested well by the simulated data. Secondly, instead of utilizing the conventional L2 norm displacement correlation term, we modify the objective function by using a spatially weighted displacement correlation term, This new formulation of the objective function is capable of reducing the boundary sensitivity of the final solution in the inverse problem. We have then proposed a novel approach to map the non-homogeneous linear elastic property distribution nondestructively by only minimizing the boundary deformation. The proof of concept of this novel method has been shown by numerical experiments. This method has potential application in non-invasive breast tumor detection with lower medical costs and high accuracy. Then, we have also presented a method that quantitatively determines the material property distribution using full-field displacement fields, zero traction boundary conditions, and partially known material properties on the boundary. We compared the performance of two regularization types and observed that TCD regularization yields well-recovered absolute elastic modulus reconstructions. Furthermore, we studied the feasibility of linear elastic approximation in solving the inverse problem in nonlinear elasticity. We found that the recovered stiffness contrast using the linear solver is overestimated, and the overestimation becomes more

significant with a larger applied deformation and higher target stiffness contrast. In addition, we extended our existing algorithms to estimate the nonhomogeneous orthotropic linear elastic property distributions of soft solids. This new feature is highly sensitive to noise in that with the high noise level, e.g., 3% noise, the anisotropic parameter distributions were poorly mapped. Finally, we have implemented a new scheme to characterize the linear viscoelastic material properties of soft tissues subjected to harmonic motion. The storage moduli are mapped well in all the numerical cases, while the reconstructed loss moduli are sensitive to the driving frequency.

The inverse algorithms in this work have been successfully analyzed and tested by simulated and phantom datasets, yet considerable efforts should still be devoted into in this area:

(1) In **Chapter 3,** we have utilized a spatially weighted displacement correlation term in the objective function. The modified objective function outperforms the prevalent displacement matching term in the L2 norm for the limited numerical cases presented in this work. However, a more general objective function should be proposed to taking account of other factors, e.g., the size of the inclusions.

(2) In **Chapter 4**, we presented a novel approach to map the nonhomogeneous elastic property distribution using only boundary displacement datasets qualitatively. In the next chapter, we further improve this approach by using the force indentation measurements to quantify the material properties. Though the presented methodology was tested well by numerical examples and the high accuracy of a digital camera correlation system to measure boundary displacements has been

verified by a simple experiment for a stiff solid, the accuracy of boundary displacement measurements of soft solids and solving inverse problem using the measured boundary datasets from experiments require further investigation for clinical application.

(3) Our inverse algorithms are now capable of mapping heterogeneous orthotropic linear elastic parameter distributions in two-dimensional space. To enhance the capability of the current algorithms in clinical practice, we should extend and generalize the current feature to 3-D space. Besides, as a large number of parameters in the anisotropic elastic constitutive law, ensuring a unique solution of the inverse problem is challenging. In particular, we solve for all the parameters in the constitutive law simultaneously in the inverse problem, which might easily induce the uniqueness issue. Therefore, we should propose methods to map each material parameter separately, and this sequential method is probably helpful to address the issue that the recovered orthotropic linear elastic parameter distributions are highly sensitive to noise.

(4) A variety of tissue types like brain tissue are very soft and viscous. Thus, the linear viscoelastic constitutive law is incapable of properly modeling the elastic behavior of those soft tissues. Thus, the nonlinear nature of the soft solids should be taken into account to accurately map the viscoelastic behavior of soft tissues.

(5) The ultimate goal of this work is to provide an effective and accurate technique to estimate the modulus distribution of soft tissues non-invasively in clinical practice. In clinical practice, however, we will face more challenges. For instance, how do

we accurately delineate the boundary of a tissue domain from clinical images; what kind of boundary conditions should we prescribe in solving the inverse problem using imaging data. Thus, the clinical feasibility of using the inverse algorithms to characterize the heterogeneous material property distribution requires more effort.

REFERENCES

[1] R. Budynas, K. Nisbett, Shigley's mechanical engineering design 9th Edition, McGraw-Hill Science/Engineering/Math, New York, 2012.

[2] A.D. Freed, Soft solids, Springer Science & Business Media, New York, 2014.

[3] K.Y. McCullough, N.A. Fleck, M.F. Ashby, Uniaxial stress–strain behaviour of aluminium alloy foams, Acta Materialia, 47 (1999) 2323-2330.

[4] T. Tsui, W. Oliver, G. Pharr, Influences of stress on the measurement of mechanical properties using nanoindentation: Part I. Experimental studies in an aluminum alloy, Journal of Materials Research, 11 (1996) 752-759.

[5] M. Attard, S. Setunge, Stress-strain relationship of confined and unconfined concrete, Materials Journal, 93 (1996) 432-442.

[6] N.S. Ottosen, Constitutive model for short-time loading of concrete, Journal of the Engineering Mechanics Division ASCE, 105 (1979) 127-141.

[7] M. Kiser, M. He, F. Zok, The mechanical response of ceramic microballoon reinforced aluminum matrix composites under compressive loading, Acta Materialia, 47 (1999) 2685-2694.

[8] M.G. Wertheim, MÉmoire sur 1'BlasticitB et la cohesion des principaux tissues du corps humain, Annales de Chimie et de Physique, 21 (1847) 385-414.

[9] E. Trowbridge, M. Black, C. Daniel, The mechanical response of glutaraldehyde-fixed bovine pericardium to uniaxial load, Journal of Materials Science, 20 (1985) 114-140.

[10] Y. Fung, Elasticity of soft tissues in simple elongation, American Journal of Physiology--Legacy Content, 213 (1967) 1532-1544.

[11] A.E. Cronkite, the tensile strength of human tendons, The Anatomical Record, 64 (1936) 173-186.

[12] J. Hildebrandt, H. Fukaya, C. Martin, Simple uniaxial and uniform biaxial deformation of nearly isotropic incompressible tissues, Biophysical journal, 9 (1969) 781-791.

[13] J.D. Humphrey, Review Paper: Continuum biomechanics of soft biological tissues, Proceedings of the Royal Society of London A: Mathematical, Physical and Engineering Sciences, The Royal Society, 2003, pp. 3-46.

[14] J. Martins, E. Pires, R. Salvado, P. Dinis, A numerical model of passive and active behavior of skeletal muscles, Computer Methods in Applied Mechanics and Engineering, 151 (1998) 419-433.

[15] D.R. Veronda, R.A. Westmann, Mechanical characterization of skin - Finite deformations, Journal of Biomechanics, 3 (1970) 111-124.

[16] Y.-C. Fung, Stress-strain-history relations of soft tissues in simple elongation, Biomechanics: Its Foundations and Objectives, 7 (1972) 181-208.

[17] S. Woo, K. Rajagopal, A single integral finite strain viscoelastic model of ligaments and tendons, Journal of Biomechanical Engineering, 118 (1996) 221.

[18] Y. Lanir, Y. Fung, Two-dimensional mechanical properties of rabbit skin—I. Experimental system, Journal of Biomechanics, 7 (1974) 29-34.

[19] Y. Lanir, Y. Fung, Two-dimensional mechanical properties of rabbit skin—II. Experimental results, Journal of Biomechanics, 7 (1974) 171IN9175-174182.

[20] A.W. Wan, Biaxial tension test of human skin in vivo, Biomedical Materials and Engineering, 4 (1993) 473-486.

[21] M.S. Sacks, A method for planar biaxial mechanical testing that includes in-plane shear, Journal of Biomechanical Engineering, 121 (1999) 551-555.

[22] K.L. Billiar, M.S. Sacks, Biaxial mechanical properties of the native and glutaraldehyde-treated aortic valve cusp: part II—a structural constitutive model, Journal of Biomechanical Engineering, 122 (2000) 327-335.

[23] K.L. Billiar, M.S. Sacks, Biaxial mechanical properties of the natural and glutaraldehyde treated aortic valve cusp—part I: experimental results, Journal of Biomechanical Engineering, 122 (2000) 23-30.

[24] A.D. Freed, D.R. Einstein, M.S. Sacks, Hypoelastic soft tissues, Acta Mechanica, 213 (2010) 205-222.

[25] J. Xie, J. Zhou, Y. Fung, Bending of blood vessel wall: stress-strain laws of the intima-media and adventitial layers, Transactions-American Society of Mechanical Engineering Journal of Biomechanical Engineering, 117 (1995) 136-136.

[26] M. Harman, X. Nguyen, E. Sirois, W. Sun, Three-point bending device for flexure testing of soft tissues, Bioengineering Conference, 2009 IEEE 35th Annual Northeast, IEEE, 2009, pp. 1-2.

[27] K.L. Johnson, Contact mechanics, Cambridge University Press, Cambridge, 1987.

[28] H. Schade, Untersuchungen zur organfunction des bindegewebes, Zeitschrift für die experimentelle Pathologie und Therapie, 11 (1912) 369-399.

[29] H. Lewis, J. Mayer, A. Pandiscio, Recording skinfold calipers for the determination of subcutaneous edema, the Journal of Laboratory and Clinical Medicine, 66 (1965) 154-160.

[30] A.A. Fischer, Clinical use of tissue compliance meter for documentation of soft tissue pathology, the Clinical journal of pain, 3 (1987) 23-30.

[31] A. Fischer, Tissue compliance meter for objective, quantitative documentation of soft tissue consistency and pathology, Archives of Physical Medicine and Rehabilitation, 68 (1987) 122-125.

[32] J.S. Jurvelin, T. Räsänen, P. Kolmonens, T. Lyyra, Comparison of optical, needle probe and ultrasonic techniques for the measurement of articular cartilage thickness, Journal of Biomechanics, 28 (1995) 231-235.

[33] G. Kalei, Some results of microhardness test using the depth of impression, Mashinovedenie, 4 (1968) 105-107.

[34] H.J. Gao, C.H. Chiu, J. LEE, Elastic contact versus indentation modeling of multi-layered materials, International Journal of Solids and Structures, 29 (1992) 2471-2492.

[35] H. Ban, P. Karki, Y.-R. Kim, Nanoindentation test integrated with numerical simulation to characterize mechanical properties of rock materials, Journal of Testing and Evaluation, 42 (2014) 1-10.

[36] S.A. Epshtein, F.M. Borodich, S.J. Bull, Evaluation of elastic modulus and hardness of highly inhomogeneous materials by nanoindentation, Applied Physics A, 119 (2015) 325-335.

[37] D.C. Lin, E.K. Dimitriadis, F. Horkay, Robust strategies for automated AFM force curve analysis—I. Non-adhesive indentation of soft, inhomogeneous materials, Journal of Biomechanical Engineering, 129 (2007) 430-440.

[38] D.C. Lin, E.K. Dimitriadis, F. Horkay, Robust strategies for automated AFM force curve analysis—II: adhesion-influenced indentation of soft, elastic materials, Journal of Biomechanical Engineering, 129 (2007) 904-912.

[39] H.K. Heris, A.K. Miri, U. Tripathy, F. Barthelat, L. Mongeau, Indentation of poroviscoelastic vocal fold tissue using an atomic force microscope, Journal of the Mechanical Behavior of Biomedical Materials, 28 (2013) 383-392.

[40] J. Ophir, I. Cespedes, H. Ponnekanti, Y. Yazdi, X. Li, Elastography: a quantitative method for imaging the elasticity of biological tissues, Ultrason Imaging, 13 (1991) 111-134.

[41] M.S. Richards, R. Perucchio, M.M. Doyley, Visualizing the stress distribution within vascular tissues using intravascular ultrasound elastography: a preliminary investigation, Ultrasound in Medicine & Biology, 41 (2015) 1616-1631.

[42] B.M. Shapo, J.R. Crowe, A.R. Skovoroda, M.J. Eberle, N.A. Cohn, M. O'Donnell, Displacement and strain imaging of coronary arteries with intraluminal ultrasound, Ultrasonics, Ferroelectrics and Frequency Control, IEEE Transactions on, 43 (1996) 234-246.

[43] S.M. Wright, M.P. McDougall, Single echo acquisition MRI using RF encoding, NMR in Biomedicine, 22 (2009) 982–993.

[44] S.K. Venkatesh, M. Yin, J.F. Glockner, N. Takahashi, P.A. Araoz, J.A. Talwalkar, R.L. Ehman, Magnetic resonance elastography of liver tumors- preliminary results, AJR. American Journal of Roentgenology, 190 (2008) 1534-1540.

[45] T.M. Nguyen, S. Song, B. Arnal, E.Y. Wong, Z. Huang, R.K. Wang, M. O'Donnell, Shear wave pulse compression for dynamic elastography using phase-sensitive optical coherence tomography, Journal of Biomedical Optics, 19 (2014) 016013-016013.

[46] J.T. Butcher, D. Sedmera, R.E. Guldberg, R.R. Markwald, Quantitative volumetric analysis of cardiac morphogenesis assessed through micro-computed tomography, Developmental Dynamics, 236 (2007) 802-809.

[47] U. Zaleska-DorobiszA, K. KaczorowskiB, A. PawluśB, A. PuchalskaB, M. InglotB, Ultrasound elastography–review of techniques and its clinical applications, Brain, 6 (2013) 10-14.

[48] A.A. Oberai, N.H. Gokhale, G.R. Feijóo, Solution of inverse problems in elasticity imaging using the adjoint method, Inverse Problems, 19 (2003) 297.

[49] S. Goenezen, P. Barbone, A.A. Oberai, Solution of the nonlinear elasticity imaging inverse problem: The incompressible case, Computer Methods in Applied Mechanics and Engineering, 200 (2011) 1406-1420.

[50] A.A. Oberai, N.H. Gokhale, S. Goenezen, P. Barbone, T. Hall, A.M. Sommer, J. Jiang, Linear and nonlinear elasticity imaging of tissue in-vivo: Demonstration of feasibility, Physics in Medicine and Biology, 54 (2009) 1191-1207.

[51] Y. Mei, M. Tajderi, S. Goenezen, Regularizing biomechanical maps for partially known material properties, International Journal of Applied Mechanics, 09 (2017) 1750020.

[52] I. Sack, B. Beierbach, J. Wuerfel, D. Klatt, U. Hamhaber, S. Papazoglou, P. Martus, J. Braun, The impact of aging and gender on brain viscoelasticity, NeuroImage, 46 (2009).

[53] H. Tzschätzsch, S. Ipek-Ugay, M. Trong, J. Guo, J. Eggers, E. Gentz, T. Fischer, M. Schultz, J. Braun, S. I., Multifrequency time-harmonic elastography for the measurement of liver viscoelasticity in large tissue windows, Ultrasound in Medicine & Biology, 41 (2015) 724-733.

[54] A.R. Skovoroda, L.A. Lubinski, S.Y. Emelianov, M. O'Donnell, Reconstructive elasticity imaging for large deformations, IEEE Trans Ultrason Ferroelectr Freq Control, 46 (1999) 523-535.

[55] Y. Zhu, T. Hall, J. Jiang, A Finite-Element approach for Young's modulus reconstruction, IEEE Transactions on Medical Imaging, 22 (2003) 890-901.

[56] T.A. Krouskop, T.M. Wheeler, F. Kallel, B.S. Garra, T. Hall, Elastic moduli of breast and prostate tissues under compression, Ultrason Imaging, 20 (1998) 260-274.

[57] M.S. Richards, M.M. Doyley, Investigating the impact of spatial priors on the performance of model-based IVUS elastography, Physics in Medicine & Biology, 56 (2011) 7223 -7246.

[58] A.G. Zanman, G. Helft, S.G. Worthley, J.J. Badimon, The role of plaque rupture and thrombosis in coronary artery disease, Atherosclerosis, 149 (2000) 251-266.

[59] http://www.who.int/mediacentre/factsheets/fs310/en/

[60] S. Budday, R. Nay, R. de Rooij, P. Steinmann, T. Wyrobek, T.C. Ovaert, E. Kuhl, Mechanical properties of gray and white matter brain tissue by indentation, Journal of the Mechanical Behavior of Biomedical Materials, 46 (2015) 318-330.

[61] R. Dickenson, W. Hutton, The mechanical properties of bone in osteoporosis, Bone & Joint Journal, 63 (1981) 233-238.

[62] S. Goenezen, Inverse problems in finite elasticity: An application to imaging the nonlinear elastic properties of soft tissues, Rensselaer Polytechnic Institute, Troy, New York, 2011.

[63] T.Z. Pavan, E.L. Madsen, G.R. Frank, O.C.A. Adilton, T.J. Hall, Nonlinear elastic behavior of phantom materials for elastography, Physics in Medicine & Biology, 55 (2010) 2679-2692.

[64] N.H. Gokhale, P. Barbone, A.A. Oberai, Solution of the nonlinear elasticity imaging inverse problem: the compressible case, Inverse Problems, 24 (2008) 045010.

[65] F. Brezzi, Existence, uniqueness and approximation of saddle-point problems arising from Lagrangian multipliers, Revue Francaise D Automatique Informatique Recherche Operationnelle, 8 (1974) 129–151.

[66] I. Babuška, The finite element method with Lagrangian multipliers, Numerische Mathematik, 20 (1973) 179-192.

[67] T.J.R. Hughes, The finite element method linear static and dynamic finite element enalysis, Courier Corporation, New York, 2012.

[68] A.M. Maniatty, Y. Liu, O. Klaas, M.S. Shephard, Higher order stabilized finite element method for hyperelastic finite deformation, Computer Methods in Applied Mechanics and Engineering, 191 (2002) 1491-1503.

[69] R.H. Byrd, P. Lu, J. Nocedal, C. Zhu, A limited memory algorithm for bound constrained optimization, SIAM J. Scientific Computing 16 (1995) 1190-1208.

[70] C. Zhu, R.H. Byrd, P. Lu, J. Nocedal, L-BFGS-B: FORTRAN Subroutines for Large Scale Bound Constrained Optimization, Tech. Report, NAM-11, EECS Department, Northwestern University, Evanston, Illinois, 1994.

[71] C. Zhu, R.H. Byrd, P. Lu, J. Nocedal, L-BFGS-B: a limited memory FORTRAN code for solving bound constrained optimization problems Tech. Report, NAM-11, EECS Department, Northwestern University, Evanston, Illinois, 1994.

[72] D. Calvetti, S. Morigi, L. Reichel, F. Sgallari, Tikhonov regularization and the L-curve for large discrete ill-posed problems, Journal of Computational and Applied Mathematics, 123 (2000) 423–446.

[73] A.V. Chvetsov, L-curve analysis of radiotherapy optimization problems, Medical Physics, 32 (2005) 2598-2605.

[74] C.R. Vogel, Non-convergence of the L-curve regularization parameter selection method, Inverse Problems, 12 (1996) 535.

[75] C.R. Vogel, Computational methods for inverse problems, Society for Industrial and Applied Mathematics, Philadelphia, PA, USA, 2002.

[76] O. Dorn, H. Bertete-Aguirre, J.G. Berryman, G.C. Papanicolaou, A nonlinear inversion method for 3D electromagnetic imaging using adjoint fields, Inverse Problems, 15 (1999) 1523.

[77] J.N. Reddy, C.N. Chin, Thermomechanical analysis of functionally graded cylinders and plates, Journal of Thermal Stresses, 21 (1998) 593-626.

[78] G.N. Praveen, J.N. Reddy, Nonlinear transient thermoelastic analysis of functionally graded ceramic-metal plates, International Journal of Solids and Structures, 25 (1998) 4457-4476.

[79] J.N. Reddy, Analysis of functionally graded plates, International Journal for Numerical Methods in Engineering, 47 (2000) 663-684.

[80] Y. Mei, S. Goenezen, Spatially weighted objective function to solve the inverse problem in elasticity for the elastic property distribution, in: B.J. Doyle, K. Miller, A. Wittek, P.M.F. Nielson (Eds.) Computational Biomechanics for Medicine: New Approaches and New Applications Springer NY, 2015.

[81] M.M. Doyley, P.M. Meaney, J.C. Bamber, Evaluation of an iterative reconstruction method for quantitative elastography, Physics in Medicine & Biology, 45 (2000) 1521-1540.

[82] S. Goenezen, J.F. Dord, Z. Sink, P. Barbone, J. Jiang, T.J. Hall, A.A. Oberai, Linear and nonlinear elastic modulus imaging: An application to breast cancer diagnosis, Medical Imaging, IEEE Transactions on, 31 (2012) 1628-1637.

[83] S. Goenezen, A.A. Oberai, J. Dord, Z. Sink, P. Barbone, Nonlinear elasticity imaging Bioengineering Conference (NEBEC), 2011 IEEE 37th Annual Northeast 2011, pp. 1 - 2

[84] T. Hall, P.E. Barbone, A.A. Oberai, J. Jiang, J. Dord, S. Goenezen, T. Fisher, Recent Results in Nonlinear Strain and Modulus Imaging, Current Medical Imaging Reviews, 7 (2011) 313-327.

[85] F. Kallel, M. Bertrand, Tissue elasticity reconstruction using linear perturbation method, Medical Imaging, IEEE Transactions on, 15 (1996) 299-313.

[86] T.J.R. Hughes, L.P. Franca, M. Balestra, A new finite element formulation for computational fluid dynamics: V. Circumventing the babuska-brezzi condition: a stable Petrov-Galerkin formulation of the stokes problem accommodating equal-order interpolations, Computer Methods in Applied Mechanics and Engineering, 59 (1986) 85-99.

[87] L. Robert, F. Nazaret, T. Cutard, J.J. Orteu, Use of 3-D digital image correlation to characterize the mechanical behavior of a fiber reinforced refractory castable, Experimental Mechanics, 47 (2007) 761-773.

[88] Y. Mei, S. Kuznetsov, S. Goenezen, Reduced boundary sensitivity and improved contrast of the regularized inverse problem solution in elasticity, Journal of Applied Mechanics 83 (2016) 031001.

[89] L. Robert, F. Nazaret, T. Cutard, J.-J. Orteu, Use of 3-D digital image correlation to characterize the mechanical behavior of a fiber reinforced refractory castable, Experimental Mechanics, 47 (2007) 761-773.

[90] Y. Mei, R. Fulmer, V. Raja, S.C. Wang, S. Goenezen, Estimating the non-homogeneous elastic modulus distribution from surface deformations, International Journal of Solids and Structures, 83 (2016) 73-80.

[91] C.L. Johnson, M.D.J. McGarry, E.E.W. Van Houten, J.B. Weaver, K.D. Paulsen, B.P. Sutton, J.G. Georgiadis, Magnetic resonance elastography of the brain using multishot spiral readouts with self-navigated motion correction, Magnetic Resonance in Medicine, 70 (2013) 404-412.

[92] R. Muthupillai, D. Lomas, P. Rossman, J. Greenleaf, A. Manduca, R. Ehman, Magnetic resonance elastography by direct visualization of propagating acoustic strain waves, Science, 269 (1995) 1854-1857.

[93] S.F. Othman, H. Xu, T.J. Royston, R.L. Magin, Microscopic magnetic resonance elastography (μMRE), Magnetic Resonance in Medicine, 54 (2005) 605-615.

[94] I. Sack, G. Buntkowsky, J. Bernarding, J. Braun, Magnetic resonance elastography: A method for the noninvasive and spatially resolved observation of phase transitions in gels, Journal of the American Chemical Society 123 (2001) 11087-11088.

[95] N.S. Shah, S.A. Kruse, D.J. Lager, G. Farell-Baril, J.C. Lieske, B.F. King, R. Ehman, Evaluation of renal parenchymal disease in a rat model with magnetic resonance elastography, Magnetic Resonance in Medicine, 52 (2004) 56-64.

[96] E.S. Burnside, T.J. Hall, A.M. Sommer, G.K. Hesley, G.A. Sisney, W.E. Svensson, N.J. Hangiandreou, Ultrasound strain imaging to improve the decision to biopsy solid breast masses, Radiology, 245 (2007) 401-410.

[97] T.J. Hall, Y. Zhu, C.S. Spalding, In vivo real-time freehand palpation imaging, Ultrasound in Medicine & Biology, 29 (2003) 427-435.

[98] D.M. Regner, G.K. Hesley, N.J. Hangiandreou, M.J. Morton, M.R. Nordland, D.D. Meixner, T.J. Hall, M.A. Farrell, J.N. Mandrekar, W.S. Harmsen, J.W. Charboneau,

Breast lesions: evaluation with US strain imaging--clinical experience of multiple observers, Radiology, 238 (2006) 425-437.

[99] R. Chan, A. Chau, W. Karl, S. Nadkarni, A. Khalil, N. Iftimia, M. Shishkov, G. Tearney, M. Kaazempur-Mofrad, B. Bouma, OCT-based arterial elastography: robust estimation exploiting tissue biomechanics, Opt Express, 12 (2004) 4558-4572.

[100] J. Schmitt, OCT elastography: imaging microscopic deformation and strain of tissue, Opt Express, 3 (1998) 199-211.

[101] M.I. Diaza, W. Aquinoa, M. Bonnet, A modified error in constitutive equation approach for frequency-domain viscoelasticity imaging using interior data, Comput. Methods Appl. Mech. Engrg., 296 (2015) 129-149.

[102] A.J. Romano, J.A. Bucaro, B.H. Houston, J.L. Kugel, P. Rossman, R.C. Grimm, R. Ehman, On the feasibility of elastic wave visualization within polymeric solids using magnetic resonance elastography, Journal of the Acoustical Society of America, 116 (2004) 125-132.

[103] J. Ophir, S.K. Alam, B. Garra, F. Kallel, E. Konofagou, T. Krouskop, T. Varghese, Elastography: ultrasonic estimation and imaging of the elastic properties of tissues, Proceedings of the Institution of Mechanical Engineers, Part H: Journal of Engineering in Medicine, 213 (1999) 203-233.

[104] P. Barbone, A.A. Oberai, J.C. Bamber, G.P. Berry, J. Dord, E.R. Ferreira, S. Goenezen, T. Hall, Biomechanical imaging: elastography beyond Young's modulus, CRC Handbook of Imaging in Biological Mechanics, (2014).

[105] E.K. Dimitriadis, F. Horkay, J. Maresca, B. Kachar, R.S. Chadwick, Determination of elastic moduli of thin layers of soft material using the atomic force Mmicroscope, Biophysical Journal 82 (2002) 2798-2810.

[106] A. Lundkvist, E. Lilleodden, W. Siekhaus, J. Kinney, L. Pruitt, M. Balooch, Viscoelastic properties of healthy human artery measured in saline solution by AFM-based indentation technique, MRS Proceedings, 436 (1996) 353-358.

[107] M. Stolz, R. Raiteri, A.U. Daniels, M.R. VanLandingham, W. Baschog, U. Aebi, Dynamic elastic modulus of porcine articular cartilage determined at two different levels of tissue organization by indentation-yype atomic force microscopy, Biophysical Journal, 86 (2004) 3269-3283.

[108] Y.Z. Zhu, Z.X. Dong, U.C. Wejinya, S. Jin, K.M. Ye, Determination of mechanical properties of soft tissue scaffolds by atomic force microscopy nanoindentation, Journal of Biomechanics, 44 (2011) 2356-2361.

[109] Z.K. Meng, R. Baker, V.V. Yakovlev, Brillouin spectroscopy reveals changes in muscular viscoelasticity in Drosophila POMT mutants, Proc. SPIE 9327, Optical Elastography and Tissue Biomechanics II, 9327 (2015) 932713.

[110] Z.K. Meng, V.V. Yakovlev, Probing microscopic mechanical properties of hard tissues with Brillouin spectroscopy, Proc. SPIE 9303, Photonic Therapeutics and Diagnostics XI, 9303 (2015) 930342.

[111] Z.K. Meng, V.V. Yakovlev, Optimizing signal collection efficiency of the VIPA-based Brillouin spectrometer, Journal of Innovative Optical Health Sciences, 08 (2015) 1550021.

[112] Z.K. Meng, V.V. Yakovlev, Brillouin spectroscopy characterizes microscopic viscoelasticity associated with skin injury, Proc. SPIE 9321, Optical Interactions with Tissue and Cells XXVI, 9321 (2015) 93210C.

[113] M. Tyagi, S. Goenezen, P. Barbone, A.A. Oberai, Algorithms for quantitative quasi-static elasticity imaging using Force Data, International Journal for Numerical Methods in Biomedical Engineering, 30 (2014) 1421-1436.

[114] J.Z. Abbas Samani, D. Plewes, Elastic moduli of normal and pathological human breast tissues: an inversion-technique-based investigation of 169 samples, Physics In Medicine and Biology, 52 (2007) 1565-1576.

[115] R.A. Baldewsing, C.L. De Korte, J.A. Schaar, F. Mastik, A.F.W. Van der Steen, Finite element modeling and intravascular ultrasound elastography of vulnerable plaques: parameter variation, Ultrasonics, 42 (2004).

[116] R.A. Baldewsing, C.L. De Korte, J.A. Schaar, F. Mastik, A.F.W. Van der Steen, A finite element model for performing intravascular ultrasound elastography of human atherosclerotic coronary arteries, Ultrasound in Medicine & Biology, 30 (2004).

[117] D.U. Silverthorn, Human Physiology: An Integrated Approach(Fifth Edition), 538 ed., Pearson/Benjamin Cummings, London, 2010.

[118] G. Falzon, S. Pearson, R. Murison, Analysis of collagen fibre shape changes in breast cancer, Physics in Medicine and Biology, 53 (2008) 6641-6652.

[119] P.E. Barbone, N.H. Gokhale, Elastic modulus imaging: on the uniqueness and nonuniqueness of the elastography inverse problem in two dimensions, Inverse Problems, 20 (2004) 283.

[120] S.W. Shore, P.E. Barbone, A.A. Oberai, E.F. Morgan, Transversely isotropic elasticity imaging of cancellous bone, Journal of Biomechanical Engineering, 133 (2011) 061002.

[121] S. Guchhait, B. Banerjee, Anisotropic linear elastic parameter estimation using error in the constitutive equation functional, Proceedings of the Royal Society a Mathematical Physical and Engineering Sciences, 472 (2016) 20160213.

[122] S.W. Tsai, N.J. Pagano, Invariant properties of composite materials, DTIC Document, 1968.

[123] G. Boyer, J. Molimard, M.B. Tkaya, H. Zahouani, M. Pericoi, S. Avril, Assessment of the in-plane biomechanical properties of human skin using a finite element model updating approach combined with an optical full-field measurement on a new tensile device, Journal of the Mechanical Behavior of Biomedical Materials, 27 (2013) 273-282.

[124] M.G. Simon, J.; Papazoglou, S.; Scholand-Engler, H.; Erdmann, C.; Melchert, U.; Bonsanto, M.; Braun, J.; Petersen, D.; Sack, I.; Wuerfel, J., Non-invasive characterization of intracranial tumors by magnetic resonance elastography, New Journal of Physics, 15 (2013).

[125] E. Park, A.M. Maniatty, Shear modulus reconstruction in dynamic elastography: Time harmonic case, Physics in Medicine and Biology, 51 (2006) 3697-3721.

[126] M. Yin, O. Rouviere, R.L. Ehman, Shear wave diffraction fields generated by longitudinal MRE drivers, Proceedings Of The International Society For Magnetic Resonance In Medicine, 2005.

[127] B. Banerjee, T.F. Walsh, W. Aquino, B. M., Large scale parameter estimation problems in frequency-domain elastodynamics using an error in constitutive equation functional, Computer Methods in Applied Mechanics and Engineering, 253 (2013) 60-72.

[128] T.E. Oliphant, A. Manduca, R.L. Ehman, J.F. Greenleaf, Complex-valued stiffness reconstruction for magnetic resonance elastography by algebraic inversion of the differential equation, Magnetic Resonance in Medicine, 45 (2001).

[129] T. Boulet, M.L. Kelso, S.F. Othman, Microscopic magnetic resonance elastography of traumatic brain injury model, J Neuroscience Methods, 201 (2011) 296-306.

[130] S. Papazoglou, U. Hamhaber, J. Braun, I. Sack, Algebraic Helmholtz inversion in planar magnetic resonance elastography, Physics in Medicine & Biology, 53 (2008) 3147-3158.

[131] A.J. Romano, P.B. Abraham, P.J. Rossman, J.A. Bucaro, R.L. Ehman, Determination and analysis of guided wave propagation using magnetic resonance elastography, Magnetic Resonance in Medicine, 54 (2005) 893-900.

[132] A. Romano, J. Guo, T. Prokscha, T. Meyer, S. Hirsch, J. Braun, I. Sack, M. Scheel, In vivo waveguide elastography: effects of neurodegeneration in patients with amyotrophic lateral sclerosis, Magnetic Resonance in Medicine, 72 (2014) 1755-1761.

[133] E.E. Van Houten, K.D. Paulsen, M.I. Miga, F.E. Kennedy, J.B. Weaver, An Overlapping Subzone Technique for MR-Based Elastic Property Reconstruction, Magnetic Resonance in Medicine, 42 (1999) 779-786.

[134] M.A. Green, L.E. Bilston, R. Sinkus, In vivo brain viscoelastic properties measured by magnetic resonance elastography, NMR in biomedicine, 21 (2008).

[135] R.M. Christensen, Theory of Viscoelasticity, Dover Publications, New York, 2003.

[136] R.S. Lakes, Viscoelastic materials, Cambridge University Press, Cambridge, 2009.

APPENDIX A

Derivation of the stabilization term

Before simplifying stabilization term, two useful equations will be introduced:

The Piola identity $$\nabla \cdot \left(J\mathbf{F}^{-T} \right) = \mathbf{0} \tag{A.1}$$

$$\frac{\partial J}{\partial \mathbf{C}} = \frac{1}{2} J\mathbf{C}^{-1} \tag{A.2}$$

Now, the stabilization term can be simplified as:

$$\begin{aligned} & D\left(\mathbf{W}^h, \mathbf{U}^h; \beta \right) \\ & = -\sum_{i=1}^{n} 2\left(\tau \nabla \cdot \left(\mathbf{F} \frac{\partial W}{\partial \mathbf{C}} \right), \mathbf{F}^{-T} \nabla q^h \right)_{\Omega_0^i} + \sum_{i=1}^{n} \left(\tau \nabla \cdot \left(p^h J\mathbf{F}\mathbf{C}^{-1} \right), \mathbf{F}^{-\mathrm{T}} \nabla q^h \right)_{\Omega_0^i} \end{aligned} \tag{A.3}$$

$$= -\sum_{i=1}^{n} 2\left(\tau \left(\mathbf{F} \nabla \cdot \left(\frac{\partial W}{\partial \mathbf{C}} \right) + \nabla \cdot \mathbf{F} \frac{\partial W}{\partial \mathbf{C}} \right), \mathbf{F}^{-T} \nabla q^h \right)_{\Omega_0^i} + \sum_{i=1}^{n} \left(\tau \nabla \cdot \left(p^h J\mathbf{F}\mathbf{F}^{-1}\mathbf{F}^{-T} \right), \mathbf{F}^{-T} \nabla q^h \right)_{\Omega_0^i}$$

(A.4)

$$= -\sum_{i=1}^{n} 2\left(\tau \mathbf{F} \nabla \cdot \left(\frac{\partial W}{\partial \mathbf{C}} \right), \mathbf{F}^{-T} \nabla q^h \right)_{\Omega_0^i} + \sum_{i=1}^{n} \left(\tau J\mathbf{F}^{-T} \nabla p^h, \mathbf{F}^{-T} \nabla q^h \right)_{\Omega_0^i} \tag{A.5}$$

From **Equation (A.4)** to **(A.5)**, $\nabla \cdot \mathbf{F} = \mathbf{0}$ is utilized as the problem domain is discretized by linear triangular elements. In this case, the displacement is interpolated by a linear function in each element, thus the second order spatial derivative of the displacement is zero. If **Equation (A.5)** is expressed in the integral form, it can be further simplified:

$$D\left(\mathbf{W}^h, \mathbf{U}^h; \beta\right)$$

$$= -\sum_{i=1}^{n} \int_{\Omega_0^i} 2\tau \mathbf{F}^T \mathbf{F}^{-T} \nabla q^h \cdot \left(\nabla \cdot \left(\frac{\partial W}{\partial \mathbf{C}} \right) \right) d\Omega_0^i + \sum_{i=1}^{n} \int_{\Omega_0^i} \tau J \mathbf{F}^{-1} \mathbf{F}^{-\mathrm{T}} \nabla q^h \cdot \nabla p^h d\Omega_0^i \tag{A.6}$$

$$= -\sum_{i=1}^{n} \int_{\Omega_0^i} 2\tau \nabla q^h \cdot \left(\nabla \cdot \left(\frac{\partial W}{\partial \mathbf{C}} \right) \right) d\Omega_0^i + \sum_{i=1}^{n} \int_{\Omega_0^i} \tau J \mathbf{C}^{-1} \nabla q^h \cdot \nabla p^h d\Omega_0^i \tag{A.7}$$

APPENDIX B

Linearization of the stabilized weak form

The linearized formulation of the stabilized weak form can be derived by perturbing an infinitesimal quantity, $\Delta\mathbf{U}^h = \left[\Delta\mathbf{u}^h, \Delta p^h\right]$, that is,

$$B\left(\mathbf{W}^h, \Delta\mathbf{U}^h; \beta, \mathbf{U}^h\right) = \lim_{\varepsilon\to 0}\frac{d}{d\varepsilon}\left(A\left(\mathbf{W}^h, \mathbf{U}^h + \varepsilon\Delta\mathbf{U}^h; \beta\right) + D\left(\mathbf{W}^h, \mathbf{U}^h + \varepsilon\Delta\mathbf{U}^h; \beta\right)\right) \tag{B.1}$$

Computing the first term on the right hand side in **Equation (B.1)** yields

$$\begin{aligned}
&\lim_{\varepsilon\to 0}\frac{d}{d\varepsilon}A\left(\mathbf{W}^h, \mathbf{U}^h + \varepsilon\Delta\mathbf{U}^h; \beta\right) \\
&= \lim_{\varepsilon\to 0}\int_{\Omega_0} w^h_{i,j}\left(\frac{dF_{im}\left(\mathbf{u}^h + \varepsilon\Delta\mathbf{u}^h\right)}{d\varepsilon}S_{mj} + F_{im}\frac{\partial S_{mj}}{\partial C_{nk}}\frac{dC_{nk}\left(\mathbf{u}^h + \varepsilon\Delta\mathbf{u}^h\right)}{d\varepsilon}\right)d\Omega_0 \\
&+ \lim_{\varepsilon\to 0}\int_{\Omega_0} w^h_{i,j}F_{im}\frac{dS_{mj}\left(p^h + \varepsilon\Delta p^h\right)}{d\varepsilon}d\Omega_0 + \int_{\Omega_0} q^h\frac{\partial J}{\partial C_{\alpha\beta}}\frac{dC_{\alpha\beta}\left(\mathbf{u}^h + \varepsilon\Delta\mathbf{u}^h\right)}{d\varepsilon}d\Omega_0
\end{aligned} \tag{B.2}$$

where

$$\lim_{\varepsilon\to 0}\frac{d\mathbf{F}\left(\mathbf{u}^h + \varepsilon\Delta\mathbf{u}^h\right)}{d\varepsilon} = \nabla\left(\Delta\mathbf{u}^h\right) \tag{B.3}$$

$$\lim_{\varepsilon\to 0}\frac{d\mathbf{C}\left(\mathbf{u}^h + \varepsilon\Delta\mathbf{u}^h\right)}{d\varepsilon} = \nabla\left(\Delta\mathbf{u}^h\right)^{\mathrm{T}}\mathbf{F} + \mathbf{F}^{\mathrm{T}}\nabla\left(\Delta\mathbf{u}^h\right) \tag{B.4}$$

Inserting **Equations (B.3)** and **(B.4)** into **Equation (B.2)** yields

$$
\begin{aligned}
&\lim_{\varepsilon\to 0}\frac{d}{d\varepsilon}A\left(\mathbf{W}^h,\mathbf{U}^h+\varepsilon\Delta\mathbf{U}^h;\beta\right)\\
&=\lim_{\varepsilon\to 0}\int_{\Omega_0} w^h_{i,j}\left(\Delta u^h_{i,m}S_{mj}+2F_{im}\frac{\partial S_{mj}}{\partial C_{nk}}F_{tk}\Delta u^h_{\mathrm{t,n}}\right)d\Omega_0\\
&+\lim_{\varepsilon\to 0}\int_{\Omega_0} w^h_{i,j}F_{im}\frac{dS_{mj}\left(p^h+\varepsilon\Delta p^h\right)}{d\varepsilon}d\Omega_0+\int_{\Omega_0}q^h\frac{\partial J}{\partial C_{\alpha\beta}}\left(\Delta u^h_{s,\alpha}F_{s\beta}+F_{\mathrm{t}\alpha}\Delta u^h_{\mathrm{t},\beta}\right)d\Omega_0\\
&=\lim_{\varepsilon\to 0}\int_{\Omega_0} w^h_{i,j}\left(\delta_{it}S_{mj}+2F_{in}F_{tk}\frac{\partial S_{nj}}{\partial C_{km}}\right)\Delta u^h_{\mathrm{t,m}}\,d\Omega_0\\
&-\lim_{\varepsilon\to 0}\int_{\Omega_0} w^h_{i,j}F^{-1}_{ji}\Delta p^h J d\Omega_0+\int_{\Omega_0}q^h JF^{-1}_{ji}\Delta u^h_{i,j}\,d\Omega_0
\end{aligned}
\tag{B.5}
$$

where $M_{ijkl}=2\partial S_{ij}/\partial C_{kl}$ is the tangent modulus. As the 2nd Piola Kirchhoff stress tensor and the right Green strain tensor are symmetry, i.e., $M_{ijkl}=M_{jikl}=M_{ijlk}$. For the strain energy density function **(2.7)**, the tangent modulus can be expressed as

$$
\begin{aligned}
M_{ijkl}&=4\frac{\partial^2 W}{\partial C_{ij}\partial C_{kl}}-2\frac{\partial}{\partial C_{kl}}\left(pJC^{-1}_{ij}\right)\\
&=2\mu e^{\kappa}\left(d_{ijkl}+\gamma Q_{ij}Q_{kl}-\frac{1}{3}C^{-1}_{kl}Q_{ij}\right)-p\chi_{ijkl}
\end{aligned}
\tag{B.6}
$$

Where

$$\kappa=\gamma\left(J^{-2/3}I_1-3\right) \tag{B.7}$$

$$d_{ijkl}=\frac{1}{6}J^{-2/3}I_1\left(C^{-1}_{ik}C^{-1}_{jl}+C^{-1}_{il}C^{-1}_{jk}\right)-\frac{1}{3}J^{-2/3}\delta_{kl}C^{-1}_{ij} \tag{B.8}$$

$$Q_{ij}=J^{-2/3}\left(\delta_{ij}-\frac{1}{3}I_1C^{-1}_{ij}\right) \tag{B.9}$$

$$\chi_{ijkl}=J\left(C^{-1}_{ij}C^{-1}_{kl}-C^{-1}_{ik}C^{-1}_{jl}-C^{-1}_{il}C^{-1}_{jk}\right) \tag{B.10}$$

To arrive at **Equation (B.6)**, we should use following relations

$$\frac{\partial I_1}{\partial\mathbf{C}}=\mathbf{I} \tag{B.11}$$

$$\frac{\partial C_{ij}^{-1}}{\partial C_{kl}} = -\frac{1}{2}\left(C_{ik}^{-1}C_{lj}^{-1} + C_{il}^{-1}C_{kj}^{-1}\right) \tag{B.12}$$

The linearization procedure of the stabilization term is very similar to that of the first term in **Equation (B.1)**, by perturbing $\left[\mathbf{u}^h, p^h\right]$ a very small quantity:

$$\begin{aligned}
&\lim_{\varepsilon\to 0}\frac{d}{d\varepsilon}D\left(\mathbf{W}^h, \mathbf{U}^h + \varepsilon\Delta\mathbf{U}^h; \beta\right) \\
&= -\sum_{i=1}^{n}\int_{\Omega_0^i}\lim_{\varepsilon\to 0}\frac{d}{d\varepsilon}\left(2\tau\nabla q^h\cdot\left(\nabla\cdot\left(\frac{\partial W\left(\mathbf{u}^h+\varepsilon\Delta\mathbf{u}^h\right)}{\partial\mathbf{C}}\right)\right)\right)d\Omega_0^i \\
&+\sum_{i=1}^{n}\int_{\Omega_0^i}\lim_{\varepsilon\to 0}\frac{d}{d\varepsilon}\left(\tau J\mathbf{C}^{-1}\left(\mathbf{u}^h+\varepsilon\Delta\mathbf{u}^h\right)\nabla q^h\cdot\nabla\left(p^h+\varepsilon\Delta p^h\right)\right)d\Omega_0^i
\end{aligned} \tag{B.13}$$

The calculus of the first term on the right-hand side of **Equation (B.13)** is shown below:

$$\begin{aligned}
&\sum_{i=1}^{n}\int_{\Omega_0^i}\lim_{\varepsilon\to 0}\frac{d}{d\varepsilon}\left(2\tau\nabla q^h\cdot\left(\nabla\cdot\left(\frac{\partial W\left(\mathbf{u}^h+\varepsilon\Delta\mathbf{u}^h\right)}{\partial\mathbf{C}}\right)\right)\right)d\Omega_0^i \\
&=\sum_{i=1}^{n}\int_{\Omega_0^i}\left(\tau\nabla q^h\cdot\lim_{\varepsilon\to 0}\frac{d}{d\varepsilon}\left(e^{\kappa\left(\mathbf{u}^h+\varepsilon\Delta\mathbf{u}^h\right)}\boldsymbol{\xi}\left(\mathbf{u}^h+\varepsilon\Delta\mathbf{u}^h\right)\cdot\left(\nabla\mu+\mu\frac{\kappa\left(\mathbf{u}^h+\varepsilon\Delta\mathbf{u}^h\right)}{\gamma}\nabla\gamma\right)\right)\right)d\Omega_0^i
\end{aligned} \tag{B.14}$$

where $\boldsymbol{\xi} = -\frac{1}{3}J^{-2/3}\mathbf{I}_1\mathbf{C}^{-1} + J^{-2/3}\mathbf{I}$. Here we also utilize the property of the linear triangular element, i.e., $\nabla\cdot\mathbf{F} = \mathbf{0}$. Using following equations:

$$R = \lim_{\varepsilon\to 0}\frac{d\kappa\left(\mathbf{u}^h+\varepsilon\Delta\mathbf{u}^h\right)}{d\varepsilon} = 2\gamma J^{-2/3}\left(\mathbf{I}-\frac{1}{3}\mathbf{I}_1\mathbf{C}^{-1}\right):\left(\mathbf{F}^T\cdot\nabla\left(\Delta\mathbf{u}^h\right)\right) \tag{B.15}$$

$$\begin{aligned}
\boldsymbol{\Theta} &= \lim_{\varepsilon\to 0}\frac{d\boldsymbol{\xi}\left(\mathbf{u}^h+\varepsilon\Delta\mathbf{u}^h\right)}{d\varepsilon} = -\frac{4}{3}J^{-2/3}\mathbf{F}^{-1}:\left(\nabla\left(\Delta\mathbf{u}^h\right)\right)^T\mathbf{I} \\
&+\frac{1}{3}J^{-2/3}\mathbf{I}_1\left(\frac{2}{3}\left(\mathbf{F}^{-1}:\left(\nabla\left(\Delta\mathbf{u}^h\right)\right)^T\right)\mathbf{C}^{-1} - 2\frac{\partial\mathbf{C}^{-1}}{\partial\mathbf{C}}:\left(\mathbf{F}^T\left(\nabla\left(\Delta\mathbf{u}^h\right)\right)\right)\right)
\end{aligned} \tag{B.16}$$

Equation (B.14) can be written as:

$$\sum_{i=1}^{n}\int_{\Omega_0^i}\lim_{\varepsilon\to 0}\frac{d}{d\varepsilon}\left(2\tau\nabla q^h\cdot\left(\nabla\cdot\left(\frac{\partial W\left(\mathbf{u}^h+\varepsilon\Delta\mathbf{u}^h\right)}{\partial\mathbf{C}}\right)\right)\right)d\Omega_0^i = \tag{B.17}$$
$$\sum_{i=1}^{n}\int_{\Omega_0^i}\left(\tau\nabla q^h e^{\kappa}\cdot\left(R\boldsymbol{\xi}\cdot\left(\nabla\mu+\mu\frac{\kappa}{\gamma}\nabla\gamma\right)+\boldsymbol{\Theta}\cdot\left(\nabla\mu+\mu\frac{\kappa}{\gamma}\nabla\gamma\right)+\boldsymbol{\xi}\cdot\left(\mu\frac{R}{\gamma}\nabla\gamma\right)\right)\right)d\Omega_0^i$$

The second term of the right hand side of **Equation (B.13)** can be simplified in the same way, yielding:

$$\sum_{i=1}^{n}\int_{\Omega_0^i}\lim_{\varepsilon\to 0}\frac{d}{d\varepsilon}\left(\tau J\mathbf{C}^{-1}\left(\mathbf{u}^h+\varepsilon\Delta\mathbf{u}^h\right)\nabla q^h\cdot\nabla\left(p^h+\varepsilon\Delta p^h\right)\right)d\Omega_0^i \tag{B.18}$$
$$=\sum_{i=1}^{n}2\int_{\Omega_0^i}\tau\left(2\frac{\partial^2 J}{C_{ij}C_{kl}}F_{ml}q^h_{,j}p^h_{,i}\Delta u_{m,k}+\frac{\partial J}{C_{ij}}q^h_{,j}p^h_{,i}\right)d\Omega_0^i$$